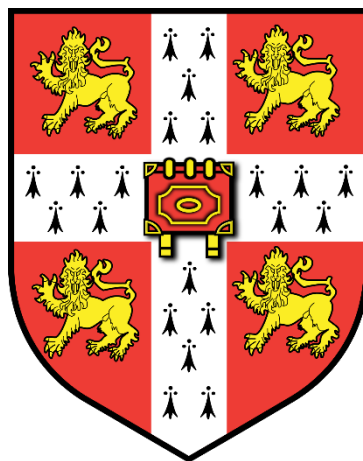# Self-assembled peptide as a
long-acting drug formulation

Sonja Kinna

Department of Engineering, University of Cambridge

This dissertation is submitted for the degree of
Doctor of Philosophy

Supervision:

Prof. Sir Mark Welland
The Nanoscience Centre, University of Cambridge

Ana Dos Santos, PhD
Biophysical Department, MedImmune

St Edmund's College   October 2019

Self-assembled peptide as a long-acting drug formulation

Sonja Kinna

Abstract

Type 2 Diabetes Mellitus (T2DM) and obesity are widespread and associated metabolic diseases with worldwide rising prevalence [1]. The gut hormone Oxyntomodulin induces satiety and normalizes hyperglycaemia without risk of hypoglycaemic excursions [2]. However, native incretin hormones are quickly degraded by peptidases and renally excreted, which has so far impaired pharmaceutical exploitation of anorectic and glucose-homeostatic activities [3]. It is known that many – if not all – peptides can be converted to self-assembled nanostructures [4]. Amyloid fibrils are characterized by enhanced chemical, biological and mechanic stability compared to soluble peptides, and allow a controlled release by dissociation of monomers from the fibril termini [5]. Here I propose self-assembled peptides as a prolonged-activity, self-mediated drug delivery system for subcutaneous injection of pharmaceutically active drugs. Oxyntomodulin is used as a model peptide due to previously futile attempts at finding long-acting analogues, and Oxyntomodulin's so far unreported self-assembly behaviour. This thesis shows a method to reproducibly form subcutaneously injectable Oxyntomodulin fibrils with high conversion yield and low polydispersity, as well as methods to characterize morphology, kinetics and thermodynamics of Oxyntomodulin self-assembly. Oxyntomodulin fibrils display amyloid-like characteristics and release soluble peptide in a peptide-deprived environment. Association and dissociation kinetics and thermodynamics are sensitively dependent on salts and temperature, with an association temperature optimum at room temperature that is unique in amyloid-type self-assembly. An alternative fibril type forms under different conditions and displays altered fibrillation kinetics and thermodynamics. The specificity of fibrillation to the peptide sequence is shown in presence of Oxyntomodulin's sister peptide glucagon and the analogue Aib-2-Oxyntomodulin. Extended release of active peptide from a subcutaneous Oxyntomodulin fibril depot has been proved in rodent studies at MedImmune [6]. As amyloid-like self-assembly is a generic feature of the peptide chain, the strategies and methods described in this project can be applied to other pharmaceutically active peptides and proteins.

Acknowledgements

My gratitude goes to Prof. Sir Mark E. Welland for supervising my PhD project. I especially appreciate the freedom of choosing experiments, lectures and workshops, and seek guidance when necessary. It is a pleasure and an honour to work in such a friendly, helpful and trusting environment.

I thank Myriam Ouberaï, PhD, for her support and feedback, and all the shared knowledge. This made it very easy for me to start, progress, and interpret my results. To the Nanoscience staff and students, thanks for the nice atmosphere and the interesting lunchtime conversations. To Rebecca Kershaw, thank you for letting my use your custom-made QCM-D sensor deposition device – chapter 5 would have been very difficult without this.

I would also like to thank Dr. Ana Dos Santos for supervising me at MedImmune. It is very helpful and motivating to get insights from industry. I always looked forward to our exceptionally enjoyable and constructive meetings. I would like to acknowledge Leanne Amery and Dr. Jay Pathak for their help with viscosity measurements, Dr. Silvia Sonzini for assistance with ITC measurements, and Frederik Becher for support with CD measurements. To the MedImmune formulation team, many thanks for the thought-provoking meetings and the generous invitation to various social and training events.

Special thanks goes to the FEI Cryo electron microscopy team at the Nanoscience Centre for providing me with 200 GB images and assistance in their interpretation.

I am incredibly lucky and grateful to have grown up in a loving and caring family. My parents Karin and Jürgen have always been overly generous in their love and support, and my sister Martina has always been a role model in her smartness and kindness. You provided me with the environment to find and develop my talents, without ever measuring me at my success and failure. Thank you. To my partner Reuben, thank you - for being generally awesome.

Abbreviations

Å	Ångström, 10^{-1} m
Aib	Aminoisobutyric acid
AFM	atomic force microscopy
ATR	attenuated total reflection
CD	circular dichroism
C_p	heat capacity
Da	Dalton (= $g\ mol^{-1}$)
DPP-4	dipeptidyl peptidase 4
EM	electron microscopy
FTIR	Fourier transform infrared spectroscopy
G	Gibbs' free energy
GCGR	glucagon receptor
GLP-1	glucagon-like peptide 1
GLP-1R	glucagon-like peptide 1 receptor
GnRH	gonadotropin releasing hormone
H	enthalpy
HPLC	high performance liquid chromatography
K	universal gas constant, ~8.314 $J\ K^{-1}\ mol^{-1}$
k_-	rate of fragmentation
k_{app}	apparent growth rate
K_D	dissociation constant
k_{off}	rate of a reverse reaction
k_{on}	rate of a forward reaction
m	soluble peptide concentration
M	fibril mass concentration
MS	mass spectrometry
MWCO	(nominal) molecular weight cut-off

NaCl	sodium chloride
nm	nanometre
Oxm	Oxyntomodulin, human/rat/mouse sequence
Oxm_{2-37}	Oxyntomodulin analogue with truncated N-terminal Histidine
PBS	phosphate buffered saline
PYY	peptide tyrosin-tyrosin
QCM-D	quartz crystal microbalance with dissipation measurement
rpm	rotations per minute
RYGB	Roux-en-Y gastric bypass
s.c.	subcutaneous application
S	entropy
SiO_2	Silicon dioxide
T	absolute temperature
T2DM	Type 2 Diabetes Mellitus
TEM	transmission electron microscopy
ThT	Thioflavin T, a fluorescent dye
Trp	Tryptophan, a fluorescent amino acid
UV	ultraviolet (spectroscopy)
Y	(conversion) yield

Contents

1 Introduction

1.1 Application of gut hormones in treatment of Type 2 Diabetes Mellitus

1.1.1 The pathophysiology and current treatment of T2DM

Diabetes is one of the most common diseases worldwide. In 2017, the prevalence of diabetes was estimated 8.8 % of adults worldwide, or 425 million people. Due to population growth, ageing and lifestyle changes especially in the developing countries, an increase to 693 million is expected by 2045 [7]. T2DM makes up about 90 % of diabetes diseases. Major risk factors for T2DM include a family history of T2DM, obesity, sedentary lifestyle, dyslipidaemia, hypertension and low birth weight [8].

In a healthy individual, glucose plasma concentration is mainly regulated by the release of glucagon from pancreatic α cells, or insulin from pancreatic β cells. Glucagon induces gluconeogenesis and glycogenolysis in liver and muscle cells, which causes an increase in blood glucose levels. Insulin inhibits glucagon-mediated pathways, promotes glucose uptake from the bloodstream, and induces glycogen formation in liver and tissue cells [9]. Insulin-sensitive cells in central and peripheral tissues ingest plasma glucose, amino acids and fatty acids in response to insulin concentration, and feed back their need for insulin to β cells [10].

Prediabetes and T2DM are initiated by the decrease of insulin sensitivity (*insulin resistance*) in peripheral cells. Isolated insulin resistance is usually asymptomatic, because the relative insulin deficiency is counteracted by increased insulin secretion from β cells. If β cells are not capable of supplying sufficient amounts of insulin, blood glucose levels rise [10]. The resulting state of impaired glucose tolerance is often referred to as prediabetes [11]. Chronic glucose challenging and toxic metabolic side products associated to hyperglycaemia lead to an irreversible destruction of pancreatic β cells. Concurrently, dysfunctions in α cells increase fasting glucagon levels, which further enhances hyperglycaemia [10].

Permanently high plasma glucose levels induce peripheral vascular disease, which is the pathophysiologic hallmark of T2DM. Structural changes of endothelial cells in capillaries and arterioles can manifest as microaneurysms, rhetinopathy, neuropathy and chronic kidney disease. Hyperglycaemic impact on macrovasculare dramatically increases the risk for atherosclerosis and cardiovascular disease [11]. A life-time treatment is implicated for T2DM patients [8].

T2DM drugs aim at restoring glucose homeostasis by increasing insulin levels, delimiting nutrient uptake in the gut, altering hepatic gluconeogenesis, or enhancing renal glucose excretion. It has been shown that a change in lifestyle towards weight loss and enhanced

physical activity increases chances to achieve a partial or complete remission of (pre)diabetes [12]. However, most antidiabetics cause weight gain, which itself is strongly associated with the progression of T2DM, the occurrence of concomitant diseases, and patient incompliance [13]. Inhibition of the renal sodium-glucose-co-transporter 2 (SGLT-2) is the only pharmaceutical T2DM treatment that effectively favours weight loss. However, the enhanced glucose excretion in urine is associated with infections of the lower urinary tract and cardiovascular complications. As discussed in chapter 1.1.2, some analogues of the human gastrointestinal hormone glucagon-like peptide 1 (GLP-1) induce moderate weight loss while effectively normalizing blood glucose levels [14].

Advanced hyperglycaemia usually requires pharmaceutically increased insulin levels. Remaining β cell function can be enhanced by administration of sulfonylureas. If this is not sufficient, recombinant human insulin (or analogues thereof) has to be administered subcutaneously [10]. The at least daily syringe application causes patient discomfort and high costs for health systems. Complications caused by noncompliance are the biggest factor in diabetes health care costs. Especially in late-stage T2DM, patients' ability to self-deliver drugs at a daily basis can be complicated by impaired vision and decreased mobility [7]. Moreover, intensive plasma glucose lowering by insulin or sulfonylureas induces weight gain, poses patients at risk of hypoglycaemic excursions, and does not reduce the risk for cardiovascular complications [15][16].

The most successful treatment of concurrent T2DM and obesity is bariatric surgery, especially Roux-en-Y gastric bypass (RYGB). While surgery is not a rational first line treatment, the observed changes in gut hormone levels following RYGB have given rise to the development of incretin based drugs for the treatment of obesity and T2DM [13].

1.1.2 The potential of gut hormone drug formulations in T2DM

Following food intake, a number of peptide hormones are released from the gut. The function of these hormones is to reduce food intake, inhibit gastric exocrine secretion, delay gastric emptying, and facilitate nutrient uptake into peripheral cells. Appetite is reduced via endocrine and vagus nerve signaling to the brain [17]. Delayed gastric emptying facilitates glucose homeostasis and mediates a sensation of fullness, which further inhibits food intake. Some peptide hormones exhibit a regulatory function on pancreatic glucagon and insulin secretion, named incretin effect [18]. After RYGB surgery, patients with T2DM and/or obesity show permanently increased levels of peptide YY (PYY), gastric inhibitory peptide (GIP), Glucagon-like peptide (GLP-1) and Oxyntomodulin (Oxm) [13]. The antidiabetic effect of gastric binding is achieved before significant weight reduction takes place [9]. These findings led to the assumption that the benefits of RYGB could be achieved by a pharmaceutically induced increase in plasma levels of gut hormones.

While all of these peptides cause appetite suppression after parenteral application, the influence on glucose homeostasis is diverging (see **Table *1-1***) [2][17]. PYY has no reported effect on glucose, insulin or glucagon levels. GIP enhances insulin release from pancreatic β cells but worsens glucose tolerance in T2DM patients. GLP-1 and Oxyntomodulin act as insulin secretagogues and glucagon release inhibitors [9]. Oxyntomodulin additionally increases energy expenditure and ketogenesis, making it a potentially more effective candidate for treating overweight [19][20].

Table 1-1: Metabolic characteristics of postprandially secreted peptide hormones

Green/black/red arrows: potentially positive/neutral/negative action in T2DM patients. For references, see main text.

peptide	secretion	proteolysis	metabolic activity
GLP-1	• Postprandial • intestinal L cells • Increased secretion after RYGB surgery	• DPP-4 • Neprilysin	• Insulin secretion ↑ • Glucagon secretion ↓ • Glucose tolerance in T2DM patients ↑ • Delayed gastric emptying • Appetite ↓ • Energy expentiture ↓
Oxynto-modulin	• Postprandial • intestinal L cells • Increased secretion after RYGB surgery	• DPP-4 • Neprilysin	• Insulin secretion ↑ • Glucagon secretion ↓ • Glucose tolerance in T2DM patients ↑ • Appetite ↓ • Energy expentiture ↑
PYY	• Postprandial • intestinal L cells • Increased secretion after RYGB surgery	• DPP-4	• Insulin → • Glucagon → • Appetite ↓
GIP	• Postprandial • intestinal K cells • Increased secretion after RYGB surgery	• DPP-4 (activation)	• Insulin ↑ • Appetite ↓ • Glucose tolerance in T2DM patients ↓
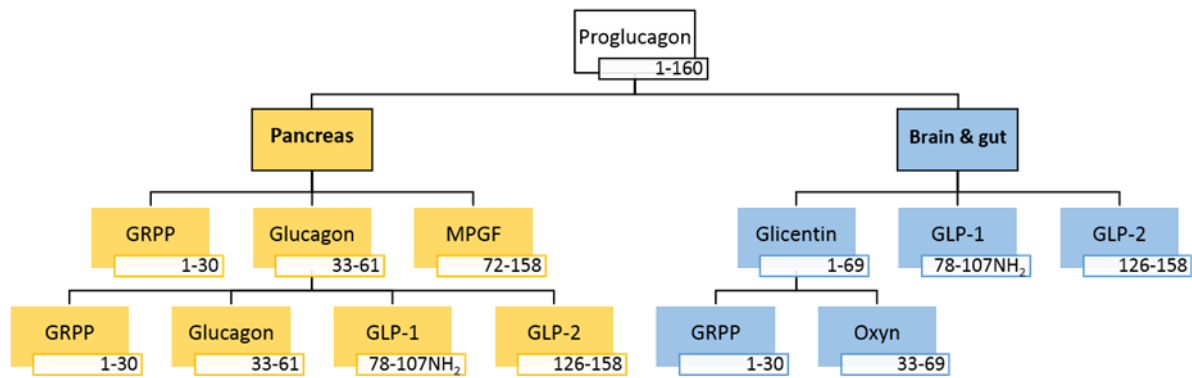
Figure 1-1: Tissue-specific cleavage of Proglucagon

Posttranslational modification of Proglucagon by prohormone convertase 2 yields glucagon as the main active gene product. The region containing GLP-1 and GLP-2 is partially secreted as the inactive major proglucagon fragment (MPGF). Metabolic functions of glicentin related pancreatic peptide (GRPP) and GLP-2 are widely unknown. In brain and gut, proteolytic processing by prohormone convertase 1/3 results in formation of GLP-1, GLP-2 and Oxyntomodulin (figure adapted from [21]).

In a healthy individual, GLP-1 and Oxyntomodulin are secreted from L cells of the small and large intestine. The magnitude of secretion is proportional to calorie intake [13]. GLP-1 and Oxyntomodulin are transcribed in the same gene as glucagon, whose precursor enzyme Proglucagon is enzymatically processed in a tissue-specific way (see Figure 1-1). In the pancreas, Prohormone convertase 2 produces glucagon as the predominant gene product. Alternative cleavage by Prohormone convertase 1 and 3 in the gut brings about GLP-1 and Oxyntomodulin as the major active substances [21]. The most abundant active form of GLP-1 is the amidated 78-107 fragment of Proglucagon [18]. Wild-type Oxyntomodulin is the 33-69 cleavage product of Proglucagon and contains the whole sequence of Glucagon with a C-terminal octapeptide extension (hence also called Glucagon-37) [21]. Due to its sequence homology to GLP-1 and Glucagon (see **Figure 2-2**), Oxyntomodulin combines the characteristics of GLP-1 and Glucagon [9]. GLP-1 and Oxyntomodulin activate local receptors on gastrointestinal cells, induce vagus nerve signalling, and reach the bloodstream by paracrine transport. Both hormones cross the blood-brain barrier [17].

```
                       1......... 11........ 21........ 31.....
Glucagon:              HSQGTFTSDY SKYLDSRRAQ DFVQWLMNT. .......
Oxyntomodulin:         HSQGTFTSDY SKYLDSRRAQ DFVQWLMNTK RNRNNIA
GLP-1(7-37):           HDEFERHAEG TFTSDVSSYL EGQAAKEFIA WLVKGRG
```

Figure 1-2: Sequence homology of Glucagon, GLP-1 and Oxyntomodulin

Oxyntomodulin, GLP-1 and GIP have different degrees of sequence homology (green) with Glucagon. Physiologically active GLP-1 is predominantly cleaved after positions 6 and/or 36 (red). Source: http://www.uniprot.org/uniprot/P01275 (20/09/2018).

GLP-1 exerts its activity via a single known receptor (GLP-1R), which is expressed in pancreatic islets, brain, heart, kidney, and the gastrointestinal tract [18]. GLP-1R activation in the gastrointestinal tract mediates a potentiating effect on α and β cells, which assists in postprandial glucose level normalization by decrease of glucagon secretion and increase of insulin secretion. Importantly, GLP-1R induced insulin secretion is glucose dependent, precluding the possibility of GLP-1 induced hypoglycaemia [2]. Moreover, GLP-1R activation was reported to cause β cell proliferation and reduced β cell apoptosis in rodents [22][23]. GLP-1 delays gastric emptying, which further regulates blood sugar levels and transmits a feeling of fullness that reduces food ingestion. However, beneficial effects of delayed gastric emptying may be negligible in chronic treatment with GLP-1 analogues due to rapid tachyphylaxis [24]. GLP-1R activation in the hypothalamus causes appetite suppression by stimulating reward centres and anorexigenic neurons, as well as inhibiting orexigenic neuron signalling [25][26]. Clinical trials showed cardio- and vasculature-protective characteristics of GLP-1 analogues [27], with the drawback of reduced energy expenditure [13].

Oxyntomodulin activates both GLP-1R and the glucagon receptor (GCGR), although with reduced affinity in comparison to the single agonists. The levels of activated second messengers differ from activation by glucagon and/or GLP-1 [17][28]. The dual receptor agonism of Oxyntomodulin brings about an antidiabetic function similar to GLP-1 accompanied by cardioprotective functions and superior weight loss in comparison to single GLP-1R targeting [29][19]. The latter can be explained by the additional satiety induction by targeting glucagon pathways, as well as the increased energy expenditure mediated by GCGR activation [30][31]. Thus, the synergistic effect of dual GCGR- and GLP-1R-agonism is potentially more effective in treatment of T2DM and obesity than GLP-1 or glucagon [19][21].

Gut hormones are evolutionarily selected for their short action in the human body. After the desired effect is achieved, circulating hormones are mainly inactivated by enzymatic

degradation, glomerular filtration, and hepatic degradation. GLP-1 and Oxyntomodulin are predominantly cleaved by the ubiquitous enzyme Dipeptidyl Peptidase 4 (DPP-4) after position A8 (GLP-1) and S2 (Oxyntomodulin) (3). Neutral Endopeptidase 24.11 (Neprilysin, NEP) has six cleavage positions in both peptides, but plays a minor role in incretin degradation [14]. Human plasma half-lives are 2 and 12 min for GLP-1 and Oxyntomodulin, respectively, which renders the exploitation of native peptide solutions inefficient for the continuous treatment of T2DM and/or obesity [32][18].

Inhibition of DPP-4 enhances intrinsic levels of GLP-1 and Oxyntomodulin. The consequently increased insulin secretion and inhibited glucagon release normalizes glucose levels. The DPP-4 inhibitors Sitagliptin and Vildagliptin have achieved pharmaceutical approval for the treatment of T2DM in combination with other antidiabetic drugs. However, the regulatory effect of DPP-4 on other peptides – especially the activation of the anorectic hormone PYY – prevents a positive overall effect on weight reduction [9].

Long-acting GLP-1R agonists have been the subject of intense pharmaceutical research for the past decades, culminating in several blockbuster antidiabetic drugs and the first incretin hormone analogue approved for weight management. Currently, there are nine approved GLP-1R agonist formulations, of which two are combination drugs containing insulin. Strategies to prevent DPP-4 degradation comprise steric hindrance by acylation (Liraglutide), and substitution of Ala7 for Glycin (Exenatide, Lixisenatide, Albiglutide, Dulaglutide) or the nonproteinogenic amino acid Amino-isobutyric acid (Aib) (Semaglutide). Acylation-driven albumin binding (Liraglutide, Semaglutide), albumin fusion (Albiglutide) or IgG4 Fc fusion (Dulaglutide) further enhance half-life by reduction of glomerular filtration and hepatic degradation. Dosing frequencies range from twice daily to once weekly, with tendentially better glycaemic control achieved by the longer-acting drugs [14]. Moderate weight reduction by GLP-1R agonists was shown in healthy and obese subjects as well as in T2DM patients [33][34]. The weight-lowering effect achieved through satiety induction is dampened by the reduction of energy expenditure mediated by GLP-1R activation in cardiac tissue [13]. Delayed gastric emptying does not seem to have a long-term beneficial effect due to habituation [24]. Nausea, vomiting and diarrhoea are frequent adverse side effects of all marketed GLP-1R agonists [9][13][14].

Although far less investigated than GLP-1, native Oxyntomodulin seems to have beneficial actions *in vivo* and in clinical studies. Oxyntomodulin improves glucose tolerance in healthy and diet-induced insulin-resistant mice [35][36]. Glucose-regulatory effects are mainly mediated via GLP-1R activation, overacting the hyperglycaemic effects of GCGR activation [35][37][38][20]. Very recently, it was shown that *i.v.* infused Oxyntomodulin regulates glycaemic excursions in healthy obese persons as well as obese T2DM patients to comparable extent as the currently market-dominating GLP-1 analogue Liraglutide [39][14]. Promising

effects of Oxyntomodulin were also shown in a mouse model of Type I Diabetes Mellitus [29]. Further functions of Oxyntomodulin comprise decreased gastric acid and exocrine secretion, inhibition of gastric emptying, cardio- and neuroprotective effects [32][40].

Oxyntomodulin has superior weight-reducing potential in comparison to single GLP-1R agonists. GCGR activation enhances appetite suppression and induces thermogenesis, lipolysis, fatty acid oxidation, and ketogenesis [21][37]. In rodents, Oxyntomodulin reduces food intake both upon peritoneal and hypothalamic administration [31]. After repeated injection, more weight loss is achieved than in an isocaloric (pair fed) control group, proving that Oxyntomodulin significantly increases energy expenditure [41]. In normal-weight humans, a single preprandial *i.v.* injection of Oxyntomodulin reduces caloric intake by 20 % [42]. Randomized, placebo-controlled studies showed that energy expenditure is increased in overweight or obese humans receiving *s.c.* Oxyntomodulin, and a 2.4 ± 0.4 % body weight decrease was reached after injecting Oxyntomodulin 30 min *s.c.* before a meal over 4 weeks [2][43]. Neither of the studies reported occurrence of nausea, vomiting or affection of food palatability.

Despite these findings, there is currently no approved compound based on Oxyntomodulin, and no Oxyntomodulin analogue has reached phase III of clinical studies. Oxyntomodulin analogues suitable as drug candidates need to address the problem of short plasma half-life as well as maintain activity at both GLP-1R and GCGR. It is increasingly acknowledged that the balance of receptor activation needs to be similar to the wild type to maintain Oxyntomodulin's beneficial effects on glucose regulation, food intake, and energy expenditure [44]. Furthermore, the native Oxyntomodulin sequence needs to adopt a helical conformation to activate its receptors [45][46][47]. It was suggested that the glucagon-identic N-terminal fraction is α-helical and followed by a short 3_{10} helix [48]. Residues 1, 4, 6, 7 and 11 and the C-terminal octapeptide seem to be crucial for GLP-1R activation, while the midsection alters GLP-1R activation levels [49]. The C-terminal octapeptide regulates gastric acid secretion [50]. GCGR activation requires Glutamine at the degradation prone position 3 [37][44].

Consequently, rational design of long-acting Oxyntomodulin analogues is a complex task. Reported modification techniques comprise amino acid substitutions, C-and N- terminal elongation, acylation, PEGylation, cholesterylation, and Fc fusion [51][52][53][40][29]. While enhanced plasma half-life is often achieved, most of the analogues upset the balance of receptor activation or lose activity at one receptor entirely. For example, N-terminal capping or substitution of the DPP4-sensitive Serine (Ser) in position 2 with any canonical amino acid is detrimental to receptor affinity [49]. Considerable is the substitution of Ser2 with the non-coding amino acids D-Serine or Aminoisobutyric acid (Aib). Although D-Serine-2-Oxyntomodulin has lowered receptor affinities and Aib-2-Oxyntomodulin is a GLP-1R biased

agonist, both substances showed better glucose tolerance and similar appetite suppression in mice as Oxyntomodulin [53]. Interestingly, a GCGR biased Oxyntomodulin analogue in fact *increased* food consumption in mice, but still lowered body weight by GCGR-mediated energy expenditure, emphasizing the complexity of chimeric agonism [54].

In 2017, we reported a novel strategy to increase the plasma half-life of Oxyntomodulin while maintaining its natural structure. Reversibly self-assembled Oxyntomodulin was administered *s.c.* to mice and rats, from where it continually diffused into the bloodstream over 5 d. The self-assembled state did not activate receptors, but receptor activation by Oxyntomodulin released from the peptide assemblies was indistinguishable from freshly dissolved human Oxyntomodulin. In rats, Oxyntomodulin released from the *s.c.* depot reduced basal glucose and improved glucose tolerance after a glucose bolus [6].

1.2 Self-assembled peptide as a long-acting drug formulation

1.2.1 Protein and peptide self-assembly in disease, physiology, and engineering

The flexibility of the peptide backbone and side chain orientations allows single peptides and proteins to adopt a three-dimensional structure. Native proteins are evolutionarily selected to be able to rapidly fold into a structure that equals a single minimum of the free energy landscape in their respective natural environment [55]. The driving force of protein folding[1] is the enthalpically favourable exclusion of hydrophobic residues from the aquatic cellular environment. Attractive interactions between side chains stabilize the conformation. During folding, unspecific protein interactions are prevented by chaperone-mediated shielding of hydrophobic patches, degradation of misfolded structures, reversible end-capping, and spatial seclusion of similar sequences in a heterogeneous mixture of molecules. Consequently, intramolecular interactions are kinetically favoured under native conditions, enabling the protein to collapse into the least-hydrophobic surface structure [56][57]. Burial of aggregation-prone patches and presence of chaperones allows the coexistence of proteins without aggregation even at supersaturated conditions [58][59].

Under certain conditions, an alternative energetic minimum can be adopted by homotypic interactions of equal parts of associating monomers. This process is termed *self-assembly* in following. As the structures resulting from packing of equivalent molecules differ from folding of heterogeneous patches within a polypeptide chain, the function of the resulting aggregate is altered or impaired [60]. Peptides and proteins can adopt various self-assembled states including fibrils, tubes, helices and globular structures [61][62][63]. Molecules within supramolecular structures may or not have structural similarity to the native fold [64].

Peptides and proteins undergoing self-assembly have long been associated with protein misfolding diseases [4][64]. Pathological effects of misfolding and aggregation include depletion of a relevant protein, formation of toxic metabolites, or aggregate deposition. Most protein misfolding diseases are caused by the formation of amyloid fibrils. Amyloid plaques in the brain are related to neuropathic diseases like Alzheimer's, Parkinson's and Huntingdon's disease. Nonneuropathic amyloidosis can be localized (e.g. amylin amyloidosis in T2DM) or systemic (e.g. lysozyme amyloidosis). However, recent findings imply that toxic effects of protein misfolding are primarily caused by the transient formation of toxic oligomers and not by the bulk of deposited aggregate [65]. A possible explanation for this

---

[1] In this thesis, the term *folding* is used for the specific adoption of intramolecular interactions and intermolecular interactions leading to a functional protein structure. *Self-assembly* is used for homotypic intermolecular interactions between multiple amino acid chains.

phenomenon is the unphysiological exposure of amino acid patches that would be buried in folded or assembled states [4].

Over the last two decades, more and more proteins have been found to accomplish a physiologic purpose in self-assembled state. Bacteria like *Escherichia coli* use extracellular amyloid fibrils for surface interactions and cell-cell contacts [5]. Chorion protein aggregates fulfil structural and protective functions in insects and fish eggs [66]. Yeast and fungi use self-assembled structures as epigenetic elements, and prion proteins are involved in long-term learning of the marine snail *Aplysia* [67][68]. Fibrils of the mammalian amyloid Pmel17 direct melanosome actions and sequester toxic melanin precursors [69]. More complex states of self-assembly are crucial for structural (collagen, microtubules) and motoric (myosin) purposes [70].

Peptides are generally too short to adopt a folded structure, and are thus more prone to undergo self-assembly. A striking example of functional self-assembled peptide is the storage of pituitary peptide hormones in secretory granules. The microenvironment inside the granules drives peptides into an amyloid state, allowing storage in a dense, pure, and physicochemically stable form. Upon hypothalamic signalling, secretory granules melt with the cell membrane and release their payload into the extracellular environment, where altered solution conditions favor the disaggregated, active state of the hormone [71]. This finding supports the rationale that self-assembled peptides or proteins could be used as a long-acting drug formulation [5][61].

Fibrillated gonadotropin releasing hormone (GnRH) analogues were shown to release functional monomer from the fibril ends, and exert prolonged *in vivo* activity by ongoing monomer release from the depot [5]. The peptide analogue Lanreotide, an approved long-acting drug for the treatment of acromegaly, is applied subcutaneously as a self-assembled hydrogel [72]. The long-acting insulin analogue insulin glargine forms reversible precipitate at the injection site, which allow sustained peptide release from a depot [73].

Beyond the use of self-assembled drugs, hydrogels consisting of self-assembled peptides can be used to physically entrap and stabilize other active molecules. Reversible attachment of drugs to peptide side chains offers a possibility for prodrug delivery with enhanced stability [74][75]. Peptides can be produced in high purity by solid phase synthesis, enabling tuneable characteristics and cheap production compared to e.g. cell culture-derived collagen. Hydrogels formed of human proteins and peptides are thus promising scaffolds for catalysis, tissue engineering and biomineralization, due to their biocompatibility, biodegradability, and mechanical properties [76][77].

1.2.2 The hierarchical structure of amyloid proteins and peptides

The term "amyloid" (*starch-like*) was populated by Rudolph Virchow in 1854 following the observation of a positive iodine staining reaction in abnormal tissue deposits. Five years later, Virchow's classification as starch- or cellulose deposits was corrected by Nicolaus Friedreich and August Kekule, who proved the proteinaceous nature of amyloid patches [78]. In 1935, William Astbury and Silvia Dickinson proposed a cross-beta arrangement from the X-Ray diffraction pattern of stretched poached egg, and indeed proposed the structure to be a ubiquitous motif in denatured protein [79]. However, only in the past few decades has it become accepted that amyloid formation is a generic feature of the polypeptide backbone, which – given the right conditions – can be adopted by all proteins and peptides [80].

Amyloid-type self-assembly is dictated by the intrinsic propensity of the peptide[2] backbone to form homotypic beta-sheet interactions in a *cross-beta* motif (see **Figure 2-3**). The amyloid core is formed by an almost infinitely repeating intermolecular beta sheet motif that can elongate by recruiting peptides to the fibril ends [70]. Individual strands align approximately parallel to each other with the peptide backbone direction approximately perpendicular to the sheet normal and fibril axis. Amino acid side chains lie on either side of the beta sheet, protruding away from the fibril [57].

In general, beta sheets in amyloid structures do not exist as singles but are paired with an opposing sheet, a structure often called *protofilament* [70]. The opposing sheets can be formed by distinct molecules, or by amyloid-like stacking of single peptides in a turn conformation [4][81]. Protofilaments may align laterally or stack with the side chains facing each other, forming a *filament*[3]. The spacial alignment of (proto)filaments represents the *fibril*. Mature fibrils have translational symmetry by definition, but often display one or more rotational symmetry elements by helical or screw twist of (proto)fibrils [82]. Most amyloid fibrils are composed of 2-8 sheets with the peptides lying parallel within a sheet and antiparallel to the opposite sheet, however more complex arrangements are known [83]. Typical amyloid fibrils are 6-20 nm wide and up to several micrometers long [70].

Amyloid fibrils are stabilized by a network of noncovalent interactions. Every sheet comprises a multitude of H bonds formed between the carbonyl oxygen atoms and the amine group hydrogen atoms of the peptide backbone. Backbone-backbone H bonds are in the sheet plane. Sheets are further stabilized by arrays of homotypic side chain interactions, especially by aromatic residue stacking (π-π-interactions), hydrophobic interactions and salt bridges between charged side chains [84].

---

[2] For easier reading, the term peptide shall be used interchangeably with protein for the current chapter.

[3] The term *protofibril* is sometimes interchangeably used for a fibrillar subclass (59). Here, I will use *protofibril* as a term for a general intermediate state with unknown structure.
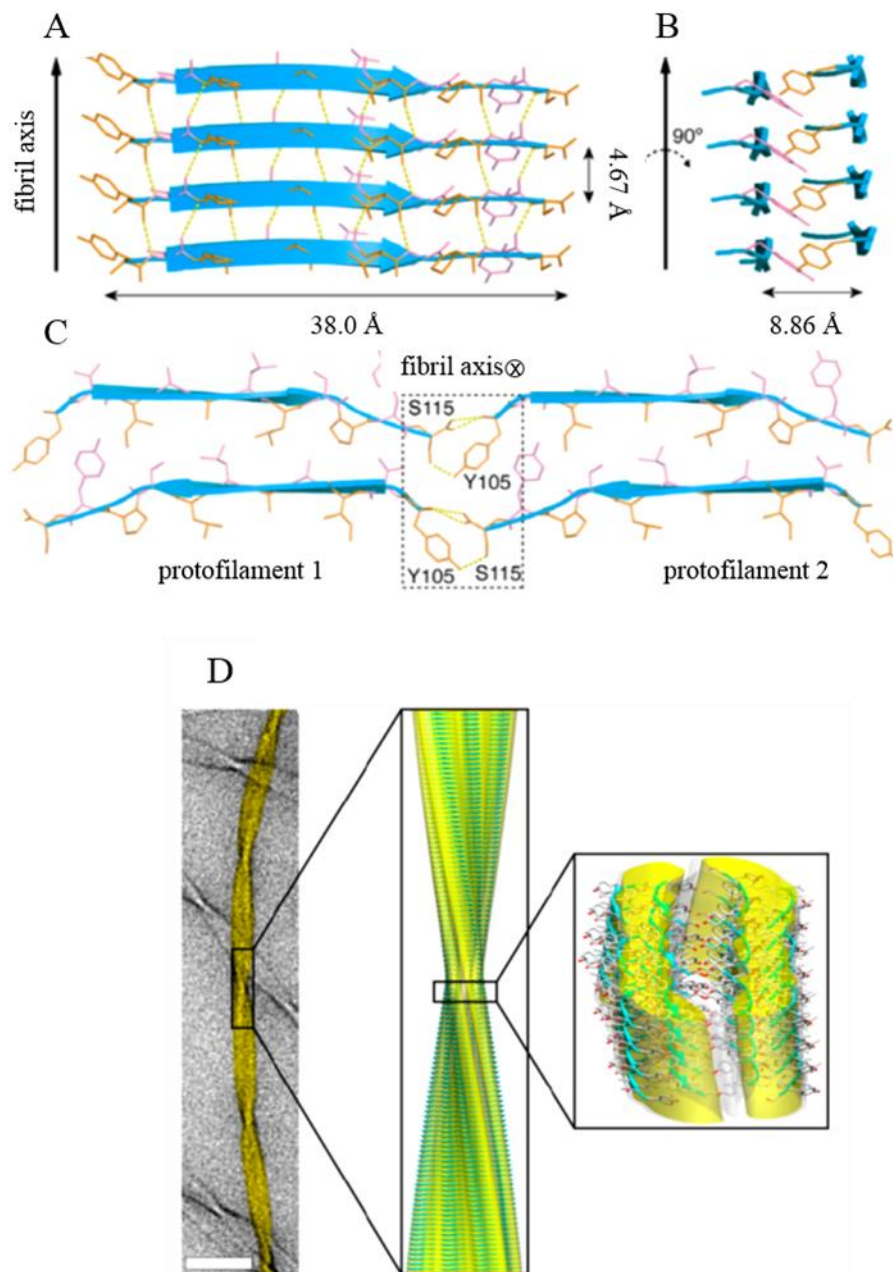
Figure 1-3: Hierarchical structure of an exemplary amyloid fibril

A-C: Atomic-resolution structure of the decapeptide TTR(105-115), determined by MAS-NMR. A, individual peptides align perpendicular to the fibril axis. The H bonds (dotted orange lines) run within the beta sheet. Amino acid residues protrude away from the fibril and stack in-register with analogous side chains of the neighbouring peptides within the sheet. B, two sheets align in parallel to form a protofilament. Peptides of opposing sheets are aligned in an antiparallel and staggered way. Side chains of sheets interdigitate. C, several protofilaments can align side by side with a head-to-tail peptide alignment. The resulting (proto)fibril is stabilized by the interaction of terminal peptide side chains. D, scanning transmission electron imaging (left) reveals the regular twist of amyloid fibrils (scale bar, 50 nm; false colour). The shown fibril is composed of three protofibrils consisting of two parallel aligned protofilaments each (model magnifications middle and right). Figures adapted from [87].

Adjacent sheets can interact by interdigitation of side chains, a motif widely known as *steric zipper*. Close side chain contacts in the dry interface of the protofibril are thermodynamically favorable because of van der Waals interactions, hydrogen bonding in a water-free environment, and the entropic gain of water exclusion (see also chapter 1.2.3). Optimal alignment may require a slight offset of sheets resulting in alternating growth competence of sheets [85]. Sidechain packing restrictions, electrostatic effects and the intrinsic chirality of peptides can also induce twisting of individual peptides and the fibril. The degree of twisting or coiling is – among others – dependent on the sequence, the number and arrangement of associated sheets, and the solvent conditions [86][87][88][89].

The amyloid structure provides a protected environment for individual peptides. Amyloid peptide fibrils are stable in a wide range of temperature, pH, and chaotropic substances [61]. Peptide sequences in the amyloid core are protected from enzymatic degradation [90]. Amyloid fibrils show remarkable mechanic stability, comprising tensile strengths in the range of steel, and stiffness (E modulus) comparable to wood or dragline silk [91].

The morphology of fibrils does not usually change along the length of a fibril. Persistence lengths of several micrometers are often observed, meaning that the structures are self-propagating over thousands of molecules with remarkably few errors [92]. Conversely, the sequence does not determine the amyloid structure, and one sequence may give rise to a multitude of polymorphic fibrils [93]. Polymorphism can occur on all structural levels from the conformation of single peptides to the bundling and interweaving of mature fibrils.

Segmental polymorphism comprises different possibilities how one peptide can form beta-sheets within a fibril (see **Figure 2-5**) [82]. The amyloid core can span the whole amino acid chain or only a fraction of it [4][94]. Beta strands are generally formed by a single peptide; however one molecule may contribute to several strands [95]. In fact, the number of residues per strand rarely exceeds 10-12. Other parts of the peptide may be unstructured, helical, or form a separate strand within the fibril. A common structural motif is the beta-arch, in which one molecule is part of two or more beta-strands in separate beta-sheets within the fibril [92]. Individual beta-strands do not need to be in extended conformation within an amyloid fibril. The resulting paired sheets are often approximately parallel and connected by an array of turns. Less frequently observed is a beta-hairpin motif, in which a peptide forms two or more antiparallel strands within the same sheet of a fibril, connected by β-turns [96]. More complex fibril core architectures such as the beta-solenoid structure of HET-s have been found [95].
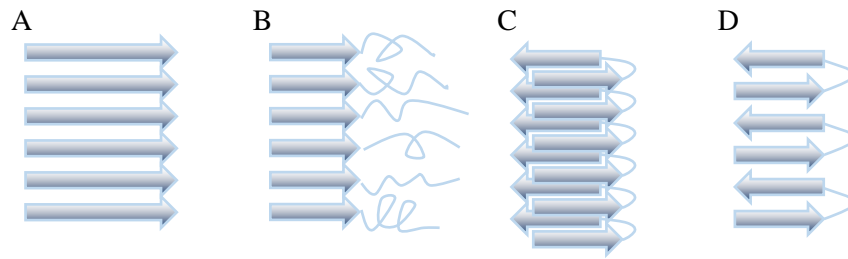
Figure 1-5: Segmental polymorphism

A, the whole sequence, or B, only a part of the sequence is part of the β-sheet. C, monomers in β-arch conformation spanning connecting two sheets; D, monomers in β-turn conformation connecting two strands.

Packing polymorphism stems from the different possibilities to align strands respectively to their neighboring strands. As shown in **Figure 2-4**, strands may be in-or out-of-register; parallel or antiparallel within a sheet [70]. In-register, parallel alignment is the predominant type in reported fibril structures, presumably due to the saturation of homotypic side chain interactions. However, other alignments may be favorable for example for short, hydrophobic strands, where the repulsion of charged termini can be a destabilizing factor in perfectly aligned, parallel sheets [93][97][98]. Opposing sheets can be oriented in the same direction or upside-down, with strands parallel or antiparallel to the paired sheet, and in- or out-of-register sheet alignment [70][98][85].
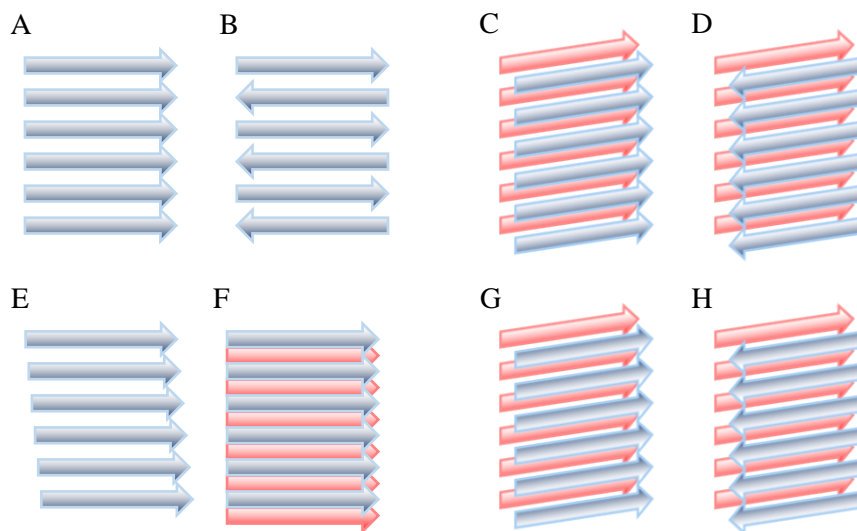

Figure 1-4: Packing polymorphism

A, parallel and B, antiparallel strand arrangement. C, D, G, H, sheet arrangements at example of parallel, in-register strands. C, G, parallel sheets, D, H antiparallel sheets. C, D, upside up, G, H, upside down sheets, represented by the shadow location. E, out-of-register alignment within a sheet; F, out-of-register alignment of opposing sheets.
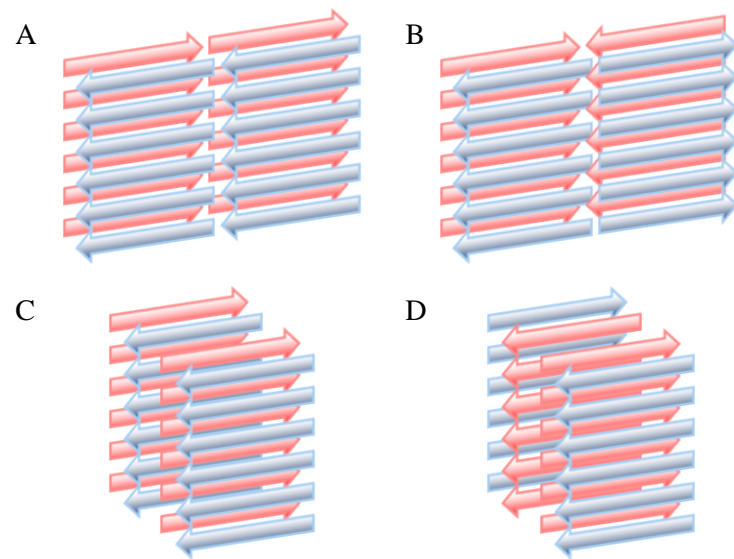
Figure 1-6: Assembly polymorphism

Protofilaments can align A, N-to C-terminus (head to tail), or B, with the same termini facing each other (head to head). Lamination occurs when protofibrils assemble with the sheets facing each other, either C, in an alternative way, or D, with a distinct inner and outer sheet.

Assembly polymorphism results from the number and alignment of protofilaments in a fibril. Examples are shown in **Figure 2-6**. Protofilaments may align laterally with N-, or C-termini facing each other, or in a "head-to-tail" alignment where sheets are facing the same direction. The latter polymorph is stabilized by the opposing charges at N- and C-terminus. Protofilaments may also stack with either of their flat sides facing each other, or form tubes by angular interactions [92][99]. For example, $A\beta_{1-40}$ may have an approximately rectangular or a hollow triangular cross-section, depending on the alignment of two or three protofilaments per fibril [100][101][102].

Side-chain polymorphism describes polymorphism based on the different orientation of side chains. Although relatively discrete, side-chain polymorphism may influence all hierarchical elements of amyloid assembly by steric hindrance [93].

By combination, even a small peptide could theoretically adopt dozens to hundreds of polymorphic states. However, for a given set of external conditions, only few conformations are kinetically and thermodynamically accessible [70]. Spontaneous structural rearrangement to more stable classes within a fibril is not usually possible, but class switching is possible by dissolution of less stable polymorphs and rearrangement in more stable fibrils (see also chapter 1.2.3) [92][103]. On a mesoscopic scale, mechanically strained twisted ribbons can reorganize to helical ribbons or closed nanotubes with water-filled cores [104]. Fibril splitting and thinning is rarely observed [83], but can lead to altered appearance despite little changes

at structural level [104]. Concentrated dispersions of amyloid fibrils can cause hydrogel formation [105][89][61][106].

Amyloid fibril morphology can be sensitive to peptide concentration, incubation time, pH, ionic strength, and the presence of pre-formed seeds [107][104][94][108][103]. Seeding with fibrils of a certain morphology often leads to inheritance of the fibril morphology, even in conditions where unseeded fibrillation leads to another fibril type [94][107][109]. For example, glucagon fibrillation has been shown to depend on peptide concentration, presence of sulphate and chloride anions, pH, and agitation [110]. At low peptide concentrations, the fibrils have a predominantly twisted morphology with a beta-turn-rich peptide arrangement. Increasing peptide concentration leads to predominant or exclusive occurrence of a straight fibril species. In seeding experiments, the twisted morphology is only inherited in low concentrations, while cross-seeding into low or high glucagon concentrations leads to straight morphology independent of the seed type [94][111]. Charge screening by salt addition enables formation of polymorphs that are not thermodynamically accessible in water [112]. pH and temperature affect the stability and morphology of glucagon fibrils [113]. Agitation is believed to give a selective advantage for a less mechanically stable fibril type, because the generation of growth-competent fibril ends is multiplied by stress-induced breakage [110]. Moreover, initial oligomeric and fibril types have been shown to convert into different types over time [103].

Despite their highly ordered nature, high-resolution structural determination of amyloid fibrils is a challenging task [82]. With few examples of short peptide sequences, amyloid structures do not crystallize [84][98][97]. X-Ray diffraction of aligned fibrils can however reveal the inter-strand distances [79][114][115][111][116]. Similarly, diffraction data can be derived from digitized electron micrographs, especially from Cryo EM images [117][99][111][85][118]. Cross-beta structures are generally characterized by a meridional ~4.7 Å diffraction, which corresponds to the distance of peptide strands within a sheet, and a weaker equatorial reflection at ~8-12 Å that represents the spacing of paired sheets [114][70]. Closely interdigitating, "dry" steric zippers diffract at 8-9 Å, while less dense packing is characterized by larger reflections [85][96]. A few high-resolution amyloid structures have been determined by helical reconstitution of Cryo-EM images, or by solid-phase NMR [117][119][85][118][95][102].

At lower resolution, imaging techniques like atomic force microscopy (AFM) or electron microscopy (EM) can differentiate polymorphic fibrils based on their dimensions and twist [83][88][104][111][94][88]. For example, the number of laterally interacting protofilaments is proportional to maximum width (by EM) or height (by AFM), allowing implicit determination of the number and dimensions of protofilaments even without resolving individual protofilaments.
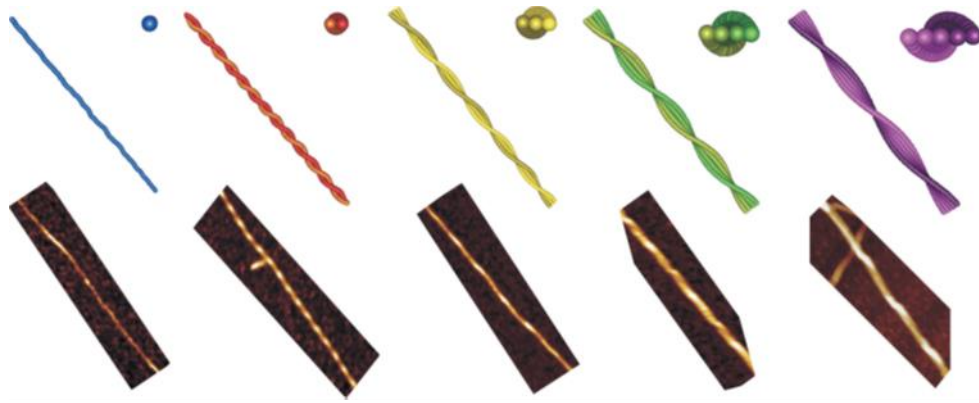
Figure 1-7: The number of protofilaments correlates with height and periodicity of amyloid fibrils

Amyloid structures of β-lactoglobulin contain different numbers of aligned protofilaments. The maximum heights of twisted fibrils are integer multiples of the thinnest observed filament. The periodicity increases with increasing height. Top: model representations of multi-stranded fibrils; bottom: AFM images with the number of filaments ranging between 1 and 5. Figure adapted from [83].

Similarly, the cross-over pitch of twisted sheets decreases with the increasing number of aligned protofilaments due to mechanical strain, making pitch distances a measure for sheet dimensions (see **Figure 2-7**) [83][107][104][88][111][94]. Imaging also provides information about oligomeric precursors, amorphic aggregates, and higher-order assemblies [103][104].

Besides cross-beta specific arrangement and fibrillar morphology, the contemporary definition of amyloid structure includes binding of an amyloid reporter-dye. Thioflavin T (ThT) is the most widely used amyloid reporter dye for *in vitro* samples [120]. Due to its low interference with the fibrillation process, easy handling and – within similar samples – quantitative fluorescence yield, it is often used to study fibrillation kinetics [121][122][123]. ThT predominantly binds to the grooves adjacent to stacked aromatic side-chains along a fibril. Immobilization restricts the conformation of the otherwise freely rotating dye molecule, and preserves its excited state [124]. However, ThT often has reduced specificity to protofibrillar species and may show false-positive fluorescence in presence of non-fibrillar hydrophobic structures and DNA [123]. If present, intrinsic Tryptophan (Trp) residue fluorescence can be a useful indicator of fibrillation and structure. The Tryptophan fluorescence maximum is blue-shifted from ~300 nm to ~330-355 nm in hydrophobic environments, and signal broadening indicates sample heterogeneity [125].

Spectroscopic methods like circular dichroism (CD) and Fourier-transform infrared spectroscopy (FTIR) are sensitive to secondary structure elements. Both methods can give estimates of the percentage of α-helices, β-sheet, turn and unordered structure. FTIR can also distinguish parallel and antiparallel alignment [126][127].

1.2.3 The interplay of kinetics and thermodynamics in amyloid-type self-assembly

Amyloid structure provides an alternative minimum of the free energy landscape that is accessible to every at least partially unfolded peptide sequence. In contrast to the single thermodynamic optimum in protein folding, the free energy landscape of amyloid-type self-assembly is multidimensional (see **Figure 2-8**, adapted from [57]). Sequence and solution conditions determine which minimum of the landscape is adopted, resulting in a multitude of possible polymorphic states [57]. Which equilibrium state is reached depends both on the thermodynamic stability of polymorphs, their nucleation and polymerization kinetics, and the energetic barriers of conversion into more stable species. The state at infinite time may not correspond to the global thermodynamic minimum, because the conversion of polymorphic states generally requires crossing of an energetic barrier (activation energy) [128][129][92]. Off-pathway aggregates can be kinetically trapped in alternative or transition states, while residual free peptide may be below the critical concentration for spontaneous nucleation [130][92].

Similarly, conversion of partially or fully folded proteins or peptides into amyloid requires an activation energy [131]. An aggregation-prone state can be reached by agitation-induced unfolding, cavitation in ultrasonic devices, the presence of chaotropic substances, or thermal stress. Thermal unfolding is a frequently reported inducer of protein fibrillation [132][133].
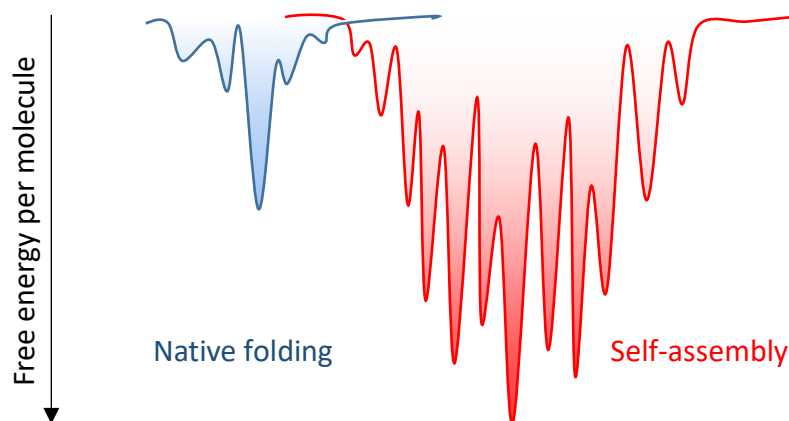
Figure 1-8: Free energy landscape of folding and self-assembly

The energy landscape of protein folding *in vivo* (blue) generally has a single global free energy minimum that corresponds to the natively folded state. Less stable optima correspond to folding intermediates on the way to full folding. In self-assembly (red), a single molecule can adopt various stable states (minima) depending on the solution conditions. Conversion between polymorphs and off-pathway intermediates can be hindered by high transition state energies (maxima).

Figure 1-9: Processes involved in amyloid formation

Amyloid fibrils adopt an equilibrium with free peptide (left) by attachment and detachment of monomers. New fibrils can be created by fragmentation (middle left), primary (middle right) and surface-catalysed secondary nucleation (right). For illustration purposes, only one protofibril with in-register β-arch conformation is shown.
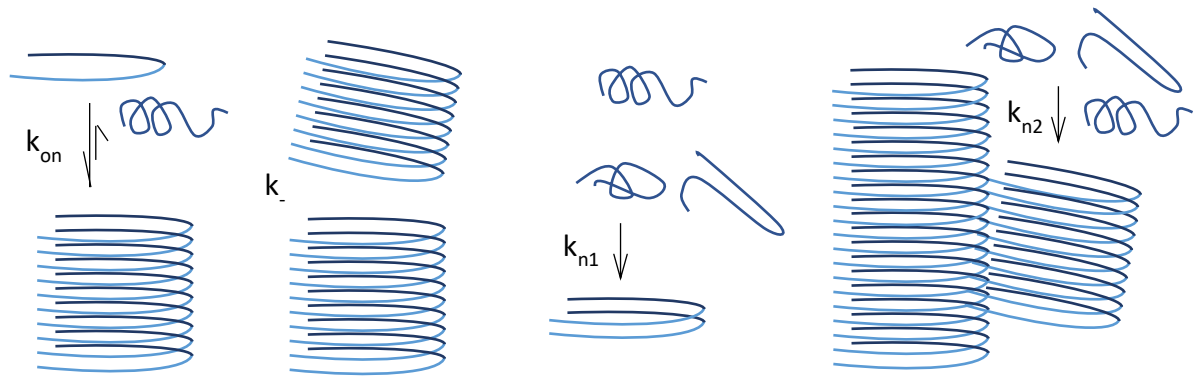
Temperature elevation may also increase the aggregation tendency of peptide aggregation by destabilization of helices and stabilization of β-sheets in peptides [134][135][136][137].

Amyloid structures are formed by elongation of nuclei (see **Figure 2-9**). A nucleus is defined as the minimal structure that can give rise to amyloid type elongation [64]. Starting from solution, oligomers are formed by random intermolecular interactions of aggregation-prone sequences. Early stage structures are not necessarily fibrillar, but can be composed of unstructured, ring-shaped or spherical aggregates [103]. Primary nucleation is independent of the presence of fibrils; secondary nuclei are formed by surface catalysis or fibril fragmentation. Growth-competent nuclei then elongate until an equilibrium between monomer incorporation and monomer release is reached [138][139].

If self-assembly is followed in presence of an amyloid specific reporter dye, a sigmoidal curve of fluorescence reflects the kinetics of amyloid formation (see **Figure 2-10**). The initial phase of low signal intensity is referred to as the lag phase, which is the time needed to form a critical amount of nuclei and fibrils to be detected by the measurement. In the following growth phase, the exponential signal increase correlates with the incorporation of peptides into the cross-beta structure. The signal increase is arrested by monomer depletion, resulting in a post-transition baseline [122]. Primary and surface-catalysed nucleation, fragmentation and elongation can occur at all stages of the self-assembly process. The conversion can alternatively be followed by circular dichroism, Fourier-transform infrared spectroscopy (FTIR), decrease of monomer concentration, time-dependent high resolution imaging of aliquots, or biosensing techniques such as quartz crystal microbalance (QCM) [83][138][140]. The conversion is often described by fitting a logistic function to the experimental data [138].
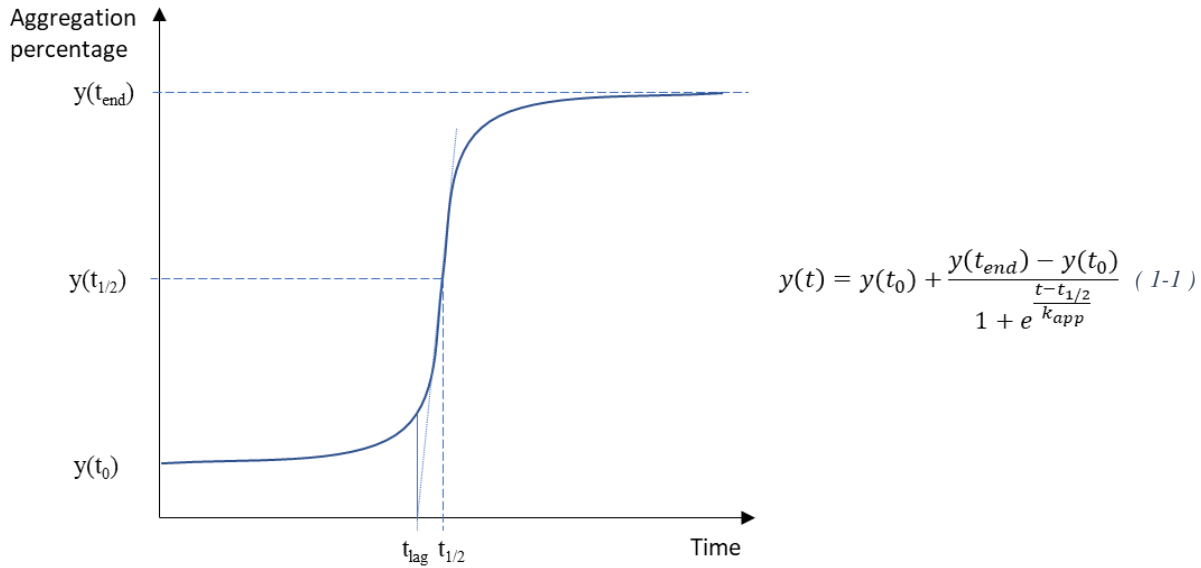
Aggregation
percentage

$y(t_{end})$

$y(t_{1/2})$

$y(t_0)$

t_{lag} $t_{1/2}$ Time

$$y(t) = y(t_0) + \frac{y(t_{end}) - y(t_0)}{1 + e^{\frac{t - t_{1/2}}{k_{app}}}} \quad (1\text{-}1)$$

Figure 1-10: Sigmoidal curve of amyloid formation kinetics

The sigmoidal course of self-assembly reflects the conversion of monomer into amyloid structures. The lag phase is characterised by the time needed for formation of nuclei. In the growth phase, the bulk of peptide is converted to the self-assembled state, resulting in a signal saturation by monomer depletion. The course of amyloid formation can often be fitted with a logistic function.
$y(t)$, signal dependent on amyloid presence, e.g. ThT fluorescence intensity; y_0, pre-transition baseline signal; y_{end}, post-transition baseline signal; t, time; $t_{1/2}$, time for reaching a half maximum signal; k, apparent growth rate [138].

The formation of nuclei can be accelerated by agitation, pH alteration, enhanced peptide concentration, temperature increase, provision with a surface or air-water-interface, or seeding with pre-formed nuclei [108][122][141].

In conditions where polymorphism can be excluded, amyloid formation can be expressed by a mean-field master equation [139]. The concentration f(t,j) of an aggregate of the size j at time t is expressed as a differential rate law taking into account primary and secondary nucleation, elongation and fragmentation:

$$\frac{\partial f(t,j)}{\partial t} = 2k_+ m(t) f(t, j-1) - 2k_+ m(t) f(t,j) +$$

$$+ 2k_- \sum_{i=j+1}^{\infty} f(t,i) - k_-(j-1)f(t,j) +$$

$$+ k_{n_1} m(t)^{n_c} \delta_{j,n_c} + k_{n_2} m(t)^{n_2} \sum_{i=n_c}^{\infty} i f(t,i) \delta_{j,n_2} \quad (1\text{-}2)$$
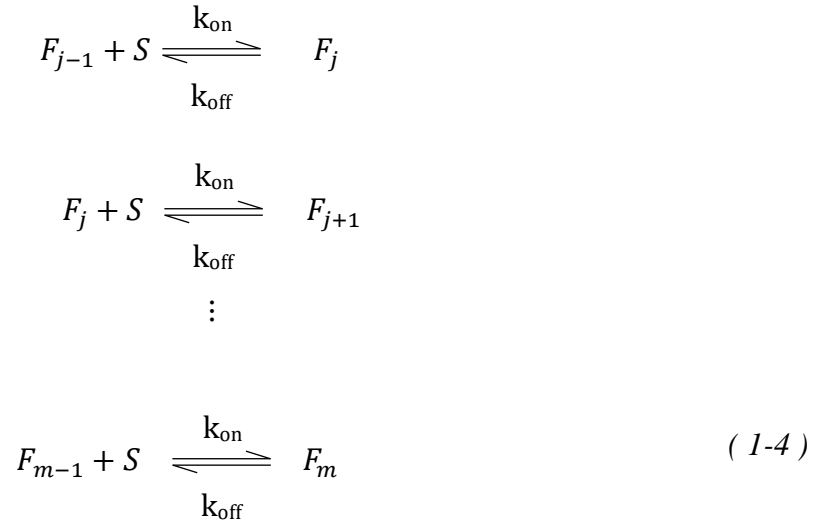
where first term accounts for the rate of formation of an aggregate sized j from monomer at concentration m(t) and fibrils at length j-1. Analogously, the second term describes the loss of fibrils at length j by addition of another monomer. k_+ is the elongation rate constant, doubled for two ends per fibril[4]. The third term stands for fibrils of length j formed by fragmentation from longer fibrils at fragmentation rate k_-, while fibril loss by breaking is included in the fourth term. The fourth term defines formation of nuclei of size n_c by primary nucleation with the nucleation rate k_{n1}. The Kronecker symbol δ is 1 for i=j and 0 otherwise. The last term describes surface-catalysed formation of secondary nuclei of size j at rate k_{n2}. Monomer concentration change is then related to the formation of fibrils of either length, and equals the opposite of total fibril mass concentration change M(t) [142]:

$$\frac{dm(t)}{dt} = - \sum_{j=n_c}^{\infty} j \frac{\partial f(t,j)}{dt} = - \frac{dM(t)}{dt} \qquad (\ 1\text{-}3\ )$$

Models have been developed to globally fit kinetic data to integrated rate laws of amyloid formation, which has helped understanding of nucleation, fragmentation and elongation processes in some systems [143][144][145][146][142]. However, these methods are beyond the scope of this thesis. Because of the relevance to this thesis, the following paragraphs will discuss kinetics and thermodynamics of elongation and dissociation at constant fibril number and morphology.

While amyloid-type aggregation is generally kinetically controlled, thermodynamic control analogous to protein folding is achieved in conditions that exclusively allow transition over a single free energy border [129]. This borderline condition is satisfied for a sufficiently seeded system where nucleation or formation of off-pathway conformers are negligible. The exclusive elongation of fibrils can be described analogously to a polymerization chain reaction [147]. In (1-4), F denotes the fibrillar state, S the soluble state, k_{on} the observable association rate constant and k_{off} the observable dissociation rate constant, j-1 the fibril length at the start of the reaction, and m the fibril length in equilibrium. The reaction constants are a function of external conditions, e.g. pH, pI, and temperature.

---

[4] It was recently shown that some amyloid fibrils have different elongation rates at both ends, but this is not easily accessible in kinetic experiments [189]. Apparent, i.e. observable rates are used in following.

$$F_{j-1} + S \; \underset{\text{k}_{\text{off}}}{\overset{\text{k}_{\text{on}}}{\rightleftharpoons}} \; F_j$$

$$F_j + S \; \underset{\text{k}_{\text{off}}}{\overset{\text{k}_{\text{on}}}{\rightleftharpoons}} \; F_{j+1}$$

$$\vdots$$

$$F_{m-1} + S \; \underset{\text{k}_{\text{off}}}{\overset{\text{k}_{\text{on}}}{\rightleftharpoons}} \; F_m \qquad\qquad (\textit{1-4})$$

As the association or dissociation process is independent of fibril length and the number of fibrils is constant, the reaction constants as well as the apparent reaction constant k_{app} are solely dependent on the soluble peptide concentration at a specific time. k_{app} incorporates the concentration of growth competent fibril ends, which is maximally twice the total fibril number N [92].

$$k_{app}\big(m(t)\big) = k_{on}\big(m(t)\big) + k_{off}\big(m(t)\big) \leq 2k_+N \qquad\qquad (\textit{1-5})$$

Exclusive elongation under limited monomer concentration is a pseudo first-order reaction with elongation rate proportional to the monomer concentration at each time point [136][141]:

$$\frac{dM(t)}{dt} = k_{app} * m(t) = -\frac{dm(t)}{dt}, \qquad\qquad (\textit{1-6})$$

which is classically solved as [148]:

$$\ln\left(\frac{m(t_0) - m(t_\infty)}{m(t) - m(t_\infty)}\right) = k_{app}t, \qquad\qquad (\textit{1-7})$$

with t_0 the reaction start and t_∞ the time where equilibrium is reached. By conversion, the time course of a measured monomer concentration in depleting conditions adopts:

$$m(t) = [\,m(t_0) - m(t_\infty)]e^{-k_{app}t} + m_{\infty}, \qquad\qquad (\textit{1-8})$$

and $m(t_0)$, m_∞ and k_{app} can be easily fitted with open-access software. Analogously, kinetic parameters can be fitted from the time-course of fibril mass concentration change $\Delta M(t)$:

$$\Delta M(t) = M(t) - M(t_0) = m(t_0) - m(t) =$$
$$= [m(t_0) - m_\infty][1 - e^{-k_{app}t}] \qquad (1\text{-}9)$$

In quasi-constant monomer concentration like at the start of a reaction or under flow of excess monomer, the kinetics are zero order, and $\Delta M(t)$ is proportional to k_{app}. Therefore, steady state monomer conditions can be easily used to investigate influence factors like pH, temperature, or salt concentration [141].

Another borderline case is reaching a (quasi) equilibrium state at long incubation times in monomer-depriving conditions. The equilibrium dissociation constant K_D is solely defined by the soluble peptide concentration m_∞ in equilibrium at given conditions [147].

$$K_d = \frac{k_{off}}{k_{on}} = \frac{M_n}{M_{n-1} * m_\infty} = \frac{1}{m_\infty} \qquad (1\text{-}10)$$

As for crystallization or amorphous aggregation, the existence of an equilibrium allows aggregate growth under supersaturated conditions, and dissolution under free-molecule-deprived conditions [149]. In many cases, the equilibrium of amyloid-type self-assembly is far on the side of fibrils, making amyloid structures quasi-irreversible in certain conditions [142]. For example, amyloid plaques accumulate in Alzheimer's or Parkinson's patients' brains, because the formation of amyloid fibrils in presence of constitutively secreted monomers exceeds monomer release. Conversely, without invading soluble monomer, a fraction of the total peptide or protein mass will always be in non-bound state and can diffuse from the fibril [148][130][150]. Because the dissociation constant is directly linked to the Gibbs' free energy ΔG, K_D or m_∞ at constant pressure and temperature can be used to investigate influence factors on the chemical potential of fibrillation [151].

$$\Delta G = -RTlnK_D \qquad (1\text{-}11)$$

T is the absolute temperature in Kelvin (K), and R is the universal gas constant (~8.314 J K^{-1} mol^{-1}). ΔG is negative for spontaneous (exergonic) processes, and positive for unfavourable (endergonic) processes. The Gibbs Helmholtz equation relates free energy to enthalpy (H) and entropy (S) changes:

$$\Delta G = \Delta H - T\Delta S \qquad (1\text{-}12)$$

Favourable enthalpic changes increase heat (exothermic reaction) or draw heat from the system (endothermic reaction). Amyloid-type fibrillation is often enthalpically favourable because of the multitude of interactions along the fibril. It is important to note that H bonds created among the backbone or side chain groups replace H bonds in bulk water and are thus not *per se* thermodynamically favourable. However, H bonds in a water-free, low dielectric environment such as inside water-free double sheets are relatively stronger than in solution [84]. Shielding of hydrophobic residues from water is an additional driving force for amyloid-type self-assembly [152][153]. Generally, enthalpy changes in amyloid formation are temperature sensitive [153][154][155][133][147]. Higher order assembly of protofibrils or mature fibrils is often strongly exothermic and favoured at increased temperature [153][154]. The enthalpy change with increasing temperature (i.e. the heat capacity ΔC_p) can be positive or negative depending on the solution conditions and the polymorphic type formed. For example, glucagon has been found to have positive ΔC_p in presence of glycine and saline, but negative ΔC_p in presence of sulphate [154].

As aggregation restricts conformational degrees of freedom, the entropy of the peptide or protein assembly is smaller than the entropy of soluble peptide or protein. The entropy term in the Gibbs-Helmholtz equation is therefore positive and increasing for temperature increase if only the peptide or protein is considered. However, water exclusion from the assembly can increase the entropy of the entire system [82][153].

Therefore, both terms of the Gibbs-Helmholtz equation can be either positive or negative depending on the solution conditions. This is reflected in the temperature dependence of amyloid formation. Many proteins only self-assemble if a critical unfolding temperature is reached and the native fold is destabilized. At moderate temperatures, the self-assembly process is often favoured by temperature increase with a measurable apparent activation energy (Arrhenius-like behaviour) [129][128]. However, at high temperatures, amyloid assemblies are destabilized, and the equilibrium is shifted towards unfolded monomers or randomly associated oligomers. For example, β_2-microgobulin, insulin, SH3 domain, and hen egg-white lysozyme fibrils start to dissociate between 60 and 140 °C [153][156][157][126]. The thermodynamic explanation for this phenomenon is that enthalpically favourable interactions saturate at a specific temperature and cannot counteract the increasing entropic cost of self-assembly. Less ordered states like soluble monomers, oligomers or amorphous aggregate are then favourable [156]. If the monomer conformation inside a fibril is partially folded, increasing temperature may also prevent cooperative folding. For example, the formation of β-hairpins is a cooperative process that is disfavoured at higher temperature [135]. Disaggregation at high temperature is then consistent with the observation that any ordered structure can only form at low-enough temperature [158].

2 Scope of this project

Self-assembly can drastically increase the chemical, physical and biological stability of peptides and proteins. Amyloid fibrils have not been taken into account as drug formulations or drug delivery vehicles for a long time because of their association with amyloid-related diseases. Increasing evidence for the safety of amyloid fibrils, and the toxicity of prefibrillar aggregates, demands the consideration of amyloid structures in pharmaceutical applications [4][5]. Protection of proteins and peptides in amyloid nanostructures provides an elegant means to form a stable, reversible self-delivery reservoir with controlled release of monomers from the fibril termini, given an undersaturated environment [5]. This project investigates the potential use of *s.c.* delivered, *ex vivo* self-assembled Oxyntomodulin as a long-acting drug delivery system. Oxyntomodulin is chosen as a model peptide for the following reasons:

- Oxyntomodulin potentially has superior effects in T2DM and obesity compared to marketed drugs, but no Oxyntomodulin-based compound has been filed for drug approval. Because the glucose dependency of Oxyntomodulin's insulinotropic action excludes the risk of hypoglycaemia, and no adverse effects like nausea are known, high doses can be administered to achieve weight control as an additional beneficiary action in overweight T2DM patients.

- Long-action formulations of T2DM drugs are favoured by patients and health care organisations to reduce discomfort and complications related to noncompliance with drug prescriptions.

- Extension of Oxyntomodulin's remarkably short plasma half-life by classical methods like amino acid substitutions or increase of the hydrodynamic radius proved very difficult due to the sensitivity of dual receptor agonism to structural changes.

- Self-assembly allows protection from external influences without the need for molecular alterations. Every peptide sequence can potentially form amyloid-like fibrils, given the right conditions. Methods and results of this project can thus be seen as a proof of concept and extended to other molecules.

- Oxyntomodulin is charged at physiologic pH, which increases the probability that Oxyntomodulin fibrils are metastable *in vivo*. Released peptide can be carried away in constant flow of peptide deprived interstitial fluid, possibly reaching pharmaceutically meaningful plasma concentrations.

- Oxyntomodulin self-assembly has not been reported in literature at the start of this project. Due to structural similarity to the well-characterized peptide hormone Glucagon, investigation of Oxyntomodulin self-assembly is scientifically valuable for a better understanding of processes in fibrillation.

This thesis comprises a description of condition screening and optimization for injectable self-assembled Oxyntomodulin; microscopic and physicochemical characterization of the formulation; investigations of kinetic and thermodynamic processes during self-assembly and peptide release; the characterization of an alternative self-assembled state; and an investigation of the cross-seeding tendency of Oxyntomodulin fibrils in presence of the structurally related peptides glucagon and Aib-2-Oxyntomodulin. Parallel to this project, postdoctoral researcher Myriam Ouberaï coordinated *in vivo* pharmacokinetic and pharmacodynamic studies in collaboration with MedImmune. Because I was only peripherally involved in *in vivo* studies, *in vivo* results are not included in the experimental section of this thesis. All experiments and discussions shown are exclusively my work unless clearly noted otherwise.

Chapter 3 describes the steps taken to achieve an injectable Oxyntomodulin fibril formulation. Conditions are screened by ThT fluorescence and AFM imaging. Promising conditions are upscaled in vials, and critical factors on self-assembly time, conversion yield, visual appearance of the formulation, and fibril morphology are derived. Seeding with pre-formed Oxyntomodulin fibrils is investigated as an accelerated and more reproducible method to produce self-assembled nanostructures. The final formulation is designed to fulfil the following parameters:

- the presence of self-assembled fibrils with low polydispersity and sufficient length to release monomers over a time course in the range of days or weeks
- fibrillation yield > 95 %
- absence of unstructured aggregate or precipitate
- reversibility of self-assembly in free peptide deprived conditions
- viscosity suitable for *s.c.* injection
- reproducibility and scalability within sample amounts needed for *in vivo* studies
- minimal use of additives

In chapter 4, the formulation optimized for *in vivo* testing is structurally characterized. A coarse fibril structure is derived from AFM and Cryo EM imaging, limited peptidolysis, FTIR, CD, ThT and Tryptophan fluorescence.

For any application of self-assembled peptides or proteins, a comprehensive understanding of the influence factors on fibril characteristics is important to define reproducible conditions and prevent complications. Chapter 5 comprises kinetic and thermodynamic characterization of self-assembled Oxyntomodulin. Fibril elongation and peptide release are tested under different solution conditions by kinetic QCM-D and ThT assays, AFM imaging, ITC, and the time course of free peptide conversion. Parameters include seeding strength, ionic strength, soluble peptide concentration, and temperature.

Chapter 6 describes a method to grow an alternative Oxyntomodulin fibril structure by altering incubation conditions. The structure is characterized similar to chapter 4, with a focus on Cryo EM.

Because of the structural similarity with human Glucagon, it is important to test if Oxyntomodulin fibrils can induce Glucagon self-assembly. Chapter 7 shows QCM-D experiments to investigate the cross-seeding ability of Oxyntomodulin fibrils in presence of glucagon. Moreover, self-assembly of the DPP-4 protected analogue Aib-2-Oxyntomodulin is compared to Oxyntomodulin self-assembly, and cross-seeding is tested.

All experimental chapters can be read widely independently. Results of each chapter will be discussed in context of the respective literature in each of the experimental chapters. Summary and interpretation will be given in chapter 8, in combination with a suggestion for future work.

3 Screening and optimization of Oxyntomodulin self-assembly

3.1 Challenges in Oxyntomodulin self-assembly

This chapter describes methods for reproducible self-assembly of Oxyntomodulin. The end product was designed for *in vivo* studies at MedImmune, and further used for characterization of the fibril architecture in chapter 4 as well as investigation of fibrillation kinetics and thermodynamics in chapter 5. Therefore, a number of methodic restrictions and quality parameters were defined before the start of screening and optimization.

While Oxyntomodulin potentially self-assembles in a multitude of experimental conditions, work presented here is focused on the *s.c.* injectability of the final sample. This excluded additives that are not widely acknowledged as biocompatible, methods that cannot be upscaled to sample amounts required for *in vivo* studies, and processes that are not repeatable in sterile conditions.

Because large *s.c.* injected particles are not expected to reach the bloodstream, regulations concerning particle diameter are not as strict as for *i.v.* injection. The particle size and concentration are however restricted by the force and pain associated with the injection of a viscous sample. Consequently, Oxyntomodulin fibrillation was aimed to be free of large (> 5 µm) structures. Possible gelation needed to be reversible by moderate dilution or shear inside a syringe. Considering injectability and reproducibility, samples should further be exempt from amorphous or otherwise unstructured aggregate.

Because of the potential toxicity of fibrillar intermediates, oligomeric species were not desired in final Oxyntomodulin samples. Due to the potentially transient or instable nature of oligomers in experimental conditions, there is no standardized method to distinguish oligomers from active, monomeric peptide. As a precaution, the sum of measurable soluble peptide in storage conditions was required to be below 5 % (w/w) of the total sample concentration. Regarding reproducibility and defined fibrillar conditions, samples with only one fibrillar morphology were preferred, and conditions with a clearly polymorphic AFM appearance were excluded.

Practically, there were three major challenges for optimization:

(1) The fibrillar and reversible nature excluded several classical methods to determine the size, purity and concentration of aggregates. Especially methods including dilution or acetic conditions like size exclusion chromatography (SEC) or high-performance liquid chromatography (HPLC) could not be performed on samples containing aggregates because of potential disaggregation in measurement conditions.

Furthermore, the separation of self-assembled structures from soluble peptide required centrifugation and filtration, increasing sample amounts per condition.

(2) There are no in-house facilities to produce Oxyntomodulin in pharmaceutical quality, and the peptide is very costly. Screening, optimization and characterization are therefore limited by the peptide amounts available.

(3) As described in chapter 9.2, Oxyntomodulin self-assembly cannot readily be screened by ThT fluorescence assay. ThT binds nonfibrillar Oxyntomodulin species but does only weakly bind protofibrils, leading to false positive and false negative read-outs. Gelation limits maximum screenable concentrations, but low concentrations prevented nucleation in reasonable time frames. ThT could therefore only be used to investigate elongation in presence of pre-formed seeds.

Due to these reasons, a condition pre-screening was performed with the Oxyntomodulin analogue Oxm_{2-37}, which was available in abundance. Oxm_{2-37} has the same molecular structure as Oxyntomodulin apart from truncation of the N-terminal Histidine and could be screened by ThT assays. Promising conditions were then investigated with full-length Oxyntomodulin.

3.2 Material and methods

Oxyntomodulin and Oxm_{2-37} were provided by Bachem, Switzerland. Both peptides were freeze-dried acetate salts with a purity of 97 %, and stored as dry aliquots at -20 °C. Salt solutions and buffers were prepared as 250 or 200 mM stocks. Salts, acids, bases, buffering agents and ThT were delivered by Sigma-Aldrich (UK) in analytical quality. HPLC grade water was bought from Fisher, UK. Phosphate-buffered saline (PBS, Sigma) was prepared by dissolution of PBS tablets. Stock solutions were passed through a 0.2 µm syringe filter into a sterile flask. In some long-term experiments, 0.02 wt.% sodium azide (NaN_3) was added for prevention of microbial growth.

3.2.1 Preparation of peptide solutions

An aliquot was defrosted at room temperature (RT) in a vacuum exsiccator for about 30 min to prevent condensation on the container. 130 % of the needed peptide mass was weighed into a single-use glass vial, and dissolved in 100 % of the theoretical solvent needed, in order to make up for contained acetate mass. Generally, peptide dissolved in water up to 25 mg mL^{-1} within few minutes; shaking or pipetting was not necessary. The clear solution was filtered at 13 000 rpm for 5 min in a disposable 0.22 µm cellulose acetate filter (Amicon ultra) in order to remove dust or pre-formed aggregates. Concentration was measured in an aliquot of the filtrate by the UV_{280} absorption on a NanoDrop 2000 spectrophotometer. The 0.1 %

(1 mg mL^{-1}) absorption coefficients for Oxyntomodulin (1.906) and Oxm$_{2-37}$ (1.996) were calculated from the theoretical extinction coefficients of the peptide sequences using the online tool Expasy ProtParam (https://web.expasy.org/protparam/). Peptide solutions were diluted to the desired concentration, stored at 8 °C, and used within 2 hours.

3.2.2 Detection of amyloid fibrils by ThT fluorescence

ThT fluorescence screenings were performed in a Fluostar Omega microplate reader equipped with 440 and 480 nm wavelength filters for excitation and emission, respectively (BMG Labtech, Germany). The microplates (Corning® 3881, 96 well half area black with clear flat bottom polystyrene non-binding surface, provided by Jencons VWR, UK) were incubated *in situ* at 37 °C for up to 5 d. Aluminum microplate sealing tape (Corning®, delivered by Sigma-Aldrich, UK) was used to prevent evaporation during incubation. ThT stock solutions were prepared at 1 mM in water and stored at 8 °C protected from light for a maximum of 3 months [123]. ThT was used at 50 uM in all conditions. Fluorescence was read every 10 or 20 min by orbital averaging of six flashes per well. Microplates were either incubated without agitation, or shaked for 5 min (600 rpm, 2 mm orbit) prior to each measurement. ThT fluorescence screenings comprised a peptide concentration range of 0.1 to 10 mg mL^{-1}. The buffer pH range was 2 to 9 for Oxm$_{2-37}$, and 6-8 for Oxyntomodulin. Self-assembly was additionally screened in PBS and in unbuffered saline containing 7.7 to 150 mM NaCl. All conditions were triplicates with 50 or 100 µL per well. Triplicates of 50 µM ThT in water were used as a negative control. Samples classified as ThT-positive showed a more than 2-fold ThT signal increase with more than 10-fold signal/noise ratio. Aliquots of all ThT positive and some ThT negative conditions were imaged by AFM.

3.2.3 Oxyntomodulin fibrillation by primary nucleation or seeding

Oxyntomodulin solutions were prepared in HPLC grade water or at low NaCl ($\leq$ 50 mM) concentration. The solutions were incubated in sealed glass vials at 37 °C in a MaxQ 4450 shaker/incubator (Fisher Scientific, UK) with continuous orbital shaking (orbit 1.9 mm) at 200 rpm. The number of revolutions reflects the agitation stress used in Oxm$_{2-37}$ ThT screening, considering that rotational energy scales with orbit diameter, and that the shaking in ThT screening was intermittent due to the reading time. Samples were either incubated with agitation until no further aggregation was detected, or stored at 37 °C in quiescent conditions after the onset of fibrillation.

Samples were visually controlled for precipitation or gelation, and aliquots were imaged by AFM to detect aggregates or fibrils (see 3.2.4). The conversion yield was assessed as described in 3.2.5.

Fibrillated samples were used to seed freshly prepared Oxyntomodulin solutions. Seeding was used to shorten the production time and inherit the seed morphology to achieve more homogeneous daughter samples. Because elongation rates scale with the number of growth competent fibril ends, the mass concentration and length of mother fibrils were measured before seeding (see 3.2.5 and 3.2.4, respectively). Short fibrils were either produced by fibrillation of NaCl-containing conditions under rotational stress, or by fragmentation of longer fibrils in a sonication bath (FB15049, FisherBrand®) for up to 15 min. Seed concentrations of 0.1 to 5 % (m/m) in respect to soluble peptide were tested.

Although not included in this thesis, a range of experiments was performed with addition of 0.02 % NaN_3 as an antimicrobial agent. It was later found that NaN_3 affected fibril morphology and equilibrium, so that antimicrobial agents were omitted further on. Contamination did not seem to be a problem in handling of Oxyntomodulin samples.

3.2.4 Atomic force microscopy

AFM measurements were performed in tapping mode on a PicoPlus^{TM} (Molecular Imaging) with a PicoSPMII controller. The AFM probes were HQ:NSC36/No Al (MikroMasch®, Windsor Scientific LTD, UK) and had a tip radius < 8 nm and force constants between 0.6 and 2.0 N/m. The scanning rate was 0.6-0.9 lines per second, at a maximum imaging area of 9x9 µm and resolutions of 512x512 or 1024x1024 pixels. 2-5 µL samples were deposited on freshly cleaved mica and dried in air for at least 30 min before imaging. Undiluted samples with salt were rinsed by pipetting 100 µL HPLC grade water on a tilted dried mica chip, followed by immediate drying in a stream of compressed air. In order to analyze individual structures in a crowded environment, samples were dispersed in water in up to 100-fold dilutions.

Images were plane-levelled and corrected for horizontal scars with the open access software Gwyddion, version 2.51 (http://gwyddion.net/). Fibril heights and lengths were measured using the line extraction tool of Gwyddion.

3.2.5 Concentrations and conversion yield measurement in self-assembled samples

The soluble (free) peptide concentration is measured in the sedimentation supernatant of a sample at 13 000 rpm for 30-60 min. Salt-free samples and samples containing short fibrils do not sediment readily and are prone to resuspension. To prevent measuring fibrils, the supernatant is additionally filtered with a 50 kDa molecular weight cut-off (MWCO) filter (Amicon Ultra 0.5 mL) at 13 000 rpm for 20 min. Note that filtration alone is not suitable to separate soluble peptide from aggregated peptide, because aggregates tend to clog the filter

and trap soluble species. Peptide concentration is then measured in the filtrate by NanoDrop analogously to 3.2.1.

Aggregated peptide concentration in a pelleted or otherwise purified sample is assessed by measuring the total peptide concentration. Three aliquots are diluted twenty-fold in 10 mM HCl and incubated at 37 °C for 60 min. The concentrations are measured by NanoDrop and averaged. Aggregate concentration equals the total concentration in the pellet less the soluble peptide concentration.

The conversion yield can be calculated from soluble peptide concentration m(t) or aggregated peptide concentration M(t) and the total peptide concentration $m(t_0)$. Either or both methods are used in this thesis depending on sedimentation and further use of the sample.

$$Y(t) = \frac{m(t_0) - m(t)}{m(t_0)} * 100 \% = \frac{M(t)}{m(t_0)} * 100 \% \qquad\qquad (\textit{3-1})$$

3.2.6 Rheological characterization

A 10 mg mL^{-1} gel in water was diluted to 1 mg/mL in water or 0.9 mg mL^{-1} NaCl. The viscosity of each dilution was measured by a rate sweep test in a Physica MCR 301 rheometer (Anton Paar, Germany). The rheometer was equipped with a flat steel plate and a 1 ° angle steel cone with 40 mm diameter (CP40-1, Anton Paar, Germany). The equipment was heated to 37 °C and primed in air before use. 350 µL of a dilution was loaded on the plate. The cone was approached to the automatically determined measurement position (~0.5 mm distance between cone and plate). The equal distribution of the sample and the eventual inclusion of bubbles was examined by eye. After a 5 min equilibration to heat the sample to 37 °C, the shear stress was measured at cone shear rates decreasing logarithmically from 1000 s^{-1} to 1 s^{-1} in 13 steps, followed by a logarithmic increase of shear rate from 1 s^{-1} to 1000 s^{-1} in 13 steps. Viscosity [mPa*s] was calculated by dividing the measured shear stress [mPa] by the applied shear rate [s^{-1}]. Viscosity curves are presented as double logarithmic plots of shear rate and viscosity.

3.3 Efficient Oxyntomodulin nucleation and monomorphic elongation require different environments

Because Oxyntomodulin was not available in high enough quantity for extensive screening, nucleation conditions were pre-screened with Oxm_{2-37} in agitated ThT assays at 37 °C. Important results are shown in Appendix 9.1. Over three days, Oxm_{2-37} at 10 mg mL^{-1} fibrillated in a range of conditions, with fastest nucleation in salt-containing solutions. Self-assembly was fast and quantitative in pH range 6.0-7.4, however buffering with phosphate salts seemed to prevent formation of long fibrils and promote amorphous aggregation. Only a small amount of fibrils were formed at pH 5 and pH 8. In presence of 50-150 mM NaCl, Oxm_{2-37} formed fibrils at concentrations from 0.5 to 10 mg mL^{-1}. Fibril length in presence of NaCl was inversely correlated with agitation stress, suggesting that fragmentation delimits elongation. Presence of salts generally favored assembly of single fibrils to higher order structures. Remarkably uniform, long fibrils were formed in water at 10 mg mL^{-1}, but nucleation was comparably slow and not seen at lower peptide concentrations.

The ionic strength dependency of nucleation can be explained with the positive charge of Oxm_{2-37}. Charge screening by solution anions stabilizes oligomeric and polymeric assemblies, while electrostatic repulsion occurs at low ionic strength. Relatively small anions like chloride may screen charges in fibrillated assemblies more effectively than large anions like phosphate. It is noteworthy that fibrillation in water contained minor amounts of acetate stemming from the peptide production process.

Human Oxyntomodulin was expected to have similar, but not the exact same fibrillation behavior as Oxm_{2-37} because of an additional N-terminal Histidine residue in full-length Oxyntomodulin. N-terminal Histidine is crucial for glucagon- and GLP1-receptor activation [49]. Histidine slightly increases the isoelectric point and provides aromatic and H-bridge interactions if included in an amyloid-type core sequence. Moreover, the terminal location of Histidine may favor side-by-side interaction of peptides that favor assembly polymorphism as described in 1.2.2.

Due to these differences, fibrillation conditions known from Oxm_{2-37} had to be repeated with Oxyntomodulin. Screening was attempted with full-length Oxyntomodulin in a five-day, agitated ThT assay at 37 °C. ThT curves and AFM images are shown in Appendix 9.2. To find the best salt conditions, an increasingly chaotropic selection of salts (Na_2SO_4, NaCl, NaI, NH_4Cl, GdnCl) were screened at 25 and 100 mM at a peptide concentration of 1 mg mL^{-1}. pH was tested in 0.5 pH unit steps from pH 6 to pH 8 in 25 mM phosphate buffer. All salt-containing conditions showed a marked, approximately sigmoidal increase of ThT fluorescence within 48 h. However, AFM imaging after 48 h only showed fibrillation in the samples containing NaCl, while other salts caused formation of non-fibrillar oligomers or unstructured precipitate.

In an equivalent ThT fluorescence assay, Oxyntomodulin self-assembly was tested at 1, 5, and 10 mg mL without salt addition. All salt-free conditions showed fibrils in AFM images after 48 h. Interestingly, no ThT fluorescence increase was seen at 1 mg mL^{-1}, and only moderate signal was seen at higher concentrations. This may imply presence of protofibrillar species with low affinity to ThT [123]. Beginning gelation at 5 and 10 mg mL^{-1} further restricted the fluorescence yield.

Because of the restrictions due to gelation, false positive and false negative results seen in ThT assays of Oxyntomodulin nucleation, no further screening of fibrillation conditions were performed by fluorescence assays. However, kinetic ThT assays proved useful to study influence factors on elongation in presence of pre-formed fibrils (see chapter 3.4 and 4.1.1).

Screened conditions where fibrillation was seen by AFM were investigated for upscaled self-assembly. Especially, 10 mg mL^{-1} solutions in water or with low NaCl concentration were tested because of the formation of long and defined fibrils, and quick nucleation, respectively. Oxyntomodulin solutions were incubated in glass vials at 37 °C with 200 rpm continuous shaking in a MaxQ^{TM} 4450 shaker/incubator. Fibrillation was followed by visual inspection and AFM imaging.

10 mg mL^{-1} Oxyntomodulin solution in water did not nucleate over 3 months at 37 °C, room temperature, or in a fridge, if no agitation was provided (results not shown). However, after continuous shaking at 200 rpm and 37 °C, initial fibrils could be seen by AFM after 6 d. After 10 d, a clear gel consisting of long, unbranched and smooth fibrils was formed (see **Figure 4-1**). Fibrils were several micrometers long and about 4-15 nm high, with the majority height of single fibrils being ~6 nm. The fibril heights may be subject to uncertainty because of soluble peptide in the imaging background. After 14 d, the conversion yield was 37 %. Fibrils did not sediment readily even after long centrifugation times, so that the fibril concentration could not be increased by removal of soluble peptide.

Because of the limited yield of Oxyntomodulin fibrils produced in water, analogous steps were taken in 25 mM NaCl. Gelation was seen after 4 d of incubation, and incubation was stopped after 7 d. Centrifugation at 13000 rpm for 30 min separated a dense, cloudy fibrillar pellet with ~45 mg mL^{-1} from clear supernatant with no measurable soluble peptide within limits of detection. The fibrils were approximately 50-200 nm long and associated laterally (see **Figure 4-2**). Aliquots of the 7 d pellet produced in 25 mM NaCl were 20-fold diluted in water, PBS, and 10 mM NaCl, and the cumulative peptide release from the fibrils was measured over 48 h. Release profiles are shown in **Figure 4-2** H. In water, fibrils showed a burst release of ~50 % within the first 1.5 h, and ~80 % peptide release by 48 h. Less than 10 % release was seen in PBS. No free peptide could be measured by resuspension in 10 mM NaCl (data not shown). Oxyntomodulin fibrillation is thus generally reversible and sensitive to environmental changes.
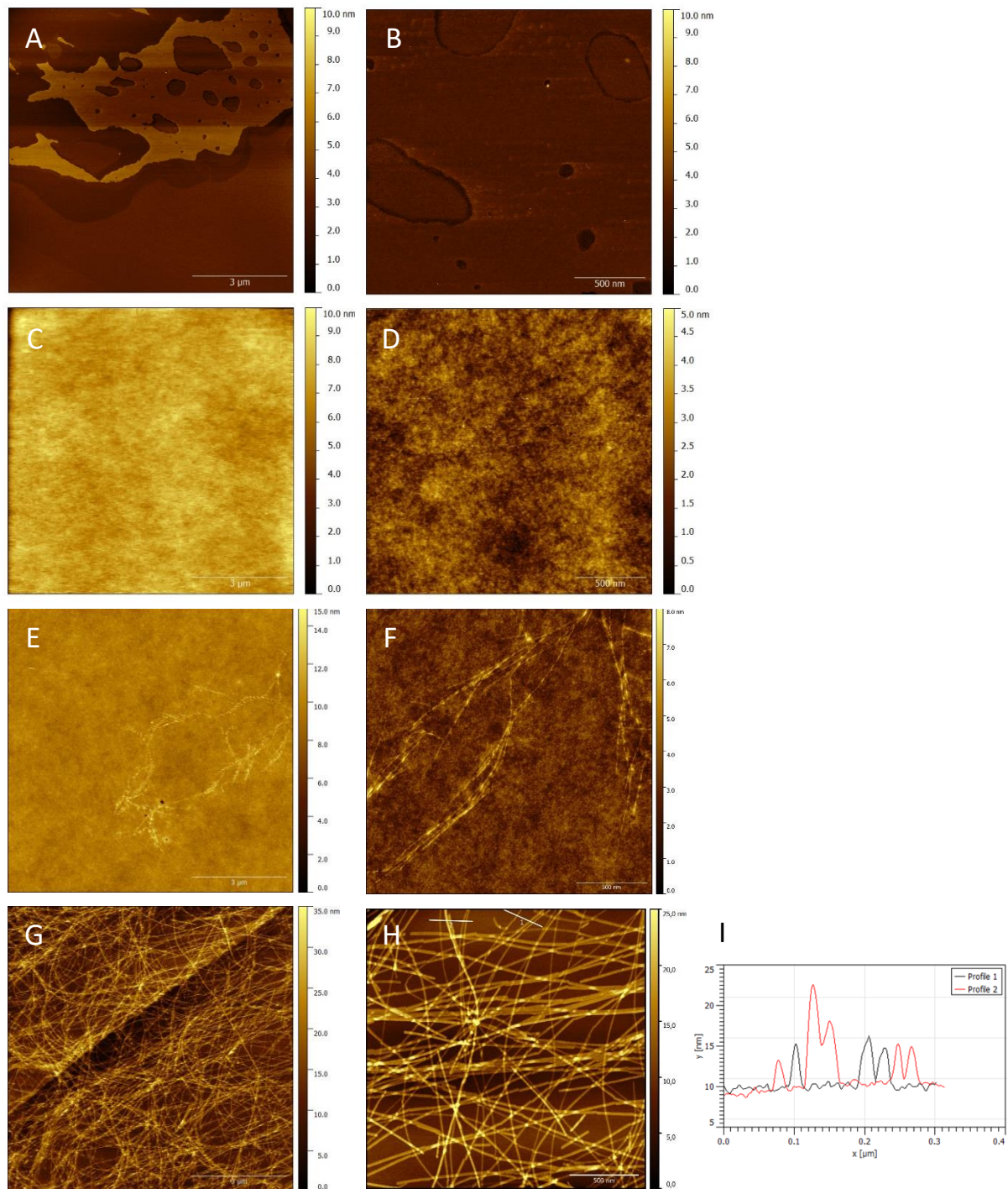
Figure 3-1: Incubation of a salt-free 10 mg mL^{-1} Oxyntomodulin solution at 200 rpm and 37 °C creates long and straight fibrils after 2 weeks

10 mg mL^{-1} solutions of Oxyntomodulin incubated at 37 °C and 200 rpm. A and B, at the start of incubation, AFM shows soluble peptide in layers (100x diluted sample); C and D, incubation in water for 24 h; E and F, incubation in water for 6 d; G and H, 100x diluted pellet after 14 d incubation; I, height profiles along line 1 and 2 in image H. Profile lines were chosen to not include fibrils over-crossing other fibrils. AFM images were processed in Gwyddion to remove imaging scars and background signal. Resolution: 512x512 pixel at scanning size 9x9 µm (A, C, E, G); 1024x1024 pixel at scanning size 2x2 µm (B, D, F, H).
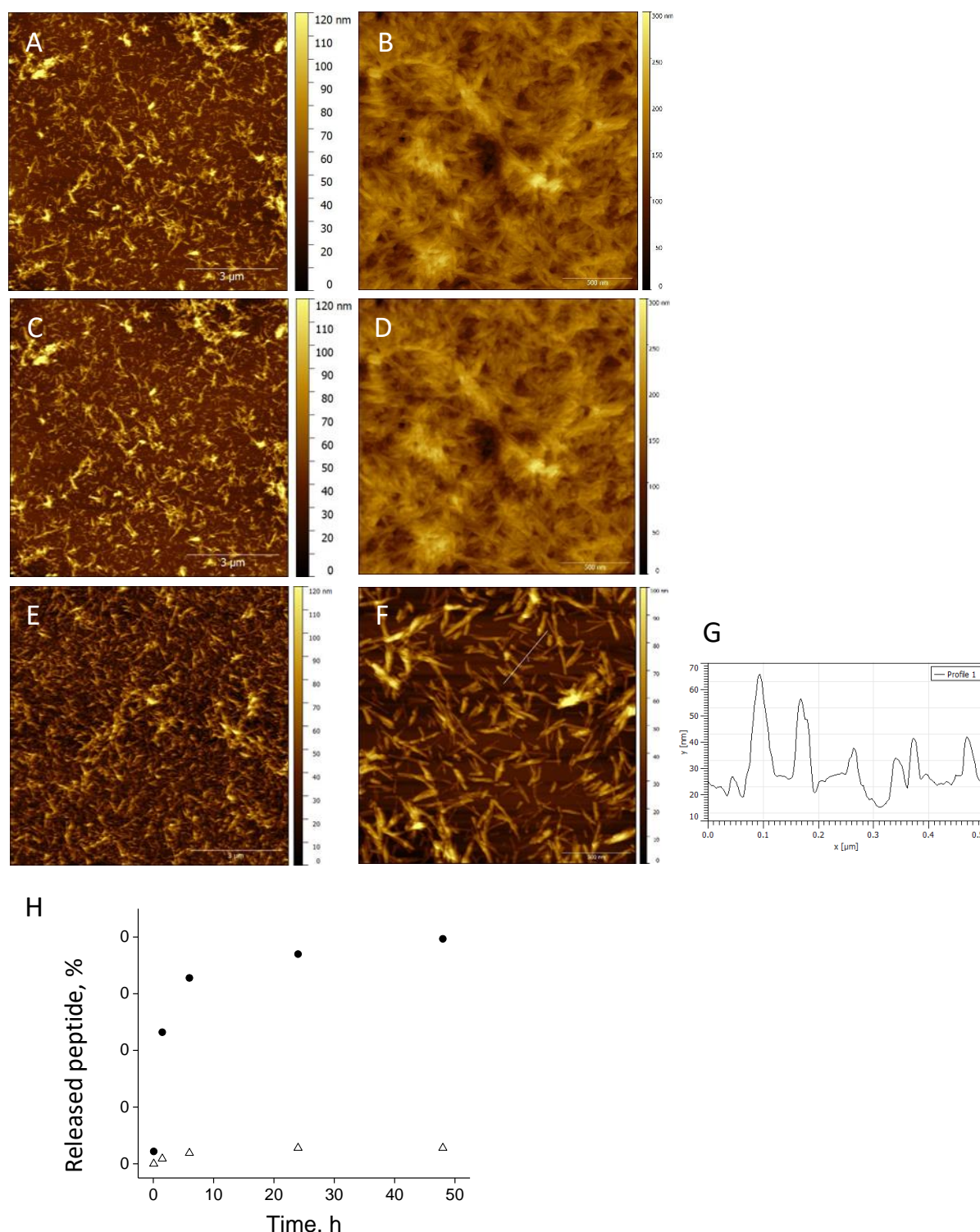
Figure 3-2: Incubation of a 10 mg mL^{-1} Oxyntomodulin solution in 25 mM NaCl at 200 rpm and 37 °C leads to fast formation of short and reversible fibrils

10 mg mL^{-1} solutions of Oxyntomodulin incubated in 25 mM NaCl at 37 °C and 200 rpm. A and B, 24 h; C and D, 4 d, 100x dilute in water; E and F, 7 d, 100x diluted in water. G, height profile along the line in E. AFM images were processed in Gwyddion to remove imaging scars and background signal. Resolution: 512x512 pixel at scanning size 9x9 µm (A, C, E); 1024x1024 pixel at scanning size 2x2 µm (B, D, F). H: Peptide release after 20-fold dilution of the 45 mg mL^{-1} Oxyntomodulin fibril pellet in water (black circles) or PBS (open triangels) and quiescent incubation at 37 °C. Peptide concentration in the supernatant was quantified after 5 min, 1.5 h, 6 h, 24 h, and 48 h. Supernatants were replaced by fresh solvent. Release is percentual of the total release in 10 mM HCl.

In the following experiments, NaCl concentration was reduced to 14.4 mM. This was for practical reasons, because gels with slightly lower salt concentrations formed more homogeneous gels and were easier to pipette. 0.9 mg mL^{-1} (14.4 mM) was chosen because it can be conveniently diluted from physiologic saline (9 g L^{-1}) for sterile production of samples for *in vivo* studies.

To find suitable conditions for nucleation and elongation, 10 mg mL^{-1} Oxyntomodulin solutions with 0.9 mg mL^{-1} NaCl were incubated at room temperature, 37 °C, and 37 °C with 200 rpm agitation. At room temperature, a turbid gel with approximately 90 % conversion yield formed after 8 weeks. As shown in **Figure 4-3**, individual fibrils at room temperature were 0.2-1 µm long and 3-12 nm in diameter. Fibrils associated to thicker bundles.

At 37 °C, the solution became viscous after 2 weeks with few fibrils, and formed a transparent gel with longer fibrils formed after 4 weeks (see **Figure 4-4**). Only 50 % conversion yield was reached after 8 weeks. Fibrils were 5-10 nm high and contained straight and twisted species.
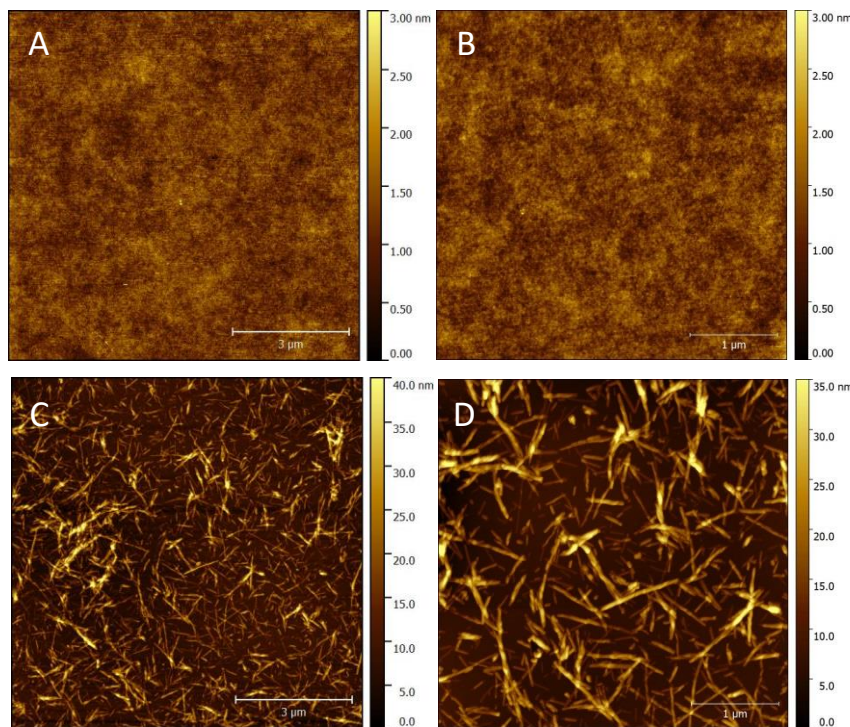
Figure 3-3: Incubation of a 10 mg mL^{-1} Oxyntomodulin solution in 0.9 mg mL^{-1} NaCl at room temperature without agitation creates short fibrils after 8 weeks

Incubation of 10 mg mL^{-1} Oxyntomodulin in 0.9 mg mL^{-1} NaCl without agitation. A and B, 2 weeks; C and D, 8 weeks. AFM images were processed in Gwyddion to remove imaging scars and background signal. Resolution: 512x512 pixel at scanning size 9x9 µm (A, C); 1024x1024 pixel at scanning size 2x2 µm (B) and 4x4 µm (D).
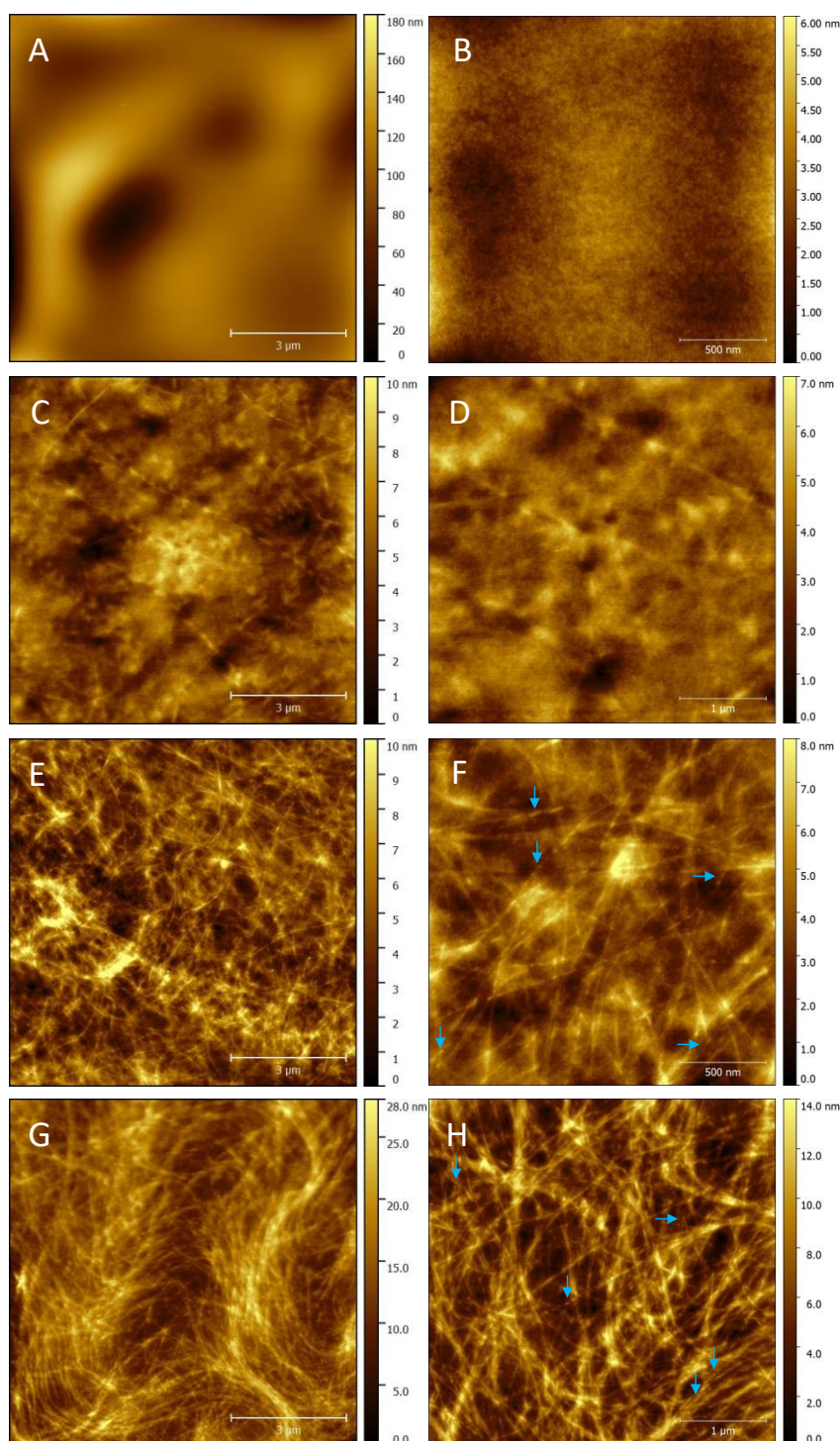
Figure 3-4: Incubation of a 10 mg mL^{-1} Oxyntomodulin solution in 0.9 mg mL^{-1} NaCl at 37 °C without agitation causes slow formation of polymorphic fibrils

Incubation of 10 mg mL^{-1} Oxyntomodulin in 0.9 mg mL^{-1} NaCl at 37 °C without agitation. A and B, 2 days; C and D, 2 weeks; E and F, 4 weeks; G and H, 8 weeks. Blue arrows, examples of twisted fibrils. AFM images were processed in Gwyddion to remove imaging scars and background signal. Resolution: 512x512 pixel at scanning size 9x9 µm (A, C, E, G); 1024x1024 pixel at scanning size 2x2 µm (B, D, F, H).

Shaking at 37 °C produced an opaque gel with 97-100 % conversion yield within 1-3 days. These fibrils were short even if the sample was incubated without agitation after nucleation, but nucleation times, gelation and fibril morphology was consistent over 5 samples and three batches of peptide. Fibrils formed in 0.9 mg mL^{-1} saline could be stored at room temperature or in the fridge for at least 12 months without visible alterations of gel appearance or fibril morphology. Dilution in 0.9 mg mL^{-1} saline did not shift the equilibrium within measurable concentrations, but fibrils were reversible after dilution in water similar to the reversibility shown in **Figure 4-2** H. The fibrillation process was indistinguishable if the pH was adjusted
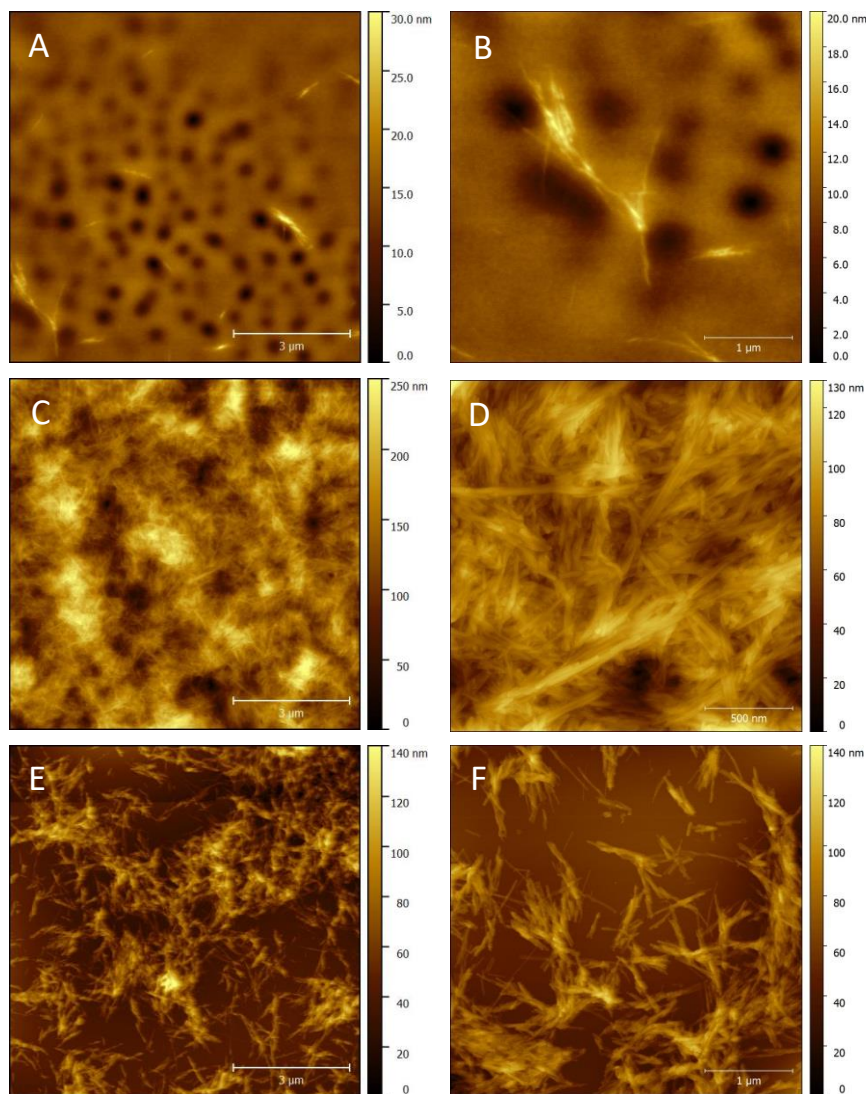
Figure 3-5: Incubation of a 10 mg mL^{-1} Oxyntomodulin solution in 0.9 mg mL^{-1} NaCl at 37 °C with 200 rpm agitation causes fast formation of short fibrils

Incubation of 10 mg mL^{-1} Oxyntomodulin in 0.9 mg mL^{-1} NaCl at 37 °C with continuous agitation at 200 rpm. A and B, 2 days; C and D, 2 weeks; E and F, 8 weeks, 10x dilute. AFM images were processed in Gwyddion to remove imaging scars and background signal. Resolution: 512x512 pixel at scanning size 9x9 µm (A, C, E); 1024x1024 pixel at scanning size 4x4 µm (B, F); 1024x1024 pixel at scanning size 2x2 µm (D).

to subcutaneous pH 7.4 with NaOH at the start of incubation[5] (data not shown).

In conclusion, Oxyntomodulin nucleation and the development of well-structured fibrils seem to require different environments.

Fibrillation in presence of NaCl is fast and quantitative, but self-seeding is too extensive to allow the formation of long fibrils even if no agitation is applied. Presumably, rapid depletion of soluble peptide in presence of numerous fibril termini and charge-screening electrolytes is the limiting factor for fibril length. This is aggravated in agitated conditions, where fragmentation decreases average fibril size and increases fibril numbers. Conversely, conditions disfavoring Oxyntomodulin's nucleation – such as absence of salt or agitation – allow the elongation of fewer fibrils. In these conditions, self-assembly is not quantitative, so that soluble peptide is available even after long incubation times. Limitations to fibril yield can be partly due to steric hindrance of diffusion and termini availability in formed hydrogels. Fibrils formed in presence of salt dissolve after dilution in water, proving that the reaction equilibrium is further on the free peptide side of the polymerization reaction in the absence of electrolytes. The thermodynamic equilibrium of soluble and self-assembled peptide additionally delimits fibrillation in water.

It was therefore not possible to satisfy the parameters set for quality, quantity, and speed of Oxyntomodulin self-assembly in a one-step reaction.

---

[5] Data are not shown here because the fibril characterization in chapters 4 and 5 was performed without pH adjustment. pH-adjusted fibril batches were used for *in vivo* studies in [6].

3.4 A three-step seeded method to efficiently produce uniform Oxyntomodulin fibrils at high yield

To combine fast nucleation, well-ordered elongation and high yield in Oxyntomodulin self-assembly, the polymerization reaction was decoupled into three steps. Short fibrils were formed in fast nucleation conditions and elongated in conditions that disfavor nucleation, so that the seed amounts and elongation conditions can be directly controlled. Elongated fibrils were then either separated from remaining free peptide, or the equilibrium was shifted to the fibril side by addition of salt.

Short fibrils were grown under agitated conditions with NaCl equivalent to **Figure 4-5** and used as seeds for elongation in water. Seeding at 0.5 % (seed mass: free peptide mass) without further processing of seed fibrils produced elongated fibrils in water at total peptide concentrations from 1 to 10 mg mL^{-1}. At 1 mg mL^{-1}, seeds initially disaggregated below detection limits by AFM, and few, thin fibrils formed after 11 d (results not shown). At 5 mg mL^{-1}, elongation could be seen from 24 h on, but the fibril morphology did not reflect the seed morphology. While seeds were straight and did not split and merge, daughter fibrils at 5 mg mL^{-1} contained several twisted types and higher order assemblies (see **Figure 4-6** A-D). Separation of the soluble fraction from the gel fraction after 13 d resulted in continued growth of twisted species in the soluble fraction, implying that different seeds were formed during the elongation process (see **Figure 4-6** F and G). At 10 mg mL^{-1}, a cloudy gel with long fibrils formed after 7 d. As shown in **Figure 4-7**, fibril morphology was similar to the seed type, with the bulk of fibrils consisting of straight, 6-8 nm high fibrils that occur single or laterally aligned. Very few twisted species coexisted with the straight type. Increase of seed concentration to 4.5 % in 10 mg mL^{-1} salt-free Oxyntomodulin produced a clear gel after 24 h with indistinguishable fibril morphology (results not shown).

It was assumed that the occurrence of polymorphism in seeded batches was a result of insufficient seeding. If the seed length were 200 nm in average, contained only two monomers per cross-section, and there were two growth competent ends available at all times, the number of fibril ends to monomers in the fibril would be 1:425 (assuming 4.7 Å β-strand spacing), so that even at 10 % seeding strength, the number ratio of monomers to fibril ends would not exceed 4250. Considering steric hindrance in a crowded environment and statistical differences in the growth competence of fibril termini, this number could easily exceed 10000. Due to the considerable amount of free peptide during elongation, spontaneous or surface-catalyzed nucleation could then produce different fibril species with little structural similarity to the seed fibrils. Here, seeding with more fibrils was not an option because it could increase salt concentration over a critical nucleation level. It was however known from literature that fibril length can be reduced and homogenized by sonication [159][129][147].
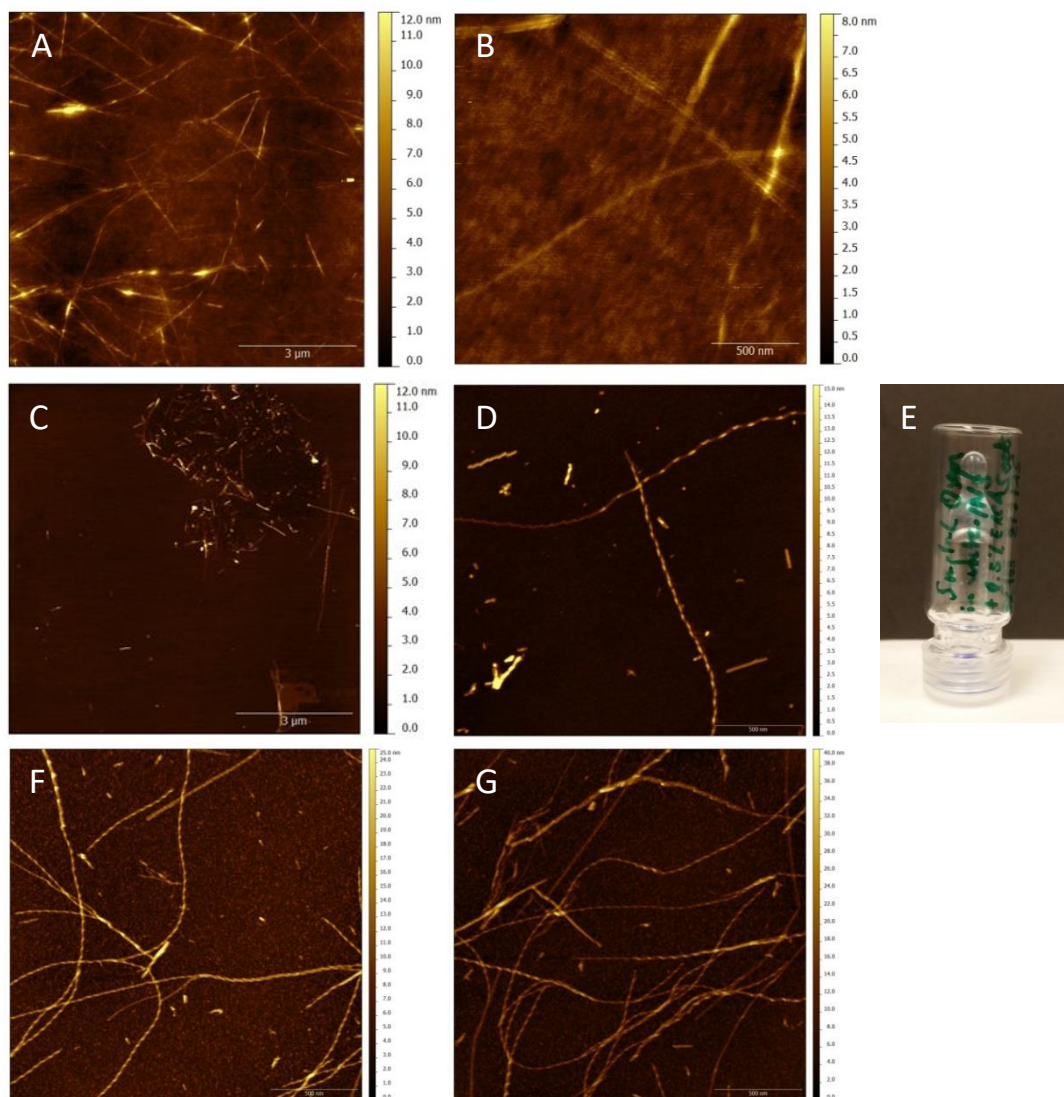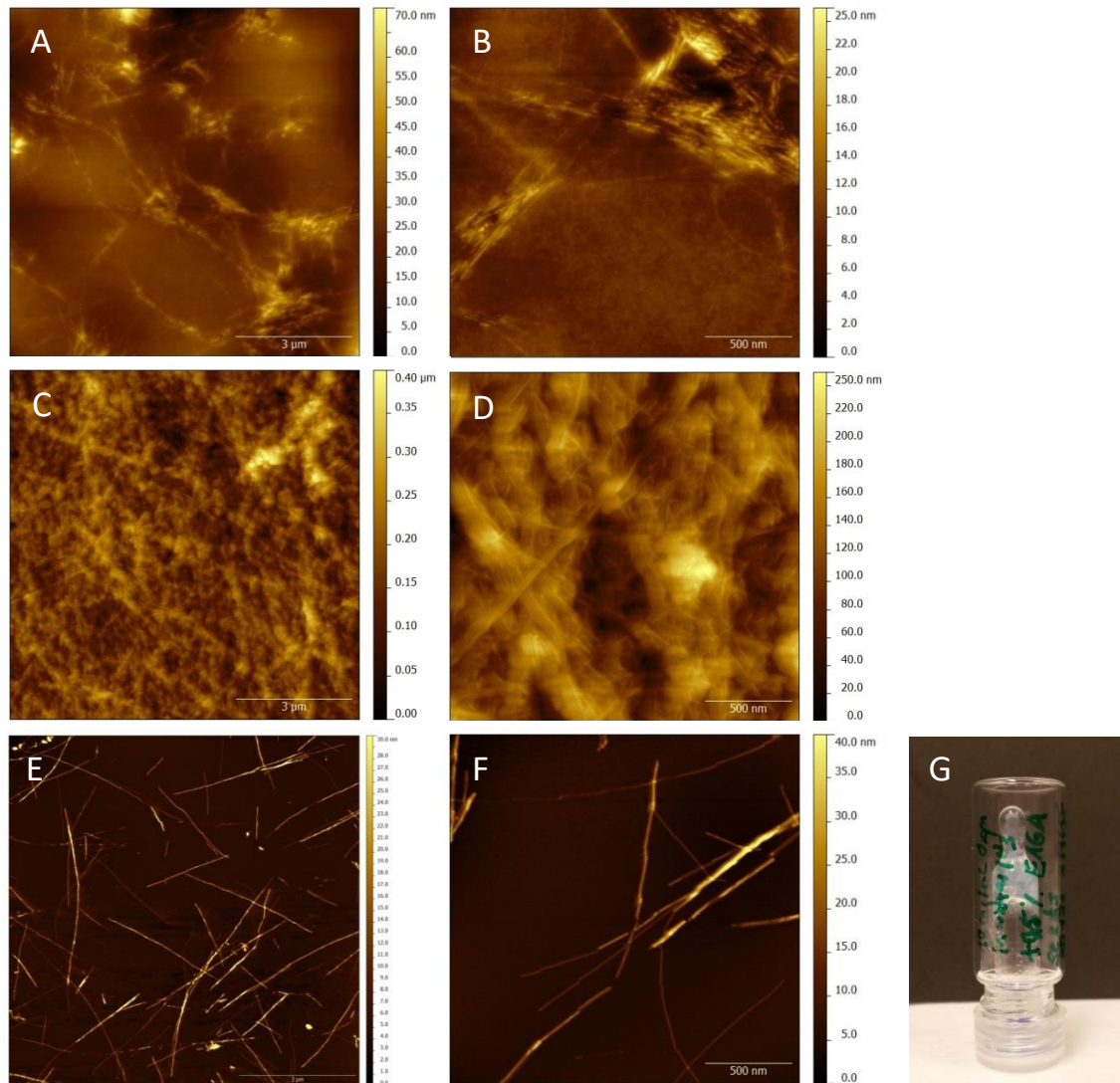
Figure 3-6: Seeding of a salt-free 5 mg mL^{-1} Oxyntomodulin solution with 0.5 % fibril seeds at 37 °C without agitation promotes formation of polymorphic fibrils

Quiescent incubation of 5 mg mL^{-1} Oxyntomodulin in water at 37 °C with 0.5 % short seed fibrils. A and B, 7 days; C and D, 13 days, 100x diluted; E, gel formed at 11 d, F and G, supernatant after 13 d re-incubated for 6 d, 100x dilute. Note the fibril splitting and merging seen in C, F and G, as well as the different heights and degrees of twisting. AFM images were processed in Gwyddion to remove imaging scars and background signal. Resolution: 512x512 pixel at scanning size 9x9 µm (A, C); 1024x1024 pixel at scanning size 2x2 µm (B, D, G).

Figure 3-7: Seeding of a salt-free 10 mg mL^{-1} Oxyntomodulin solution with 0.5 % fibril seeds at 37 °C without agitation causes conversion to long fibrils within 7 d

Quiescent incubation of 10 mg mL^{-1} Oxyntomodulin in water at 37 °C with 0.5 % short seed fibrils. A and B, 24 h; C and D, 7 days; E and F, 7 d, 100x dilute; G, gel formed at 7 d. AFM images were processed in Gwyddion to remove imaging scars and background signal. Resolution: 512x512 pixel at scanning size 9x9 µm (A, C, E); 1024x1024 pixel at scanning size 2x2 µm (B, D, F).

Fibril fragmentation was tested in a sonication bath. The pellet of an aqueous sample grown for 13 d at 10 mg mL^{-1} in presence of 1 % short fibrils was diluted to 1 mg mL^{-1} in water and sonicated for different times. Fibril length was assessed by AFM. As shown in **Figure 4-8** and **Figure 4-9**, initial fibrils were >3 µm long and shortened increasingly during sonication. The fibrillar shape was maintained even after 30 min sonication. Fibril length shortened slightly if not used instantly due to the dilution in water, however no complete dissolution or reassembly was seen over the course of 48 h (results not shown).
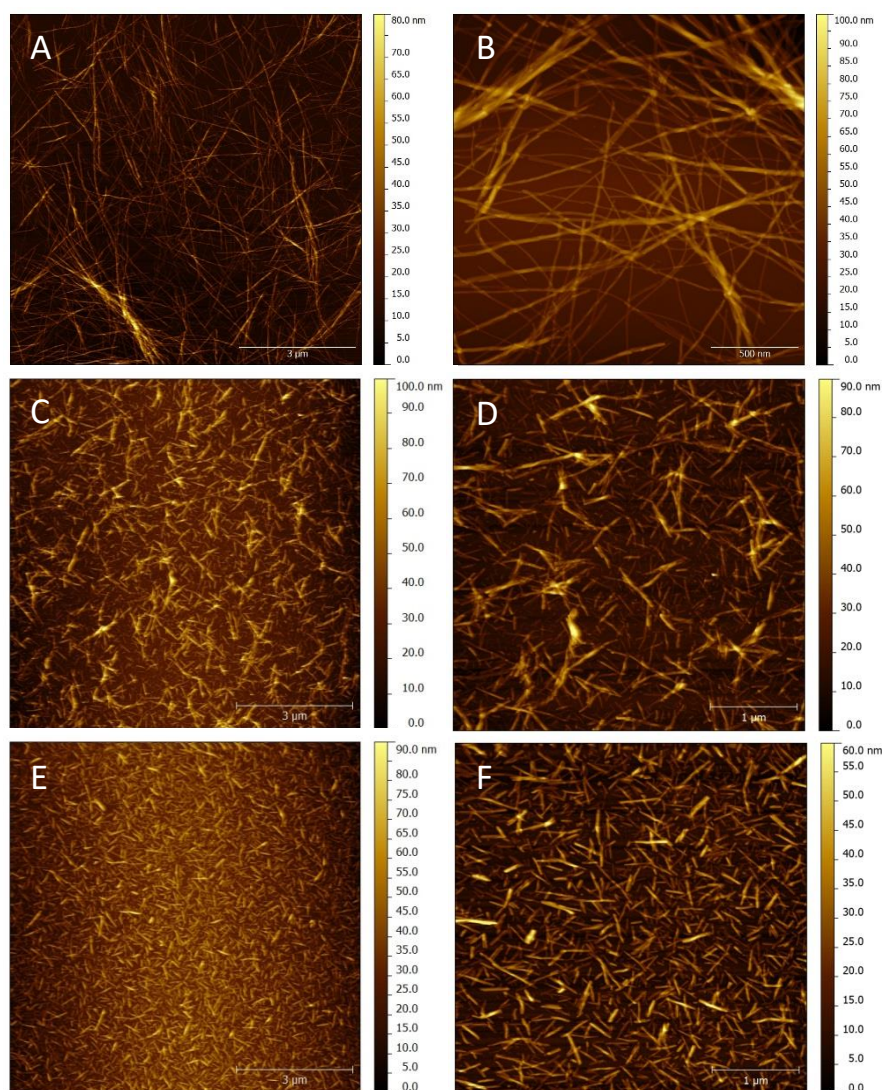
Figure 3-8: Fragmentation of salt-free 0.5 mg mL^{-1} Oxymtomodulin fibril samples by sonication (I)

A and B, 26 mg mL^{-1} fibril stock before sonication, 100x dilute. C and D, fibrils after 30 s sonication, 10x dilute; E and F, fibrils after 60 s sonication, 10x dilute. AFM images were processed in Gwyddion to remove imaging scars and background signal. Resolution: 512x512 pixel at scanning size 9x9 µm (A, C, E); 1024x1024 pixel at scanning size 2x2 µm (B) and 4x4 µm (D, F).
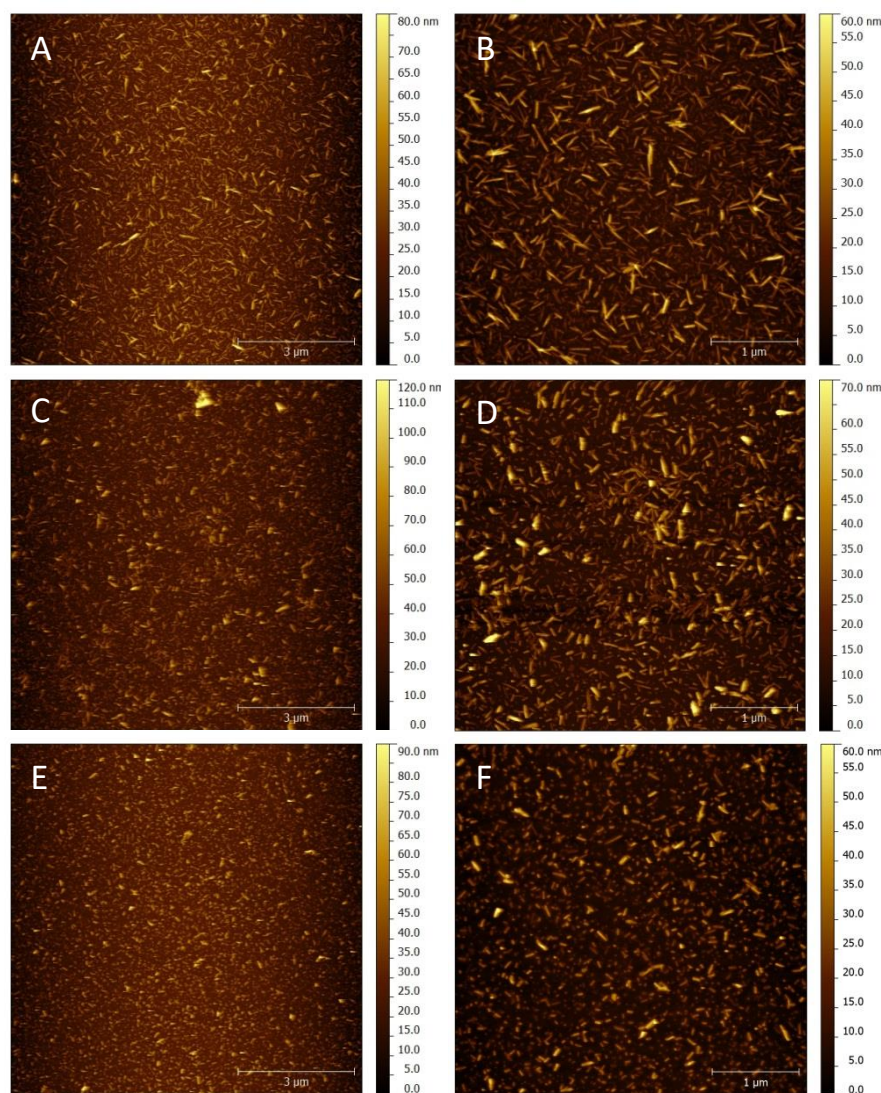
Figure 3-9: Fragmentation of salt-free 0.5 mg mL^{-1} Oxymtomodulin fibril samples by sonication (II)

A and B, fibrils after 2 min sonication. C and D, fibrils after 10 min sonication; E and F, fibrils after 30 min sonication. AFM images were processed in Gwyddion to remove imaging scars and background signal. Resolution: 512x512 pixel at scanning size 9x9 µm (A, C, E); 1024x1024 pixel at scanning size (B, D, F).

Sonicated fibrils were then used to seed freshly prepared Oxyntomodulin solutions. Elongation of 15 min sonicated fibrils was tested in presence of 0.9 mg mL^{-1} saline and in salt-free conditions. In presence of NaCl, conversion to fibrils was quantitative within 24 h from 0.5 to 10 mg mL^{-1}, but only relatively short, clumped fibrils were formed (see **Figure 4-10** A and B). Samples were difficult to handle due to the sticky nature of the gels.

Seeding aqueous samples with 15 min sonicated fibril samples created clear gels with long, predominantly single fibrils within 24 h (see **Figure 4-10**). Further incubation led to a conversion yield of approximately 50 % by day 7 and 65 % by week 8, which did not increase

at longer incubation times. Salt-free fibrils could be produced reproducibly and were used for biophysical characterization in chapter 4. Fibrillation kinetics were followed in a seeded ThT assay without agitation at 1, 5, and 10 mg mL^{-1} in water (see **Figure 4-11**). Consistent with the theoretical kinetics of exclusive elongation (1-9), approximately linear signal increase was seen[6]. Linear elongation kinetics and the monomorphic fibril appearance suggest that addition of 1 % sonicated fibrils provided enough seeds to prevent secondary nucleation.
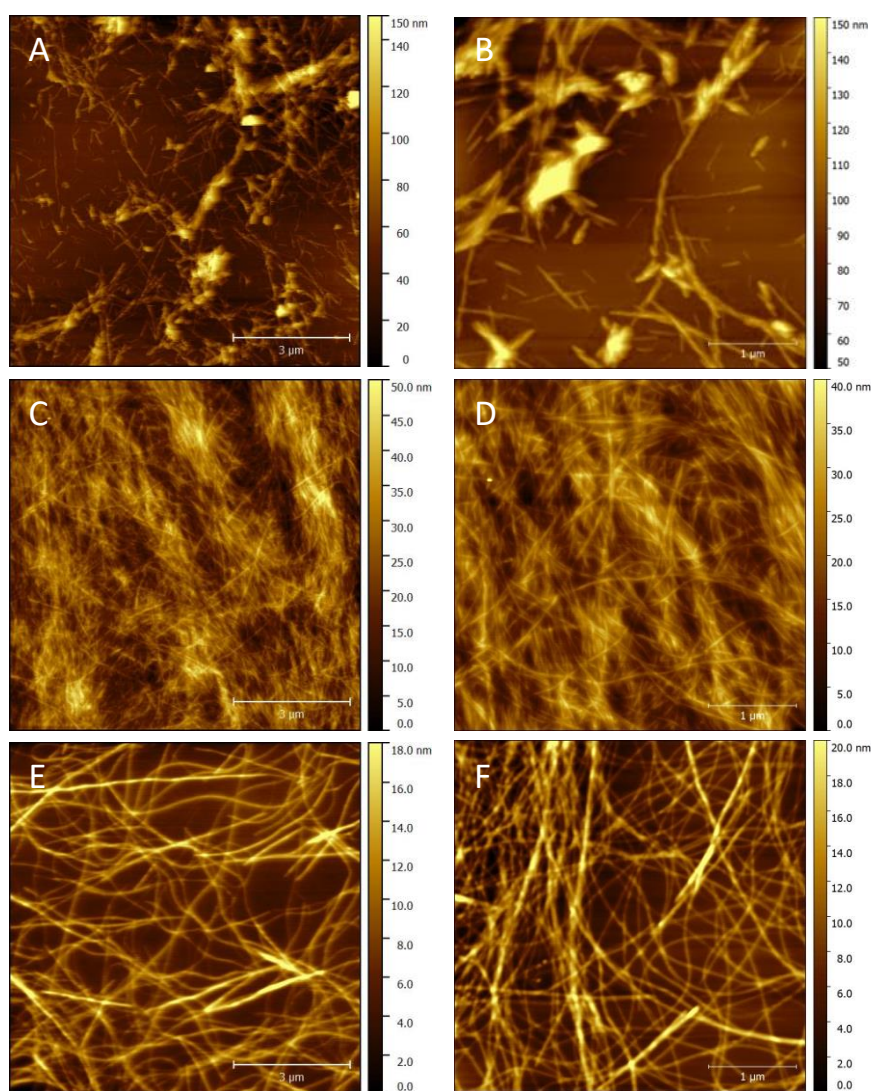
Figure 3-10: Seeding of a salt-free 10 mg mL^{-1} Oxyntomodulin solution with 1% fragmented fibrils leads to fast formation of long fibrils

Seeding of 10 mg mL^{-1} Oxyntomodulin solutions with 1 % seeds fragmented by 15 min sonication. A and B, Elongation in 0.9 mg mL^{-1} NaCl after 48 h, 100x dilute. C and D, Elongation in water after 48 h; E and F: Elongation in water after 6 d, 100x dilute. AFM images were processed in Gwyddion to remove imaging scars and background signal. Resolution: 512x512 pixel at scanning size: 9x9 µm (A, C, E); 1024x1024 pixel at scanning size 4x4 µm (B, D, F).

[6] Kinetic ThT assays at more than 1 mg mL^{-1} peptide concentration could not be performed in presence of NaCl, because the fluorescence signal was quenched by gelation.
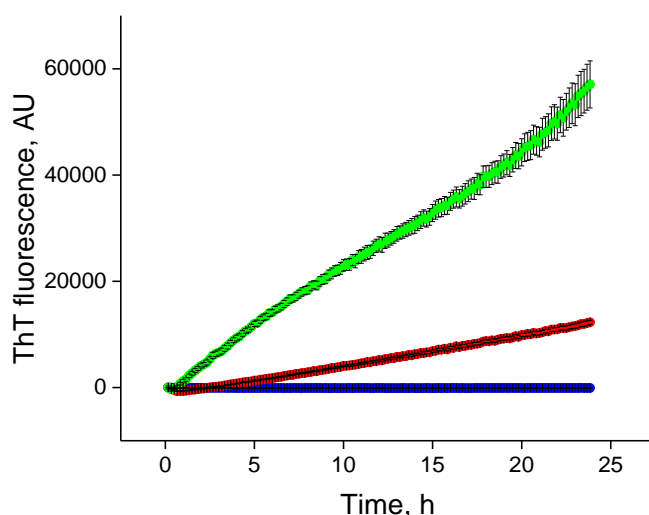
Figure 3-11: ThT kinetics of Oxyntomodulin seeding with sonicated fibrils in water

Seeding of 1 mg mL^{-1} (blue), 5 mg mL^{-1} (red) or 10 mg mL^{-1} (green) Oxyntomodulin with 1 % (w/w) seed fibrils in presence of 50 µM ThT. Seeds were derived from 10 min sonication of mature fibrils in water. Images show averages of triplicate data with 10 fluorescence readings per hour. No agitation was applied apart from the movement of the microplate under the detector.

Addition of saline to elongated fibrils in water shifted the equilibrium to the fibril side within 24 h. Individual fibril morphology was maintained, although fibrils showed more lateral association after addition of salt. For further biophysical and kinetic studies in chapters 4 and 5, the fibrillar fraction was concentrated by sedimentation at 13000 rpm, washed in 10-fold volume of water, and stored at 10-20 mg mL^{-1} in the fridge. No alteration in gel or fibril morphology was seen within one year. Fibril stocks could be used to seed new, morphologically indistinguishable samples by the same process of (1) fragmentation by sonication for 15 min at 1 mg mL^{-1} in water (=*seeds*), (2) elongation by quiescent one-week incubation at 37 °C after seeding a 10 mg mL^{-1} salt-free Oxyntomodulin sample with 1 % sonicated fibrils (=*protofibrils*), and (3) shifting of the equilibrium by addition of NaCl to elongated samples (= *mature fibrils*). A new fibril generation could be produced by steps (1) to (3) within nine days including imaging and measurement of conversion yield.

For *in vivo* studies, seeded 10 mg mL^{-1} aqueous gels were diluted to 0.9 mg mL^{-1} NaCl and 1 mg mL^{-1} total peptide concentration. This formed a viscous fluid as described in [6]. The rheological behaviour of the viscous fluid was characterized in a rate sweep test. Prior to analysis, a 17 mg mL^{-1} gel was diluted to 1 mg mL^{-1} in water or 0.9 mg mL^{-1} NaCl. The viscosity curves are shown in **Figure 4-12**.
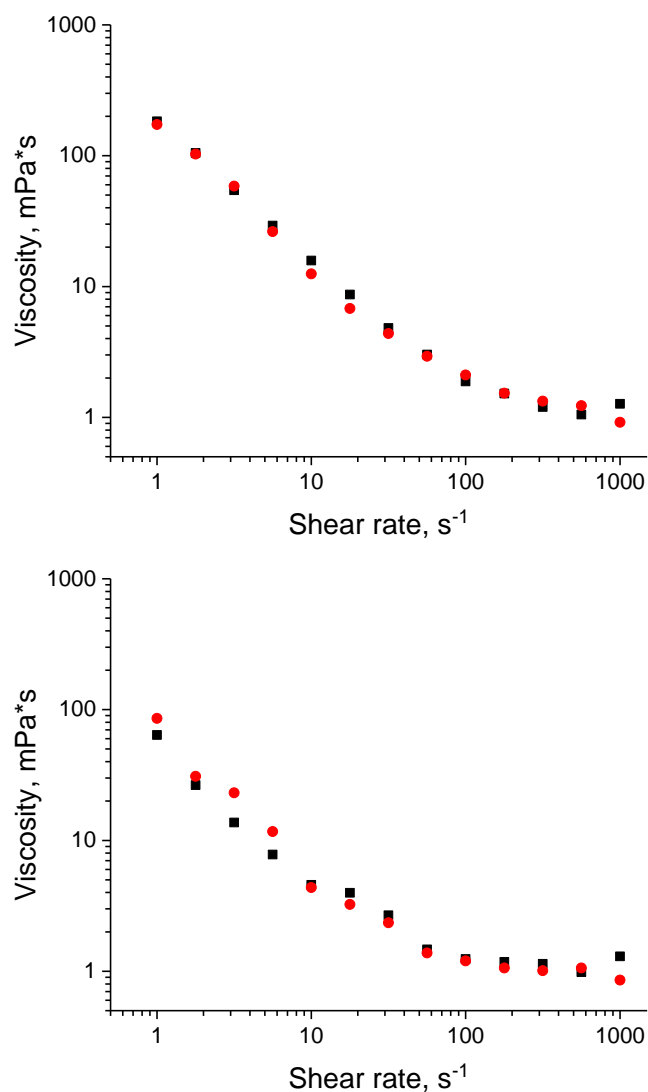
Figure 3-12: Oxyntomodulin gel viscosity

Rate sweep test in a Physica MCR 301 rheometer equipped with a flat plate and a 40 mm 1° angle cone. Shear stress was measured at 37 °C in response to a shear rate reduction from 1000 s^{-1} to 1 s^{-1} (black) and reverse (red). A 17 mg mL^{-1} Oxyntomodulin gel was diluted to 1 mg mL^{-1} in (A) water and (B) 0.9 mg mL^{-1} NaCl and measured immediately.

Samples showed shear-thinning behaviour with a linear dependency of logarithmic shear rate and viscosity at low shear stress, which is characteristic for a weak gel [160]. It is noteworthy that the maximum and minimum viscosity is lower for samples containing salt than for formulations in water, which is advantageous for needle injections. Samples could be injected subcutaneously with a 27-gauge needle, as advised by Dr Jay Pathak, drug formulation specialist at MedImmune, Gaithersburg, USA.

4 Structural constraints of Oxyntomodulin fibrils

As described in chapter 3, Oxyntomodulin readily self-assembles to fibrils in a range of conditions. A seed-elongation method was developed to prepare visually homogeneous sample gels that contained several μm long fibrils. In elongation conditions without salt addition, a protofibrillar type with predominantly single, straight, unbranched fibrils was formed. Addition of salt shifted the conversion yield from ~50 % to ~100 %. Fibrils were then predominantly clustered to laterally aligned bundles. The aim of this chapter is to:

(1) test if the protofibrils and fibrils display amyloid-type characteristics

(2) assess if protofibrils and fibrils are distinguishable at molecular level, and

(3) identify constraints to the fibril architecture at molecular level.

4.1 Methods

4.1.1 ThT and intrinsic Tryptophan fluorescence

ThT fluorescence was used to probe binding of the amyloid specific dye to soluble Oxyntomodulin, mature Oxyntomodulin fibrils, and protofibrils in water. Triplicate 100 μL aliquots at 1 mg mL^{-1} containing 50 μL ThT were scanned in Corning 3880 microplates in a F-7000 FL (Hitachi, Japan) plate reader. Top reading mode was used at 440 nm excitation and 450 to 600 nm emission, at a slid width 5 nm. Results of protofibrils in water were corrected for 35 % free peptide in the protofibril sample by scaling of fluorescence yield to 1 mg mL^{-1} fibril content.

Intrinsic tryptophan fluorescence was measured to compare the microenvironment hydrophobicity in soluble and fibrillar Oxyntomodulin. The samples and setup were analogous to ThT fluorescence measurements on the Hitachi plate reader, however no ThT was added. Samples were excited at 277 nm and emission was recorded at 285 to 500 nm at a slid width of 2.5 nm and a response time of 2 s. Results of protofibrils in water were corrected for free peptide by subtracting the signal of a 0.35 mg mL^{-1} concentrated soluble peptide background signal, and scaling the corrected fluorescence yield to 1 mg mL^{-1} fibril content. This is different to correction in ThT fluorescence measurement because Trp fluorescence is present in soluble Oxyntomodulin, while ThT fluorescence in soluble peptide and water are indistinguishable.

4.1.2 Secondary structure by Attenuated Total Reflection Fourier Transform Infrared Spectroscopy

ATR-FTIR spectra of soluble and fibrillar Oxyntomodulin were recorded on a Frontier FTIR spectrometer (PerkinElmer, US) within a wavenumber range from 2000 to 1000 cm^{-1}, with 1 cm^{-1} resolution and 8 accumulations per sample. A 2 μL sample of 1 mg mL^{-1} total peptide concentration was deposited on the crystal window and left to dry in air before scanning. A background scan in air was deduced from the spectra. Results of protofibrils were corrected for free peptide analogous to Trp fluorescence spectra, and all spectra were normalized to the amide II signal at 1550 cm^{-1}.

4.1.3 Secondary structure by Circular Dichroism

Far-UV CD spectra were recorded from 260 to 180 nm on a Jasco J-815 spectropolarimeter (Jasco, US), with a scanning resolution of 1 nm, 20 nm s^{-1} scan speed, and automatic averaging of 4 scans per sample. (+)-10-camphorsulfonic acid was used as a standard to calibrate the instrument according to manufacturer's instructions. Fibril- and soluble peptide spectra were recorded at 1 mg mL^{-1} total peptide concentration in a quartz cuvette with 0.1 mm path length[7] (Starna, UK) at 25 °C with 10 min thermal equilibration before measurement. Measurements were independently repeated three times. The solvent signal was deduced from measured spectra, and corrected spectra were deconvoluted with the online tool DichroWeb (http://dichroweb.cryst.bbk.ac.uk/html/home.shtml) to estimate the percentage contributions of helices, sheets and turns to the overall spectrum. The best fits compared to molecular library set 6 are computed with the algorithms CONTIN-LL, SELCON3 and CDSSTR [161][162]. Prior to analysis in DichroWeb, results of protofibrils were corrected for 35 % free peptide in the measured sample analogous to spectrum correction in Trp fluorescence. Algorithm fits are averaged for each triplicate measurement, and results are expressed as averages ± standard deviations of triplicates.

4.1.4 Identification of amyloid core structure by limited peptidolysis

Soluble peptide and fibrils were digested with trypsin at 37 °C and pH 8 (NaOH in water) or in PBS pH 7.35. Trypsin (mass spectrometry grade, Sigma Alrich) was reconstituted from freeze-dried aliquots according to manufacturer's instructions, and used at 5 % (w/w) with 0.5 mg mL^{-1} peptide or fibrils. Aliquots were separated by HPLC in a 1260 Infinity II system with a ZORBAX 300SB-C18 analytical column (Agilent Technologies, UK), bead size 5 μm,

---

[7] CD is sensitive to the combination of concentration and pathlength, and deconvolution algorithms only accept a certain range of absolute absorbance (Calero and Gassett, 2005). Oxyntomodulin samples were also tested at 0.5 mg mL^{-1} and in 0.01 and 10 mm cuvettes, however the combination of 1 mg mL^{-1} and 0.1 mm path length gave the most reproducible and evaluable data.

250 mm. Samples were eluted at 1 mL min^{-1} flow rate in a linear gradient from 100 % solvent A (94.9 % water, 5 % Acetonitrile, 0.1 % trifluoric acid) to 80 % solvent B (94.9 % Acetonitrile, 5 % water, 0.1 % trifluoric acid) over 30 min, followed by a 5 min rinsing step at 100 % B. Elution was detected at 214 and 280 nm. The system was cleaned with 100 % acetonitrile for 20 min and stored in solvent B. Samples were centrifuged at 13000 rpm for 30 min prior to injection to avoid clogging of the column with particles. Self-digestion of Trypsin was tested in the same conditions.

4.1.5 X-ray fiber diffraction

X-ray diffraction patterns were recorded on a Bruker D8 Quest X-ray diffractometer. Sample preparation was done according to [116]. Briefly, a drop of 10 mg mL^{-1} fibril sample was placed between two wax-sealed capillaries. After drying overnight, a stretched, partly aligned fibril thread formed. The fibril thread was aligned in the beam path and exposed for 120 s.

4.1.6 Fibril imaging by Cryo Electron Microscopy

Sample preparation and image capture were a service of FEI at the Nanoscience Centre, University of Cambridge. Samples were blotted and flash frozen in liquid ethane using a Vitrobot MKV and quantifoil R1.2/1.3 300 mesh grids, made hydrophilic by glow discharge at 0.39 mbar for 60 s at 25 mA. The Vitrobot was operated at 4 °C, 100 % relative humidity, 25 s blot time, and 2 μL sample application volume at 1 mg mL^{-1} total peptide concentration in the sample. Blot force was calibrated to create a wedge of thick ice on roughly one third of the grid, with a gradient of ice thickness on the other two thirds of the grid, corresponding to a setting of -6 on the instrument. Vitrifies samples were stored in liquid nitrogen. Images were acquired on a Titan KriosTM (FEI, ThermoScientificTM) run at 300 kV. Mature fibrils were detected with an Atlas 2 electron detection camera. Images of protofibrils and the twisted fibril species in chapter 6 were recorded as movies with a Falcon 3 direct electron detector, followed computational image reconstruction in MotionCore from acquired movies, to correct for drift caused by beam-induced motion. Vitrified samples were stored in liquid Nitrogen. Files were obtained in .mrc format and had a resolution of 1.07 pixels per Å. Images were processed with the automatic brightness and contrast tool in Fiji (ImageJ) and exported in .jpeg format. Polygon selections were transformed with the FFT (fast Fourier transform) tool to display the diffraction pattern of single fibrils. The line selection tool was used to measure lateral dimensions and plot profiles as a function of grey values.

4.2 Oxyntomodulin fibrils display amyloid-specific fluorescence

As reviewed in chapter 1.2.2, ThT is a marker for cross-beta alignment, while Tryptophan fluorescence is a measure for the hydrophobicity of the microenvironment of a Tryptophan residue. ThT and intrinsic Tryptophan fluorescence were measured in free peptide, protofibrils and fibrils. Fluorescence emission curves are shown in **Figure 5-1**.

Freshly dissolved peptide does not bind ThT, consistent with the random- and α-helical conformation of soluble Oxyntomodulin reported in the literature [48]. Protofibrils show very weak ThT binding, confirming the low ThT binding in screening (**Figure *9-13***) and aqueous seed elongation (**Figure 4-11**). ThT fluorescence was more than 10-fold higher in samples that contained 0.9 mg mL^{-1} NaCl at the same fibril concentration.

Different levels of ThT binding are not *per se* an evidence for a difference in amyloid structure. Weak ThT binding can imply a less structured fibril architecture, e.g. the presence of an amyloid core that is partially shielded by unstructured sequences. However, it is well known that ThT has lower affinity to thinner structures on or off the pathway to mature fibril formation, and markedly decreased affinity to positively charged surfaces because of the dye molecule's positive charge [123][124].
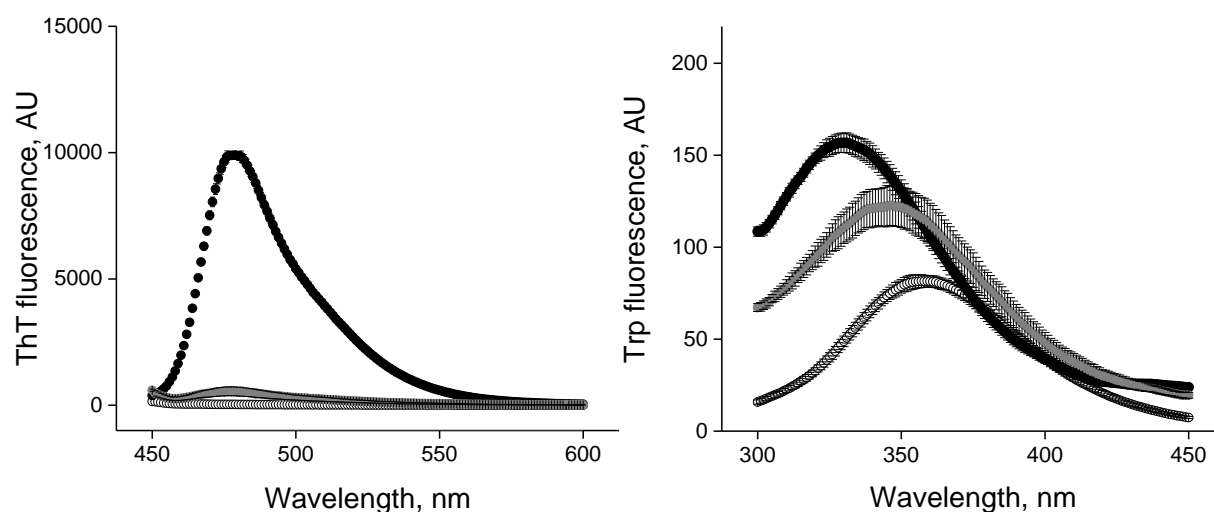
Figure 4-1: ThT and Tryptophan fluorescence of soluble, protofibrillar and fibrillar Oxyntomodulin

Left, ThT fluorescence curves of soluble (transparent), protofibrillar (grey) and fibrillar (black) Oxyntomodulin samples, measured by excitation at 440 nm and emission at 450 to 600 nm. Right, fluorescence of the Tryptophan residue at amino acid position 25 in soluble (transparent), protofibrillar (grey) and fibrillar (black) Oxyntomodulin samples, measured by excitation at 277 nm and emission from 285 to 500 nm at a slid width of 2.5 nm. Both fluorescence curve types are formed with the same samples at room temperature on a Hitachi F-7000 FL fluorescence plate reader. Results of triplicate averages ± standard deviation are shown at a slid width 5 nm (ThT) and 2.5 nm (Trp).

Both protofibrillar and fibrillar Oxyntomodulin samples exhibited a blue-shifted emission peak of intrinsic Tryptophan fluorescence, compared to soluble peptide. This proves that the Tryptophan residue at amino acid position 25 in the Oxyntomodulin sequence is incorporated in a more hydrophobic environment inside fibrillar structures, as seen for the core structures of amyloid-like proteins [125]. The more marked blue shift in mature fibrils compared to protofibrils may imply a denser or more structured local packing, possibly facilitated by masking of surface charges in presence of electrolytes. Independent of fibril core structures, the lateral assembly of fibrils in salt-containing environments is also expected to shield residues from the solvent. It is not possible to distinguish the contributions of either effect in this experiment.

4.3 Insights into secondary structure of Oxyntomodulin fibrils

The secondary structure of soluble, protofibrillar and fibrillar Oxyntomodulin was assessed by ATR-FTIR and CD. FTIR and CD are orthogonal spectroscopic methods that can be used to measure helical, sheet, and turn conformations. While CD is traditionally used for soluble proteins [163], FTIR has been extensively used for investigations of self-assembled structures [164][165][127][126][166][167]. The methods are complimentary in that FTIR can distinguish between parallel and antiparallel β-sheet alignment, and CD can distinguish between 3_{10} and α-helix [126][127][48]. CD signals are easier to quantify, allowing an estimation of secondary structure contents in a structure.

Infrared spectroscopy measures the interaction of infrared radiation with a sample. In FTIR, the wavenumber[8] shifts measured by an interferometer are reverse-transformed to an absorption spectrum. Generally, absorption occurs when the frequencies of radiation and vibration of a polar bond are equal, and when vibration causes a change in dipole moment. The magnitude and exact wavelength of absorption depend on the polarity of vibrating bonds and can thus be influenced by neighbouring groups [166]. In Attenuated Total Reflection (ATR) spectroscopy, infrared light propagates by total reflection inside a crystal before detection. Light reflection at the sides of the crystal creates evanescent waves that protrude into the surrounding medium. Deposition of a sample on one side of the crystal absorbs the radiation of evanescent waves, so that the detected intensity is dampened. Because the intensity of the evanescent wave decays exponentially with distance from the crystal surface, the measurement of very thin films such as dried proteinaceous samples is possible, and IR absorption by water is avoided [168]. IR absorption in proteins and peptides can occur at all polar bonds including backbone and side-chain bonds. The amide I band (1700-1600 cm^{-1}) has the strongest absorption of infrared light, little contributions of side-chain interactions, and sensitivity to hydrogen bonding pattern in the molecule or supramolecular arrangements. Amide I absorption is mainly caused by C=O stretching vibrations with minor contributions from C-N stretching and N-H bending vibrations [168][169]. In a hydrogen-bonded secondary structure, coupling of transition dipoles causes interference of vibration modes. The superposition of local modes in a secondary structure is termed normal mode [127].

Native β-sheets absorb between 1623 and 1643 cm^{-1} with a possible weaker band from 1689 to 1693 cm^{-1}; α-helices between 1662 and 1645 cm^{-1} with a typical maximum between 1654 and 1658 cm^{-1}; 3_{10} helices between 1660 and 1666; β-turns between 1666 and 1687 cm^{-1}, and random alignment between 1646 and 1650 [169]. Because of the alternating alignment in antiparallel β-sheets, the direction of local and normal modes has a larger contribution rectangular to the sheet plane than in parallel alignment [127]. Native antiparallel β-sheets

---

[8] By IUPAC guidelines, IR absorption spectra are plotted as a function of decreasing wavenumber. Wavenumber is the inverse of wavelength and expressed in cm^{-1}.

thus show a strong band near 1630 cm^{-1} corresponding to the modes in sheet direction, and an additional weaker band near 1685 cm^{-1} corresponding to C=O stretches in strand direction [166]. In parallel sheets, C=O stretches from local and normal modes align. Due to coupling of transition dipoles, the main absorption peak of parallel β-sheets is slightly blue-shifted (higher wave number) compared to antiparallel β-sheets of the same dimensions, with less or absent contribution of a second band at higher wavenumbers [126][127][166]. Because of overlapping bands, band broadening due to sample inhomogeneities, and shifted peaks due to twisting of extended secondary structures, band assignment is not always inambiguous [166].

In ext ended β-sheets such as in the cross-β alignment of amyloid fibrils, local and normal modes interfere constructively, generally leading to red-shifted β-sheet absorption bands compared to native proteins. Typically, amyloid fibrils show the highest absorption band between 1615 and 1630 cm^{-1}, corresponding to orchestrated β-sheet absorption [164][126]. The extent of red-shift is a measure for the size and rigidity of amyloid structures. Large, well-ordered amyloid structures absorb near 1620 cm^{-1}, and smaller, less ordered fibrils absorb near 1630 cm^{-1} [127]. Further parallel sheet absorption bands can be seen between 1660 and 1670 cm^{-1} [126]. Parallel and antiparallel sheet alignment can thus not be distinguished by the wavenumber of the main absorption band. Antiparallel β-sheets in amyloid fibrils create a high frequency band around 1685 cm^{-1}, however similar bands may stem from twisted parallel β-sheets. Therefore, the presence of a strong absorption band between 1615 and 1630 cm^{-1} in absence of a high wavenumber FTIR band is a strong indicator for parallel β-sheet, but the presence of an absorption band around 1685 cm^{-1} is only an indicator for antiparallel alignment [164][126][127][166]. FTIR cannot distinguish β-arches and β-turns in amyloid configuration [127].

Soluble Oxyntomodulin showed a single maximum at 1654 cm^{-1}, corresponding to a predominantly α-helical conformation in solution. A slightly broadened shoulder at higher wavelength and at 1645 cm^{-1} indicates presence of unstructured arrangements. This is in agreement with reported structural characteristics of native Oxyntomodulin [48].
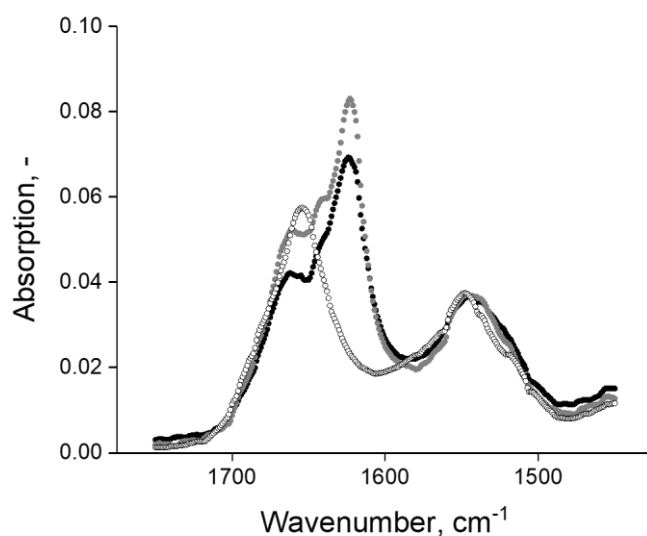
Figure 4-2: ATR-FTIR spectrum of soluble and fibrillar Oxyntomodulin

1 mg mL^{-1} samples dried on ATR crystal before measurement. Spectra are normalized to the signal at 1650 cm^{-1}. Open circles: soluble Oxyntomodulin; black circles: fibrils; grey circles: protofibrils, spectrum corrected for 35 % soluble peptide.

Oxyntomodulin protofibrils and mature fibrils show remarkably similar absorption spectra. Absorption in mature fibrils is generally weaker, however this may be due to steric shielding from radiation by partially aligned fibrils. The absorption bands overlap within experimental error. The main absorption band is a sharp peak centred around 1624 cm^{-1}, indicating a well-ordered β-sheet. A further β-sheet absorption band is seen at 1640 cm^{-1}. A broad peak between 1660 and 1670 additionally indicates parallel β-sheet, but may also contain contributions from residual α-helix conformation. Absorption beyond 1675 cm^{-1} is lower than for soluble Oxyntomodulin and lacks a peak. Therefore, FTIR strongly indicates that the architecture of Oxyntomodulin protofibrils and fibrils is a well-ordered, parallel β-sheet. Although weak, the shoulder at 1667 cm^{-1} suggests a turn within the molecule. A folded arch- or turn-conformation would be in accordance with the 6 nm diameter of protofibrils, which is about half the stretched length of a 37 amino acid peptide.

Because of the ambiguous band assignment in FTIR, Oxyntomodulin structures were additionally measured by Far-UV CD. CD measures the difference between a sample's absorption of right- and left-circularly polarized light as a function of wavelength. Contributions from helices, sheets and turns can be quantified by computational fitting to a library of structures with known secondary structure [162][170]. CD deconvolution algorithms cannot distinguish between different types of helices, sheets and turns. As the existing libraries are predominantly composed of (crystal) structures of globular proteins, the quantification of secondary structure composition in self-assembled peptides is only to be
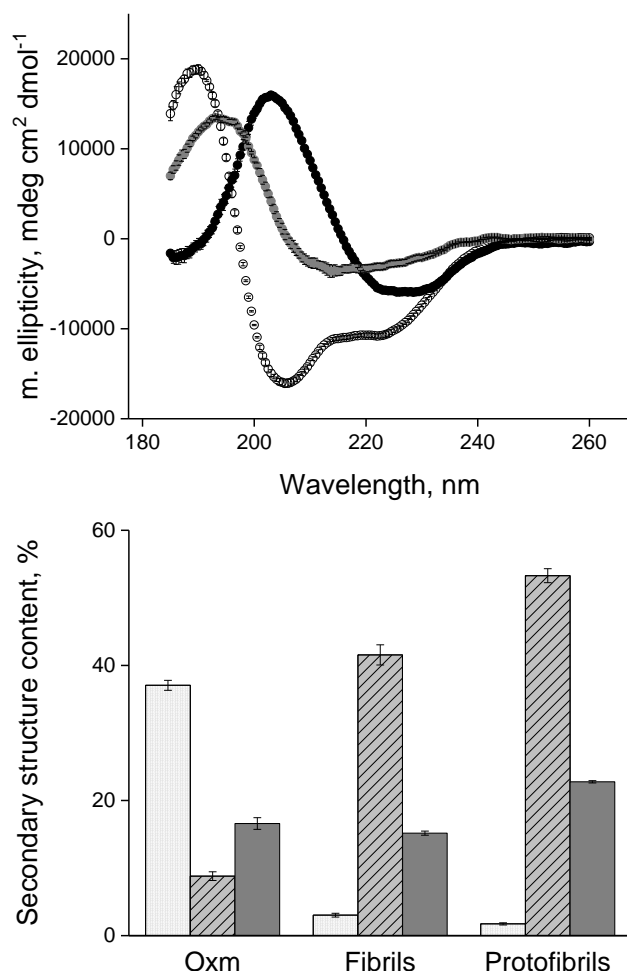
Figure 4-3: Secondary structure contributions in soluble and fibrillar Oxyntomodulin by Far-UV CD

Top: background-corrected CD spectra of 1 mg mL^{-1} Oxyntomodulin samples in wavelength range 240-185 nm. Open circles, soluble Oxyntomodulin; grey, protofibrils without correction for soluble peptide; black, fibrils. Shown is average of 3 independent measurements with 4 averaged runs each, ± standard deviation (n=3). Bottom: data deconvoluted with the online tool Dichroweb using the algorithms CONTIN-LL, SELCON 3 and CDSSTR for each sample. Shown are averages of 3 independent sample runs ± standard deviation. Transparent, dotted: helix; grey, striped: sheet; dark grey, solid: turns.

taken as an estimate [163]. The ratio of molecular ellipticity at 222 and 208 nm is a measure for the ra tio of α-helix and 3_{10} helix [48].

Soluble Oxyntomodulin has a predominantly helical CD spectrum. The transient nature of helical peptide structure in solution is reflected by contributions from unordered structures. Presence of a turn and a differential negative absorption at 222 and 208 nm implies the presence of a 3_{10} helix in addition to an α helix. Values are in accordance with published data on Oxyntomodulin, within experimental error [48].

Fibrils and protofibrils do not contain helices at considerable amounts. Rather, the spectra suggest a predominant sheet structure with turn conformations. Protofibrils show a more ordered structure than fibrils, however this may be a result of light scattering at higher order fibril structures seen in salt-containing conditions. Generally, the results correspond to secondary structure elements derived from ATR-FTIR spectra.

From FTIR and CD, it is not clear if the whole Oxyntomodulin molecule is incorporated into the amyloid core. Spectroscopic measurements cannot distinguish if spectral contributions implying unstructured sequences stem from less defined regions in turns, or from entirely unstructured parts of the molecule. Unlike the fibril core structure, unstructured regions are prone to enzymatic degradation [171][172][173][174]. Trypsin is a widely used peptidolytic enzyme which cleaves after Lysin, Arginine and Cysteine. Trypsin is active in neutral to weakly basic environment, with optimal activity at pH 8. Oxyntomodulin has 6 tryptic cleavage positions; after K12, R17, R18, K30, R31 and R33 (see **Figure 2-2**).

Tryptic digestion of soluble and fibrillar Oxyntomodulin was performed at 37 °C in an unbuffered environment at pH 8 (NaOH), and in PBS pH 7.35. Digestion was followed by HPLC separation after 1 and 24 h. Trypsin was prone to self-digestion, so that further incubation was not conclusive. After 1 h, the monomer peak of soluble Oxyntomodulin at 16.0 min had nearly disappeared, while only small peaks could be seen for fibrillar Oxyntomodulin (not shown). After 24 h, five main peaks were detected at 16.9, 9.0, 7.8, 16.5, and 6.3 minutes retention time, in decreasing order of absorption at 214 nm. Additional smaller peaks between 4 and 17 min indicate partial cleavage due to the proximity of cleavage positions 30, 31 and 33 (see **Figure 4-4**). Fibril digestion produces the same peaks after 24 h. Overall quantities are approximately 60 % lower due to centrifugation of residual fibrils before sample injection. Similar results were found at pH 8 in absence of phosphate.

The absence of preferentially cleaved sequences in presence of peaks corresponding to complete Oxyntomodulin digestion indicates that fibrils are not directly digested, but that soluble peptide in equilibrium is enzymatically cleaved. Peptidolysis effectively removes soluble peptide from the polymerization equilibrium, analogous to peptide removal in a stream of peptide-deprived liquid. This is indirect proof that an equilibrium of soluble and fibrillar Oxyntomodulin exists even in salt-containing conditions like PBS. Although peptidolysis did not prove unstructured regions within Oxyntomodulin fibrils, short unstructured elements are possible, because Trypsin requires several accessible amino acids for cleaving.
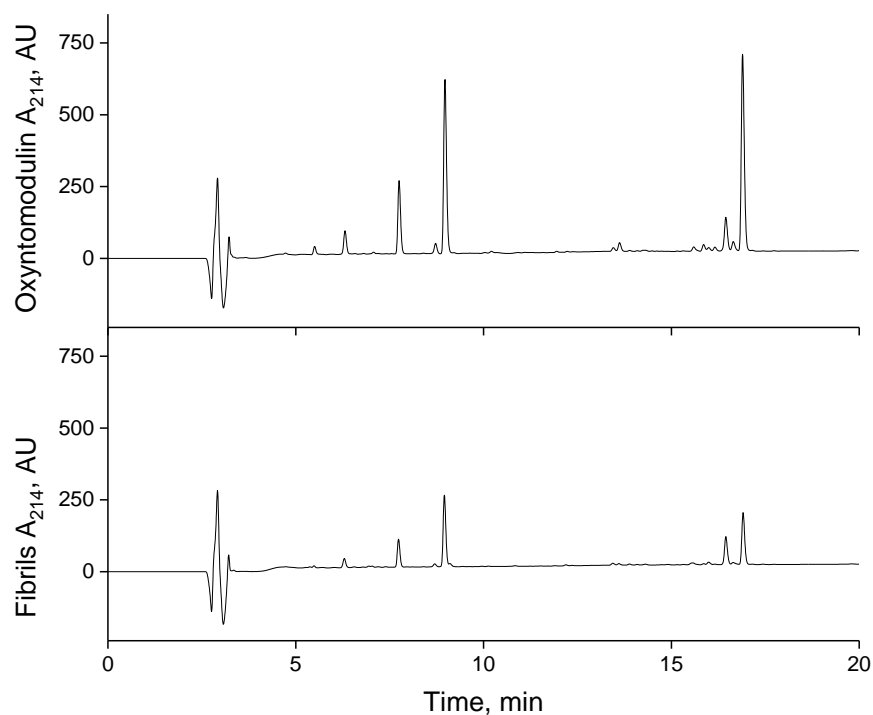
Figure 4-4: Tryptic digestion of soluble and fibrillar Oxyntomodulin

HPLC chromatograms of 0.5 mg mL^{-1} Oxyntomodulin (top) and mature Oxyntomodulin fibrils (bottom) after 24 h of incubation with trypsin in PBS pH 7.35 at 37 °C. Samples were centrifuged before analysis to remove eventual particles. Solvent front, 3-4 min. Native Oxyntomodulin eluted at 16.0 min.

4.4 Insights into tertiary structure of Oxyntomodulin fibrils

X-ray diffraction is traditionally used to reveal the cross-beta diffraction pattern of amyloid fibrils. Aligned fibrils show a strong 4.7-4.8 Å diffraction pattern on the meridian, which corresponds to the inter-strand spacing along the fibril axis. A weaker equatorial reflection at 8-12 Å measures the distance between opposing sheets, which is dependent on the size of side chains, their ability to interdigitate, and the presence or absence of water molecules between the sheets [116][71].

X-ray diffraction of Oxyntomodulin fibrils revealed weak reflections at approximately 4.7 and 8.6 Å. The 4.7 Å reflection overlaid with the strong background signal of wax diffraction, so that a clear indication for cross-beta architecture could not be derived from X-ray diffraction. The presence of an 8.6 Å diffraction is interesting from a structural perspective, because the indicated inter-sheet spacing is smaller than for most reported amyloid structures. Such close interaction requires a dry interface with side-chain interdigitation. The same spacing has been reported for amyloid-like structures of TDP-43, which have a β-hairpin architecture [96]. X-ray diffraction thus provides further indication for a folded conformation of Oxyntomodulin within fibrils. A turn conformation with the whole hairpin in one sheet (as in TDP-43) requires antiparallel sheet alignment, which contradicts the parallel FTIR spectrogram. An arch conformation where the peptide spans two sheets allows close packing of opposing sheets while providing parallel strand alignment.
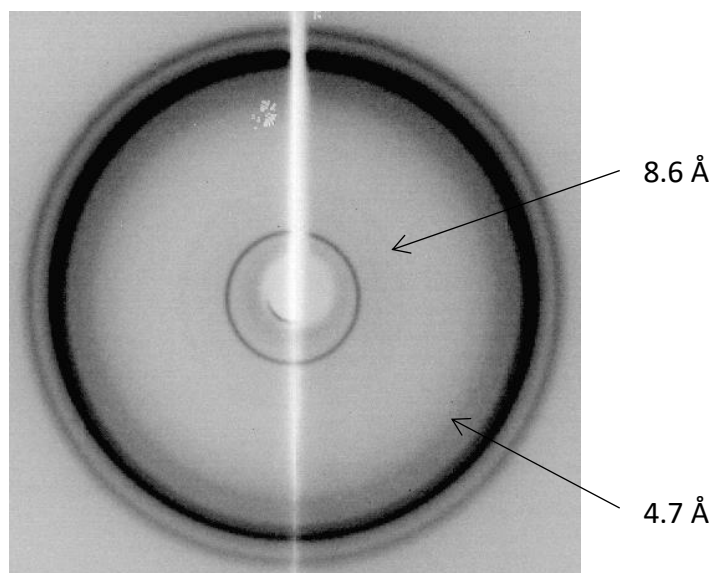
Figure 4-5: X-Ray diffraction indicates a dry interface in Oxyntomodulin fibrils

X-Ray fibre diffraction of aligned Oxyntomodulin fibrils, measured on a Bruker D8 Quest X-ray diffractometer. Weak reflections can be seen at 4.7 and 8.6 Å, indicating inter-strand and inter-sheet distance, respectively.

Cryo transmission electron microscopy was performed to consolidate and complement results from AFM, FTIR, CD and X-ray diffraction. Transmission electron microscopy produces 2D projections of the electron density of objects, allowing a theoretical resolution in the range of the electron beam's wavelength. In Cryo EM, surrounding vitreous ice protects the structures from radiation damage without the necessity of negative staining. Flash freezing furthermore captures the hydrated state, allowing imaging in the 3D conformation adopted in solution [175]. This is a marked difference to AFM, where samples are dried on a substrate before imaging. TEM does not directly measure height but can provide limited depth perception via the electron density of a structure [86][176]. In addition to lateral dimensions and electron density, diffraction information is accessible by reverse Fourier transformation of digitized electron micrographs or selected features [99][87].

Cryo electron micrographs were taken of the same mature Oxyntomodulin fibril batch as used for *in vivo* experiments in [6]. The fibrils were several micrometres long and contained approximately parallel aligned ~6-7 nm wide, smooth substructures, which also appeared as single fibrils (see yellow arrows in **Figure 5-6**). The diameter and appearance of these substructures is indistinguishable of protofibril AFM images, including the uncurled appearance and long-distance bending. The electron dense outer walls and electron lucent centre of such fibrillar subspecies suggests a tubular architecture similar to Cryo electron micrographs of Aβ(11-25) peptide fibrils [99]. Fibril alignment occurred predominantly in a side-by-side way, resulting in ribbons of aligned fibrils that sometimes showed a long-distance helical twist around a common axis. Less ordered three-dimensional bundles were also present. Assembled fibrils had overhanging single fibril ends and seemingly random numbers of substructures, suggesting that the alignment to superstructures is of physical (e.g. electrostatic) nature and not directly correlated to the elongation process.

In summary, the fibril images further solidify the assumption that mature fibrils are superstructures consisting of laterally aligned protofilaments. To test this hypothesis, Cryo EM images were taken from protofibrils. Representative examples are shown in **Figure 5-7**. Protofibrils appeared as predominantly single, unbranched, several µm long and ~6-7 nm wide structures. Some protofibrils aligned to higher order fibrils, analogous to the fibril structures discussed above. The dimensions of protofibrils and fibril substructures were indistinguishable by Cryo EM images.

At the time of protofibril imaging, an improved detection method was available which overlaid images taken from a movie to reduce blurring caused by minimal thermal drifts and vibrations during imaging. Thus, more structural information could be derived from protofibril images. Closer inspection of the electron density of protofibrils revealed that there are not always two striations lining the fibril, but often there are three electron dense areas intersected by two electron lucent areas.
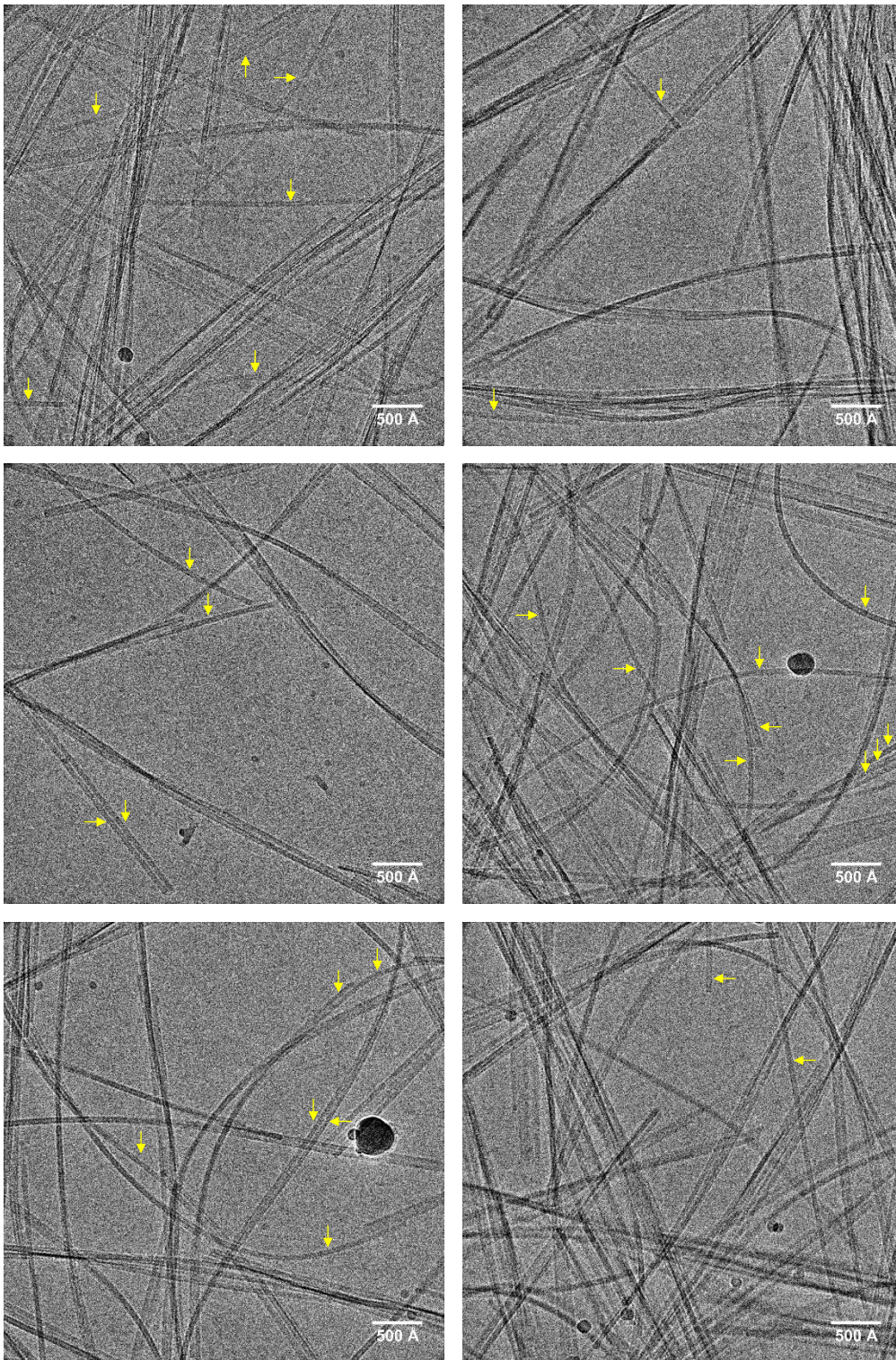
Figure 4-6: Cryo EM indicates that fibrils are assemblies of protofibrils

Cryo EM images of the mature Oxyntomodulin fibril batch used for *in vivo* studies. Fibrils were imaged on a Titan Krios™ G3i in transmission mode without motion correction. Whole images were corrected for brightness and contrast in Fiji. Scale bars, 500 Å. Yellow arrows show singled fibrillar structures with approximately 60 Å diameter that are indistinguishable from protofibril images in **Figure *4-7***.
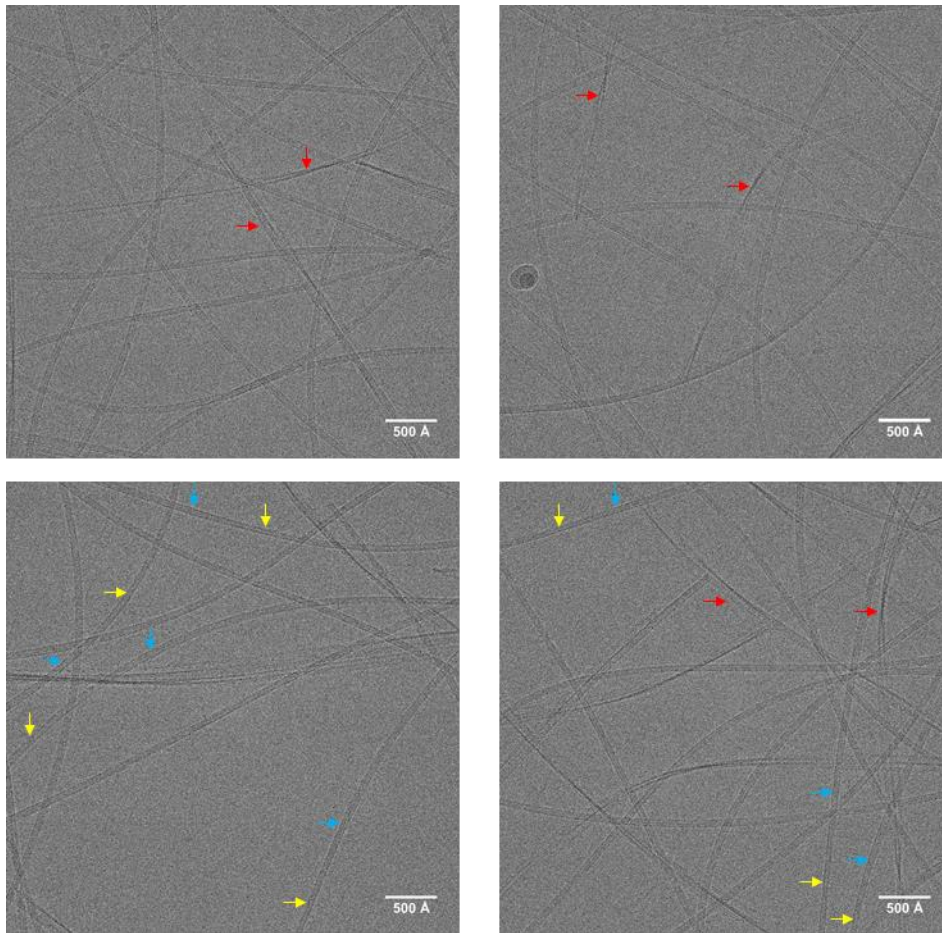
Figure 4-7: Cryo-EM of protofibrils suggests triangular cross-section

Cryo TEM images of the Oxyntomodulin protofibrils formed in salt-free conditions. Protofibrils were imaged on a Titan Krios^{TM} G3i with a Falcon 3 detector with motion correction. Whole images were corrected for brightness and contrast in Fiji. Scale bars, 500 Å. Only few fibrils are associated to bundles (red arrows) Examples for single fibrils are highlighted with blue and yellow arrows. Positions marked yellow have a 60 Å diameter and two areas of high electron density along the fibril axis. Blue arrows show examples where the same fibril converts to 70 Å with three areas of high electron density along the fibril axis.

If there are three striations, the fibril is ~70 Å wide instead of ~60 Å for the cross-sections with two stripes. In some images, a change of pattern and width was seen over the length of a fibril, suggesting that both observations are different projections of the same structure. An approximately triangular cross-section with arch-like folded peptides spanning the sides of the triangle is consistent with the features seen. If one side of the triangle is perpendicular to the image plane, the electron beam only passes through two electron dense areas, and the diameter corresponds to the altitude of a regular triangle ($\frac{1}{2}\sqrt{3} * 70 \text{ Å} = 60.6 \text{ Å}$). If the fibril is oriented in other angles, the theoretical electron density has three parallel maxima lines, and a width between altitude and side is seen. A cartoon representation is shown in *Figure 5-10*.
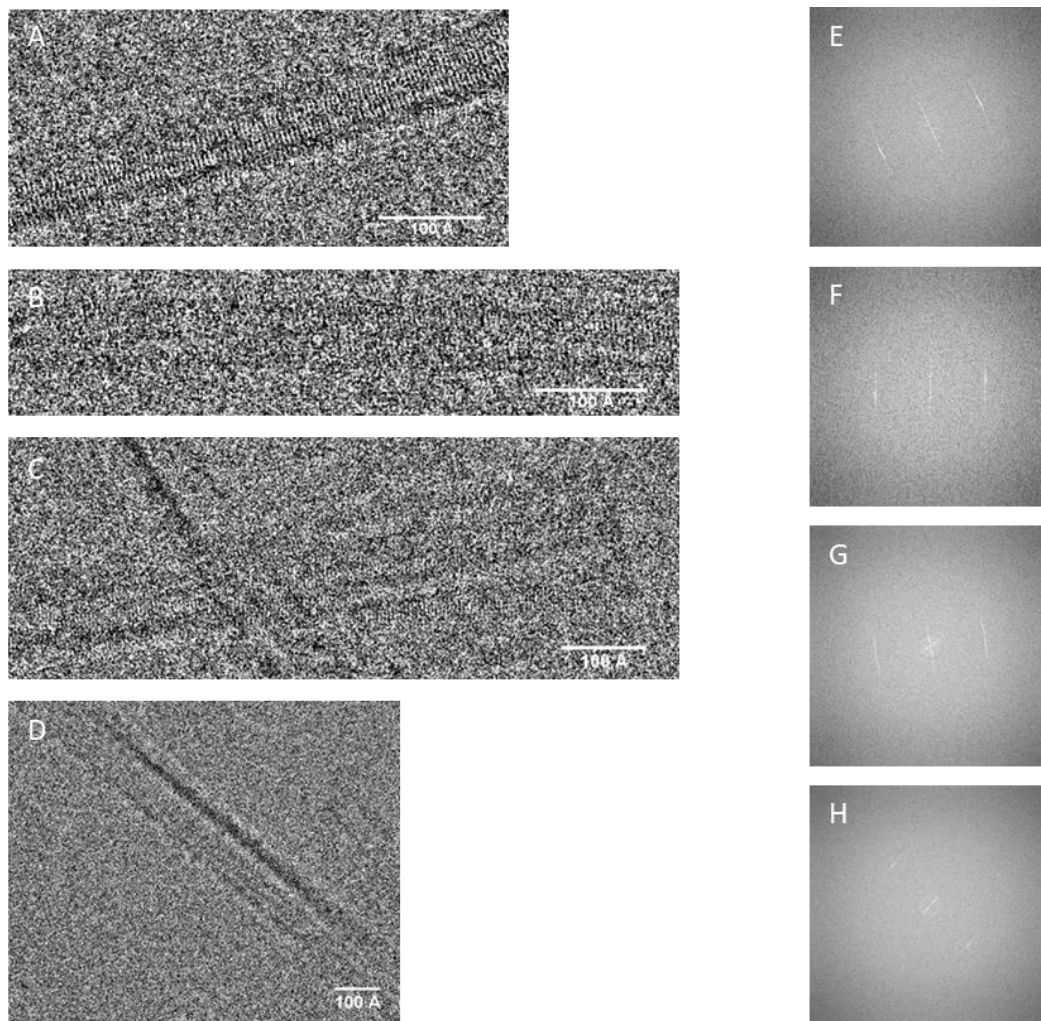
Figure 4-8: Direct observation of the 4.7 A diffraction pattern by Cryo EM

Cryo TEM images of the Oxyntomodulin protofibrils formed in salt-free conditions. Protofibrils were imaged on a Titan Krios[TM] G3i with a Falcon 3 detector with motion correction. Whole images were corrected for brightness and contrast in Fiji. Scale bars, 100 Å. Striations approximately perpendicular to the fibril axis can be directly seen in images of single fibrils (A, B) or bundled fibrils (C, D). E-H, fast Fourier transforms of images A-D, respectively. Maximum reflections are at 4.6-4.7 Å.

Fast Fourier transforms of single fibril selections revealed a characteristic 4.7 Å diffraction pattern perpendicular to the fibril axis. This is consistent with the theoretical spacing of β-pleated sheets. Remarkably, parallel striations with 4.7 Å spacing were directly visible in magnifications of single protofibrils in high resolution images (see **Figure 5-8**). The pattern could be detected over more than 0.1 µm long distances with no visible change in spacing or angle of the striations to the long axis, even if the fibril was bent. Stromer and Serpell argue that direct observation of a fibril's β-sheet structure is suggestive of the presence of several β-strands perfectly in register. Reinforcement of electron interactions by several peptide layers produces a high enough signal to make the fibril structure visible [86].
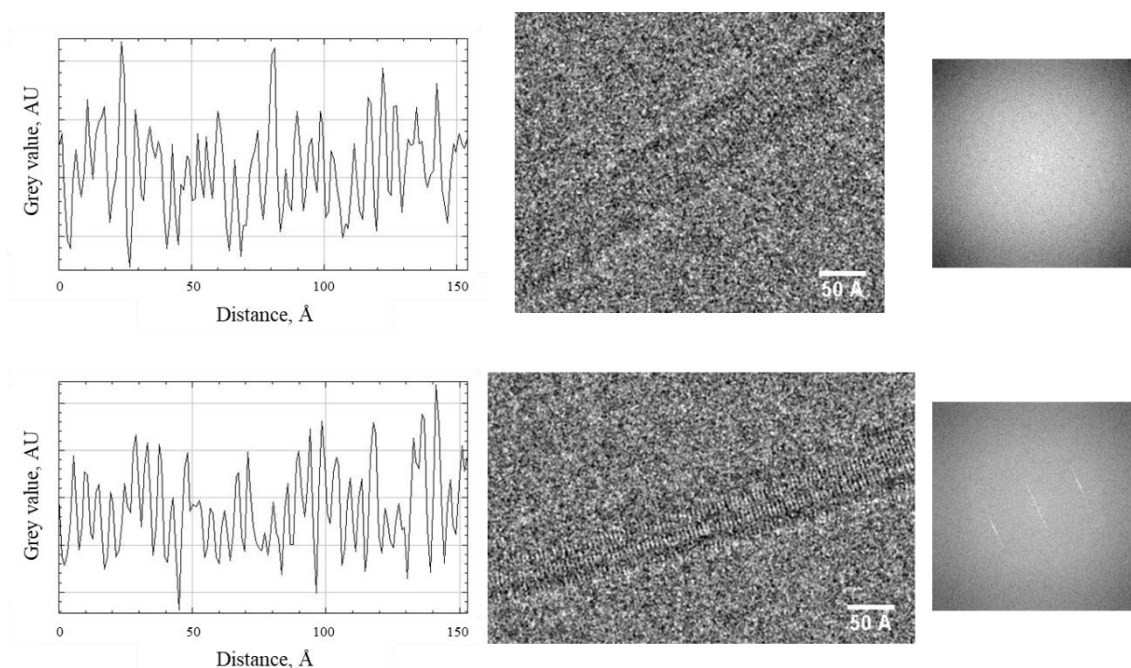
Figure 4-9: Visualization of the cross-β strand spacing in Cryo EM images

Cryo TEM images of the Oxyntomodulin protofibrils formed in salt-free conditions. Protofibrils were imaged on a Titan Krios^{TM} G3i with a Falcon 3 detector with motion correction. Whole images were corrected for brightness and contrast in Fiji. Scale bars, 50 Å. Left, grey value plot of a line along the fibrils shown in the middle. Right, fast Fourier transform diffraction pattern. Top: grey value plot shows 4.7 Å cross-beta spacing even though no striations or 4.7 Å diffraction pattern is seen. Bottom: positive control with a diffracting fibril and sufficient alignment for direct visualization of strand spacing.

In this work, not all fibrils had a characteristic 4.7 Å diffraction pattern and/or directly visible peptide layers. High and low resolution seemed clustered within images rather than within different fibrils. It is assumed that the fibril axis needs to be perfectly perpendicular to the incident angle of the X-ray beam so that aligned strands can produce a reinforced image. If the fibril is for example not level within the sample holder because of a locally imperfect ice layer, the image will blur and conceal the pattern. The grey value intensity along a fibril can reveal the regularity of the pattern, even if striations are not visible by eye (see **Figure 5-9**). Cross-β alignment is therefore present even if the alignment is not regular enough to directly visualize strands. By measurement of 60 individual fibrils with visible β-sheet pattern, it was found that the angle of striations is not perfectly perpendicular to the fibril axis, but 5-10 ° offset (results not shown). Analogous patterns were found in laterally assembled and twisting protofibrils. This implies an offset in strand alignment along the fibril such as illustrated in **Figure 2-4** E. A possible explanation for sheet offset is the salt bridge formation between oppositely charged residues.

The existence of a regular 4.7 Å diffraction (and image-) pattern rules out the possibility of a β-turn configuration with both strands in the same sheet. Such a structure would show differences in the spacings along the fibril, with every other spacing > 4.7 Å. Furthermore, a ladder-like offset of opposing stands with side chain stacking over each other (such as in **Figure 2-4** F) instead of between each other can be excluded, because this would create an additional regular diffraction pattern at < 4.7 Å. Moreover, direct visualization of peptide strands in amyloid fibrils is suggestive of several layers of perfectly aligned peptide backbones [99]. This implies that strands in a cross-section of Oxyntomodulin protofibrils are in-register and not, for example, spanning a continuous β-helix.

Combining results shown in this chapter, a possible protofibril cross-section could have three arch-shaped monomers spanning a regular triangle with a hollow core. Sheets are arranged in a prism-like configuration, where the triangle motifs spanning the prism are slightly tilted from the axis. Each peptide may have a few amino acids that are not included in the arch conformation at either terminus. This structure is known from one fibrillar type of $A\beta_{1-40}$ [100]. A model for a possible coarse-grain 3D structure and its dimensions is shown in **Figure 5-10**. The following structural constraints are considered:

- From AFM, Cryo EM, FTIR and CD: Fibrils contain one or several protofibrils, therefore the molecular arrangement within a fibril is supposedly equivalent to the protofibril structure.

- From AFM and Cryo EM: Protofibrils and the fibril substructures are approximately half as wide as the stretched Oxyntomodulin sequence.

- From FTIR and CD spectroscopy: (Proto)fibrils have a high proportion of β-sheet, almost no α-helical content, and a turn element.

- From FTIR: (Proto)fibril peptide strands within one sheet are parallel.

- From enzymatic degradation: Fibrils do not entail cleavable unstructured regions, therefore none or only few amino acids can be excluded from the fibril core.

- From ThT binding, X-Ray diffraction, Cryo-EM: Oxyntomodulin forms amyloid-like cross-β fibrils with a 4.6-4.7 Å diffraction pattern.

- From Cryo-EM: Electron density in protofibrils and fibrillar substructures suggests a hollow core. Protofibrils show two or three lines of electron density maxima along the fibril axis with cross-sectional diameters corresponding to the side length and altitude of a regular triangle. Visibility of the regular 4.6-4.7 Å in magnified image sections excludes β-turn arrangement of a peptide within one sheet, as well as an offset alignment and/or a continuous β-helix. To accommodate the turn, one peptide must span two sheets in a β-arch conformation. The β-strands on either side of the turn need to be in the plane of electron beam incidence. β-strands in one sheet are 5-10 ° offset to the fibril axis.
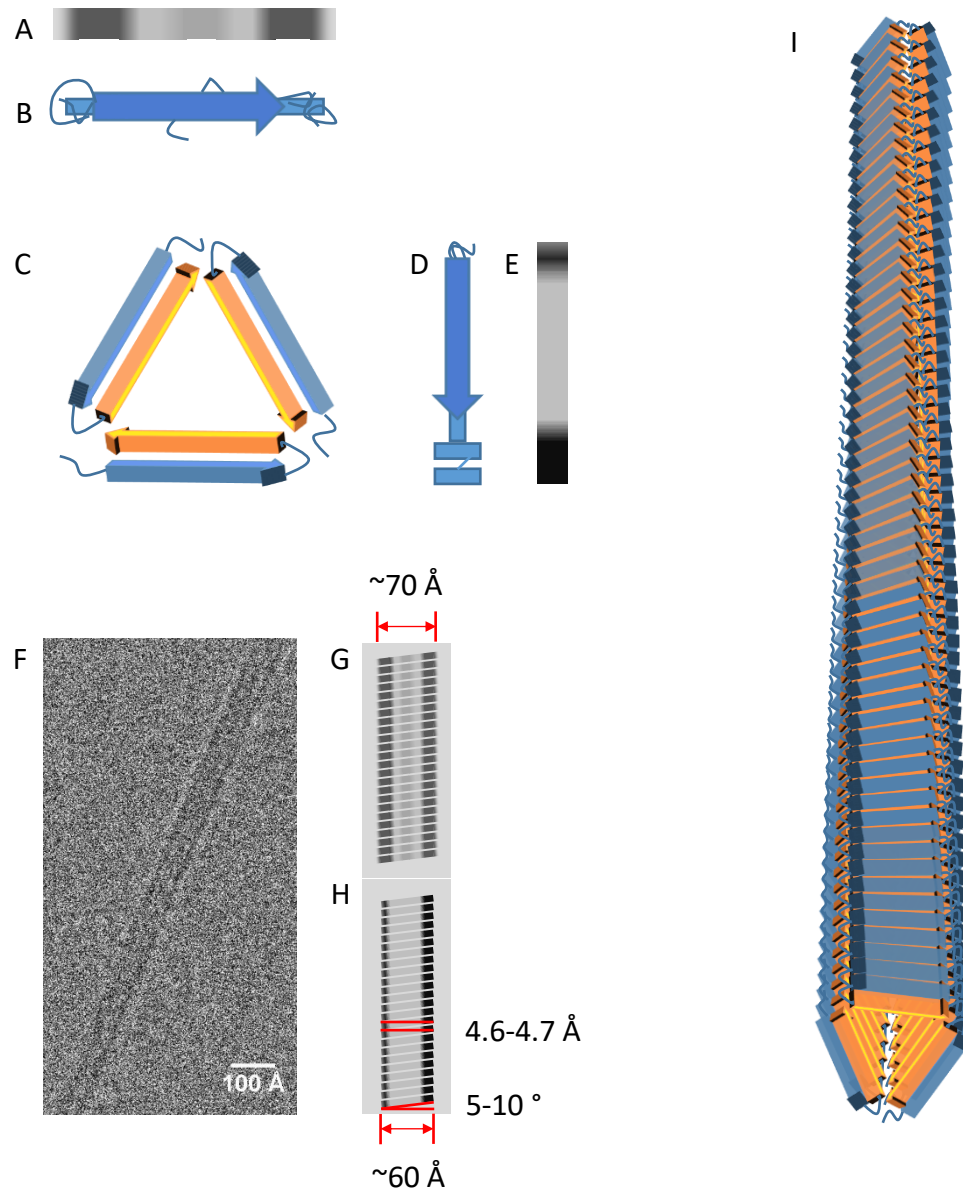
Figure 4-10: Tentative 3D structure of Oxyntomodulin protofibrils

Low-resolution 3D structure of an Oxyntomodulin protofibril and its structural motifs, with structural constraints gathered from Cryo-EM, AFM, FTIR, CD, enzymatic degradation and X-Ray diffraction. C, cartoon representation of the triangular motif that is consistent with structural constraints of a protofibril's cross-section. β-sheets (arrows) are shown outwards twisted for illustration purposes. Dimensions of β-sheets, turns and unstructured regions are arbitrary. Monomers adopt a β-arch conformation that contributes β-strands to two opposing sheets, with possible small unstructured regions (drawn at the outside termini). Three monomers span a double-walled triangle. B, D: cartoon representations of an upwards (B) or sideways (D) projection of (C), with respective expected electron density sketched in (A) and (E). (F), magnification of a fibril part showing a cross-sectional electron density according to (A) in the top half and (B) in the bottom half. Scale bar, 100 Å. G, H: magnified sketch of theoretical electron density along a fibril with characteristic lengths. Striations offset is drawn at 7 ° from perpendicular to the fibril axis. I: cartoon representation of strand alignment, seen along the fibril. Long-distance twist is drawn as an arbitrary 1 ° offset of triangular subunits respective to each other. Blue arrows, outer sheets; orange arrows, inner sheets; blue lines, turns and possible unstructured regions.

The structural constraints discussed in this chapter cannot describe which amino acids are contained in either of the β-sheets, how long the sheets are exactly, how the turn is formed or if and where there is a possible unstructured region. It is furthermore unknown which parts of adjacent peptides in a triagonal substructure interact with each other. Because the fibrils are smooth and do not have a regular twist, an atomic-resolution structure cannot be derived from single-particle analysis of Cryo EM images. From the presented results, there is no indication for a differential composition of protofibrils and fibrillar substructures, and the only difference is the rather single or bundled appearance. However, it cannot entirely be excluded that fibril elongation in water or salt-containing conditions leads to locally changed morphology, e.g. the composition of a turn or the frequency of imperfectly aligned peptides.

5 Kinetics and thermodynamics of Oxyntomodulin fibrils

5.1 Methods

All fibril stocks used in the experiments of this chapter were 10 mg mL^{-1} fibril dispersion with no measurable soluble peptide, derived from a 3-step seeding method as described at the end of chapter 3.4. Two stocks were used for all experiments in this chapter. The stocks were indistinguishable by AFM and showed no difference in elongation kinetics by QCM-D (data not shown). All experimental data shown together are derived from one fibril stock. Peptide solutions were prepared according to 3.2.1, and free peptide was measured analogous to 3.2.5. AFM imaging was performed as in 3.2.4, and kinetic ThT assays without shaking were measured as described in 3.2.2.

5.1.1 Oxyntomodulin fibril elongation and dissociation studies in bulk

Peptide release from fibrils was measured after incubation of diluted aliquots of a mature fibril stock. As discussed in [6], the equilibrium of soluble Oxyntomodulin and fibrils in salt-containing conditions is so far on the fibril side that no peptide is measurable within the detection limit of common spectroscopic measurements. Here, essentially salt-free conditions were used to qualitatively assess the release kinetic of the system. The fibril stock was diluted to 0.5 mg mL^{-1} in water incubated in 0.5 mL Eppendorf® vials sealed with Parafilm. Every sample was mixed by inversion once daily to overcome possible limitations by sedimentation or steric inhibition. Triplicate vials were measured for each condition and time point. No sample was measured more than once. Morphology and apparent shortening were followed by AFM imaging at each time point and condition. Soluble peptide concentrations were measured in the fibril supernatant after centrifugation and 50 kDa MWCO filtration, and fibril concentrations in the pellet were measured after acidic dissolution as a control. Tested release conditions comprised:

- Initial fibril concentrations 0.5 mg mL^{-1} incubated at 37 °C for 1; 4; 24; 48 h

- Initial fibril concentration 0.5 mg mL^{-1} incubated at 6 °C, 25 °C, 32 °C, 37 °C, 42 °C for 1, 4, 7 and 14 days, respectively

The incubation temperatures were selected for mimicking typical storage conditions in fridge (6 °C) and at room temperature (25 °C), as well as limits for physiological temperature (subcutaneous temperature 32 °C, body temperature 37 °C, high fever 42 °C).

A similar method was used for quantifying elongation at different temperatures: freshly prepared 0.5 mg mL^{-1} Oxyntomodulin solutions in 0.9 mg mL^{-1} saline were seeded with fibril fragments derived from bath-sonicating an aliquot of a mature fibril stock for 15 min. Seeded

triplicate Oxyntomodulin solutions were incubated in 0.5 mL Eppendorf® vials sealed with Parafilm, at the temperatures mentioned above. Elongation was followed by AFM imaging at each time point and temperature. Measurement of free peptide was performed analogously to peptide release experiments. As a control, fibril concentration was additionally assessed by acidic dissolution of pellets.

Reversible stabilization by salts was tested by partially dissolving a 0.5 mg mL^{-1} fibril sample in water for 1 d, splitting the homogenized dispersion into 0.5 mL Eppendorf® vials, and adding 14.4 mM (the equivalent of 0.9 mg mL^{-1} NaCl) NaCl, LiCl, CsCl, or CsI. Soluble peptide concentration was measured before salt addition, and after 7 d with or without addition of salts.

5.1.2 Quasi-real-time elongation and dissolution by Quartz Crystal Microbalance

QCM-D experiments were performed on a QSense E4 Analyzer (Biolin Scientific) equipped with a High Precision Multichannel Dispenser (Ismatec). The instrument allowed simultaneous or sequential measurement of up to 4 sensors. Sensors used in this work (QSX303, Biolin Scientific) had an active sensing area of 1 cm^2, silicone dioxide (SiO$_2$) coating, and a surface shape that allowed equal flow over all parts of the active surface. The method described here was used for all QCM-D experiments in chapter 5.3, 5.4, 5.5 and chapter 7. Chapter 5.1.1 shows the method development, control experiments and determination of the mass sensitivity constant of Oxyntomodulin elongation on SiO$_2$ QCM-D sensors.

<u>Sensor preparation</u> Prior to experiments, sensors were cleaned by immersion in 2 % (w/v) Sodium Dodecyl Sulphate (SigmaAldrich, UK) and incubation at 37 °C for 45 min. The sensors were then rinsed with Ethanol and water, dried in a stream of Nitrogen, and cleaned in a UV/ozone ProCleaner™ (Bioforce Nanosciences) for 20 min. Sensors were either used without modification (blank), or with sonicated fibrils (seeds) physically adsorbed to the surface by drying of a seed dispersion on the SiO$_2$ surface. Sonication was used to homogenize the length of the fibril population within and across experiments, and to enhance the sensitivity of sensing by increased availability of growth-competent fibril ends. To confine deposited sample drops to the active surface of the sensor during drying, a custom-made PTFE block with a circular hole matching the active surface was clamped to each chip. Seed dispersions were diluted to 0.01 mg mL^{-1} in HPLC grade water (Fisher, UK), and 40 μL dilution was pipetted on each chip. Sensors were dried overnight and imaged by AFM before installation in the QCM-D machine. 4 sensors treated with the same seed stock were used for each experiment.

<u>Measurement</u> Sensors were equilibrated to the measurement temperature in 0.9 mg mL^{-1} saline for at least 1 h before solvent or a freshly prepared peptide solution was flown over the surface at a rate of 0.1 mL min^{-1}. Elongation was measured in constant stream of peptide for 15 min, followed by a 10 min rinsing step with 0.9 mg mL^{-1} saline to prevent further elongation by the remaining peptide in the sensing chamber and tubes. Only frequency shifts from 2 min after the start of peptide flushing were taken into account to separate unspecific peptide adsorption from fibril elongation. Sensors were imaged by AFM before and after experiments to confirm elongation. Resonance frequency shifts and dissipation were recorded at 75-200 measurements per minute, depending on the number of simultaneously measured sensing chambers. Each sensor within an experiment experienced the same amount of flushing to minimize differences in fibril numbers on the surface. Results shown here are true triplicates, i.e. a condition was modified for the 4 chips in one experiment, and the whole experiment including seed preparation, deposition, equilibration and measurement was repeated on a different day. Due to differences in sonication efficiency, pipetting and drying in separate experiments, it was not possible to provide the same amounts of fibrils across triplicates. To correct for fibril number differences, one condition was measured in all experiments and used as an internal standard: 0.5 mg mL^{-1} Oxyntomodulin in 0.9 mg mL^{-1} saline at 37 °C.

<u>Measurements at different temperatures</u> QCM-D is very sensitive to temperature changes. Analytes are heated to the sensing chamber temperature before passing the sensor. Elongation measurement at different temperatures required re-equilibration of the system for at least 45 min after a temperature change. To exclude effects of previous incubation temperatures on elongation at different temperatures, the sequence of temperature measurement within one experiment was shuffled across triplicates (e.g. measurement from low to high and high to low temperature). The QSense E4 Analyzer is not equipped to control temperature below ambient temperature. For measurements below room temperature, the entire apparatus was incubated in a custom-built insulated box with cooling modules before and during measurement at 15 and 20 °C. An open petri dish with silica gel was incubated with the QCM-D apparatus to prevent condensation on the electric contacts. After measurement, the equipment was re-equilibrated without cooling for measurements of the two remaining sensors at 25 and 37 °C, to provide the internal standard and a further measurement point which overlapped with measurements above room temperature (25; 32; 37; 42 °C).

<u>Control experiments</u> As a control for the integrity of fibrils during the experiment, a sensor with Oxyntomodulin fibril seeds was flushed with 10 % saline. To exclude frequency shifts by multilayer deposition or aggregation during the experiments, QCM-D frequency shifts were measured during exposure of a fibril-free sensor to a solution of 0.5 mg mL^{-1} Oxyntomodulin at 0.1 mL min^{-1}.

<u>Analysis</u> In ideal conditions, the relationship of mass and frequency in QCM-D is described by the Sauerbrey equation $\frac{\Delta f_n}{n} \approx -\Delta m$, where Δf_n is the change in the n-th overtone resonance frequency, and Δm is the change in mass in a given time interval. Elongation of fibrils on the sensor surface results in linear frequency decrease, where the slope is a measure for the elongation rate [177]. In experiments with Oxyntomodulin, the first two minutes of interaction were dominated by adsorption of soluble peptide to the surface of the sensor that was not covered by fibrils. This time was not included in the analysis of elongation kinetics. Linear frequency decrease after physisorption indicates mass deposition by elongation of fibrils. The slope of $\frac{f_3}{3}$ frequency change during 8-10 min after adsorption was used as a measure of elongation kinetics. Elongation rates were expressed relative to the slope recorded at the internal standard condition to normalize for the amount of seeds deposited per batch.

Fibril dissolution experiments were performed analogously, except that each sensor contained 4 µg non-sonicated fibrils, and peptide-free medium was flushed over the surface.

5.1.3 Fibril elongation enthalpies by Isothermal Titration Calorimetry

ITC heating curves were recorded on an automated MicroCal Auto-iTC200 system (Malvern and GE Healthcare, UK). Cell and pipette were cleaned according to manufacturer's instructions before use and between measurements. The cell contained 450 µL of a 0.1 mg mL^{-1} seed solution with 15 min sonicated mature fibrils, in 0.9 mg mL^{-1} saline. The pipette solution was 1 mg mL^{-1} soluble Oxyntomodulin in 0.9 mg mL^{-1} saline. The pipette doubled for stirring the cell content at 1000 rpm. After thermal equilibration, 2 µL were injected into the cell for removing air from the syringe. 5 min later, 12 µL peptide were injected, and the thermal response was followed for 20 min. 3 injections of 12 µL were followed into the same solution, then the cell and syringe were cleaned, and another measurement was performed with a new seed solution. Measurements were triplicates of 2 µL + 3*12 µL, but only the first 12 µL injection was taken into account for quantification, for reproducibility reasons. Triplicates were performed at 8 °C, 15 °C, 20 °C, 25 °C and 32 °C on one day, and at 25 °C, 32, 37 °C and 42 °C on another day. Differences in repeated conditions were non-significant; only one repeat is shown. Samples were split because the time needed for measurement and cleaning could cause alteration in the stored samples. 0.9 mg mL^{-1} saline was injected to the seed solution analogous to the measurements (triplicate) at each temperature to quantify the heat flux created by dilution. Water-to-water injection was used to control cleaning and measurement. Background signals were deducted from the measurements, and resulting heat flux (in µcal s^{-1}) was integrated over time with the manufacturer's customized origin software to estimate enthalpy (in µcal). Averaged triplicates were divided by the number of injected free peptide for plot representation in µcal mol^{-1}.

5.2 Development of a QCM-D assay for quasi real-time measurement of Oxyntomodulin fibril elongation

Quartz crystal microbalance with dissipation monitoring (QCM-D) is a *quasi* real-time, highly sensitive, label-free biosensing technique that measures the resonance frequency of a quartz sensor as a function of mass bound to the sensor. Binding events can be followed with up to 200 measurement points and sub-nanogram sensitivity, according to manufacturer's information. QCM-D requires low sample amounts and can be performed in different solvent conditions and temperatures. QCM-D has been used to measure fibril elongation kinetics and thermodynamics. In the absence of adsorption of crystallization events on the sensor, elongation of fibril seeds bound to the sensor creates a linear signal decrease that is a measure for the elongation rate [178][159][129]. Here, QCM-D was used to study the elongation of Oxyntomodulin fibril seeds attached to the surface of a QCM-D sensors in different solvent conditions.

A QCM-D sensor is a piezoelectric quartz disk with a possible coating or functionalization on the solvent-exposed side. Application of a rapidly oscillating alternating current via gold electrodes stimulates the sensor to vibrate at its resonance frequency. Changes in resonance frequency are recorded computationally. An increase of the resonator`s mass, e.g. by adsorption or binding of molecules, results in dampening of the resonance frequency. The relation of mass and frequency is described by the Sauerbrey equation $\frac{\Delta f_n}{n} = -a\Delta m$, where Δf_n is the change in the n-th overtone resonance frequency, Δm is the change in sensor mass in a given time interval, and a is *a* mass sensitivity constant that depends on the properties of the deposited material [179][180]. For the sensors used here, *a* adopts the constant -17.7 ng Hz^{-1} for formation of a rigid monolayer. In a liquid environment, additional frequency dampening can be caused by coupling of solvent and surface. Mass sensitivity is then a function of solvent viscosity and immobilization of solvent molecules on or between binding analytes (soft layer). For the known viscoelasticity of smooth, homogeneous soft layers on the surface (e.g. a protein monolayer), *a* can be modelled from the dampening of oscillations after interruption of the electrode current, expressed as the energy dissipation factor D [181]. The QCM-D used here measures D online from the exponential decay of frequency after disconnection from the drive.

Fibril elongation on the surface of a QCM-D sensor can neither be assumed to be a rigid, nor as a soft layer. Fibrils need to be scarce to allow elongation without mutual restrictions in space, and the viscoelastic properties of the fibril-surface-system are unknown. Aternatively, the mass sensitivity can be calculated from an estimation of added fibrillar material to the surface. The fibril number density on the surface Γ and the length increase Δl can be assessed by AFM imaging of the fibrils on a sensor before and after an experiment. With the known fibril diameter d and sensing surface A$_s$, fibril shape approximation by a cylinder, and

assumption of a fibril density equivalent to the density in protein crystals, the mass sensitivity factor can be estimated [177]:

$$n = -\frac{\Delta m}{\Delta f} = \frac{(\frac{d}{2})^2 \pi * \Delta l * \rho * A_s * \Gamma}{\Delta f} \qquad (\ 5\text{-}1\ )$$

Knowing *n*, the frequency difference during the elongation phase can be related to the average length- or mass-increase of fibrils. If fibril number is (in good approximation) constant during and across experiments, and fibril length increase is small enough to not cause partial fibril detachment, dissipation changes can be neglected. The slope of a single frequency overtone decrease is then a quantitative measure for the elongation kinetics.

Resulting from the nature of the measurement and the fibrillar system, the following factors needed to be assessed to develop a QCM-D assay for kinetic and thermodynamic studies of Oxyntomodulin fibril elongation:

- Adsorption of soluble peptide to the not-covered surface area should not interfere with the elongation signal. The elongation signal should be linear in good approximation.

- Fibril length and concentration needed to be selected for providing enough fibril ends to produce measurable mass changes during experiments of different kinetics. Fibrils should be equally distributed over the surface and scarce enough in numbers to prevent frequent crossing-over during elongation.

- No or only minimal fibril loss should be seen during an experiment.

- Monomer concentration for elongation should not be selected too high to prevent influence of viscosity changes on measured frequency changes.

- Experiments should be short enough to prevent spontaneous nucleation.

- Experimental setup should be reproducible within one experiment and in repetitions with independently prepared seed dispersions and peptide solutions.

- Elongation needed to be measurable by AFM to confirm QCM-D signals and estimate the mass sensitivity of Oxyntomodulin fibril elongation.

To test if the adsorption of soluble Oxyntomodulin to the surface of a SiO_2 surface creates a signal that interferes with fibril measurement, a fibril-free SiO_2 sensor was exposed to a stream of freshly prepared 0.5 mg mL^{-1} solutions of Oxyntomodulin in 0.9 mg mL^{-1} saline. At a flow rate of 100 µL min^{-1}, an analyte solution passed through tubing dead volume for about 60-90 s before reaching the sensor's surface.
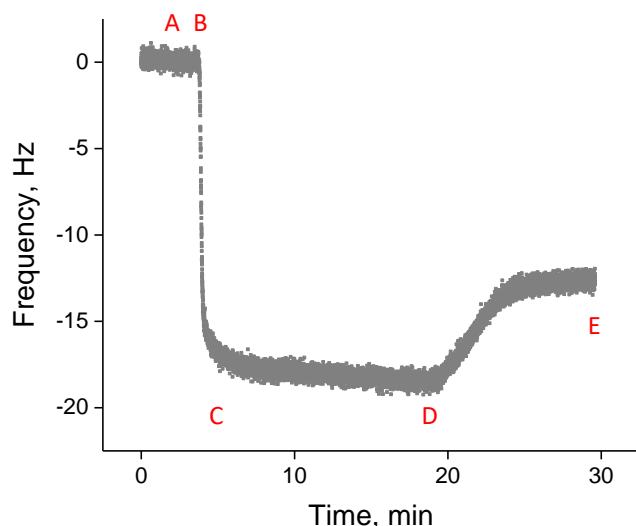
Figure 5-1: QCM-D frequency background of peptide adsorption and desorption

A-D, Frequency shifts during injection of 0.5 mg mL^{-1} Oxyntomodulin in 0.9 mg mL^{-1} saline; D-E, flushing with 0.9 mg mL^{-1} saline, on SiO$_2$ coated QCM-D sensor without fibrils at 25 °C. A-B, time required to pass the dead volume before sensor contact; B-C, adsorption dominated phase; C-D, frequency slope ~-0.11 Hz min^{-1} – this is the range where elongation is measured in following experiments; D-E, partial desorption during flushing without peptide.

As shown in *Figure 6-1*, adsorption of Oxyntomodulin to the surface caused a sharp frequency decrease for approximately 20-30 s, followed by a very shallow frequency decrease of -0.11 Hz min^{-1}. Subsequent flushing with 0.9 mg mL^{-1} saline caused an increase in frequency, suggesting partial removal of peptide from the surface. AFM images of the sensors before and after exposure to peptide were indistinguishable, therefore it is assumed that the adsorbed material that does not detach during flushing forms a smooth layer. Because the background signal (A-B in *Figure 6-1*) was generally small compared to the measurement signal, and adsorbing peptide did not seem to interfere with fibril elongation, the free sensor surface was not passivated.

The repeatable frequency range of fibril elongation was tested by repetitive injection of 0.1 to 1 mg mL^{-1} Oxyntomodulin on sensors with 2 µg fibrils that were sonicated for 2 min prior to deposition. Every sensor experienced 5 cycles of peptide- and 0.9 mg mL^{-1} saline injection. Frequency slopes were measured from 2 min after the start of peptide injection to ensure that the surface was saturated with peptide and the fluid used for thermal equilibration was fully replaced by the peptide solution. Frequency slopes were approximately proportional to peptide concentration (see **Figure 6-2**).
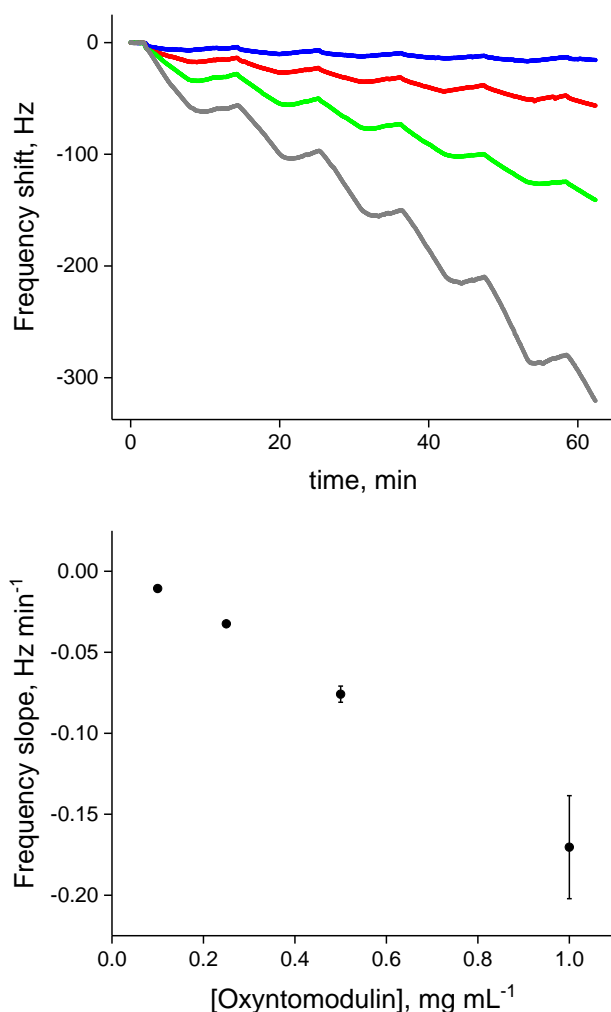
Figure 5-2: Sensitivity and saturation of Oxyntomodulin elongation measurement by QCM-D

Top: Elongation of surface-bound Oxyntomodulin fibrils by repetitive injection of 0.1 (blue), 0.25 (red), 0.5 (green) and 1.0 (grey) mg mL^{-1} Oxyntomodulin for 5 min followed by rinsing with 0.9 mg mL^{-1} saline for 5 min, at 37 °C. Only the f_3 frequency signal is shown. Bottom: average $\pm$ standard deviation (n=5) of frequency slope after nonspecific adsorption. Each sensor had 2 µg of 2 min sonicated fibrils physically adsorbed to the SiO$_2$ surface.

At 0.1 mg mL^{-1}, the slope was as shallow as -0.01 Hz min^{-1}, and signals returned nearly to the starting value after flushing with peptide-free medium, indicating that signal changes were governed by layer adsorption rather than by elongation. AFM imaging after QCM-D measurement showed fibril length and density indistinguishable from imaging before measurement (see *Figure 6-3* A-D). Between 0.25 and 1 mg mL^{-1}, signals did not return to the initial value after peptide removal, and frequency slopes were significantly steeper than the adsorption signal on an empty sensor. Slopes were repeatable with a standard deviation below 0.005 Hz min^{-1} for 0.25 and 0.5 mg mL^{-1}, indicating that elongation is not sterically
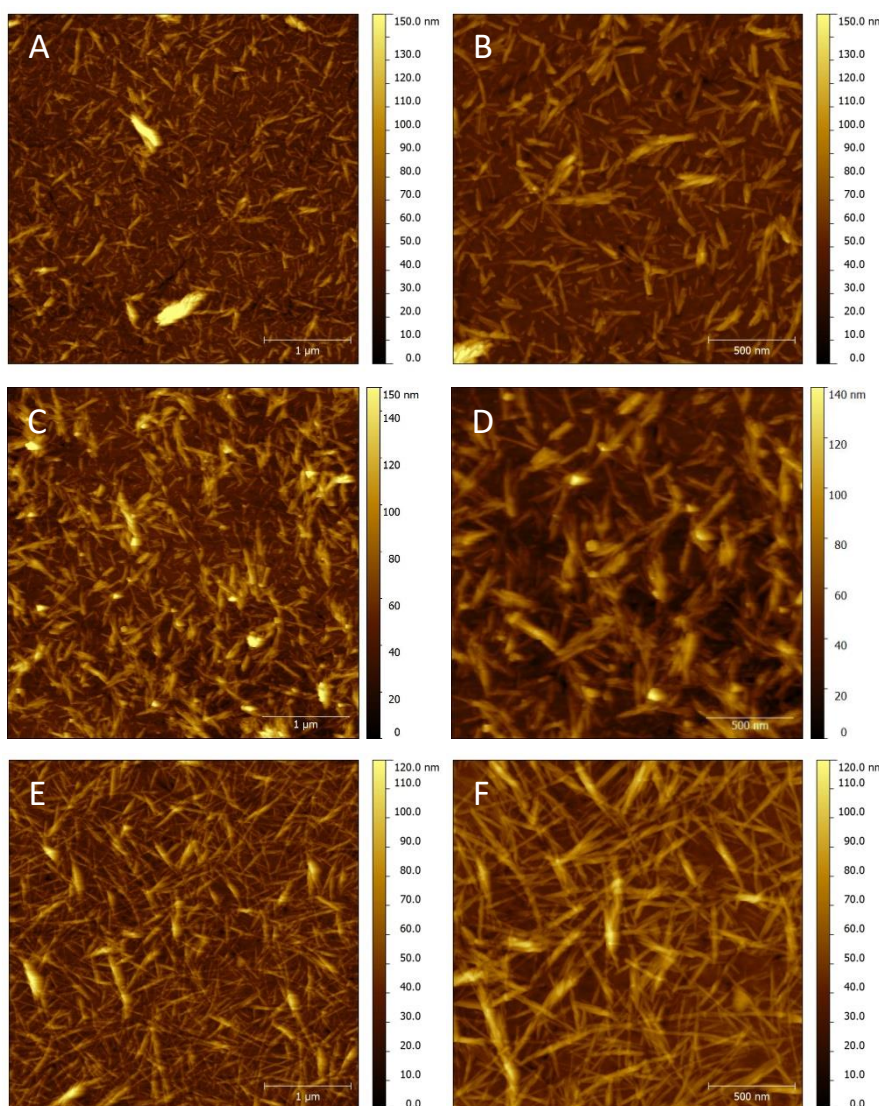
Figure 5-3: AFM imaging of QCM-D sensors confirms fibril elongation

A, B: SiO_2 QCM-D sensor with adsorbed fibril seeds before QCM-D experiment. C, D: Sensor after exposure to 0.1 mg mL^{-1} Oxyntomodulin in 0.9 mg mL^{-1} NaCl for 5*5 min. E, F: Sensor after exposure to 1 mg mL^{-1} Oxyntomodulin in 0.9 mg mL^{-1} NaCl for 5*5 min. AFM images were processed in Gwyddion to remove imaging scars and background signal. Resolution: 512*512 pixel at 4*4 µm scanning size (A, C, E), 1024*1024 pixel at 2*2 µm scanning size (B, D, F).

hindered, and the sensitivity of frequency measurement is not impaired by viscosity, dissipation or saturation. The repeatability of elongation is suggestive of constant fibril concentration on the sensors and elongation along the surface. At 1 mg mL^{-1}, the cumulated signal change was doubled in comparison to 0.5 mg mL^{-1}, and higher variability of measurements may be associated to increased dissipation caused by fibrils elongating into the liquid. AFM imaging after QCM-D measurement showed approximately doubled length and fibril crossover in fibrils elongated at 1 mg mL^{-1} for a combined exposure time of 25 min.

To avoid inaccurate measurement due to excessive fibril crossing or elongation into the bulk, elongation measurements were subsequently limited to single elongation periods of 5-20 min at or below 0.5 mg mL^{-1}, and 15 min at 1 mg mL^{-1}. In all following experiments, a reduced mass of fibrils sonicated for 15 min (in contrast to 2 min) was adsorbed to sensor surfaces. Increased fragmentation was supposed to homogenize the fibril length and gain sensitivity by the availability of more fibril ends, while consuming less fibril material.

Elongation measurement in absence of covalent fibril attachment is in contrast to literature examples, where fibril seeds were chemically conjugated to an activated surface before incubation in the QCM-D [182]. To show that the positively charged Oxyntomodulin fibrils interact strongly enough with the polar charged SiO$_2$ surface, fibril numbers were counted by AFM before and after elongation experiments. Typical fibril number densities of 26-40 µm^{-2} were measured after drying of a drop containing 0.2 µg of 15 min sonicated fibrils per sensor (= per cm^2), by counting fibrils in two 4*4 µm AFM frames of 4 sensors each. No changes in fibril number densities were seen after injection of 0.5 mg mL^{-1} peptide in 0.9 mg mL^{-1} saline at 37 °C for 5, 10, 15, and 20 min, respectively, and rinsing with 0.9 mg mL^{-1} saline.

The average seed length of 15 min sonicated fibrils before QCM-D experiments was 76±2 nm, assessed from measuring 400 fibril lengths each in three independently sonicated and deposited fibril seed batches. Seed diameters were approximately 20-40 nm by AFM, but could not be measured exactly on QCM-D sensors due to the rough nature of the SiO$_2$ coated gold surface. Assuming cylindrical shape, 76 nm average length, 0.2 µg deposited material and the density of a protein crystal (1.2 g cm^{-3}), the average diameter was calculated to be 28 nm, or 4-5 protofibril diameters in cross-section.

To estimate the QCM-D mass sensitivity factor, four chips with known fibril length and density were incubated in the QCM-D with 0.5 mg mL^{-1} Oxyntomodulin in 0.9 mg mL^{-1} saline at 37 °C for 3.5, 8.5, 13.5, and 18.5[9] min. Frequency shifts were assessed by extrapolating the linear frequency slope during the last 3-18 min to respective times, because elongation during the 30 s adsorption phase was assumed to take place even though the signal was concealed by the adsorption signal. Fibril length was assessed by AFM after the experiment by measuring 400 fibrils per sensor. The mass sensitivity factor was estimated according to equation (5-1) for each sensor. Measured and calculated values are summarized in **Table 6-1**.

The average mass sensitivity factor is 17.7±3.4 Hz min^{-1}, which is in exact accordance with the theoretical mass sensitivity of a rigid layer formation. This is a striking result, because fibrils only cover a part of the chip surface and are in equilibrium with an adsorbed peptide

---

[9] The unconventional times are due to 90 s lag time in the equipment caused by dead volume.

Table 5-1: Direct measurement of QCM-D mass sensitivity during Oxyntomodulin fibril elongation

Γ, fibril density on QCM-D sensor; Δl, elongation during QCM-D experiment; Δf, frequency change during elongation extrapolated from $f_3/3$ slope; n, calculated mass sensitivity; ρ, average protein crystal density, 1.2 g cm^{-3}; A_s, sensing surface, 1 cm^2.

Elongation time Δt, min	Γ, fibrils μm^{-2}	Δl, nm	Δf, Hz	n, μg Hz^{-1}
(method)	AFM, fibrils in 32 μm^2	AFM, 400 fibril lengths	QCM-D	$\Delta f * \rho * \left(\dfrac{d}{2}\right)^2 * \pi$ $* \Delta l * \Gamma * A_s$
3.5	40.75	9	-1.50	-18.07
8.5	34.84	35	-3.90	-23.1
13.5	38.66	26	-4.10	-15.1
18.5	26.77	75	-8.55	-14.54

layer. The mass sensitivity result indicates that no additional dissipation is caused by the fibril elongation, and any dissipation increase during the experiment is a result of nonspecific adsorption with little contribution to overall mass in the elongation phase. In fact, the measured dissipation signal only increased little during the elongation phase, compared to the adsorption phase (not shown). The rigidity of fibrils is given by the generally stiff nature of mature amyloid-like fibrils [91]. Exclusive elongation does not necessarily change the water content of the system, because the incorporation of water within fibrillar material is included in the assumed crystal density, and the expected increase of water adsorption due to increased surface roughness replaces water bound to the presumably unstructured peptide layer. Therefore, within small elongation and in the absence of fibril loss, Oxyntomodulin fibril elongation can be modelled like a rigid monolayer, and frequency slopes are in good approximation proportional to mass changes in the fibrillar material.

As fibril numbers are proportional to elongation rate, even small differences between experiments would prevent quantitation of elongation rates. Use of a direct mass correlation requires the measurement of fibril density on each sensor before and after each experiment, because deviations in amounts of deposition are caused by the pipetting of small amounts of viscous fibril stocks, the sonication step and the drying on sensor surfaces. Imaging and counting of each sensor before and after experiment was however not practicable.
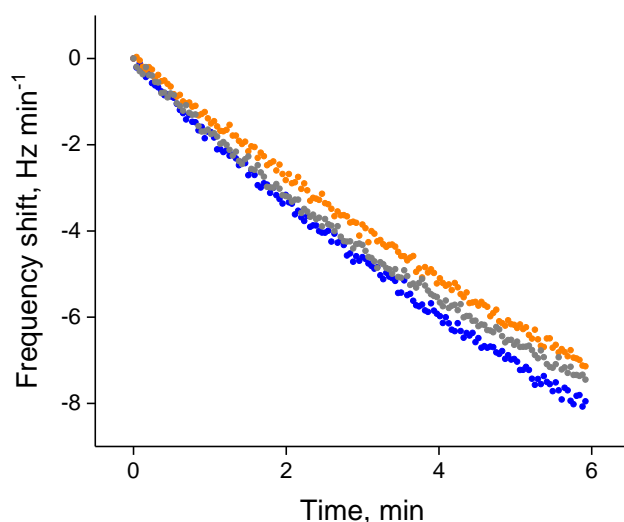
Figure 5-4: Repeatability of internal QCM-D standard

QCM-D f_3 signals of three sensors (orange, grey, blue) during incubation of a stream of 0.5 mg mL^{-1} Oxyntomodulin in 0.9 mg mL^{-1} saline with 0.4 µg fibril seeds adsorbed to the SiO$_2$ sensing surface with a standardized deposition device. Measurements at 37 °C. Signals are taken 2 min after start of peptide flow to omit frequency changes by unspecific adsorption. Slopes after linear fitting are -1,25±0.05 Hz min^{-1}, R$^2 \geq 0.99$.

As seen in **_Table 6-1_**, fibril numbers per frame were not constant for deposition of the same seed stock. To standardize liquid coverage on the surface during the drying of a seed dispersion, sensor deposition was performed using a deposition device for following measurements. Sensors were centrally aligned in a water-tight, sealed PTFE chamber that only exposed the active surface, and immobilized with springs. A 40 µL drop per chip was contained by the PTFE walls during drying, enabling even drying on the whole surface, as opposed to direct drop deposition with preferential fibril accumulation in the middle of the drop.

Fibril number differences due to pipetting and sonication could not be standardized. Therefore, an internal standard condition was inserted in all experimental setups. This condition was chosen as a 15 min, 100 µL min^{-1} injection of 0.5 mg mL^{-1} Oxyntomodulin in 0.9 mg mL^{-1} saline at 37 °C, due to the observed moderate frequency shifts and elongations at these parameters. Using the proportionality of fibril mass and frequency decrease at equal fibril numbers, the elongation slopes in each experiment can be shown as a relative elongation rate in proportion to the slope of the standard condition. Experimental repeats are then independent of the number of fibril ends, and deviations are only due to the nature of external conditions tested in the respective experiment. Repeatability within 3 sensors of one experiment is shown in (**Figure 6-4**), where f_3 frequency slopes were -1.25 Hz min^{-1} at a standard deviation of 0.05 Hz min^{-1}.

5.3 Electrolytes accelerate Oxyntomodulin self-assembly and stabilize fibrils

In chapter 3.3 and 3.4, it was observed that Oxyntomodulin's nucleation and fibril elongation is promoted in presence of electrolytes. Moderate amounts of sodium chloride (< 20 mM) accelerated fibril formation without precipitation and shifted the equilibrium of soluble and assembled peptide to the fibril side. It is assumed that chloride anions stabilize associated Oxyntomodulin molecules by shielding positive surface charges. Here, fibril elongation and peptide release from fibrils is studied in more detail in presence or absence of sodium chloride. The impact of anion size on fibril stabilization is tested with different salts.

A QCM-D seed elongation assay was performed at sodium chloride concentrations from 0.09 mg mL^{-1} to 9 mg mL^{-1}. This corresponds to a range of 1-100 % physiologic saline. All other experimental parameters correspond to the internal standard condition. Results are presented as the ratio of elongation slope to the elongation slope of the internal standard at 0.9 mg mL^{-1} sodium chloride (10 % saline).

As shown in the top panel of **Figure 6-5**, the frequency slopes steepened drastically with increasing saline concentration. Relative elongation rates were in good approximation linearly dependent on salt concentration. At 0.09 mg mL^{-1} sodium chloride, the frequency slope was not significantly steeper than the background signal caused by adsorption of soluble peptide to the sensor's surface. AFM images showed fibril shortening compared to the fibril seeds before the elongation experiment (see **Figure 6-6** A and B). From the internal standard elongation condition at 0.9 mg mL^{-1} to 4.5 mg mL^{-1} sodium chloride, the elongation rate increased by factor 6. Further increase to 9 mg mL^{-1} sodium chloride approximately doubled the relative elongation rate compared to 4.5 mg mL^{-1} sodium chloride. Variability between independent repeats increased with increasing salt concentration, which may be due to nonlinearity of the mass-to-frequency relationship when fibrils extend into the medium. As shown in **Figure 6-6** C-E, fibril elongation at increasing sodium chloride concentration was observable by AFM-imaging.

While 100 % saline has approximately the molarity of subcutaneous fluid, it needs to be stressed that subcutaneous fluid only contains trace amounts of sodium chloride and is mostly composed of carbonates and minor amounts of phosphates. In chapter 3, it was shown that monomer release occurs in PBS but not in 0.9 mg mL^{-1} saline. No fibril nucleation occurred in ThT screenings containing PBS. While not experimentally tested, it is assumed that carbonate-ions have a minor stabilizing effect on Oxyntomodulin self-assembly, due to the more delocalized negative charges compared to phosphate- and chloride-ions. Therefore, the results shown here do not contradict peptide release seen *in vivo* in [6].
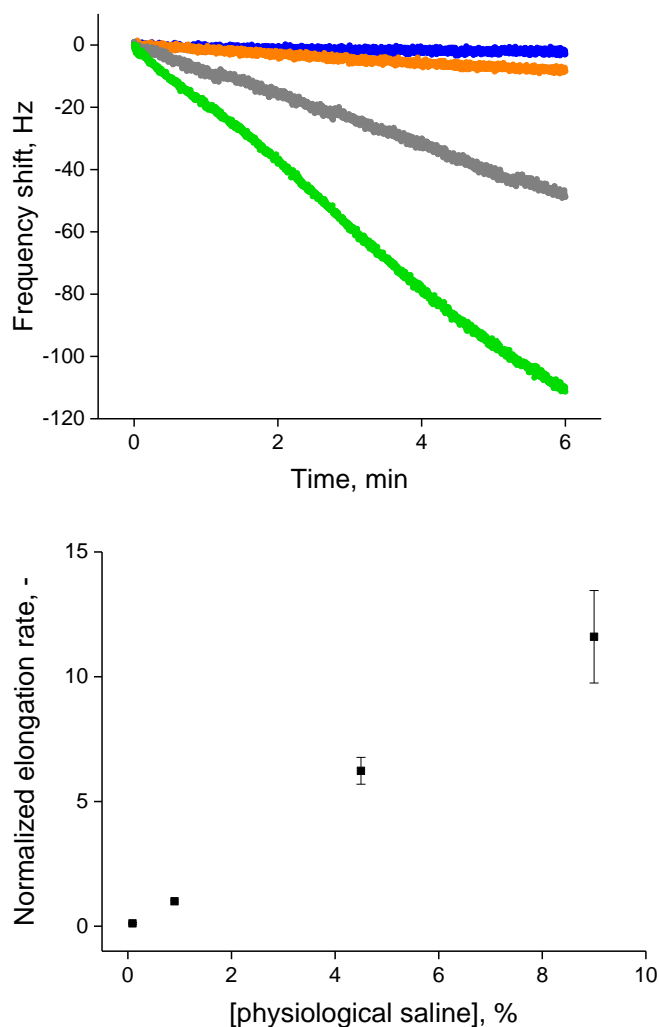
Figure 5-5: Oxyntomodulin fibril elongation rate dependence on NaCl concentration by QCM-D

QCM-D elongation of Oxyntomodulin seeds in presence of 0.5 mg mL^{-1} soluble Oxyntomodulin at 37 °C and increasing concentration of saline (NaCl). Seeds: mature Oxyntomodulin fibrils sonicated for 15 min, 0.4 µg per sensor physically adsorbed per SiO$_2$ QCM-D sensors. Top: exemplary f$_3$/3 slopes of one repeat, at 0.09 mg mL^{-1} (blue), 0.9 mg mL^{-1} (orange), 4.5 mg mL^{-1} (grey) and 9 mg mL^{-1} (green) saline, from 2-10 min of peptide injection. Bottom: slopes of linear approximation of each repeat's f$_3$/3 data divided by the internal standard slope at 0.9 mg mL^{-1} saline of each repeat (physiologic saline contains 9 mg mL^{-1} NaCl). 3 independent repeats presented as average ± standard deviation.
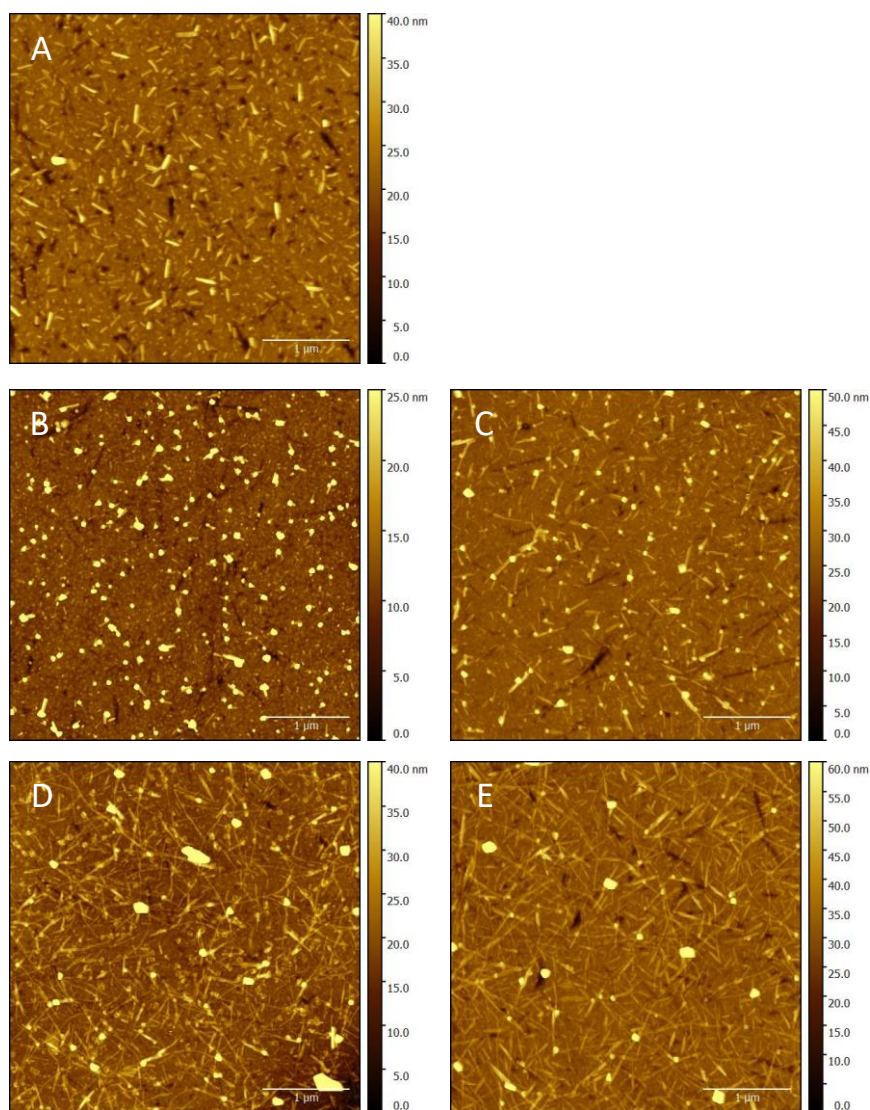
Figure 5-6: AFM imaging of QCM-D sensors confirms elongation promotion by NaCl

AFM imaging of the SiO_2 QCM-D sensors matching the top panel in **Figure 5-5**, before (A) and after (B-E) a total exposure of 8 min to 0.5 mg mL^{-1} soluble Oxyntomodulin at 37 °C and increasing NaCl concentrations. After peptide exposure, sensors were rinsed in the respective peptide-free medium. B, 0.09 mg mL^{-1} NaCl; C, 0.9 mg mL^{-1} NaCl; D, 4.5 mg mL^{-1} NaCl; E, 9 mg mL^{-1} NaCl. AFM images were processed in Gwyddion to remove imaging scars and background signal. Resolution: 512*512 pixel at 4*4 µm scanning size. Note that fibril length in B is shorter than before the experiment, and fibril length increases successively from C-E. >50 nm high spherical or edged features are artefacts stemming from salt crystallization during sensor drying.

Fibril degradation was tested by QCM-D in flow of water and 0.9 mg mL^{-1} saline. As shown in **Figure 6-7**, in presence of sodium chloride, only little frequency shift was seen over 5 h of flow. The frequency increase was linear in good approximation (R^2=99.5 %) with a slope of 7.36 Hz h^{-1}. Assuming this slope stems from peptide release from a constant number of seeds and the mass correlation is analogous to fibril elongation (see chapter 5.2), this corresponds to a release of 0.65 µg (16.2 %) over 5 h. In water, frequency shifts were approximately linear (R^2=96.3) with a slope of 320 Hz h^{-1} in the first 30 min, followed by a nonlinear increase to 181 Hz by 5 h. This corresponds to 3.2 µg (80.2 %) release. The signal nonlinearity is consistent with fibril loss by dissolution. At the end of the experiment, only few fibrils were seen by AFM imaging of the sensor, while fibril density was markedly higher on in images of a sensor flushed with 0.9 mg mL^{-1} saline (see **Figure 6-7** B-D).
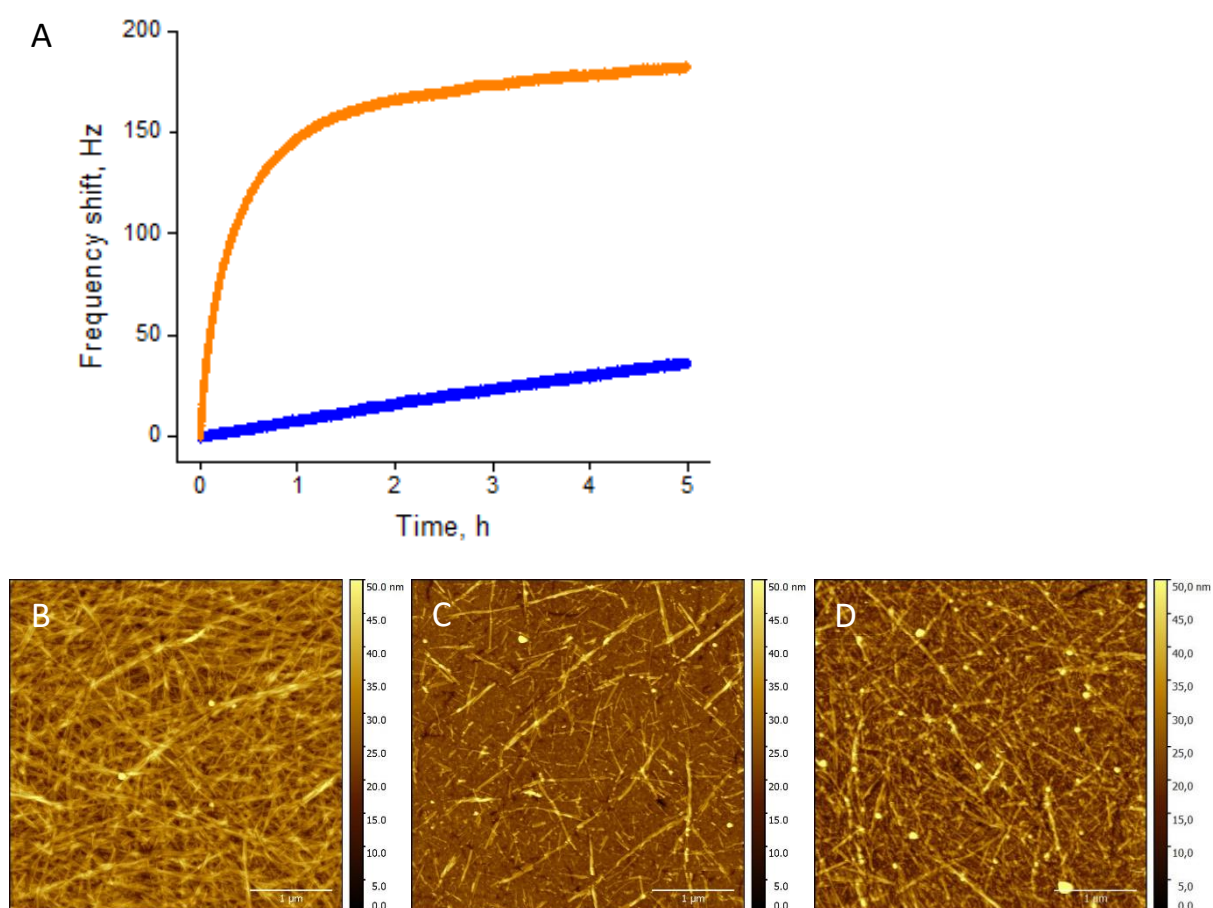
Figure 5-7: Fibril degradation in flow of peptide-free medium

A, QCM-D frequency shift during 100 µL min^{-1} flow of water (orange) and 0.9 mg mL^{-1} saline (blue) over sensors with 4 µg Oxyntomodulin fibrils physically adsorbed to the SiO$_2$ surface. B-D, QCM-D sensor imaging by AFM. B, before experiment; C, after incubation in water for 5 h, D, after incubation in 0.9 mg mL^{-1} saline for 5 h. AFM images were processed in Gwyddion to remove imaging scars and background signal. Resolution: 512*512 pixel at 4*4 µm scanning size.

While these results indicate faster off-kinetics in water compared to 0.9 mg mL^{-1} saline, it is not possible to exclude an additional signal contribution from fibril detachment from the sensor's surface. Fibril loss may be substantial because of higher fibril-fibril repulsion in absence of salt compared to presence of salt; increased adsorbed fibril mass per sensor compared to elongation experiments, and prolonged incubation under flow. Release kinetics derived from QCM-D may therefore represent an upper limit of fibril dissociation.

In bulk release experiments without solvent replacement, no measurable free peptide was found in presence of 0.9 mg mL^{-1} saline. If the detection limit of NanoDrop spectrophotometry of 0.001 mg mL^{-1} (225 nM) is taken as the upper limit of equilibrium concentration in equations (1-10) and (1-11), the Gibbs' free energy of Oxyntomodulin fibrillation at 37 °C in presence of 0.9 mg mL^{-1} saline is more negative than -38.2 kJ mol^{-1} (-9.1 kcal mol^{-1}). At otherwise constant conditions, bulk release in water reached an equilibrium of approximately 0.3 mg mL^{-1} (67 μM) after 4 h, as shown in **Figure 6-8**. This corresponds to a Gibbs' free energy of -24.0 kJ mol^{-1}. Similar values have been reported for amyloid-type fibrillation of other peptides [147][183][157].
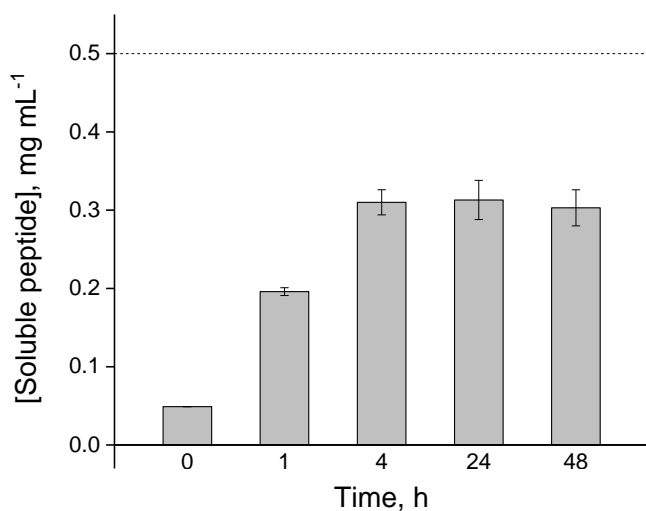
Figure 5-8: Equilibrium of soluble peptide and fibrils in water

Peptide release from Oxyntomodulin 0.5 mg mL^{-1} fibrils in water at 37 °C. Released peptide is measured form the A$_{280}$ signal of fibrillar supernatant after centrifugation and filtration with 50 kDa MWCO. Dotted line, total peptide.
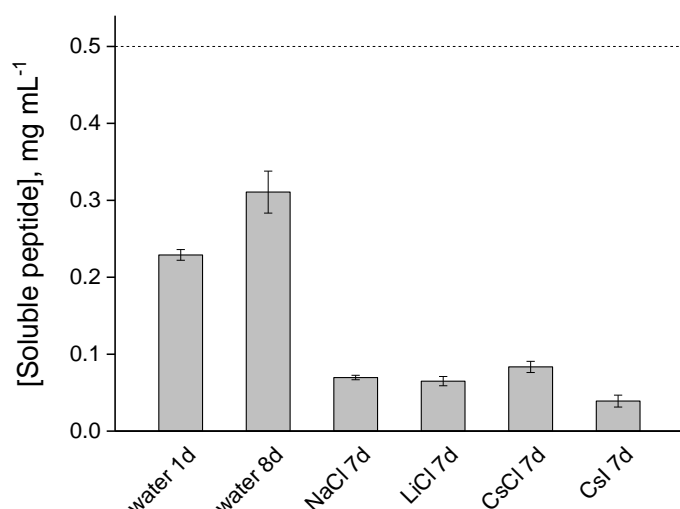
Figure 5-9: Stabilization of destabilized fibrils by salt addition

Oxyntomodulin fibrils partially disaggregated by incubation in water for 24 h (left column) and incubated for further 7 d in water and different salts at 37 °C. Released peptide is measured using the A_{280} signal of fibrillar supernatant after centrifugation and filtration with 50 kDa MWCO. Salt concentration, 15.4 mM. Results are presented as average ± standard deviation, n=3. Dotted line, total peptide.

To test if partially disaggregated fibrils can be re-stabilized, a fibril stock was diluted to 0.5 mg mL^{-1} in water and incubated for 24 h, reaching a free peptide concentration of 0.23 mg mL^{-1}. Addition of 14.4 mM (the equivalent of 0.9 mg mL^{-1} NaCl) NaCl, LiCl, CsCl, or CsI to three samples each, and further incubation for 7 d at 37 °C shifted the equilibrium below 0.1 mg mL^{-1} free peptide, while control samples in water had 0.3 mg mL^{-1} soluble peptide at the same time (see **Figure 6-9**). Salts were selected for the hydrodynamic radius of cation and anion: NaCl and LiCl contain comparably small anions and cations, CsCl has a small anions paired with large cations, and CsI has large cations and anions. As all salts shifted the thermodynamic equilibrium of soluble and assembled Oxyntomodulin in a similar degree, it would be implausible to assume that ions structurally integrate in the fibril structure. Rather, the stabilization effect may be due to electrostatic shielding of charges on the fibril surface, or destabilization of the monomeric state compared to assembled states.

In summary, salts not only accelerate the conversion of soluble Oxyntomodulin into fibrils, but also shift the equilibrium and therefore allow access of a different thermodynamic landscape.

5.4 Oxyntomodulin elongation is a quasi first order reaction in absence of secondary nucleation

It was seen in chapter 3.4 that the concentrations of soluble Oxyntomodulin and fibril seeds can affect the rate of conversion to fibrils. QCM-D elongation experiments analogous to *Figure 6-7* were performed in presence of different soluble peptide concentrations to follow self-assembly at different peptide concentrations in *quasi* real time. **Figure 6-10** shows frequency shift of an exemplary repeat and average elongation rates in dependence of peptide concentration.
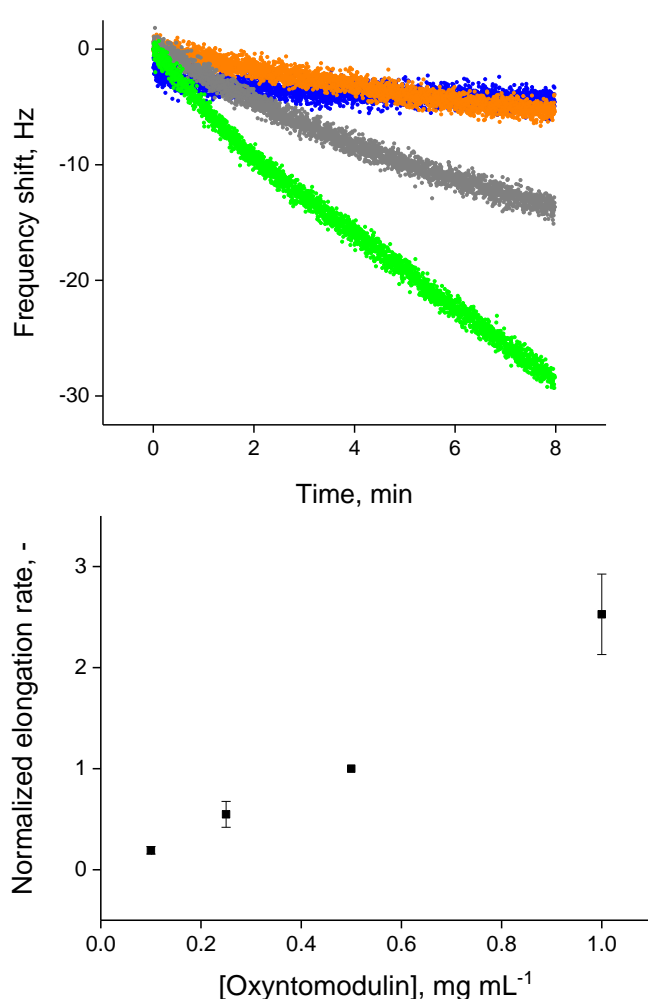
Figure 5-10: Effect of soluble Oxyntomodulin concentration on fibril elongation

QCM-D elongation of Oxyntomodulin seeds in presence of 0.9 mg mL^{-1} NaCl at 37 °C and increasing Oxyntomodulin concentration. Seeds: mature Oxyntomodulin fibrils sonicated for 15 min, 0.4 µg physically adsorbed per SiO$_2$ QCM-D sensors. Top: exemplary f$_3$/3 slopes of one repeat, at 0.1 (blue), 0.25 (orange), 0.5 (grey) and 1 (green) mg mL^{-1} Oxyntomodulin, from 2-10 min of peptide injection. Bottom: slopes of linear approximation of each repeat's f$_3$/3 data divided by the internal standard slope at 0.5 mg mL^{-1} Oxyntomodulin of each repeat. 3 independent repeats presented as average ± standard deviation.
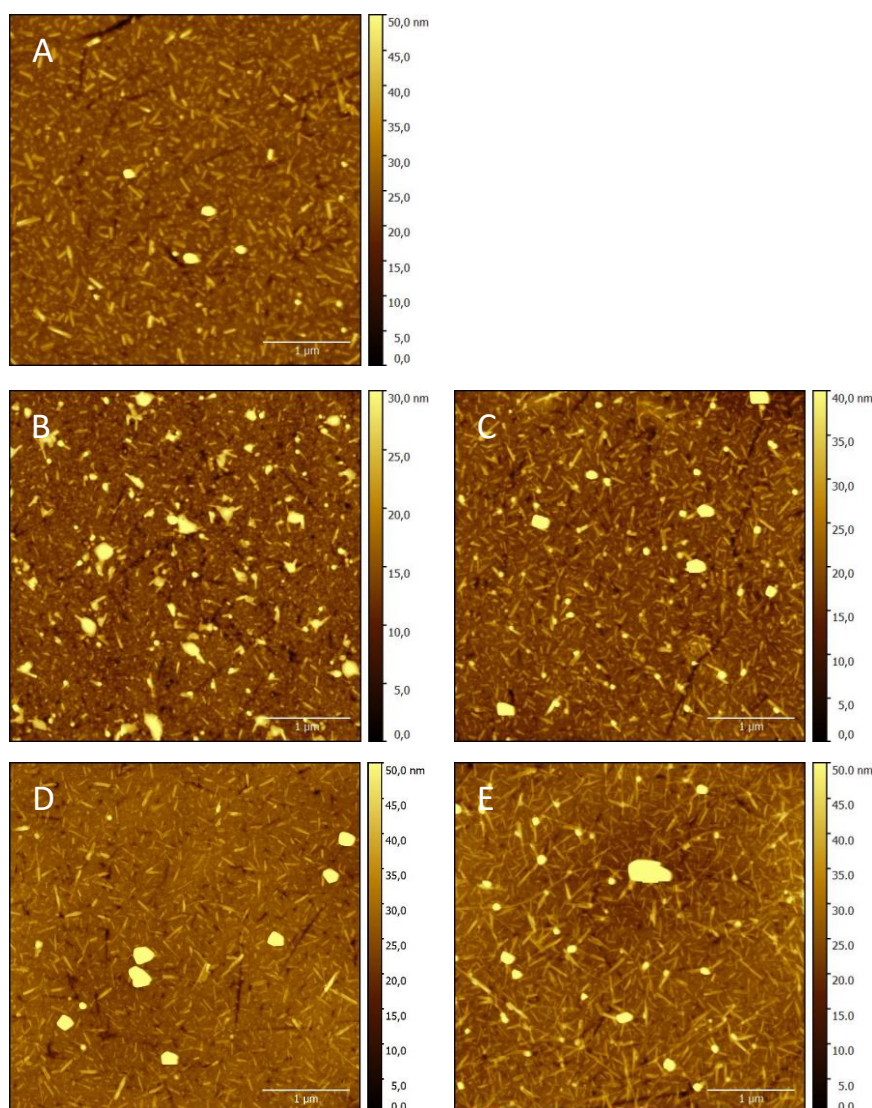
Figure 5-11: AFM imaging of QCM-D sensors confirms concentration dependency of Oxyntomodulin elongation

AFM imaging of the SiO_2 QCM-D sensors matching the top panel in **Figure 5-10Figure 5-5**, before (A) and after (B-E) exposure to increasing Oxyntomodulin concentrations in 0.9 mg mL^{-1} NaCl at 37 °C. After peptide exposure, sensors were rinsed in 0.9 mg mL^{-1} NaCl. B, 0.1 mg mL^{-1}; C, 0.25 mg mL^{-1}; D, 0.5 mg mL^{-1}; E, 1.0 mg mL^{-1} Oxyntomodulin. AFM images were processed in Gwyddion to remove imaging scars and background signal. Resolution: 512*512 pixel at 4*4 µm scanning size. >50 nm high spherical or edged features are artefacts stemming from salt crystallization during sensor drying.

At 0.1 mg mL^{-1}, signals were not significantly different from the background signals of peptide adsorption, and no elongation was seen in AFM images of sensors after the QCM-D experiment. AFM imaging after elongation in 0.25 mg mL^{-1} to 1 mg mL^{-1} showed increasing elongation in dependence of soluble Oxyntomodulin concentration. Frequency shifts were linear in good approximation during elongation, which is consistent with exclusive elongation at constant monomer concentration. Importantly, the relative elongation rate was directly

proportional to peptide concentration. This is in accordance with the concentration-dependent apparent elongation rate k_{app} in an elongation chain reaction (see equation (1-5)) and the theoretical pseudo first-order reaction type of exclusive elongation shown in equation (1-6). The elongation rate of Oxyntomodulin fibrils at constant peptide concentration is therefore – among others – limited by diffusion, and within the concentrations tested here, growth competent fibril termini on the senor surface are not saturated.

While not formally shown here, the fibril seed concentration also has an influence on the kinetics of elongation, trivially because of the multiplication of growth competent ends with the same elongation rate per end. It was seen in chapter 3.4 that low seed concentration decelerates elongation, but also favors polymorphism. Formation of a potentially more thermodynamically stable fibril species under conditions with slow elongation kinetics will be discussed in chapter 6.

5.5 Oxyntomodulin fibrillation has a unique temperature optimum at room temperature

Temperature has an impact on folding and amyloid formation of many proteins and peptides. Native proteins are selected by evolution for structural stability and low aggregation tendency in their natural environment. At relatively low temperatures, the enthalpic gain of shielding hydrophobic residues from the aqueous environment is greater than the entropic cost of adopting an ordered structure, making the hydrophobic effect the main driving force for protein folding. Temperature increase – e.g. by fever – both alters the solubility of side chains and increases the entropic cost of folding, eventually resulting in thermal denaturation [156]. Every folded structure has an unfolding ("melting") temperature range where the folded structure becomes thermodynamically destabilized compared to denatured states. Partial or complete unfolding is necessary to align molecules in an amyloid-like pattern. Therefore, the propensity to form self-assembled structures from naturally folded proteins generally rises with temperature increases, and temperature optima of amyloid formation are substantially higher than body temperature for most proteins and peptides (see also chapter 1.2.3).

The thermal behavior of Oxyntomodulin self-assembly was investigated to determine optimal elongation temperatures for fast and monomorphic elongation, to assess the stability of fibrils in storage conditions, and to test the response to temperature changes in the context of subcutaneous injection. Conditions were considered up to 42 °C to prevent chemical denaturation of the peptide. Storage temperatures were assumed as 6-8 °C (fridge) and 25 °C (room temperature). 25 °C doubled as a lower limit of subcutaneous temperature for high dermal layers or in case of hypothermia. 32 °C represents the average subcutaneous temperature. 37 °C (physiological body temperature) was tested as an upper limit of subcutaneous temperatures and to determine thermal effects during transition of soluble peptide from subcutaneous space to the blood stream. 42 °C was chosen to investigate effects of hot climates or high fever on a subcutaneous depot.

Oxyntomodulin fibril elongation was tested by a kinetic QCM-D assay analogous to the effects of salt- and monomer concentration. Every experiment tested four temperatures including the internal standard elongation condition at 37 °C, to account for differences in seed numbers per sensor batch. A separate triplicate experiment series with internal standard and an overlapping measurement at 25 °C was performed under external cooling for elongation measurement at 15 and 20 °C.

As shown in (**Figure 6-12**), the QCM-D elongation assay suggests a temperature optimum of elongation between 25 and 32 °C. Elongation was fastest at 25 °C, with about threefold elongation rate compared to 37 °C. The elongation rate at 25 °C was insignificantly higher in

the measurement series at lower temperatures, and no effect of changing the sequence of measurement or the measurement chambers was seen. AFM imaging confirmed considerable elongation at 25 °C and 32 °C, while less elongation was seen at other temperatures (see exemplary images in **Figure 6-13**).
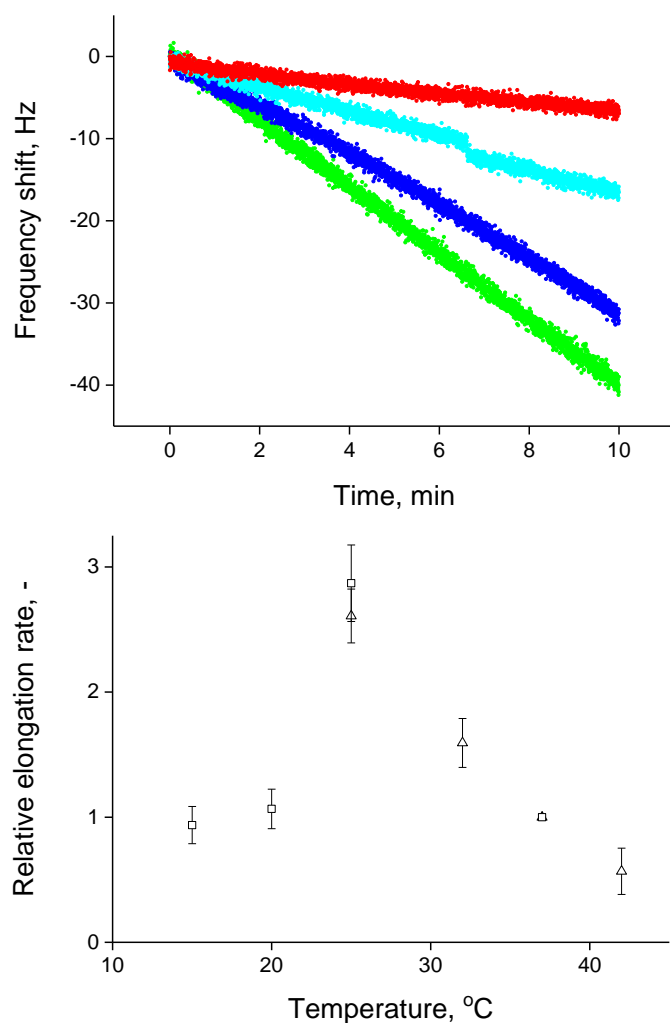
Figure 5-12: QCM-D reveals Oxyntomodulin fibril elongation optimum at room temperature

QCM-D measurement of Oxyntomodulin fibril elongation in presence of 0.9 mg mL^{-1} NaCl and 0.5 mg mL^{-1} Oxyntomodulin at different temperatures. Seeds: mature Oxyntomodulin fibrils sonicated for 15 min, 0.4 µg physically adsorbed per SiO$_2$ QCM-D sensors. Top: exemplary $f_3/3$ slopes of one repeat, at 25 (green), 32 (blue), 37 (cyan) and 42 (red) °C, measured from 2-10 min of peptide injection. Bottom: slopes of linear approximation of each repeat's $f_3/3$ data, divided by the internal standard slope at 0.5 mg mL^{-1} Oxyntomodulin of each repeat. Triangles: measurement at 25, 32, 37, 42 °C; squares: measurement at 15, 20, 25, 37 °C with external cooling at 15 and 20 °C. 3 independent repeats presented as average ± standard deviation.
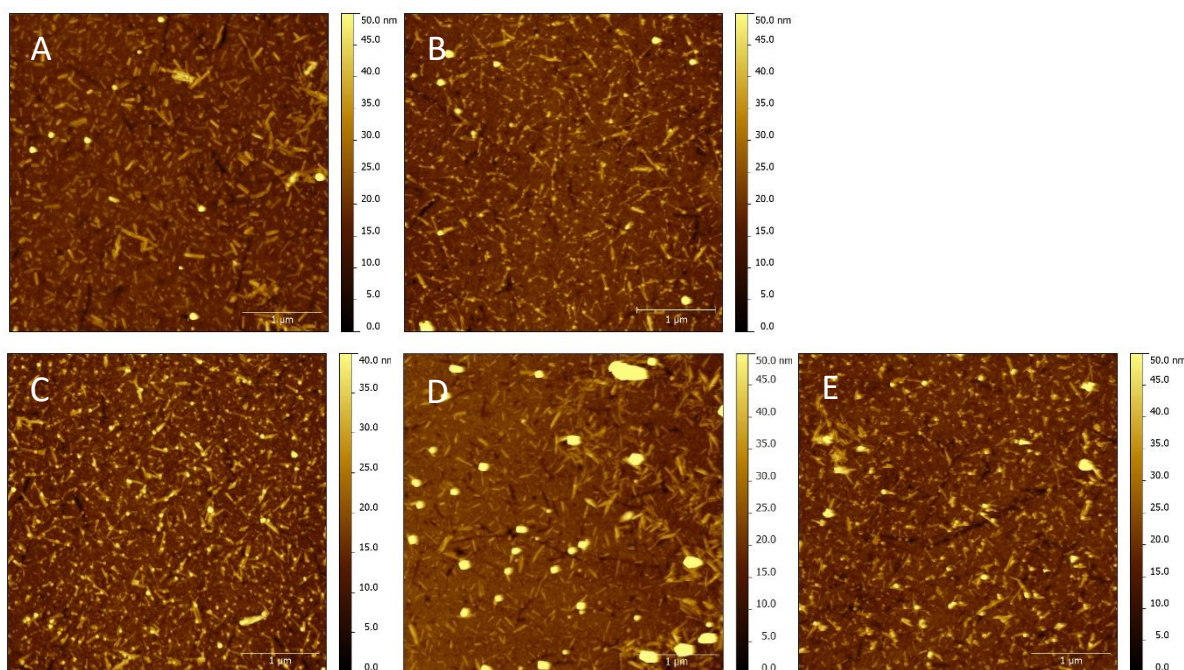
Figure 5-13: AFM imaging confirms maximum elongation rate at 25 and 32 °C

AFM imaging of the SiO$_2$ QCM-D sensors matching the top panel in **Figure *5-12***, before (A) and after (B-E) exposure to 0.5 mg mL^{-1} Oxyntomodulin in 0.9 mg mL^{-1} NaCl at different temperatures. After peptide exposure, sensors were rinsed in 0.9 mg mL^{-1} NaCl. B, 25 °C; C, 32 °C; D, 37 °C; E, 42 °C. AFM images were processed in Gwyddion to remove imaging scars and background signal. Resolution: 512*512 pixel at 4*4 µm scanning size. >50 nm high spherical or edged features are artefacts stemming from salt crystallization during sensor drying.

The thermal response of Oxyntomodulin fibril elongation seen in QCM-D elongation assays is highly unusual. No amyloid-type aggregation optimum below body temperature has been reported in the literature, neither for proteins nor for peptides. In a QCM-D fibril elongation assay with similar setup to the experiments shown here, A. Buell et al. showed increasing elongation with increasing temperature for nine amyloid-forming peptides and proteins in the temperature range from 25 to 45 °C [129]. One of the tested peptides was human glucagon, which corresponds to the 29 N-terminal amino acids of Oxyntomodulin. In other studies, it was shown that amyloid-like self-assembly of peptides and short proteins like amyloid β, bovine insulin, α-synuclein and β$_2$-microglobulin do have a temperature optimum, but non-Arrhenius behaviour or disaggregation only occur beyond 60 °C [184][156][133][147][185][153]. A similarly narrow optimum has been described for hen egg white lysozyme, which thermally unfolds at 55 °C followed by fibrillation maximum at 60 °C and amorphous aggregation at 65 °C [132].

Due to the independent reproducibility of the QCM-D results and the confirmation by AFM imaging, it is unlikely that the measured kinetics are an artefact of measurement at different

conditions. It was confirmed by the QCM-D manufacturer's customer service that measurement at different temperatures does not interfere with absolute frequency changes or mass sensitivity after thermal equilibration. To exclude a surface-mediated effect, analogous QCM-D elongation experiments were performed on sensors with 50 % OH- and 50 % CH_3-terminated polyethyleneglycol self-assembled monolayers. Similar effects were observed, however the fibrils did not interact strongly enough with the surface to provide consistent fibril concentrations during the experiment, resulting in reduced signal-to-noise ratio and less linear frequency slopes (results not shown).

To test if there is a thermal optimum in bulk and at longer incubation times, seeded kinetic assays were performed for 15 h at 25; 32; 37 and 42 h in presence of the fluorescent amyloid-reporter dye ThT. Lower temperatures could not be measured because it was technically not possible to cool the fluorescence plate reader. The ThT elongation profiles shown in **Figure 6-14** are in accordance with results from QCM-D, showing a non-Arrhenius reaction type with more ThT binding and hence faster assembly kinetics for lower temperatures. Curves could be fitted with an exponential function analogous to equation (1-9) with $R^2 > 97 \%$, confirmed exclusive elongation of pre-formed seeds in absence of secondary nucleation.
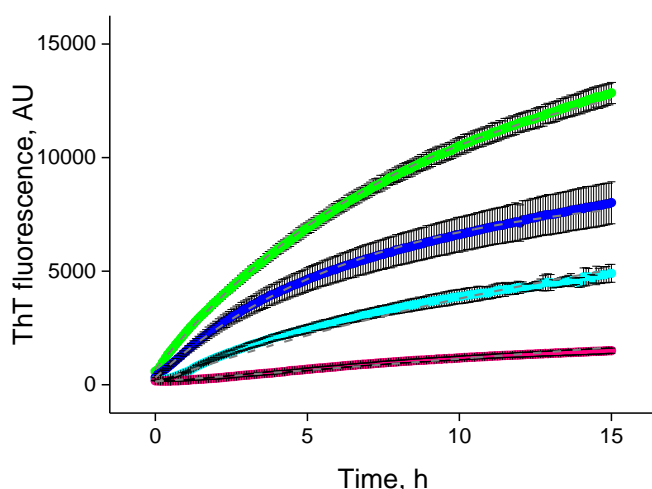
Figure 5-14: ThT kinetics confirm inverse Arrhenius behaviour of Oxyntomodulin fibril elongation beyond room temperature

ThT fluorescence in presence of 0.5 mg mL^{-1}, 0.9 mg mL^{-1} saline and 50 µM ThT and 1 % Oxyntomodulin seeds at different temperatures, in Corning® 3881 microplates with non-binding surface. Seeds were derived from 15 min sonication of a mature Oxyntomodulin stock. Green, 25 °C; blue, 32 °C, cyan, 37 °C, red, 42 °C. Results are presented as average ± standard deviation, n=6. Dotted lines, exponential fitting with the ExpDec2 function in Origin; $R^2 > 97 \%$.

Fitted association rates decreased from 0.115 h^{-1} at 25 °C to 0.002 h^{-1} at 42 °C. At longer incubation times in ThT conditions at 37 and 42 °C, secondary nucleation occurred, and the twisted fibril type appeared in AFM images after three days (data not shown). It was thus not possible to derive information on the equilibrium concentrations by ThT assay.

A seeded bulk elongation assay in dye-free conditions was performed to investigate the impact of temperature on the thermodynamic equilibrium of soluble and fibrillar peptide. Concentrations of soluble and assembled peptide were assessed after 1, 4, 7 and 14 days of incubation at 6 °C, 25 °C, 32 °C, 37 °C and 42 °C. AFM imaging confirmed the presence of fibrils and absence of unstructured aggregate at each end point. As displayed in **Figure 6-15**, the conversion of soluble peptide was fastest at 25 °C, with less than 20 % free peptide after 24 h and no measurable soluble peptide after 7 d. At other temperatures, approximately 50 % fibril yield was reached after 24 h, but further assembly was slower and only reached full conversion at 6 °C after 14 d. Lowest conversion was seen at 37 °C, with only 78 % fibril yield after 14 d. Remarkably, AFM images after 7 and 14 d showed the presence of thin twisted fibrils in samples at 37 °C and 42 °C, while the fibrils at or below 32 °C exclusively represented the straight fibril type of seed fibrils (see **Figure 6-16**). In storage conditions at fridge or room temperature, the equilibrium is therefore far on the fibril side and kinetics are fast enough to prevent formation of alternative species. The fast and robust reproduction of mother fibrils is reassuring for storage stability of Oxyntomodulin fibrils in a fridge or at
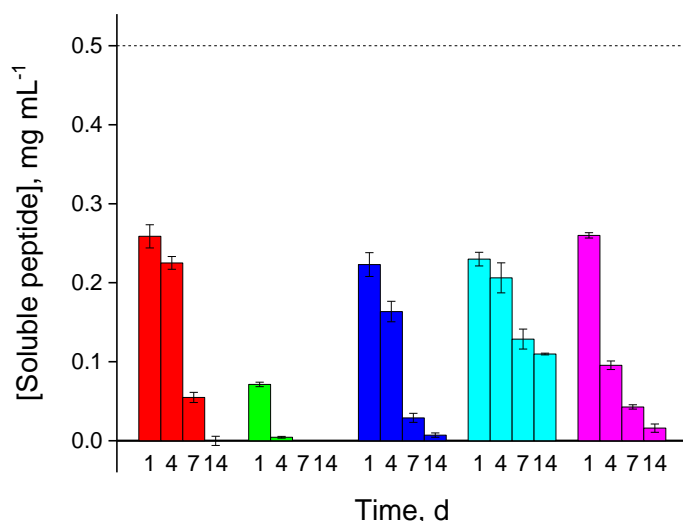
Figure 5-15: Bulk elongation confirms temperature optimum at room temperature

Soluble peptide after quiescent incubation of 1 % Oxyntomodulin fibril seeds in 0.5 mg mL^{-1} Oxyntomodulin for 1, 4, 7 and 14 days. Remaining soluble peptide measured by NanoDrop absorption at 280 nm after 30 min sedimentation of fibrils at 13 000 rpm and 50 kDa MWCO filtration of supernatants. Red, 6 °C; green, 25 °C; blue, 32 °C; cyan, 37 °C; purple, 42 °C. Results are presented as averages of independent triplicates ± standard deviation.

room temperature even after partial dissolution. This reflects the absence of changes in fibril samples over months of storage of fibril stocks. Kinetics at or above body temperature are not only slower, and equilibrium is not only shifted to the soluble peptide side, but prolonged incubation at these conditions also favours formation of a structure with an alternative minimum of the free energy landscape. This is in agreement with the observation of polymorphism after prolonged incubation in ThT conditions or in the elongation of longer fibrils in 5 mg mL^{-1} Oxyntomodulin at 37 °C. Metastability at body temperature may be a driving factor for the peptide release seen *in vivo* [6].

While results from QCM-D, ThT kinetics and bulk elongation reproduce a unique temperature optimum of Oxyntomodulin fibril elongation at 25 °C, it is not clear why this low and narrow temperature optimum is adopted. To gain insights into the enthalpic driving
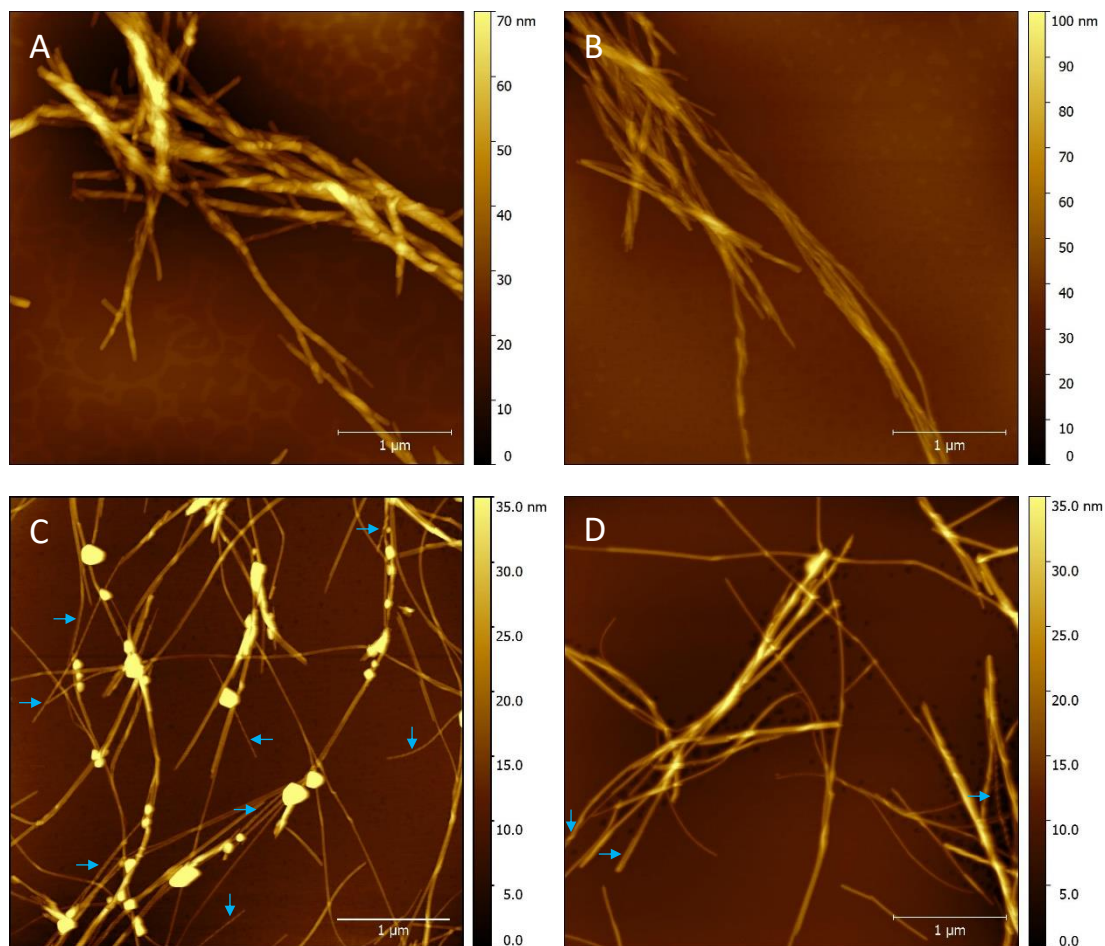
Figure 5-16: AFM shows polymorphism after prolonged incubation at thermodynamically and kinetically unfavourable conditions

AFM imaging before concentration measurement of 14 d samples shown in **Figure 5-15**. Elongation at 25 °C (A) and 32 °C (B) exclusively reproduced the seed fibril morphology. Elongation at 37 °C (C) and 42 °C (D) additionally caused growth of twisted fibril types (blue arrows). AFM images were processed in Gwyddion to remove imaging scars and background signal. Resolution: 512*512 pixel at 4*4 µm scanning size.

factors of Oxyntomodulin self-assembly, seed elongation was studied by isothermal calorimetry (ITC). ITC is classically used to measure heat effects of ligand binding and protein-protein association. One binding partner is equilibrated to measurement temperature in an insulated, stirred chamber, and heat flux is controlled and measured. Addition of a binding partner creates or consumes energy dependent on the type of interaction, causing negative or positive peaks of heat flux to maintain the set temperature. After subtraction of dilution heat and division by the molar amount of added ligands, the area under the heat flux curve is equivalent to the change of reaction enthalpy ΔH [cal mol^{-1}]. The change of reaction enthalpy over temperature defines the change of heat capacity ΔC_p [cal mol^{-1} K^{-1}] [147]. Some publications describe heat effects of amyloid fibril extension by ITC. Pre-formed fibrils and soluble peptide or protein represent the binding partners, and heat flux is measured during monomer consumption [147][154][133].

Heat capacity changes in amyloid fibrillation can be caused by several factors. The cross-beta backbone alignment and formation of steric zippers between sheets require the exclusion of side chains from an aquatic environment. Burial of hydrophobic residues is generally enthalpically favourable and becomes more favourable with an increase of temperature (negative ΔC_p). Conversely, exclusion of polar or charged residues from bulk water is thermodynamically unfavourable and generally increases ΔC_p [153][154]. A potentiating effect can be caused by surface burial during thermally driven association of fibrils. Large exothermic heat effects preceding thermal disaggregation have been attributed to the thermal effects of surface burial during fibril association at increased temperatures for several amyloid-forming peptides and proteins [147][153][186]. It is assumed that favourable enthalpic interactions saturate at higher temperatures [153].

In addition to side-chain and backbone interactions of fibrils, water within the fibril can have an impact on thermodynamics. If water molecules are excluded during fibril elongation or association, hydrophobic interactions and hydrogen bonding within the fibril or fibril bundle become enthalpically more favourable [155]. Inclusion of water in fibrils can create negative and positive heat capacity changes, depending on the hydrophilicity of the microenvironment and the degree of mobility within the fibril. For instance, hydration of polar or charged residues is enthalpically favourable, driving the thermodynamic potential of association at higher temperatures [153]. However, hydration of nonpolar residues is thermodynamically unfavourable and perturbs hydrophobic interactions. Restriction of water mobility additionally creates an entropic cost that scales with temperature, which may overall prevent association due to a positive free energy balance.
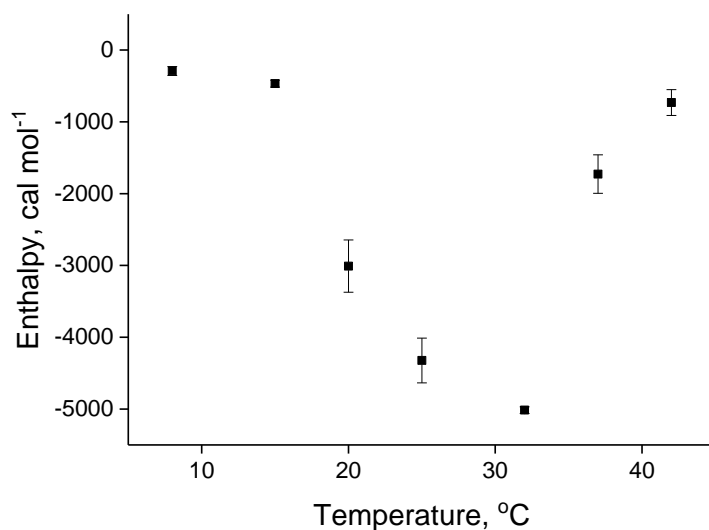
Figure 5-17: ITC reveals exothermic Oxyntomodulin fibril elongation with optimum below body temperature

Oxyntomodulin fibril elongation enthalpies measured by isothermal titration calorimetry at 8 °C, 15 °C, 20 °C, 25 °C, 32 °C, 37 °C, 42 °C. Enthalpies derived from integration of heat flux per monomer, after injection of 12 µL 1 mg mL^{-1} Oxyntomodulin into 450 µL 0.1 mg mL^{-1} seeds derived from 15 min sonication of mature Oxyntomodulin fibrils, both in 0.9 mg mL^{-1} NaCl. Heat flux is corrected for heat flux of peptide dilution in 0.9 mg mL^{-1} NaCl. Points represent averages of three independent measurements ± standard deviation.

In this experiment, the reaction cell contained a 0.1 mg mL^{-1} seed solution with 15 min sonicated mature fibrils in 0.9 mg mL^{-1} saline. This condition was chosen because it provided sensitive enthalpy peaks while allowing completion of the assembly reaction (i.e. recovery of heat peaks to baseline), used an amount of fibrils that could be sonicated in one batch, and had a fibril concentration at least 100-fold higher than the equilibrium concentration in 0.9 mg mL^{-1} saline. For the latter reason, fibril dissociation in the cell could be assumed negligible. The pipette contained a 1 mg mL^{-1} solution of Oxyntomodulin in 0.9 mg mL^{-1} saline. For heat flux measurement, 12 µL were pipetted into 450 µL seed dispersion. With the seed dimensions estimated in chapter 5.2, the cell contained $8.0*10^{11}$ fibrils, and 2.7 nmol peptide ($1.6*10^{15}$ molecules) were added per measurement, corresponding to a 2000-fold excess of monomer numbers to fibril numbers. Quantitative conversion to fibrils would create an average 26.7 % fibril elongation. It was technically not possible to recover samples after the reaction for AFM control of fibril elongation. A complete conversion to fibrils was assumed due to knowledge on equilibrium and kinetics of elongation in salt-containing condition, the low excess of monomer to fibril compared to QCM-D, ThT, and bulk elongation measurements, rigorous mixing in the reaction cell, and the recovery of thermal peaks to baseline within less than 10 min. Consecutive peptide injections into the same fibril dispersion created lower signals than the first elongation period, and signals did in some cases

not return to baseline within 10 min. This may be due to fibril association resulting in lower availability of growth-competent fibril termini, and hence reduced elongation kinetics [147]. Only first injections were used for the following analysis.

As shown in **Figure 6-17**, Oxyntomodulin fibril elongation was enthalpically favourable (exothermic) in the measurement range from 8 °C to 42 °C. At 6 °C, 15 °C, 37 °C and 42 °C, the reaction was only moderately exothermic, whereas large enthalpy changes from -3 kcal mol^{-1} to -5 kcal mol^{-1} were measured from 20 to 32 °C. The experimental optimum was at 32 °C, however the true optimum may be between 25 and 32 °C. By definition, an optimum in enthalpy corresponds to a change of sign in heat capacity.

It is not possible to explain the heat effects during Oxyntomodulin fibril elongation without an atomic-resolution fibril model. However, knowledge of the enthalpy, rate and equilibrium changes allows some reasoned assumptions on influence factors:

Firstly, comparison of the elongation rates measured by QCM-D, temperature dependence of bulk elongation kinetics and equilibrium concentrations, and temperature dependence of reaction enthalpy show a striking similarity of kinetic, free energy, and enthalpic changes with alteration of temperature. Oxyntomodulin fibril elongation is therefore at least partially driven by enthalpy.

Secondly, the strongly exothermic reaction at 25 °C and 32 °C cannot exclusively be explained by single binding events. Heat effects caused by association of fibrils are not impossible, but as fibril seeds are incubated at the reaction temperature before the event, the reaction is rigorously stirred, and elongation is small even after total consumption of free peptide, thermodynamic effects of fibril association during elongation cannot be large. However, a small effect of fibril association could explain the more exothermic reaction at 32 °C than at 25 °C, while a kinetic optimum at 25 °C was seen at comparable reaction times in QCM-D. A potentially favourable thermodynamic effect of association at higher temperatures has no impact in QCM-D experiments due to the immobilization of fibrils.

Thirdly, the sign change in heat capacity and drastic reduction of reaction enthalpy over a relatively small temperature range suggests a mechanistic change in elongation at enhanced temperatures. One explanation may be that the reaction is not quantitative above skin temperature due to the enhanced entropic cost of self-assembly at increased temperatures. As the magnitude of Gibbs' free energy is greater than -9.1 kcal mol^{-1} for Oxyntomodulin fibrillation at 37 °C (see 5.3), there must be an entropic compensation. Consequently, entropically unfavourable events directly affect the equilibrium. Mechanistic or statistical changes in e.g. water exclusion from the fibril influence heat capacity and entropy changes during fibrillation, which feeds back to experimentally measured enthalpy and elongation rate due to an overall incomplete, slower reaction. A different explanation for anti-Arrhenius kinetics and thermodynamics may be that Oxyntomodulin's net charge (or the screening of

charged residues) changes as a function of temperature. This can be mediated by subtle changes of the fibril structure that enhances charge-charge repulsion, such as reduced screening by anions in a dry environment. Changes of the medium, e.g. the increased dissociation of water at enhanced temperatures, can have an impact on fibril compactness and the structure of soluble peptide. Negative, zero, and positive heat capacity changes have been reported for elongation of glucagon fibrils derived from different environments. Importantly, it was shown that glucagon fibrils can lose or maintain positive charges during elongation [154]. Due to Oxyntomodulin's structural similarity to glucagon, a change in charge patterns as a function of temperature is not unlikely. An experimental setup analogous to [154] was however not possible with Oxyntomodulin fibrils due to Oxyntomodulin's fibrillation sensitivity to ions.

Fourthly, temperature may have an influence on the architecture of soluble peptide monomers, making the soluble species more or less prone to self-assembly depending on environmental conditions. For instance, the 1-40 peptide fragment of amyloid β transforms from random to beta sheet when heated from 0 to 37 °C, accompanied by an increase in amyloid formation tendency [187][137]. As Oxyntomodulin is a human and rodent hormone, low tendency for aggregation at core body temperatures may be evolutionarily selected for. The helical molecular structure reported in literature has been confirmed with synthetic Oxyntomodulin at 37 °C in chapter 4.3 [48]. Generally, helical structures are sensitive to temperature increase [134][188].

To test the influence of temperature on the structure of soluble Oxyntomodulin, the change of secondary structure was measured by circular dichroism at increasing temperatures. Measurement was performed analogously to structural measurement described in 4.1.3 with an additional 5 min of thermal incubation before measurement. As shown in **Figure 6-18**, the helical content of Oxyntomodulin decreased gradually with increasing temperature from 45 % at 8 °C to 32 % at 47 °C. Reduced helicity may be a driving factor for increasing fibril elongation rate and enthalpy with temperature increase at sub-physiologic temperatures. No significant alteration in other secondary structural elements was seen, indicating that the formation of unfavourable conformations of soluble peptide is not involved in the non-Arrhenius kinetics and thermodynamics of Oxyntomodulin fibril elongation at elevated temperatures. As results from FTIR, CD, X-Ray diffraction and Cryo-EM imply, Oxyntomodulin likely adopts a β-arch fold in fibrils. The adoption of the folded conformation required for fibril elongation is likely to be disadvantaged at higher temperatures, as secondary structure formation is generally favourable at lower temperatures [135][134][158][164]. Fibril elongation is then limited by the native structure at low temperatures and by the thermodynamics of folding at high temperature.
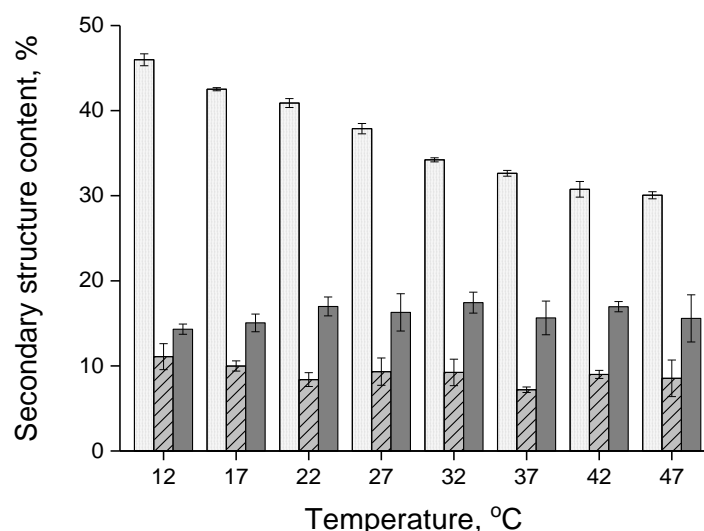
Figure 5-18: Helicity of soluble Oxyntomodulin decreases with increasing temperature

Secondary structure of Oxyntomodulin by circular dichroism spectroscopy from 260 to 180 nm. Data deconvoluted with the online tool Dichroweb using the algorithms CONTIN-LL, SELCON 3 and CDSSTR for each sample. Shown are averages of 3 independent sample runs ± standard deviation. Transparent, dotted: helix; light grey, striped: sheet; dark grey, solid: turns.

If the folding thermodynamics of Oxyntomodulin are a major limiting factor in fibril elongation at higher temperatures, peptide release from fibrils must become more favourable with increasing temperatures, as any structured state would become destabilized. Because fibril release in elongation conditions was below the detection limit of conventional quantification methods, release was measured after dilution of essentially salt-free fibrils in water. Analogous to elongation experiments in bulk, soluble peptide was quantified in the filtered supernatant, and dissociation was controlled by AFM.

Figure 6-19 shows that peptide release becomes faster with increasing temperatures, and higher soluble peptide concentrations are reached after 7 d. At 6 °C, only approximately 10 % released peptide is measured after 7 d, implying a kinetic and/or thermodynamic conservation of the fibril state at storage conditions. At 25 °C, release is markedly higher and faster. Highest release is reached at physiologic temperatures, where between 50 and 60 % soluble peptide were measured after one week of incubation.
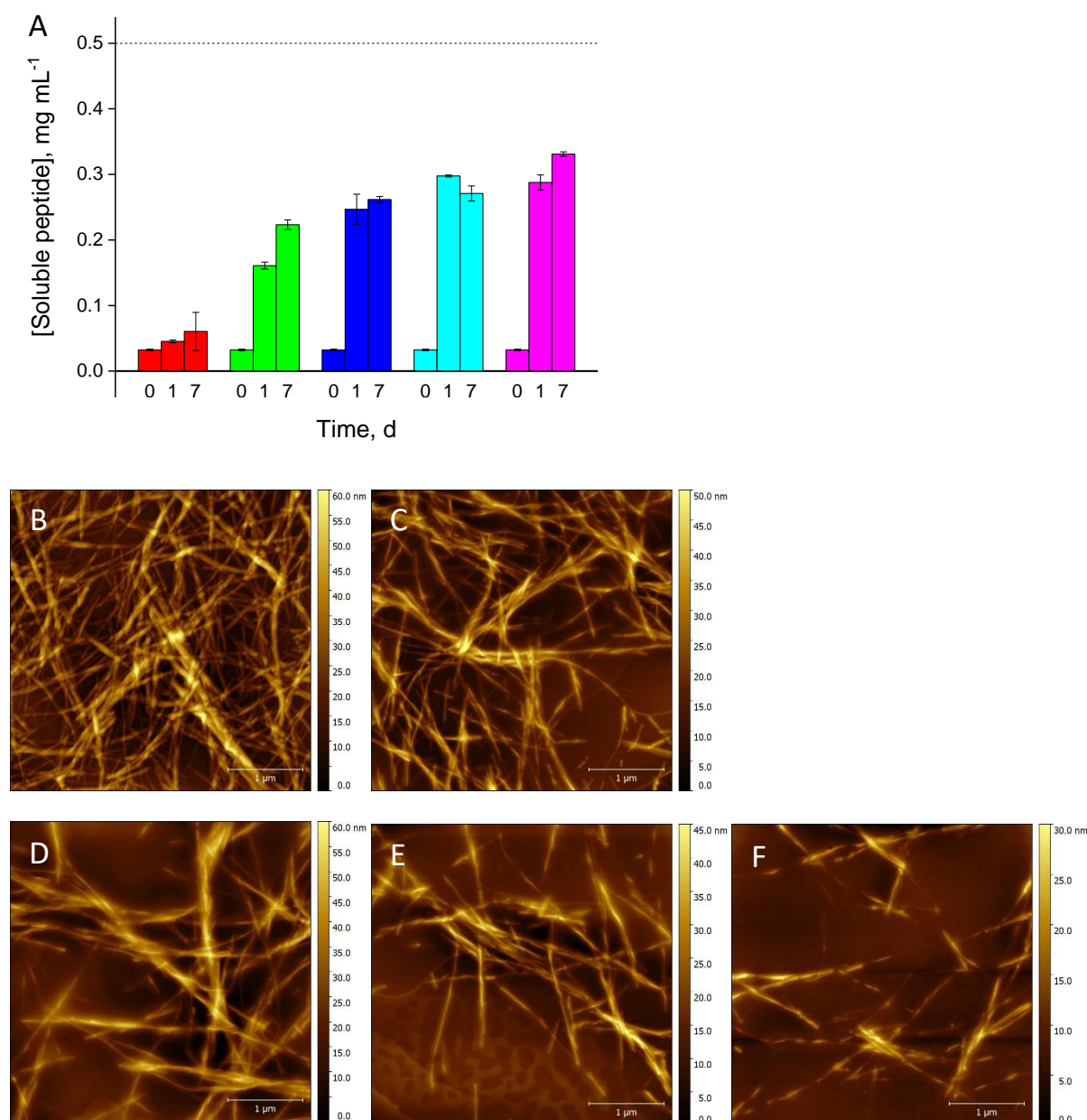
Figure 5-19: Oxyntomodulin fibril dissociation is favoured at increased temperatures

A, Soluble peptide after quiescent incubation of 0.5 mg mL^{-1} essentially salt-free, mature Oxyntomodulin fibrils in water for 1 and 7 days, measured by NanoDrop spectrophotometric absorption at 280 nm, after 30 min sedimentation of fibrils at 13 000 rpm and 50 kDa MWCO filtration of supernatants. Red, 6 °C; green, 25 °C; blue, 32 °C; cyan, 37 °C; purple, 42 °C. Results are presented as averages of independent triplicates ± standard deviation. B-F, AFM imaging after 1 d shows preferential peptide release at increased temperatures, judged by the shortening and number reduction of fibrils and the increasingly blurry appearance of fibrils in enhanced soluble peptide concentrations. B, 6 °C; C, 25°C; D, 32°C; E, 37 °C; F, 42 °C. AFM images were processed in Gwyddion to remove imaging scars and background signal. Resolution: 1024*1024 pixel at 4*4 µm scanning size.
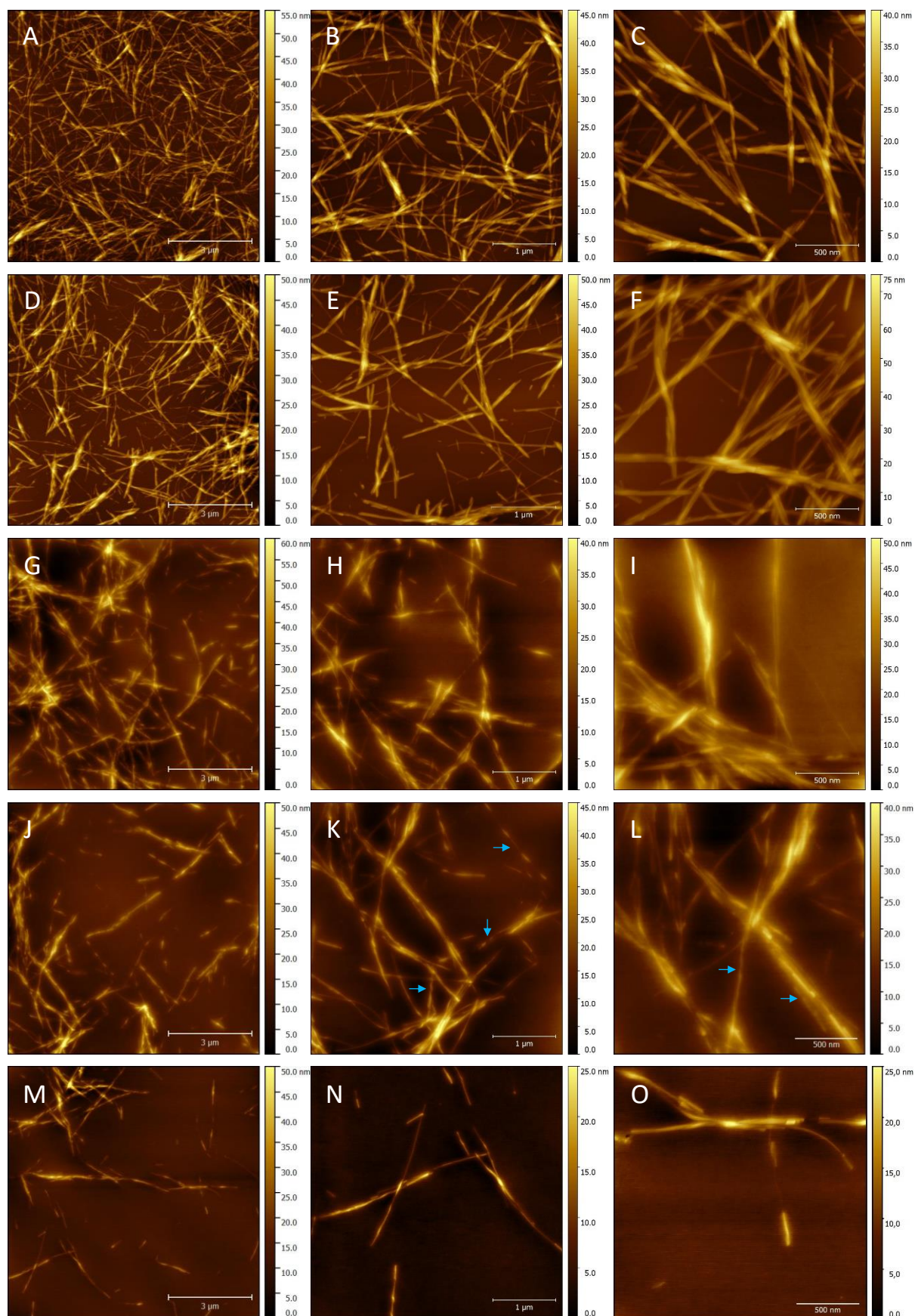
Figure 5-20: Oxyntomodulin fibril reversibility and fibril polymorphism depends on incubation temperature

(continued on following page)

Figure 6-20 (continued): AFM imaging after 7 d incubation of 0.5 mg mL^{-1} essentially salt-free, mature Oxyntomodulin fibrils in water. Incubation temperature A-C, 6 °C; D-F, 25°C; G-I, 32°C; J-L, 37 °C; M-O, 42 °C. Images show preferential peptide release with increasing temperature, judged by the shortening and number reduction of fibrils and the blurry appearance of fibrils in enhanced soluble peptide concentrations. Blue arrows, formation of twisted fibril species at 37 °C. AFM images were processed in Gwyddion to remove imaging scars and background signal. Resolution: A, D, G, J, M, 512*512 pixel at 9*9 µm scanning size; B, E, H, K, N, 1024*1024 pixel at 4*4 µm scanning size; C, F, I, L, O, 1024*1024 pixel at 2*2 µm scanning size.

Importantly, soluble peptide concentration decreased from day 1 to day 7 at 37 °C, along with the appearance of twisted fibrils by day 7. This structural rearrangement is analogous to the formation of an alternative fibril species after several days of ThT- or bulk elongation experiments at similar conditions. At other temperatures, only the straight, partially associated fibril type was seen. As shown in **Figure 6-19** B-F and **Figure 6-20**, the increasing shrinking of fibrils from low to high temperatures could be followed by AFM imaging. Blurring of images implies successive release of soluble peptide without formation of microscopic non-fibrillar aggregates. All fibrils appeared less bundled after incubation in water compared to stocks containing trace amounts of salt, and more single fibrillar structures with the morphology of protofibrils appeared. This supports the theory that mature fibrils are reversible assemblies of protofibrils, and that the electrolytes contained in mature fibril samples – among other effects – shift the equilibrium to the fibril side by enabling thermodynamically favourable lateral association.

To quantify the dissociation rate, ThT kinetics were measured as a function of temperature under conditions where Oxyntomodulin fibrils completely dissolved. Complete dissolution was defined as a condition where the ThT fluorescence after release was not higher than the ThT fluorescence of release in 10 mM HCl after 1 h (not shown). It was found that 0.1 mg mL^{-1} mature fibrils completely dissolved in water within 3 h in a ThT assay. It is noteworthy that ThT is a chloride salt; the assay thus contained 50 µM chloride anions. As shown in **Figure 6-21**, the initial ThT signal at different concentrations was not the same for different temperatures. ThT fluorescence is mildly sensitive to temperature, however the difference seen here is several orders of magnitude higher than differences in ThT sensitivity [132]. Rather, different fluorescence at the beginning of incubation is a result of preparation and measurement of independent dilutions from a concentrated fibril stock. ThT measurements at different temperatures had to be performed at different days because the equipment can only incubate at one temperature. Although care was taken to keep the times between sample preparation and the start of fluorescence reading minimal and constant, it is probable that the first few time points at rapidly dissociating conditions have been missed due to the instrumental lag time before measurement.
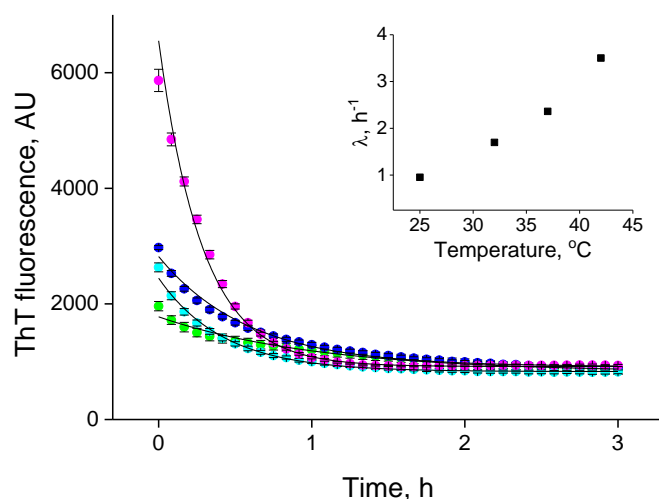
Figure 5-21: Peptide release from Oxyntomodulin fibrils by ThT kinetics

ThT fluorescence during incubation of 0.1 mg mL^{-1} essentially salt-free, mature Oxyntomodulin fibrils in water with 50 µM ThT at different temperatures. Shown are averages ± standard deviations of 6 repetitions per condition. Solid lines, exponential decay functions fitted to the average data points in Origin. Conditions and fitting parameters: green, 25 °C, λ = 0.953 h^{-1}, R^2 = 97.4 %; blue, 32 °C, λ = 1.698 h^{-1}, R^2 = 98.9 %; cyan, 37 °C, λ = 2.362 h^{-1}, R^2 = 99.3 %; purple, 42 °C, λ = 3.502 h^{-1}, R^2 = 98.7 %. Insert, plot of average decay constants derived from each repeat, normalized by the 37 °C decay constant, ± standard deviation.

An exponential decay function was fitted to the average signals to quantify release. The exponential coefficient corresponds to the release constant of the fibril continuum λ (i.e. the time for signal reduction, in h^{-1}) rather than a molecular k_{off} parameter (i.e. the time for release of one ligand from one binding partner, in s^{-1}). The insert in **Figure 6-21** shows the relative dissociation rate defined by the quotient of dissociation constants by the dissociation constant at 37 °C. Dissociation is 1.5 times faster at 42 °C than at 37 °C, while release rate is reduced to 41 % and 72 % at 25 and 32 °C, respectively.

Results and possible explanations of thermal response in Oxyntomodulin structure and Oxyntomodulin fibril elongation and dissociation are summarized in **Figure 6-22**. The unusually low and narrow thermal optimum of Oxyntomodulin fibril elongation has been shown by four orthogonal techniques: QCM-D, monomer depletion in bulk, ThT elongation assay, and ITC heat flux measurement. The optimum is measurable in elongation time frames from minutes to weeks, by bulk- and surface-bound techniques, and by measurements of mass change, concentration change, amyloid-reporter dye binding, and enthalpy measurement. Elongation kinetics, thermodynamic equilibrium and enthalpy loss show comparable thermal responses. It was shown that temperature increase destabilizes the native secondary structure of Oxyntomodulin, but also favors peptide release in undersaturated conditions.
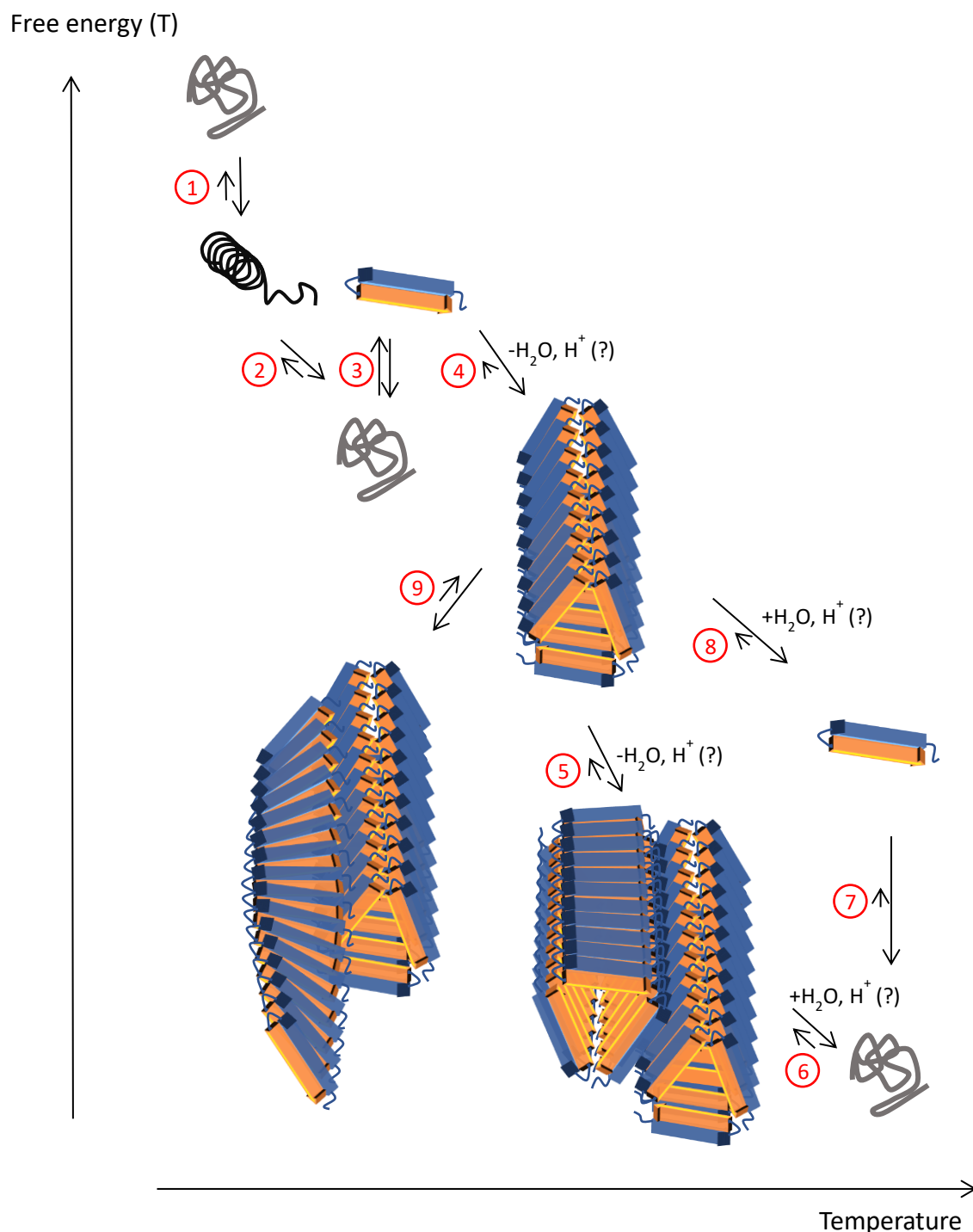
Figure 5-22: Tentative energy landscape of Oxyntomodulin self-assembly

Thermodynamically favoured states depending on temperature; reaction arrow length indicates kinetics and equilibrium. 1, the native helical monomer (black) is the favoured species at low temperatures; 2, heating disfavours the helical state and promotes formation of random species (grey); 3, arch formation (blue and orange) is presumably an energetically unfavourable intermediate step which is kinetically driven by 4, fast conversion to fibrils; 5, further temperature increase promotes enthalpically favourable fibril association; 6, after saturation of enthalpically favourable events, further temperature increase is disadvantageous for the assembled state due to entropic cost, and the system's equilibrium shifts to unordered soluble state; 7 and 8, formation of folded species is generally disfavoured at high temperatures. 9, Polymorphism is presumably favoured after prolonged incubation at step 3.

While no definite explanation can be given for the temperature-dependent kinetics and thermodynamics of Oxyntomodulin self-assembly, a comprehensive model of the free energy landscape can be drawn from structural, kinetic and thermodynamic results. Structural reorganization events shown in *Figure 6-22* are reasoned in the following list:

- Reactions 1 and 2: As shown by CD spectroscopy of soluble Oxyntomodulin, the native helical fold is favored at low temperatures, but destabilized at increasing temperatures.

- Reaction 3: It is assumed that destabilization of the native helix conformation allows the formation of a thermodynamically disfavored (hence not observed) intermediate species that resembles the arch structure of monomers in the fibril. This may not be a soluble species but a structural reorganization catalyzed at the fibril terminus. Possibly, the rate-limiting step is the formation of a turn, as known from beta hairpin formation [135].

- Reaction 4: Above room temperature, fibril elongation is kinetically and thermodynamically favored over monomeric species. Enthalpy measurement by ITC implies that the exclusion of hydrophobic residues from the aquatic environment is a driving factor. Elongation is presumably additionally driven by the entropically favorable exclusion of water [82], as a dry interface was shown by X-ray diffraction and Gibbs' free energy of Oxyntomodulin fibrils cannot be exclusively explained by the measured enthalpic contribution. Elongation is accelerated and thermodynamically more favorable in presence of salts, indicating that electrostatic repulsion is a limiting factor in self-assembly. Partial loss of charges like for Oxyntomodulin's sister peptide Glucagon is a possible further driving factor for self-assembly.

- Reaction 5: Strongly exothermic fibril association has been reported to be preferred at increased temperatures and may contribute to the strongly exothermic fibrillation reaction at 32 °C. Enthalpy loss by close association can be accompanied by entropy loss due to release of surface-bound water molecules. Looser packing can however increase the system's entropy by immobilization of water molecules.

- Reaction 6: After saturation of enthalpically favorable interactions, the entropic cost of temperature increase cannot be counteracted by enthalpy loss. The peptide release reaction is then favored, as shown by ThT and bulk dissociation studies.

- Reactions 7 and 8: Folding is thermally prevented at high temperatures, slowing the elongation reaction. As the dissociation reaction is faster at increased temperatures, a net dissociation of fibrils is observed.

- Reaction 9: Enhanced incubation at semi-stable conditions enables access to alternative minima of the thermodynamic landscape in form of polymorphism. The observed twisted Oxyntomodulin fibrils will be characterized in the following chapter.

6 An alternative Oxyntomodulin fibril structure

In chapter 3.4, it was observed that low seed- and peptide concentration can favor the formation of morphologically different fibrils with a twisted appearance at long incubation times. This species was not seen at high (10 mg mL^{-1}) peptide concentration both in presence or absence of seeds. Twisted fibrils were also observed in chapter 5.5 after extended fibril incubation in ThT- and bulk elongation assays and in a release assay in water. This was seen after several days of incubation in water or 0.9 mg mL^{-1} saline at 37 and 42 °C, but not at or below 32 °C. The appearance of twisted fibrils in addition to originally straight fibrils also shifted the equilibrium to the assembled side. It was suspected that conditions with generally slow kinetics, or extended incubation with low seed amounts allow the formation of an alternative fibril species by secondary nucleation in bulk or on the surface of fibrils. Formation of the twisted species may be kinetically suppressed in conditions with fast elongation rates of the straight fibril type, but twisted fibrils may represent a generally more thermodynamically stable structure. In this chapter, the following questions shall be addressed:

- Under which conditions can the twisted type be produced for analysis?

- Is the fibril type more stable towards disaggregation than the straight type?

- Is the fibril type structurally different from the straight type?

To test the influence of seed concentration on (straight) Oxyntomodulin fibril elongation and formation of polymorphic species, elongation was studied in presence of different seed amounts. Triplicates of 0.5 mg mL^{-1} Oxyntomodulin samples were incubated in polypropylene centrifugation tubes with 0.5, 1.0 and 5.0 % fibril seeds for 7 d. This was performed at 37 °C, in quiescent conditions or with agitation at 300 rpm and 1.9 cm orbit. Analogous samples were incubated at 25 °C as a positive control for the growth competence of seeds. Fibril morphology was assessed by AFM imaging after 7 d, and conversion yield was measured from the peptide concentration in the 50 kDa MWCO filtered supernatant of sedimented samples.

At 25 °C and at 37 °C with shaking, the conversion yield was approximately 97 % after 7 d, and no twisted fibrils were seen in AFM images irrespective of the seed concentration (see **Figure 7-1**). At 37 °C, conversion yield was approximately 60 % for 0.5 and 1 % seeding, and 81 % for 5 % seeding. Polymorphism was observed at 37 °C in quiescent conditions. Twisted fibrils were the predominant species at lower seeding strengths and appeared scattered at 5 % seeding. Similar behavior was observed in a three-day ThT elongation assay at different seed strengths.
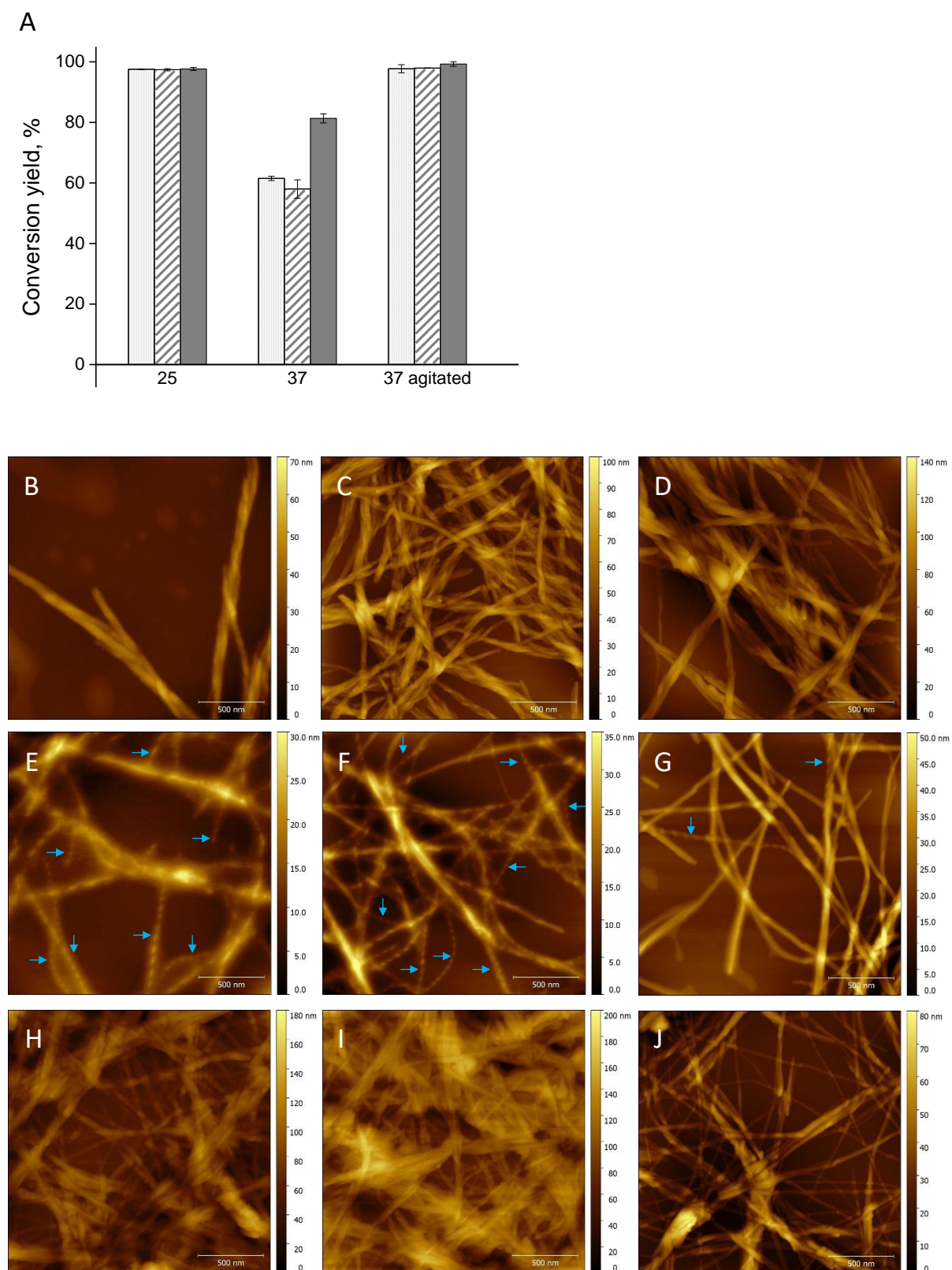
Figure 6-1: Alternative Oxyntomodulin fibril formation is preferred at slow elongation conditions

(details see next page)

(continued from *Figure 6-1*) Oxyntomodulin seed elongation at different conditions with increasing seeding strength. Seeds were derived from 15 min sonication of a mature Oxyntomodulin fibril stock. A, conversion yields of $0.5\,\text{mg mL}^{-1}$ initial soluble Oxyntomodulin in $0.9\,\text{mg mL}^{-1}$ saline after 7 d incubation with seeds at 25 °C, 37 °C, and 37 °C with 200 rpm shaking. Dotted, 0.5 % seeding strength; striped, 1% seeding strength; solid, 5 % seeding strength. B-J, Representative AFM images after 7 d incubation. B-D, 25 °C; E-G, 37 °C, H-J, 37 °C 200 rpm. B, E, H, 0.5 % seeding; D, F, I, 1 % seeding; C, G, J, 5 % seeding. Blue arrows, twisted fibrils. AFM images were processed in Gwyddion to remove imaging scars and background signal. Resolution: 1024*1024 pixel at 2*2 μm scanning size.

To analyze the structure of twisted fibrils, parameters for exclusive growth of the twisted species had to be found. Despite extensive screening, no condition without co-occurrence of the straight species was found. Therefore, the twisted type was selected for by repetitive seeding: A first generation of fibrils was grown from seeding 0.5 or 1 mg mL^{-1} Oxyntomodulin aliquots with 0.5 or 1 % seeds derived from 15 min sonication of (straight) mature Oxyntomodulin fibrils. The sample containing the highest prevalence of twisted species after two weeks was a 1 mg mL^{-1} aliquot with 0.5 % seeds. This sample was used to seed freshly prepared Oxyntomodulin solutions at the same conditions. After two further analogous rounds of seeding, elongation and selection, more than 80 % twisted fibrils were found by AFM imaging in one sample (see **Figure 7-2**). The conversion yield was 50 %. Fibrils could not be separated from soluble peptide because pellets after centrifugation did not resuspend readily. The third-generation sample was used for Cryo electron microscopy, FTIR, CD, ThT and Tryptophan fluorescence, and for seeding further generations. After three more generations, a similar sample was chosen for a release experiment in salt-free conditions. Generally, high contents of twisted fibrils were not found reproducibly. Even after six generations, most seeded samples contained predominantly straight fibrils, and only single samples inherited the twisted morphology. Mixed fibril samples did not convert to either type of fibrils within several months of incubation.

As shown in **Figure 7-2**, twisted species adopted at least two morphologies. One type was tightly twisted with inter-twist differences (pitch) of approximately 55 nm and height differences of ~1.2 nm along the fibril length. The other type had a wider twist with approximately 80 nm pitch and ~2.5 nm height difference.

Twisted fibrils were analyzed by CD, FTIR, ThT- and Tryptophan fluorescence analogous to mature fibrils and protofibrils. Results are summarized in **Figure 7-3**. As raw spectra were an overlay of 50 % fibrils and 50 % nonfibrillar peptide in the samples, background-corrected spectra corresponding to half the total peptide concentration were deducted from background-corrected raw spectra of twisted fibrils. Resulting spectra were doubled before analysis to reflect the same fibril amount as free peptide and protofibrils. Error bars therefore contain uncertainty of fibril- and free peptide measurement. Potential differences in the signals of
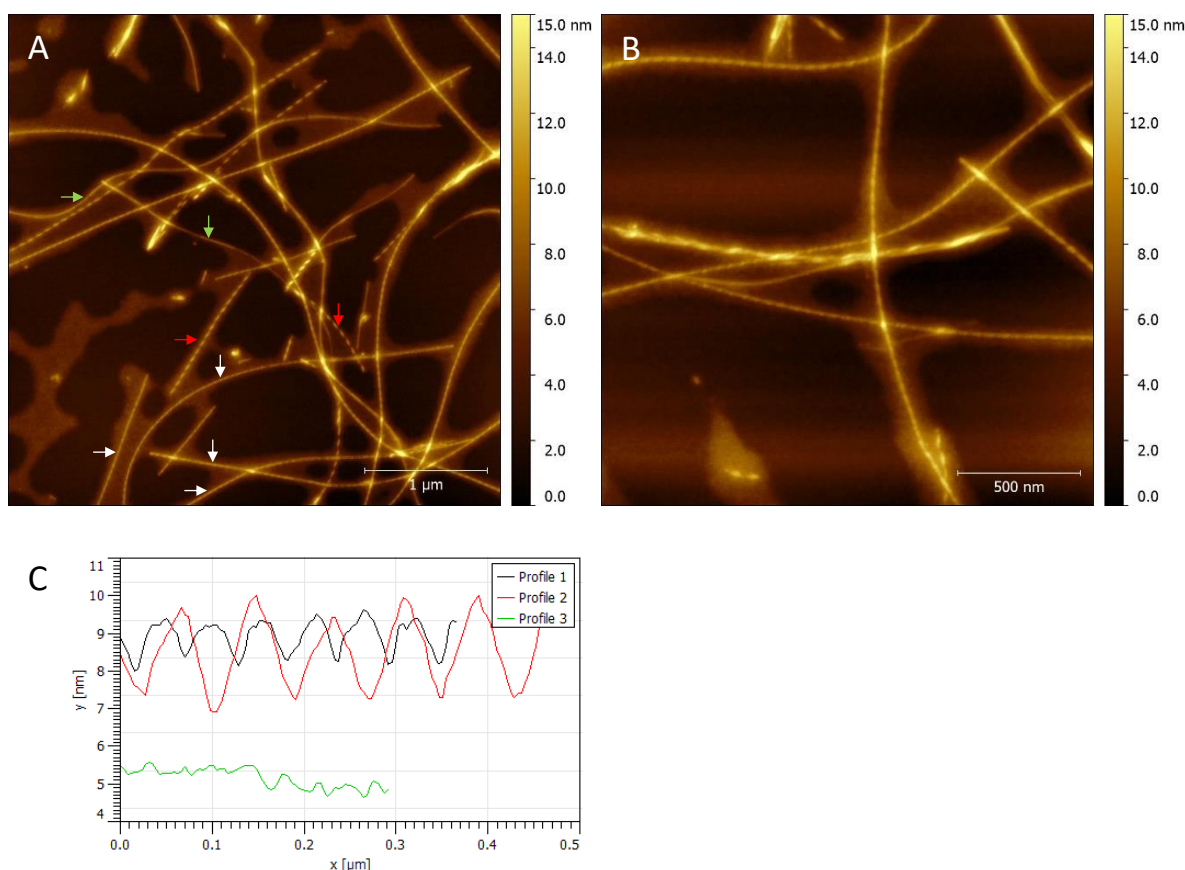
Figure 6-2: AFM images of Oxyntomodulin fibrils after repeated seeding and selection for twisted species

Fibrils after 3 generations of seeding 1 mg mL^{-1} Oxyntomodulin in 0.9 mg mL^{-1} saline with 0.5 % seeds at 37 °C and selection for the sample with the highest twisted fibril occurrence for further seeding. White arrows, tight twisting; red arrows, less tight twisting; green arrows, straight fibril type. AFM images were processed in Gwyddion to remove imaging scars and background signal. Resolution: 1024*1024 pixel at 4*4 µm (A) and 2*2 µm (B) scanning size. C, height profiles along fibrils marked in A; tightly twisted fibrils have a pitch of 55 nm and height difference of 1.2 nm along the fibril; less tightly twisted fibrils have a pitch of 80 nm and height difference of 2.5 nm along the fibril.

freshly dissolved peptide and soluble peptide in twisted fibril samples (e.g. oligomerization) could not be reflected due to limitations in fibril amounts. Therefore, results presented here can only be seen as an estimation of fibril structure.

Structural determination by ThT- and Tryptophan fluorescence revealed an amyloid-specific ThT fluorescence increase and Tryptophan fluorescence blue shift comparable to mature Oxyntomodulin fibrils. Decreased blue-shift and signal broadening in Tryptophan fluorescence implies a higher degree of polymorphism in the twisted fibril sample. Quantification of secondary structure elements by CD does not reveal a significant difference of straight and twisted fibrils. FTIR signals were generally higher for twisted fibrils, but the peak locations were not distinguishable from signals of mature Oxyntomodulin fibrils.
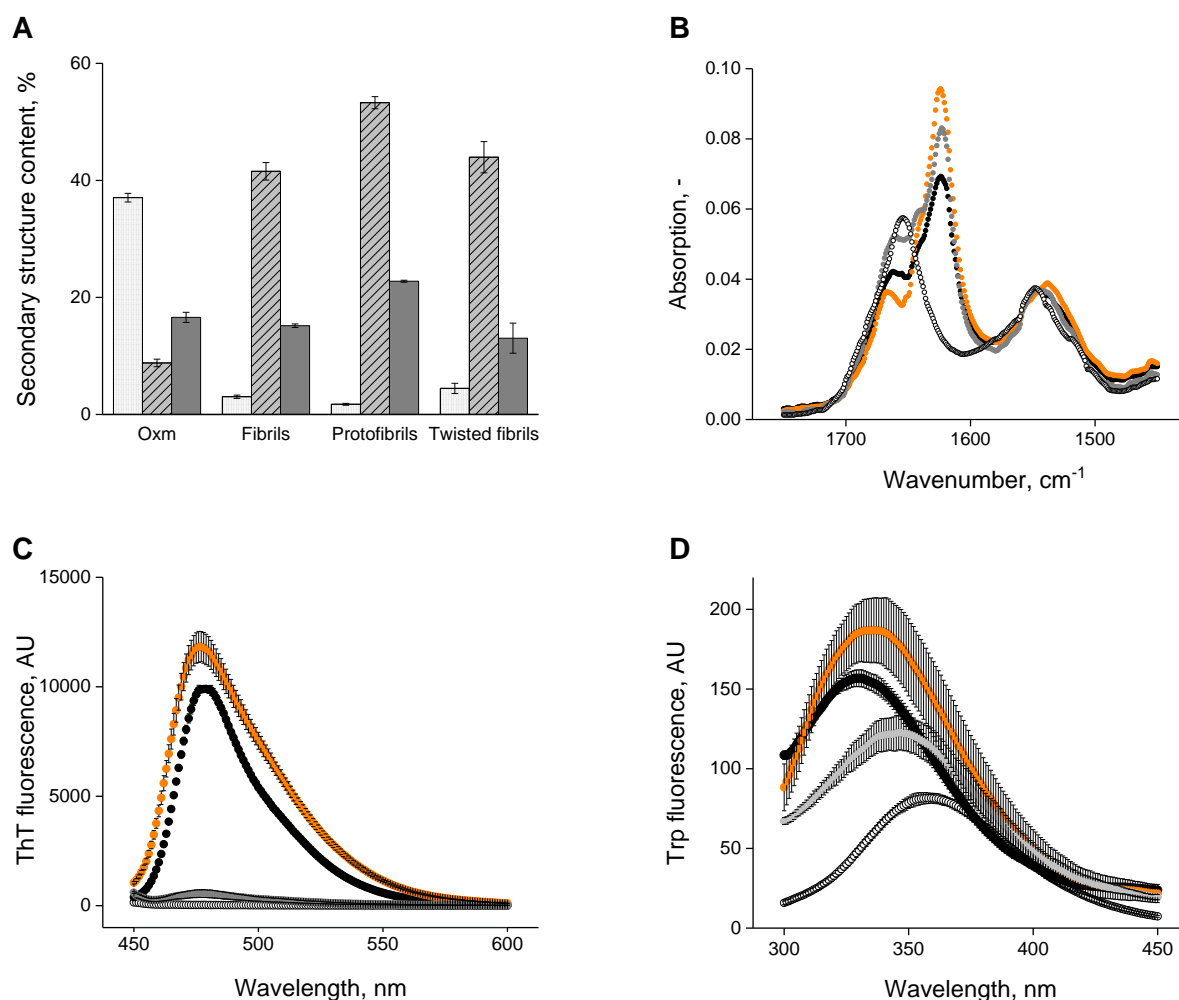
Figure 6-3: Biophysical characterization of twisted fibrils

Comparison of A, Circular dichroism spectroscopy; B, FTIR spectroscopy; C, ThT end-point fluorescence; D, intrinsic Tryptophan fluorescence of soluble peptide (open circles), protofibrils (light grey), mature fibrils (black) and twisted fibrils (orange). All data are presented as averages of triplicate measurements ± standard deviation. Data were acquired and analysed analogous to description in 4.1 and 4.2. Twisted fibril signals were corrected for 50 % free peptide.

As twisted fibrils only appeared under unfavorable conditions for the elongation of straight fibrils, it is obvious to assume that twisted fibrils populate an alternative minimum of the free energy. Absence of changes in morphology over enhanced incubation periods indicate that the twisted species is not an on-pathway intermediate structure for formation of straight fibrils. The reorganization of straight fibrils to twisted fibrils after partial fibril dissolution implies that twisted fibrils form from – or catalyzed by – straight fibrils. Fibril species are consequently separated by high energy barriers that prevent rearrangement to the more thermodynamically stable species. It is however not known which species populates the lower accessible free energy minimum.
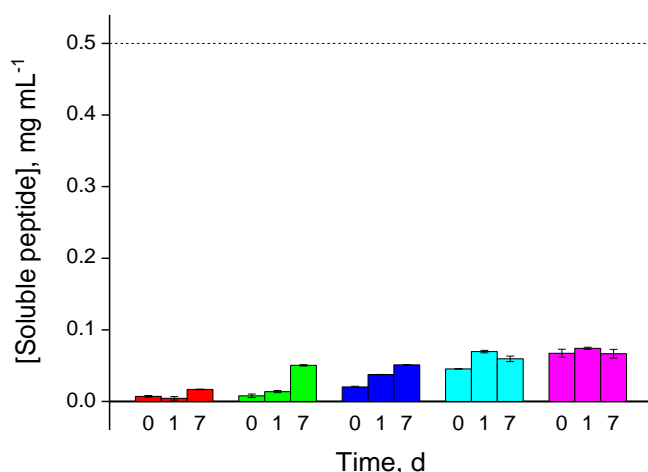
Figure 6-4: Twisted fibrils are more thermodynamically stable than straight fibrils

Soluble peptide concentration after quiescent incubation of 0.5 mg mL^{-1} essentially salt-free, twisted Oxyntomodulin fibrils in water for 1 h (0 days), 1 and 7 days, measured by NanoDrop spectrophotometric absorption at 280 nm, after 30 min sedimentation of fibrils at 13 000 rpm and 50 kDa MWCO filtration of supernatants. Red, 6 °C; green, 25 °C; blue, 32 °C; cyan, 37 °C; purple, 42 °C. Results are presented as averages of independent triplicates ± standard deviation.

The dissolution and equilibrium concentration of twisted fibrils was assessed in salt-free conditions and at different temperatures. Before incubation, twisted fibrils were separated from soluble species and salt by centrifugation, and the pellet was re-dispersed in water and pelleted again. Fibril concentration was assessed photometrically after dissolution in 10 mM HCl, and aliquots were incubated in water at 0.5 mg mL^{-1} initial fibril concentration. Soluble peptide concentrations were measured after 1 h, 1 d and 7 d.

As shown in **Figure 7-4**, the twisted fibrils sample generally dissolved more with increasing temperature, but release was substantially lower than in straight fibril samples (compared to **Figure 6-19**). Considering the presence of some straight fibrils in the twisted fibril sample, it is possible that the majority of released peptide stems from straight fibrils, and the thermodynamic equilibrium of soluble and twisted fibrils is far on the fibrillar side. This is not in contrast to the 50 % elongation yield measured above, as elongation may be hindered sterically or by formation of growth-incompetent, submicroscopic oligomers.

Twisted fibrils were imaged by Cryo EM to gain insights into the structural differences to the straight species. Cryo EM confirmed that twisted fibril samples contained several different species, with a minority of straight fibrils and laminated twisted sheets and at least two types of helically twisted fibrils.
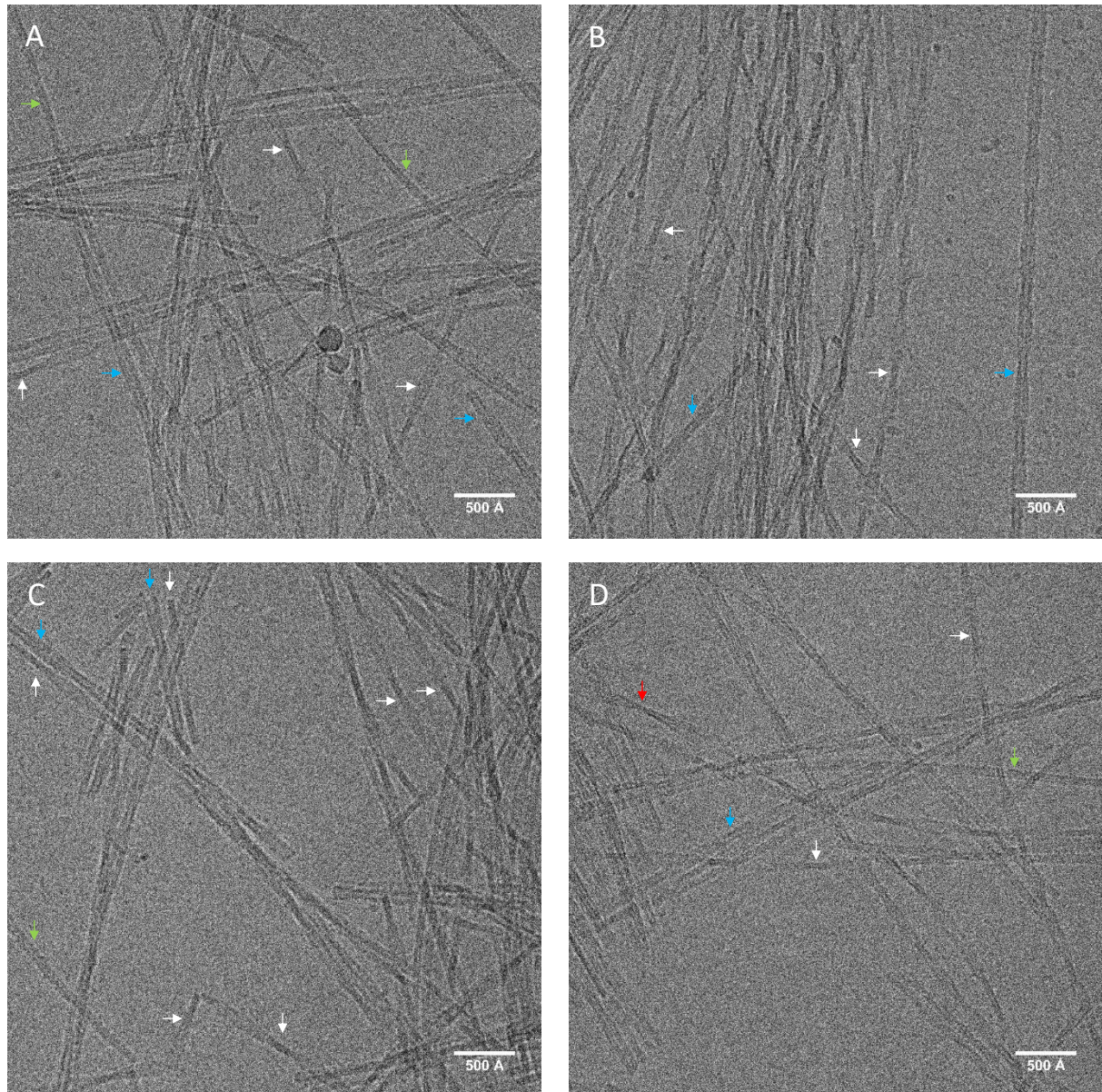
Figure 6-5: Overview of polymorphic structures in a twisted fibril sample

Cryo electron micrographs of the same sample as imaged by AFM in *Figure 6-2*. Images are taken on a Titan Krios™ G3i with a Falcon 3 detector with motion correction. Whole images were corrected for brightness and contrast in Fiji. Scale bars, 500 Å. Green arrows: there are few straight fibrils corresponding to the protofibrils shown in *Figure 4-7*. Red arrow: very few fibrils have several laterally aligned sub-fibrils that form a twisted sheet. White arrows: obviously helically twisted fibril type with two sub-fibrils (type 1). Blue arrows, seemingly parallelly twisting pairs of fibrils (type 2). Note that fragmented fibrils in image C maintain the twist, that the distance between fibril ends and cross-over points is random, and that fibrils do not contain overhanging fibril ends.

The few straight fibrils were indistinguishable from protofibrils described in chapter 4.4, and the very rarely occurring twisted sheet type correspond to laterally aligned protofibrils that occasionally occurred in protofibril and mature fibril samples. Both twisted types were approximately equally populated. The formation of twisted sheets implies that the alignment of individual peptides differs from the triangular alignment in protofibrils and fibrils, however a potential parallel alignment could not be formally proved. All fibril types had a 4.6-4.7 Å diffraction pattern. In some cases, the inter-strand spacing was directly visible from magnified images.

The twisted fibril type with the longer pitch-to-pitch distance was called type A, and the type with the shorter distance type B. For comparison, both are shown in **Figure 7-6**. Type A had an obviously helical morphology with two thin sheets twisting around a common axis. Type B intuitively appeared as two thin sheets twisting next to each other but around separate axes. This will be discussed later. Measurement of critical distances in 150 type A and B fibrils revealed a clear difference in distances between the thin areas of high electron density. The distance was 794±74 Å in type A (n=94), and 664±57 Å in type B (n=56). The widths at the same locations differed with 50±7 and 80±12 Å for type A and B, respectively. Between the high-density areas, widths were indistinguishable with 124±13 and 126±8 Å, respectively. Fibril ends were randomly located in respect to high density areas. In none of over 180 images, fibrils with overhanging ends of more than a few nanometers were found. As shown in **Figure 7-5** C and **Figure 7-6** B, the twists were conserved in short fragments of fibrils.
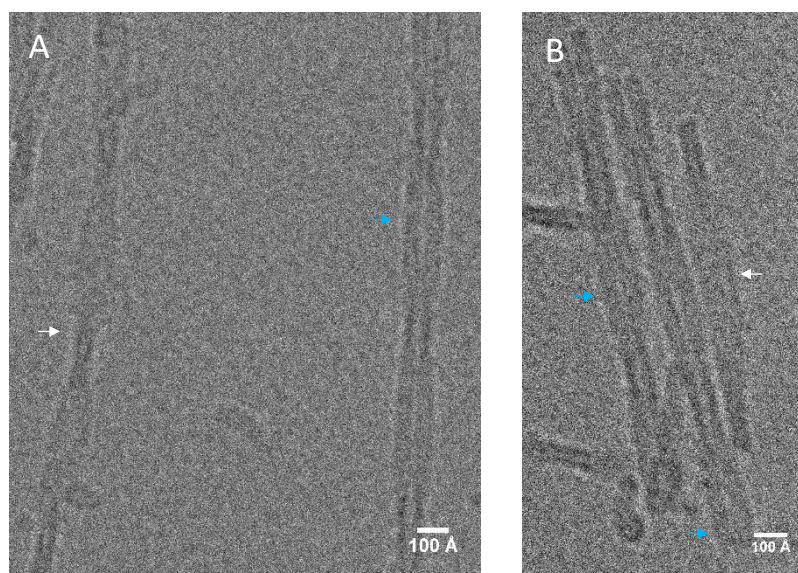
Figure 6-6: Comparison of the two predominant fibril types in twisted fibril samples

Cryo electron micrographs of the same sample as imaged by AFM in *Figure 6-2*. Images are taken on a Titan Krios[TM] G3i with a Falcon 3 detector with motion correction. Whole images were corrected for brightness and contrast in Fiji. Scale bars, 500 Å. White, type 1 fibrils; blue, type 2 fibrils. Note the different widths and distances between high density areas of type 1 and 2 fibrils.
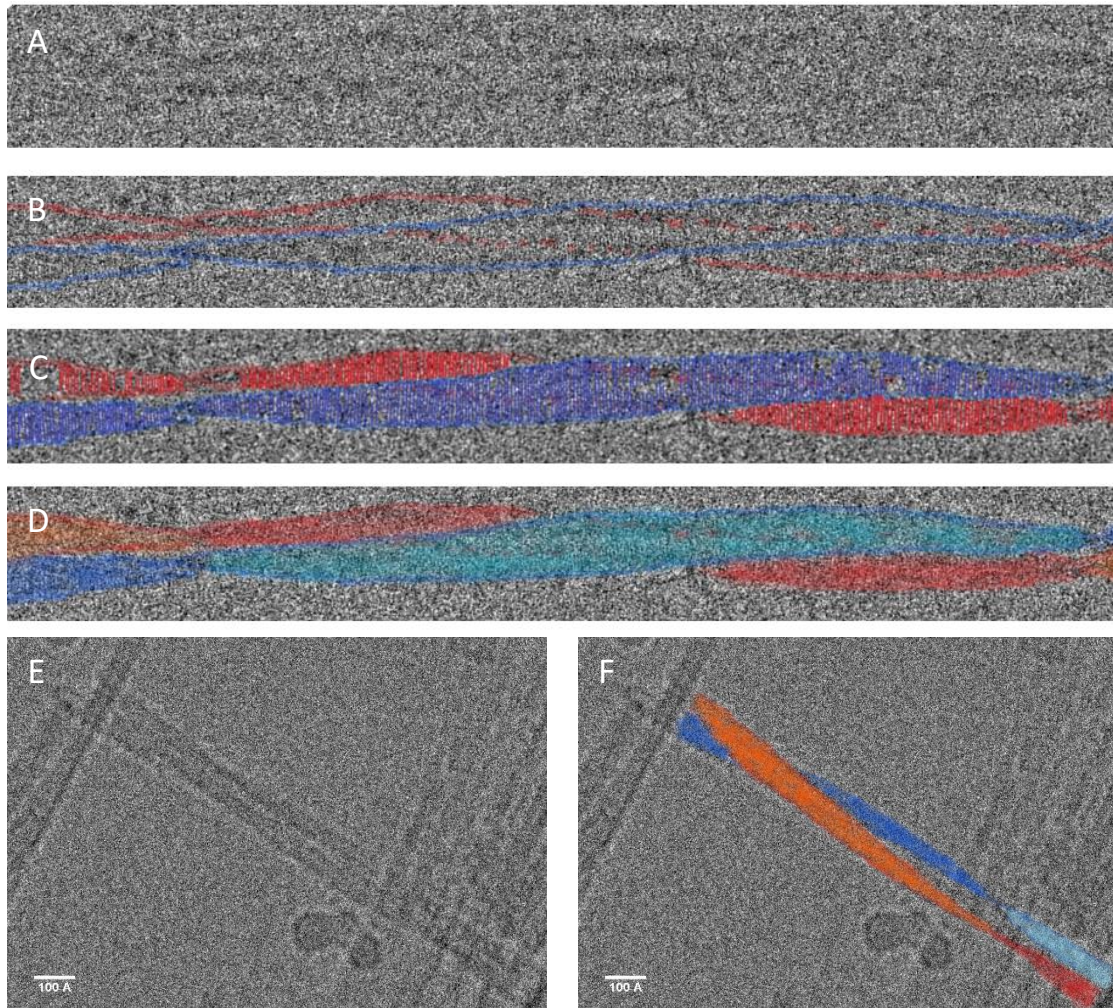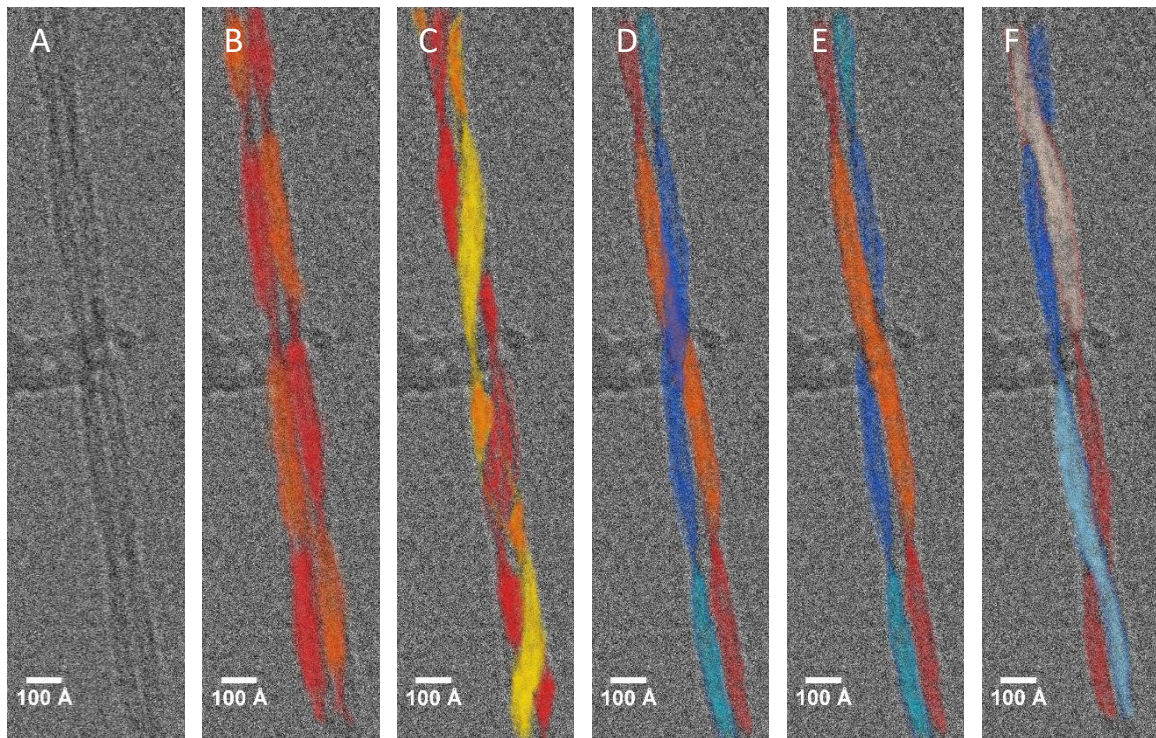
Figure 6-7: Tentative structure of type A twisted fibrils reconstructed from Cryo EM

Cryo electron micrographs of the same sample as imaged by AFM in *Figure 6-2*. Images are taken on a Titan Krios™ G3i with a Falcon 3 detector with motion correction. Whole images were corrected for brightness and contrast in Fiji. Visualization of patterns performed in Microsoft Paint. A, Cryo EM image of a type 1 fibril, image height 160 Å; B, highlighting of areas of high electron density that imply sheet edges, sheet overlaps, and sheet side-views; C, highlighting of the visible 4.7 Å striation pattern; D, double helical fibril model with inner sheet faces drawn in red and dark blue, outer sheet faces drawn in orange and light blue. E, F: Similar reconstruction in a fibril without visible diffraction pattern and a morphology more similar to type 2. There is less certainty in the dimensions of the sheets due to an offset of pitches in opposing sheets.

Closer examination of the density patterns in type A fibrils revealed that the most consistent structural model is a double helix consisting of two sheets that are approximately two protofibril distances (or two half peptide lengths) wide. As shown in **Figure 7-7** A-D, a fibril structure could be reconstructed from electron dense areas indicating sheet edges, cross-over points and side views of sheets, and the striations from the 4.7 Å inter-strand spaces. In the double helical model, two sheets face each other and twist around a common axis. The electron dense, narrower "pitches" alternated slightly in their appearance and in the grey scale

in the electron lucent space between the highest densities. This further implies a double helical twist where one high density area corresponds to the crossing-over of sheets, and the next high-density area shows sheets sideways separated by an electron lucent area. The "pitches" then correspond to a 90 ° turn of the fibril. A similar structure was reported in [176]. As shown in *Figure 7-7* E and F, classification is not unambiguous. The fibril highlighted clearly has a double helical structure, but sheets are more separated than in the fibril shown above. This indicates that several alignments are possible.

A double helical structure contradicts the height patterns observed in AFM. According to AFM, every ~800 Å spaced "pitch" corresponds to a 180 ° turn due to height differences, and the only structure consistent with this pitch would be a double-pleated sheet twisting around its centre. An aligned double-pleated sheet would explain strong diffraction patterns in some type 1 fibrils due to reinforcement by several peptide layers. However, the density patterns in Cryo EM images are not consistent with this structure: there are theoretically dense areas missing in Cryo EM images if a double-pleated sheet is assumed, and additional dense structures seen that are not explained by a double-pleated sheet. As only type 1 "pitch" matches in Cryo EM and AFM, and the type 2 pitch is different, it is probable that the observed pitch differs in flash-frozen and dried samples. The Cryo EM images taken here were not numerous enough to enable computational helical reconstruction of the different fibril classes.

Type B fibrils intuitively seem to twist parallel to each other and interact in a side-by-side manner. While this structure is the visually most obvious possibility, no physicochemical explanation for this behaviour could be found. If there were an attractive force leading to the side-by-side alignment of twisted fibrils, there would be occasional fibril splitting and merging visible in the case of a weak interaction, and raft-like alignments of more than two (proto)fibrils in the case of a strong interaction. No such structures were seen in 180 images with approximately 10 type B fibrils per image. Moreover, the absence of overhanging fibril ends strongly implies that elongation occurs parallel or alternating on each sheet, but not independent from each other as in a fibril with longer-range interactions to another fibril. Therefore, a fibril as sketched in **Figure 7-8** B lacks a physical explanation. A densely twisted structure as shown in **Figure 7-8** C is more consistent with pitches seen by AFM, but not consistent with the density patterns seen in Cryo EM. Moreover, such a structure would require a more tilted angle of cross-beta patterns that was not observed in images. From density patterns and dimensions of spaces between the denser areas, it is probable that type B also represents a double helical structure. Where and how exactly sheets cross over each other cannot be reconstructed from transmission Cryo EM images, as depicted in **Figure 7-8** C-E.

Figure 6-8: Tentative structure of a type 2 twisted fibril by Cryo EM

Cryo electron micrographs of the same sample as imaged by AFM in *Figure 6-2*. Images are taken on a Titan Krios™ G3i with a Falcon 3 detector with motion correction. Whole images were corrected for brightness and contrast in Fiji. Visualization of patterns performed in Microsoft Paint; lighter areas face the observer; darker areas face the inside of a fibril. A, Cryo EM image of a type 2 fibril; B, visually tentative but not physicochemically explicable side-by-side alignment of twisted sheets; C, double helical model with every electron dense area corresponding to a side view of sheets. This model is not consistent with observed electron density patterns. D, E, F: double helical structures consistent with all features seen by Cryo EM. Handedness (D, E) and the location of cross-over (F) are not distinguishable.

In summary, there is evidence that twisted Oxyntomodulin fibril species represent an alternative thermodynamic minimum to the straight fibril species. Due to the comparably slow nucleation and elongation of twisted species but high stability under diluted conditions, it is probable that the twisted species represents a deeper minimum on the thermodynamic landscape. The fast-forming straight species is presumably a metastable kinetic trap with a high thermodynamic barrier to formation of the more stable, twisted species. A comparably low stability of straight fibrils also explains the reversibility of straight species upon dilution or incubation at physiological conditions. Twisted fibrils only form in conditions that destabilize straight species and cause co-incubation of peptide and fibrils for several days. It is not sure if such conditions could occur *in vivo*. Subcutaneously applied concentrations of straight fibrils are several times higher than the concentrations where twisted fibrils occur, and released peptide is likely to be removed from the fibril depot by the flow of interstitial fluid. However, straight fibrils have been found to be destabilized by phosphates and at

physiological temperatures, and it is not sure how fast released peptide is removed from the fibrils *in vivo*. Because formation of insoluble species *in vivo* is not desired for pharmacokinetics, and can potentially cause toxic or immunogenic side-effects, the long-term morphology of fibrils should be tested *in vivo* or in a biomimetic perfusion model. Interestingly, glucagon shows a very similar condition-dependent polymorphism. A twisted morphology was reported at low peptide concentrations and could only be inherited in seeding experiments at low concentrations. At high concentrations, a straight fibril type prevailed and was conserved in seeded daughter generations [94][111].

Evidence of twisted sheets in twisted Oxyntomodulin fibrils further implies that the peptide alignment in twisted fibrils is markedly different to straight fibrils. As no difference in fluorescence or spectroscopic measurements was seen, the different morphology and stability is most certainly caused by the alignment of peptide monomers to each other, rather than the conformation of monomers. Possibly, but admittedly speculative, monomers in twisted sheets are aligned parallel to each other rather than in a triangular shape. Surface catalysis of twisted-type nucleation is consistent with the frequent observation of twisted fibril nucleation in presence of straight fibrils, as sketched in **Figure 6-22**. Results from Cryo EM strongly indicate an overall double helical morphology of fibrils, but the exact alignment of sheets and monomers within sheets could not be determined from the Cryo EM data. According to FEI technicians, high-resolution helical reconstruction of both identified helical fibril classes may be possible with a substantially higher number of images and fibril type classification according to pitch-to-pitch distances.

7 Cross-seeding of Oxyntomodulin and -fibrils

One concern for the *in vivo* use of Oxyntomodulin fibrils was if they can serve as a template for fibril formation by other peptides. Subcutaneous tissue is deprived of peptides and proteins, and fibril interaction with cells is limited to cell membrane molecules or – in the case of occasional cellular fibril fragment uptake – sequestered inside phagosomes and thus separated from the intracellular environment. However, it is possible that fibrils reach the bloodstream after an injury. Due to glucagon's sequence similarity to Oxyntomodulin, prevalence in the bloodstream, and known ability to form fibrils in a range of conditions, it was important to test if glucagon can be seeded by Oxyntomodulin fibrils.

QCM-D fibril elongation assays were performed with Oxyntomodulin fibril seeds on the sensor surface and Glucagon in the peptide stream. Glucagon was dissolved at an approximate concentration of $10\,\text{mg}\,\text{mL}^{-1}$ in 10 mM HCl, filtered with a $0.22\,\mu\text{m}$ centrifuge filter to remove potential aggregates, and pH-neutralized with 10 mM NaOH. The concentration was measured photometrically by NanoDrop with a theoretical 1 % extinction coefficient of glucagon, as computed using the online ProtParam tool of Expasy. Glucagon was then diluted to $0.5\,\text{mg}\,\text{mL}^{-1}$ in $0.9\,\text{mg}\,\text{mL}^{-1}$ saline and used within one hour to prevent spontaneous aggregation in bulk.

QCM-D sensors with or without Oxyntomodulin fibril seeds were prepared and thermally equilibrated as described in 5.1.2. Glucagon was flown over an empty chip as a negative control, and Oxyntomodulin was flown over Oxyntomodulin seeds as a positive control. Glucagon was incubated with Oxyntomodulin seeds to test the cross-seeding ability of Oxyntomodulin fibrils.

Glucagon's adsorption to an empty sensor was slower than for Oxyntomodulin. As described in chapter 5.2, Oxyntomodulin adsorption was complete after two minutes before a constant frequency slope of -0.11 Hz min^{-1} was reached. Glucagon adsorption went on for three more minutes before adopting a comparable approximately linear frequency change with a slope of -0.10 Hz min^{-1}. On sensors with Oxyntomodulin fibrils and soluble Glucagon, even less overall frequency change was measured, indicating that glucagon does not or only minorly bind to fibrils, but to the sensor surface between fibrils. No fibril elongation was seen by AFM after cross-seeding of Oxyntomodulin fibrils with glucagon. Results are shown in **Figure 8-1**. If Oxyntomodulin was flushed over QCM-D chips after incubation of Oxyntomodulin fibrils with glucagon, approximately half of the frequency change and elongation than without previous glucagon application was found compared to direct application of Oxyntomodulin on Oxyntomodulin fibrils. Therefore, the peptide layer formed by glucagon reduced the growth competence of Oxyntomodulin fibrils (results not shown).
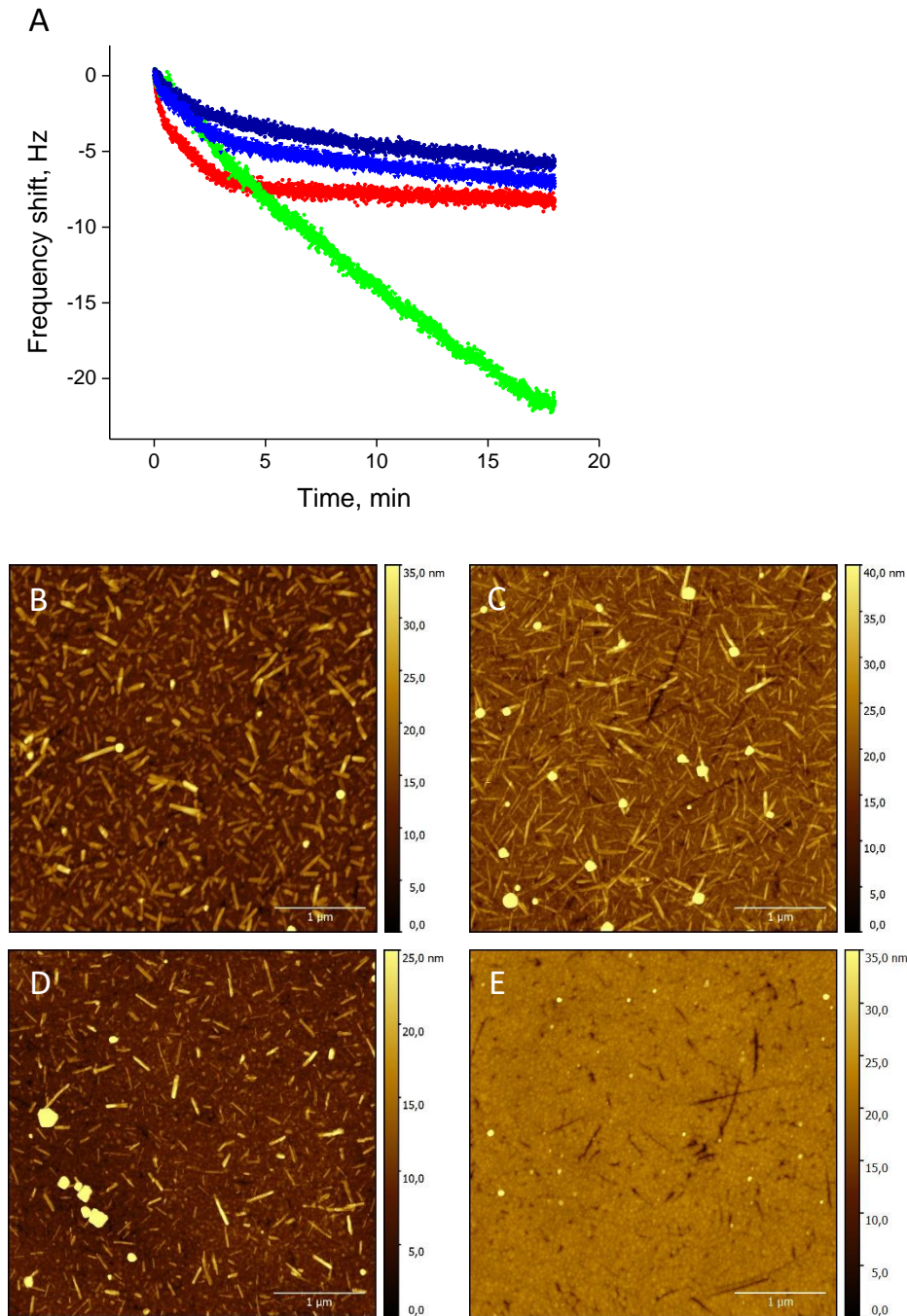
Figure 7-1: Oxyntomodulin fibrils do not elongate in presence of Glucagon

QCM-D fibril elongation assay with Oxyntomodulin seeds in presence of Oxyntomodulin and Glucagon. Both hormones were applied at 0.5 mg mL^{-1} at pH 6.5 in 0.9 mg mL^{-1} saline and at 37 °C. A, QCM-D frequency shifts from 2-18 min after start of peptide flushing; green, Oxyntomodulin fibril seeds incubated with Oxyntomodulin (positive control); navy and royal blue, glucagon incubated with Oxyntomodulin seeds; red, glucagon incubated with a fibril-free sensor (negative control). B, sensor with Oxyntomodulin fibril seeds before incubation; C, positive control after experiment; D, sensor after Oxyntomodulin fibril incubation with glucagon; E, negative control after experiment. AFM images were processed in Gwyddion to remove imaging scars and background signal. Resolution: 1024*1024 pixel at 4*4 µm size.

Self-assembly of the Oxyntomodulin analogue Aib-2-Oxyntomodulin was investigated by postdoctoral researcher Myriam Ouberaï parallel to the Oxyntomodulin fibril project described in this thesis. Aib-2-Oxyntomodulin has reduced affinity to GCGR and enhanced affinity to GLP-1R compared to human Oxyntomodulin, making it a potential drug candidate with higher expected activity in blood sugar regulation, but less activity in regulation of appetite and energy expenditure. Due to substitution of serine in position 2 with the non-coding amino acid aminoisobutyric acid (Aib), Aib-2-Oxyntomodulin is not degraded by the enzyme DPP4 in the bloodstream. Aib-2-Oxyntomodulin was found to self-assemble in similar conditions as Oxyntomodulin, however fibrillation was generally slower and fibrils dissolved more readily. Fibrils were formed using the three-step method described in 3.4, with a 1.8 mg mL^{-1} saline instead of a 0.9 mg mL^{-1} in salt-containing conditions, and an incubation temperature of 25 °C instead of 37 °C. Fibrils were provided by Myriam Ouberaï.

Sonicated Oxyntomodulin- and Aib-2-Oxyntomodulin fibril seeds were adsorbed on SiO$_2$ QCM-D sensors and thermally equilibrated as described in chapter 5.1.2. Oxyntomodulin or Aib-2-Oxyntomodulin in 0.9 mg mL^{-1} saline were flown over the sensor surface. All experiments were carried out at 25 °C at a flow rate of 0.1 mg mL^{-1}. Incubation of Oxyntomodulin fibril seeds with 0.5 mg mL^{-1} Oxyntomodulin caused a frequency slope of -1.19 Hz min^{-1}. Equivalent conditions with Aib-2-Oxyntomodulin and Aib-2-Oxyntomodulin fibril seeds did not cause a frequency decrease distinguishable from the slope of peptide adsorption to an empty sensor. Upon increase of the soluble peptide concentration to 2 mg mL^{-1}, a frequency slope of -1.09 Hz min^{-1} indicated moderate elongation, and elongation was visible by AFM imaging. Oxyntomodulin fibril elongation at 2 mg mL^{-1} caused frequency shifts as high as -4.97 Hz min^{-1} and drastic elongation visible by AFM imaging.

AFM furthermore showed that sonicated Aib-2-Oxyntomodulin fibril seeds were more numerous than Oxyntomodulin fibril seeds on QCM-D sensors. Therefore, the measured four- to five-fold difference in elongation rate is an overestimation of Aib-2-Oxyntomodulin fibril seeds elongation rate.

Figure 8-2 shows triplicate measurements of fibril incubation with the respective peptide at 2 mg mL^{-1} peptide concentration. **Figure 8-2** B demonstrates incubation of Oxyntomodulin fibrils with 0.5 mg mL^{-1} for comparison; a control experiment for peptide adsorption on an empty sensor; incubation of Aib-2-Oxyntomodulin fibril seeds in a stream of 0.9 mg mL^{-1} saline; and cross-seeding of Aib-2-Oxyntomodulin fibril seeds with 0.5 mg mL^{-1} soluble Oxyntomodulin. Cross-seeding caused only marginally higher frequency shifts than control experiments, and no elongation was measured by AFM imaging. While minor cross-seeding is possible, it is probable that the increased surface area on seed-containing QCM-D sensors caused slightly higher peptide adsorption and/or water immobilization during adsorption.
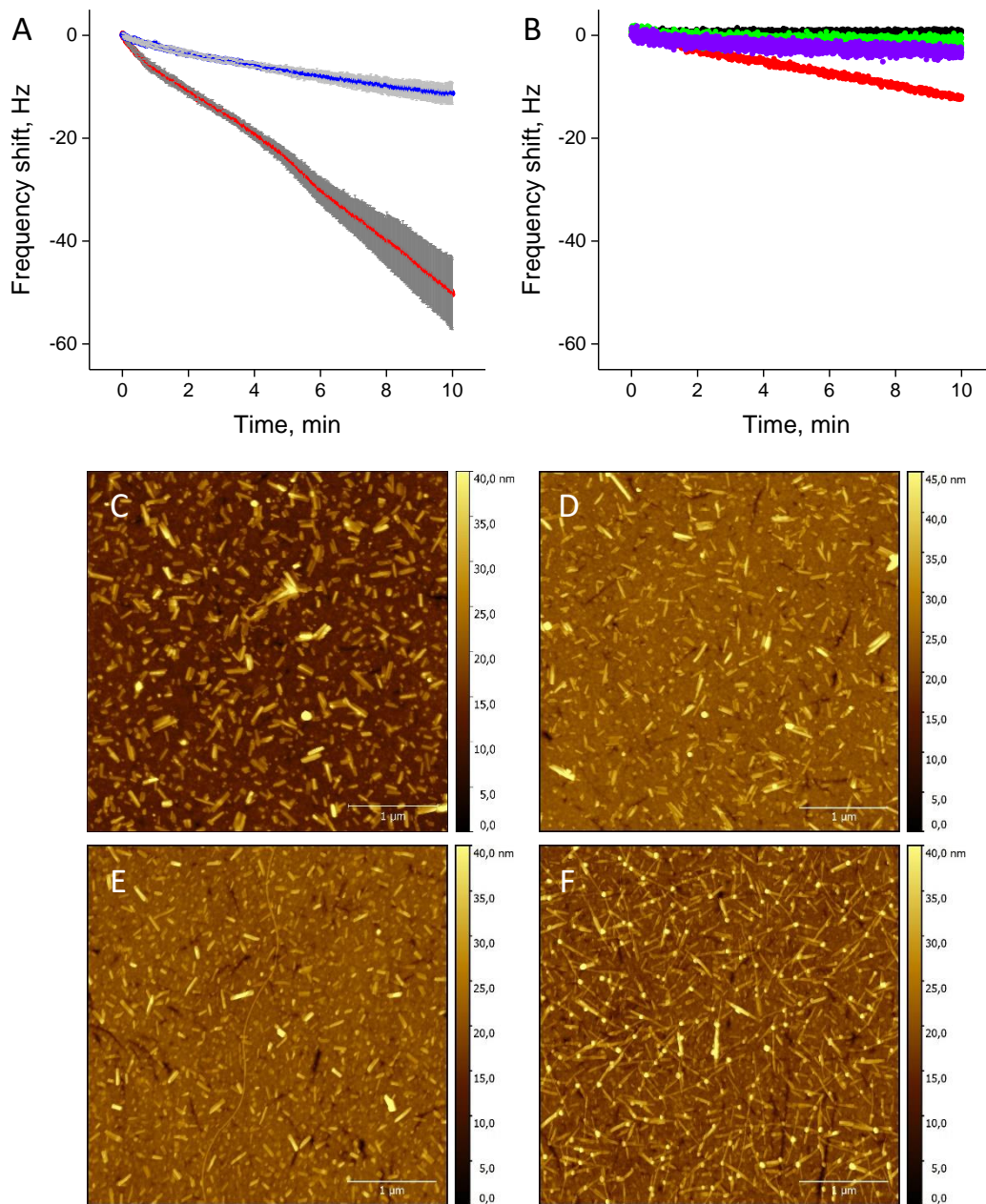
Figure 7-2: Aib-2-Oxyntomodulin fibril elongation is slower than Oxyntomodulin fibril elongation and does not cross-seed Oxyntomodulin

QCM-D fibril elongation assay with Oxyntomodulin fibril seeds and Aib-2-Oxyntomodulin fibril seeds, in 0.9 mg mL^{-1} saline at 25 °C. A, elongation of: blue, Aib-2-Oxyntomodulin fibrils; red, Oxyntomodulin fibrils with 2 mg mL^{-1} Aib-2-Oxyntomodulin or Oxyntomodulin, respectively. Shown is the average frequency slope ± standard deviation of three experiments (grey), R^2>0.99. B, frequency shifts of control experiments: black, Aib-2-Oxyntomodulin fibrils incubated with 0.9 % NaCl; green, empty SiO$_2$ sensor incubated with 0.5 mg mL^{-1} Oxyntomodulin at 25 °C; purple, Aib-2-Oxyntomodulin fibrils incubated with 0.5 mg mL^{-1} Oxyntomodulin; red, Oxyntomodulin fibrils incubated with 0.5 mg mL^{-1} Oxyntomodulin. C, Aib-2-Oxyntomodulin fibrils before and D, after incubation with 2 mg mL^{-1} of Aib-2-Oxyntomodulin. E, Oxyntomodulin fibrils before and F, after incubation with 2 mg mL^{-1} Oxyntomodulin. AFM images were processed in Gwyddion to remove imaging scars and background signal. Resolution: 1024*1024 pixel at 4*4 µm size.

Although the results presented here only show seeding in the context of fibril elongation, and cross-seeding was only tested with two similar peptides, the absence of measured elongation in both setups is a strong indication for the specificity of fibril elongation for one sequence. As glucagon is known to be prone to fibril formation and is part of the Oxyntomodulin primary sequence, fibril elongation by glucagon was indeed expected before the experiments. Similarly, the discrete modification in Oxyntomodulin's and Aib-2-Oxyntomodulin sequence brought about different kinetics and prevented Aib-2-Oxyntomodulin from cross-seeding Oxyntomodulin. As these peptide analogues cannot be cross-seeded by Oxyntomodulin fibrils, or cross-seed Oxyntomodulin, it is unlikely – but not excluded – that less related peptides are able to elongate Oxyntomodulin fibrils.

8 Future work

This work was designed to provide proof of concept for the use of self-assembled, amyloid-like peptides as a self-delivery system for enhanced exposure with pharmaceutical peptides released from a subcutaneous depot. Oxyntomodulin was chosen as a model peptide because of the potential use in T2DM and obesity, short plasma half-life, and the sensitivity of the mechanism of action towards structural changes that would allow a longer plasma half-life.

Oxyntomodulin readily formed self-assembled, fibrillar structures in a range of conditions. Presence of sodium chloride and agitation promoted nucleation, while nucleation in absence of salts only occurred after weeks of incubation of concentrated peptide solutions. However, only short fibrils grew in conditions with fast nucleation. Formation of long fibrils with high conversion yield was achieved by nucleation in presence of sodium chloride, fibril elongation in salt-deprived conditions, and subsequent addition of sodium chloride. This method allowed reproducible formation of indistinguishable fibril batches within two weeks. It is acknowledged that a one-step fibrillation method would be favorable regarding time and scalability.

While it cannot be excluded that there are conditions for a single-step formation of fibrils that meet requirements for production time, quality and quantity, previous results suggest that effective nucleation and elongation require different environments. It is however suspected that initial seed formation and elongation conditions can be optimized to allow a two-step method. Considering results from this work, sensible optimization parameters include pH, salt concentration, seed concentration and temperature. pH optimization could allow reduced concentration of salt by neutralization of side chains, which potentially accelerates nucleation and elongation while reducing lateral association. Sodium chloride was found to allow efficient nucleation and stabilize the formulation, but the range of concentration is limited by unspecific aggregation and clumping at higher saline concentrations, and slow kinetics at low concentrations. As other salts were not found to induce fibrillation but stabilize partially dissolved fibrils, seeding into solutions containing different salts could allow efficient elongation without further nucleation. Increasing seed number concentration was found to generally accelerate fibrillation and decrease risk of polymorphism. A simple way to achieve faster conversion into fibrils would therefore be extended seed sonication or application of higher seed mass concentrations. *De novo* fibrillation was almost exclusively screened at 37 °C because increased temperature was initially expected to accelerate fibrillation. However, results from chapters 5 and 6 prove a fibrillation temperature optimum at ~25 °C that prevented polymorphism in otherwise destabilizing conditions like low peptide-, salt- and seed concentrations. Elongation at 25 °C could therefore not only accelerate fibrillation but also increase the robustness of the fibrillation process.

Presence of a narrow thermal optimum of fibril elongation kinetics below body temperature was shown by kinetic elongation assays in bulk, QCM-D, ITC elongation and ThT. These methods comprise orthogonal measurement typed with different microenvironments, sample sizes and agitation. A similarly low temperature optimum of fibrillation has so far not been reported in the literature. Stabilization of fibrils and native α-helical soluble peptide was inversely correlated with temperature increase. It is assumed that the unique temperature optimum of Oxyntomodulin fibril elongation is a result of several temperature-dependent stabilizing and destabilizing factors.

The found thermal effects have implications on the handling of peptide- and fibril samples and possible effects *in vivo*. Temperatures at or below room temperature are beneficial for storage of fibrillar samples, while physiological temperatures are presumably a driving factor for peptide release from the *s.c.* fibril depot. These effects are desired, however it needs to be investigated how sensitive fibrils are to repeated changes in temperature. For example, *s.c.* temperatures depend on ambient temperature, contact with hot or cold objects, and alterations in core body temperature such as thermal changes during female menstrual cycle, hypothermia or fever. The repeated temperature shifts experienced *in vivo* could be mimicked in a thermocycler or in a kinetic ThT assay, and thermal effects on morphology and peptide release can be measured by taking aliquots at critical time points. Changes in secondary structure of fibril samples could be quantified CD spectroscopy as a function of temperature changes. In addition to elongation studies, ITC could be used to gain insights to fibril dissolution at different temperatures by dilution of mature fibril sample with peptide-free medium in the measurement cell. Similarly, differential scanning calorimetry (DSC) could provide valuable information on the melting temperature of fibril samples. Because of the high sensitivity of ITC and DSC, it may be possible to study effects of different solution conditions in addition to thermal effects.

Three fibril types were found and characterized in this work. The *mature* fibril type formed in presence of sodium chloride is with high certainty a lateral alignment of the *protofibril* fibril type in water. This hypothesis is justified by the very similar fibrillation conditions, dimensions by AFM and Cryo EM, dissociation of mature fibrils into fibrils with protofibril morphology in water, and very similar FTIR and CD spectroscopic results. The most obvious differences of mature fibrils compared to protofibrils are the enhanced binding of ThT, drastic reduction of free peptide concentration and lateral association of individual fibrils. By combination of fluorescence, spectroscopy, imaging and limited peptidolysis, a potential coarse-grain structure could be suggested. It needs to be stressed that the proposed alignment of arch-shaped peptides in a triangular cross-section was partially derived from single methods and exclusion of possibilities that would contradict measured parameters. A definite structure will require further work.

While 3D reconstruction of straight fibril types by Cryo EM is not possible due to the absence of a clear twist, more information on spacings within the fibril could be derived from additional diffraction data by Cryo EM or fibril X-Ray diffraction with synchrotron radiation. It was concluded from enzymatic degradation studies with trypsin that the fibril structure does not contain long sequences of unstructured peptide. Because trypsin only cleaves after Lysine, Arginine and Cysteine and requires several amino acids surrounding the cleavage position, a potentially unstructured region can still exist in Oxyntomodulin fibrils. Similar studies with other enzymes could provide further information. Especially, cleavage by the human enzyme DPP-4 could determine the protection or location of the N-terminus within fibrils. Enzymatic degradation could be analyzed on-line with an LC-MS peptide mapping approach in order to assign peaks to peptide fragment masses.

Twisted fibrils formed under different conditions as straight fibril types, displayed a different morphology and showed higher stability upon dilution. Stability was only assessed by bulk release in water and should be confirmed with other methods such as a kinetic ThT assay to solidify the assumption of a *quasi*-irreversible fibril type. Because an alternative fibril type is not desired for *in vivo* use, the conditions under which the twisted type forms and potentially dissolved should be closely examined. Due to the regular structure, determination of a high-resolution 3D structure will be attempted by Cryo EM. Fibrils will be sorted into classes dependent on the pitch-to-pitch distance, and fibrils in these classes will be computationally devided into single particles and realigned with single particle reconstitution software. Preparation for further Cryo EM experiments is currently ongoing, and fibril structure determination will be a central part of a recently started research project at the Nanoscience Centre, University of Cambridge.

Proof of fibril reversibility has been given *in vitro* and *in vivo*. Upon incubation with peptide-free medium in presence or absence of salts, fibrils released active peptide [6]. However, it is not yet understood if fibrils dissolve completely in a stream of peptide-free medium, especially in presence of salts such as in *s.c.* fluid. A possible setup could be incubation of fibrils separated from surrounding medium by a dialysis membrane, with frequent replacement of the medium outside of the fibril depot and concentration measurement in the medium. Because the presence of salts decreases released concentrations below the detection limit of photometry, a concentrating step or a more sensitive quantification method would be required. This could be achieved by peptide concentration in e.g. ion exchange chromatography followed by photometric measurement, by mass spectroscopy, or ideally by receptor activation quantification as described in [6]. Subcutaneous fluid could be mimicked by physiological salt composition in a CO_2 incubator.

Significantly increased Oxyntomodulin concentrations were found in the bloodstream of rodents after up to 5 d after *s.c.* injection of Oxyntomodulin fibrils [6]. Extended *in vivo*

studies will be required to assess the maximum time of Oxyntomodulin release from a *s.c.* fibril depot. Although no acute cytotoxicity was found, potential local tissue alterations or immunologic responses should be assessed *in vivo*. As receptors will be chronically challenged with unphysiological concentrations of an endogenous peptide, food uptake studies and glycemic control studies should be performed after repeated dosing of Oxyntomodulin fibrils to investigate potential habituation effects. Ideally, pharmacologic effects should be tested in a rodent model of T2DM and obesity.

Due to the general propensity of peptides and proteins to form amyloid-like fibrils, concepts and methods shown in this study could potentially be applied to other pharmaceutically active substances. Initial data on fibrillation and *in vivo* effects of the fibrillated DPP-4 resistant Oxyntomodulin analogue Aib-2-Oxyntomodulin are currently being published. It needs to be investigated if Aib-2-Oxyntomodulin shows similar thermal behavior and polymorphic alternative fibrils as Oxyntomodulin. Finally, reversible fibrillation can be investigated as a formulation strategy for other molecules such as lipidated GLP-1 analogues, structurally unrelated peptides, and therapeutically active proteins.

9 Appendix

9.1 Pre-screening of self-assembly conditions with Oxm$_{2-37}$

For reasons of peptide availability, ThT screening for nucleation conditions was mainly performed with Oxm$_{2-37}$. Some of the results are shown here, as the most promising conditions were then tested with (native) Oxyntomodulin. The lag time of the ThT-positive conditions was not consistent, and in some positive conditions, not all wells showed increased ThT fluorescence. Therefore, the screening could only be used for detection of amyloid formation conditions, but not for kinetic analysis.

An initial screening comprised Oxm$_{2-37}$ concentrations ranging from 0.1 to 5.0 mg mL^{-1} in water and in 25 mM phosphate buffer pH 7.4. At fixed peptide concentration of 0.5 mg mL^{-1}, ThT fluorescence was measured in PBS, 50/100/150 mM NaCl, and 25 mM buffers pH 2/5/6.5/8. This screening was performed at the maximum agitation frequency (5 min shaking followed by 5 min reading) for 3 days to avoid false-negative results.

The results are summarized in **Table *9-1***, and ThT raw results are shown in **Figure 10-2**, **Figure 10-3** and **Figure 10-4**. In water and at pH 7.4, no ThT increase was detected at any concentration over three days. AFM images of these conditions showed a not-assembled peptide layer similar to the AFM images of freshly prepared peptide solutions (see **Figure 10-1** A and B). Although the concentrations used for salt- and pH-screening were 10-fold lower than the highest concentration in water or pH 7.4, Oxm$_{2-37}$ self-assembled in some conditions. Buffering at pH 5 induced ThT increase and the formation of short fibrils with diameters between 10 and 20 nm. The scarce appearance of fibrils in the AFM images C and D of **Figure 10-1** is due to detachment of fibrils during the rinsing process of AFM chips. Rinsing was necessary to avoid imaging mistakes and cantilever damage by salt crystallization on the surface. In presence of 50-100 mM NaCl, nearly all samples bound ThT. AFM images of these samples show large amounts of aggregate consisting of very short fibrils (see **Figure 10-1** E). The grainy appearance could be explained by fibril fragmentation during the experiment. Imaging of a well at the onset of ThT signal increase (F) revealed long, spiraled fibrils without unstructured aggregate.

Table 9-1: Oxm$_{2\text{-}37}$ self-assembly screening by ThT fluorescence assay

Incubation of Oxm$_{2\text{-}37}$ at 37 °C in different solvent conditions containing 50 µM of the amyloidophilic fluorescent dye ThT. 6 fluorescence measurements per hour (λ_{ex}=440 nm, λ_{em}=480 nm) in bottom reading mode for 88 h. 5 min shaking at 600 rpm with 2 mm orbit before each measurement. Incubation of triplicates with 100 µL sample volume per well in low-binding polystyrene 92 well microplates (Corning® 3881). Selected conditions were imaged by AFM after the incubation.

condition	pH	ThT binding	AFM imaging
concentration screening in water			
0.1 mg mL^{-1}	6.6	no	n.a.
0.5 mg mL^{-1}	6.6	no	no fibrils
1.0 mg mL^{-1}	6.6	no	n.a.
5.0 mg mL^{-1}	6.6	no	no fibrils
concentration screening in 25 mM phosphate buffer pH 7.4			
0.1 mg mL^{-1}	7.4	no	n.a.
0.5 mg mL^{-1}	7.4	no	n.a.
1.0 mg mL^{-1}	7.3	no	n.a.
5.0 mg mL^{-1}	7.4	no	no fibrils
pH screening in 25 mM buffers			
0.5 mg mL^{-1} in pH 2 HCl/NaCl	3.7	no	n.a.
0.5 mg mL^{-1} in pH 5 acetate	5.3	yes (2/3 wells)	short fibrils + precipitate
0.5 mg mL^{-1} in pH 5 citrate	5.0	yes	n.a.
0.5 mg mL^{-1} in pH 8 phosphate	8.1	yes (1/3 wells)	precipitate
salt screening			
0.5 mg mL^{-1} in PBS	7.3	no	n.a.
0.5 mg mL^{-1} in 50 mM NaCl	6.3	yes (2/3 wells)	short fibrils + precipitate
0.5 mg mL^{-1} in 100 mM NaCl	6.4	yes	very short fibrils
0.5 mg mL^{-1} in 150 mM NaCl	6.0	yes	very short + long fibrils
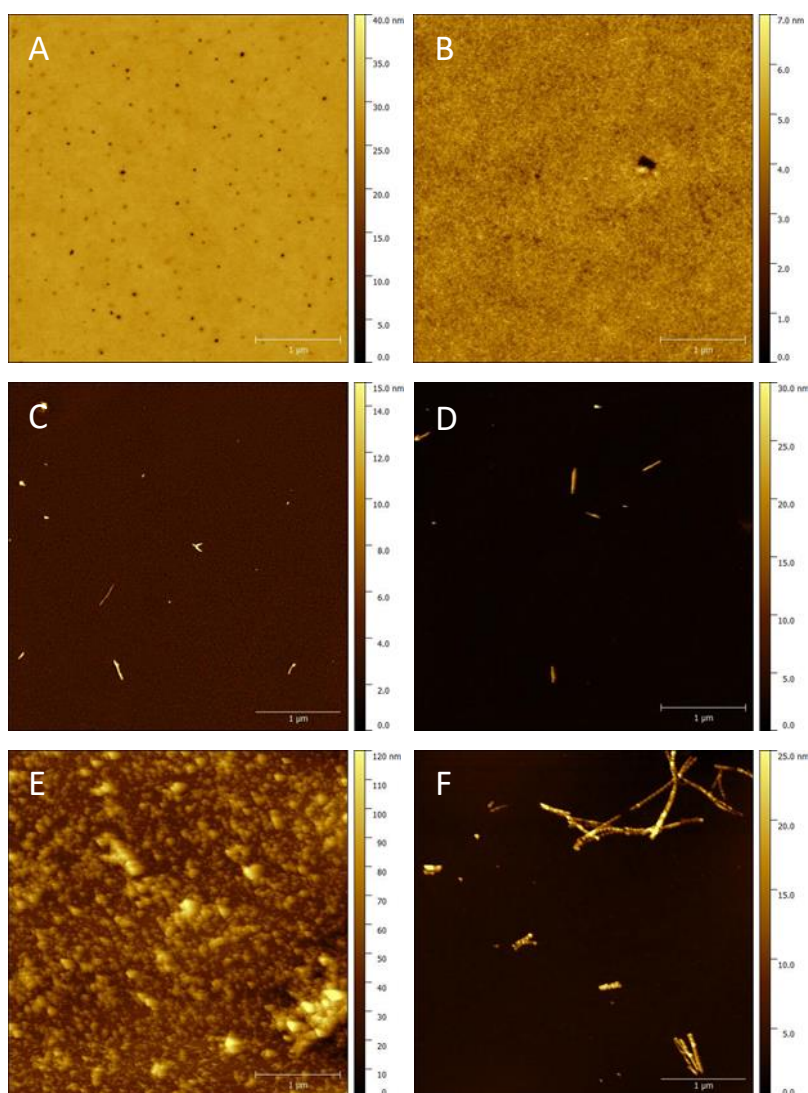
Figure 9-1: Representative AFM images of Oxm$_{2\text{-}37}$ samples after ThT screening (1)

A, 0.5 mg mL^{-1} Oxm$_{2\text{-}37}$ in water before incubation. B, 0.5 mg mL^{-1} Oxm$_{2\text{-}37}$ in water after incubation. C, 0.5 mg mL^{-1} Oxm$_{2\text{-}37}$ incubated in HCl buffer pH 2; D, 0.5 mg mL^{-1} Oxm$_{2\text{-}37}$ incubated in acetate buffer pH 5. E, 0.5 mg mL^{-1} Oxm$_{2\text{-}37}$ incubated in 100 mM NaCl. F, 0.5 mg mL^{-1} Oxm$_{2\text{-}37}$ in 100 mM NaCl, beginning logarithmic phase of ThT kinetic curve. All AFM samples were produced by drying a 5 µL sample aliquot on freshly cleaved mica. Chips C-F were rinsed with 100 µL HPLC grade water before imaging to avoid imaging of salt crystals. All images were processed in Gwyddion to remove imaging scars and background signal. Resolution: 512x512 pixel; scanning size 4x4 µm.
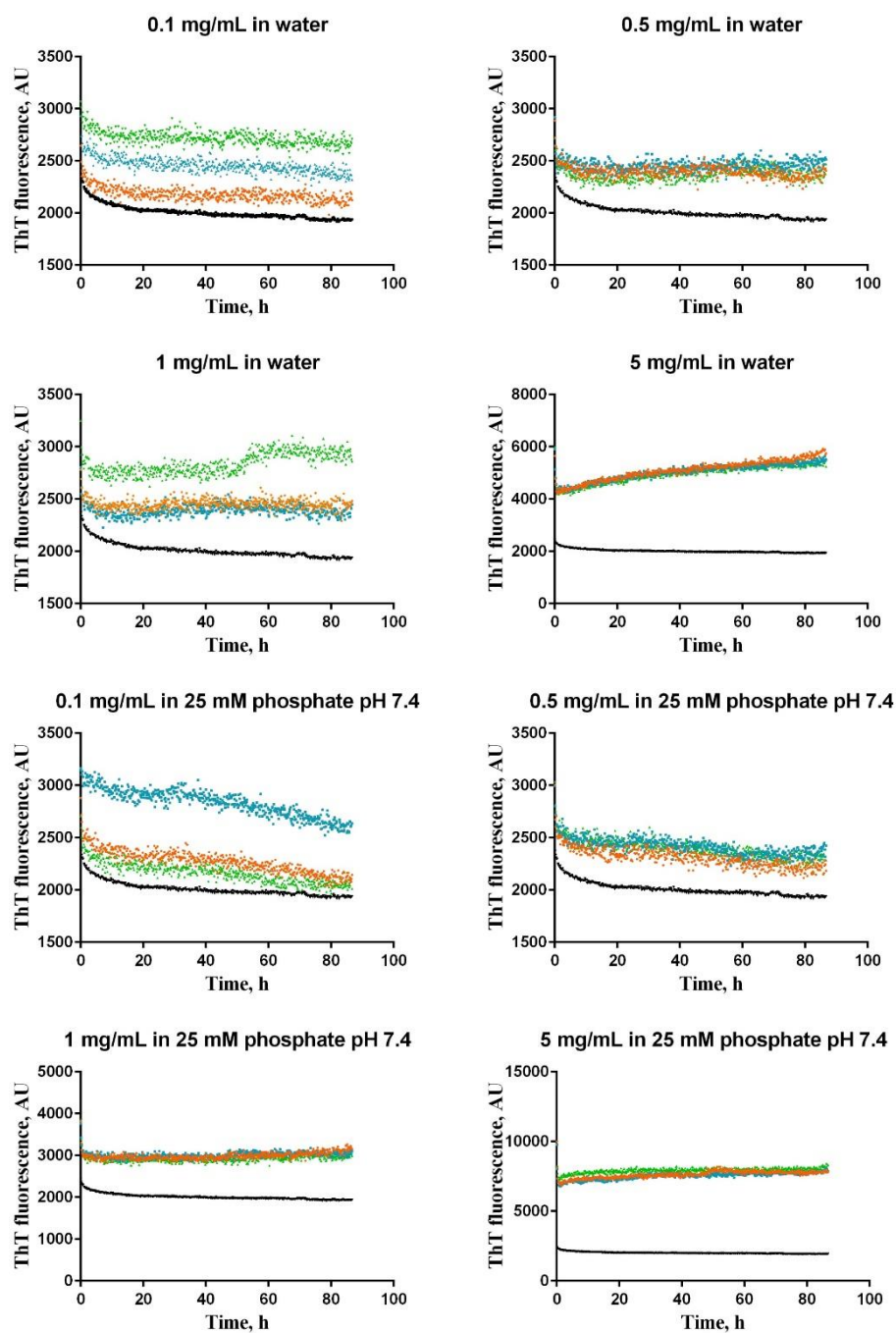
Figure 9-2: Oxm₂₋₃₇ concentration ThT screening

Incubation of 0.1-5 mg mL^{-1} Oxm$_{2-37}$ with 50 mM ThT in water or 25 mM phosphate buffer pH 7.4. Cycles of 5 min shaking and 5 min reading for 3.5 days. Black, control (50 mM ThT in water); coloured, triplicates of a condition.
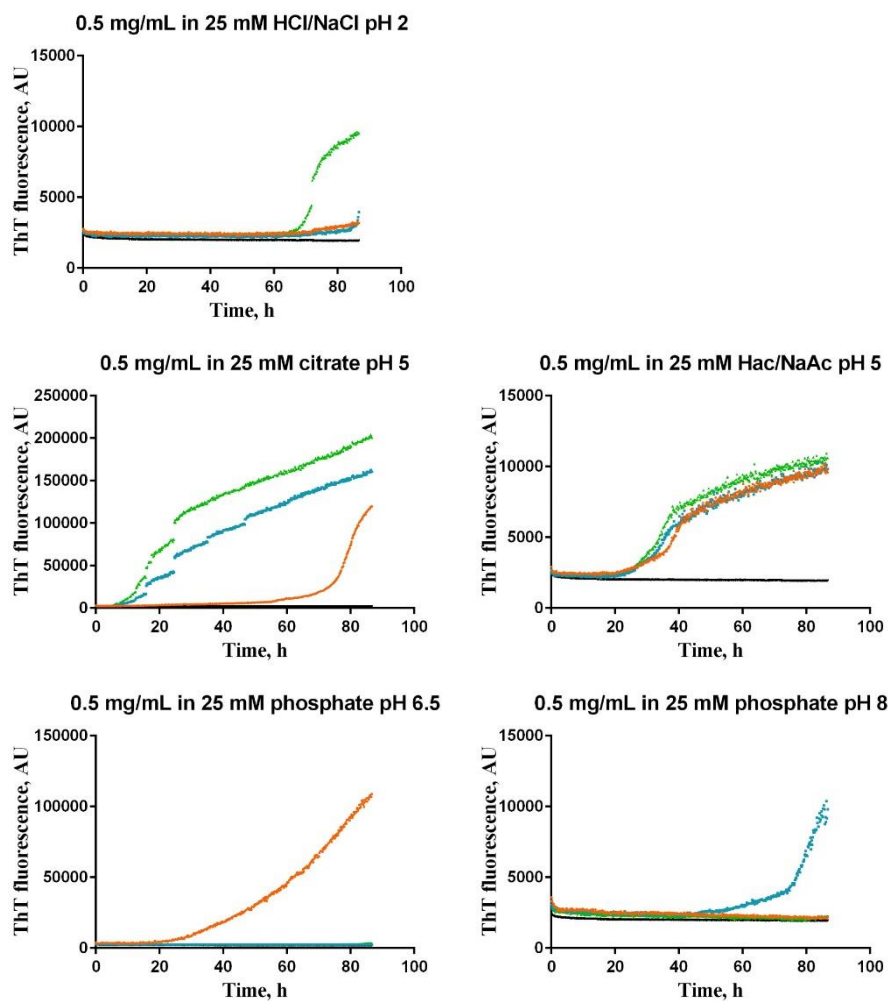
Figure 9-3: Oxm$_{2-37}$ ThT screening in different pH buffers

0.5 mg mL^{-1} Oxm$_{2-37}$ in 25 mM buffers pH 2-8. Cycles of 5 min shaking and 5 min reading at 37 °C for 3.5 days. Black, control (50 mM ThT in water); coloured, triplicates of a condition.
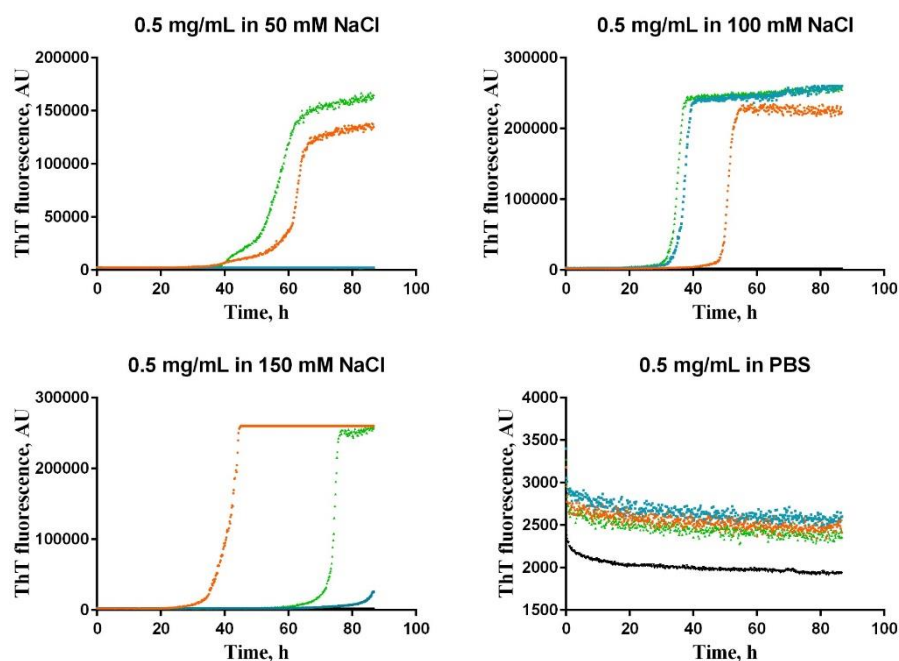
Figure 9-4: Oxm$_{2\text{-}37}$ ThT screening in different salt solutions

0.5 mg mL^{-1} Oxm$_{2\text{-}37}$ in 50-150 mM NaCl and PBS, with 50 mM ThT. Cycles of 5 min shaking and 5 min reading at 37 °C for 3.5 days. Black, control (50 mM ThT in water); coloured, triplicates of a condition.

To reduce fragmentation, the agitation frequency was decreased to 3x5 min agitation per hour in the following experiments. At 3x5 min agitation per hour and Oxm$_{2\text{-}37}$ concentrations of 0.5 or 1 mg mL^{-1} in 100 mM NaCl, no ThT signal or fibrillation was observed (results not shown) over 3 d. In the same conditions, 10 mg mL^{-1} solutions of Oxm$_{2\text{-}37}$ in water or 100 mM NaCl induced an increase in ThT within 24 h. The fibril morphology in presence of salt was markedly different from incubation in water (see *Figure 10-5* A-D). In water, long and spiraled fibrils with diameters of 5-15 nm were seen at the end of 3-day incubation in ThT screening conditions. In saline, the bulk of fibrils was short and clumped. Longer fibrils were straight and < 10 nm in height, and mostly associated to parallel bundles. An analogous setup with 100 mM NaCl and 10 mg mL Oxm$_{2\text{-}37}$ was stopped at the beginning of ThT increase (5 h) and incubated for further 24 h without shaking. Fibril seeds formed after 5 h elongated during quiescent elongation, showing that the fibrils in NaCl are prone to fragmentation caused by agitation. Fibrils produced in water did not associate laterally, and almost no unstructured aggregate was seen at the end of 3-day incubation in ThT screening conditions.
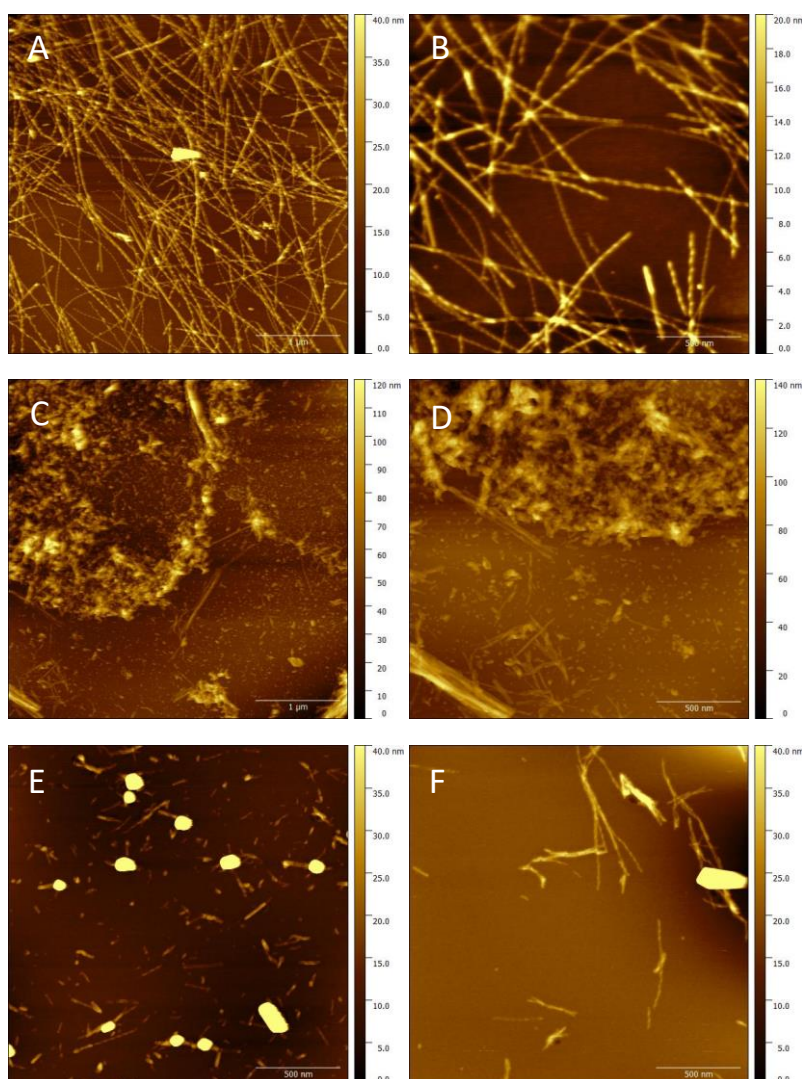
Figure 9-5: Representative AFM images of Oxm$_{2-37}$ samples after ThT screening at increased peptide concentration and reduced agitation

A and B, 10 mg mL^{-1} Oxm$_{2-37}$ incubated in water. C and D, 10 mg mL^{-1} Oxm$_{2-37}$ incubated in 100 mM NaCl. E, 10 mg mL^{-1} Oxm$_{2-37}$ incubated in 100 mM NaCl until the start of ThT fluorescence increase (5 h). F, condition E incubated without shaking for further 24 h. All AFM samples were produced by drying a 5 µL sample aliquot on freshly cleaved mica. Samples C and D were rinsed with 100 µL HPLC grade water before imaging to avoid imaging of salt crystals. All images were processed in Gwyddion to remove imaging scars and background signal. Resolution: 512x512 pixel; scanning size: 4x4 µm (A and C); 2x2 µm (B; D-F).

10 mg mL^{-1} Oxm$_{2\text{-}37}$ solutions were further screened for self-assembly at different pH values. Incubation in PBS was used as a salt containing control condition. Because the initial pH screening at low peptide concentration indicated a preferential self-assembly in neutral pH conditions, the pH influence was tested in a range of pH 6.0-8.0. All solvents except PBS were 25 mM phosphate buffers. After concentrated Oxm$_{2\text{-}37}$ stocks, the pH dropped ~0.5 units due to the acetate formulation of Oxm$_{2\text{-}37}$. ThT fluorescence was measured for 3.5 days, followed by AFM imaging of aliquots.

ThT binding was seen in all conditions (results not shown). In pH 6.0, 6.5, 7.0 and PBS, the half-maximum fluorescence intensity was reached within 24 h. At pH 7.4 and pH 8.0, the signal started to increase within the last day of incubation and did not reach a plateau phase. Fibrils formed in all conditions. At pH 6.0, a mixture of twisted fibrils and small unstructured aggregates were found. Incubation at pH 6.5 or pH 7.0 led to the formation of dense fibril networks. Imaging of less populated frames revealed a twisted fibril species and small aggregates. Individual fibrils had diameters < 10 nm and were partly associated. In pH 8, the same morphology was seen, however in very few numbers (see **Figure 10-6**). A comparison of fibril formation at physiologic pH (7.4) without salt and with salt (PBS) in **Figure 10-7** shows the influence of salt on fibril morphology. While the fibrils formed in the absence of salt were similar to the structures at neutral pH, the incubation in PBS induced the formation of grainy aggregate and very short fibrils.
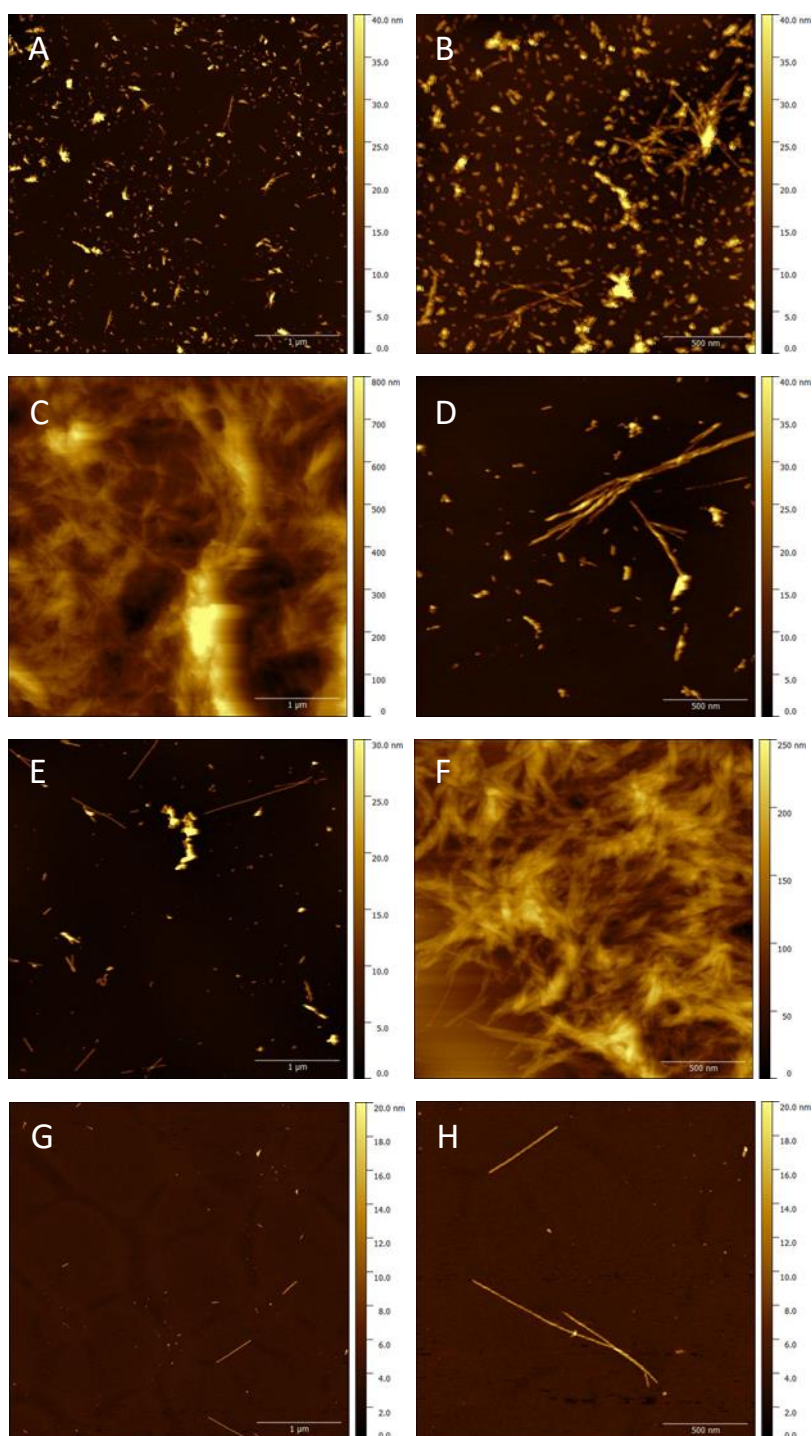
Figure 9-6: Oxm$_{2-37}$ after ThT screening in phosphate buffer pH 6-8

10 mg mL^{-1} Oxm$_{2-37}$ in 25 mM phosphate buffers. Images were taken after ThT assay in low binding Corning® 3881 microplates. Incubation with 50 µM ThT, 50 µL per well, triplicate, incubation at 37 °C with 3x5 min shaking at 600 rpm per hour for 3.5 days. A and B, pH 6.0; C and D, pH 6.5; E and F, pH 7.0; G and H, pH 8.0. AFM chips were rinsed with 100 µL water prior to imaging. All images were processed in Gwyddion to remove imaging scars and background signal. Resolution: 512x512 pixel; scanning size: 4x4 µm (left side) and 2x2 µm (right side).
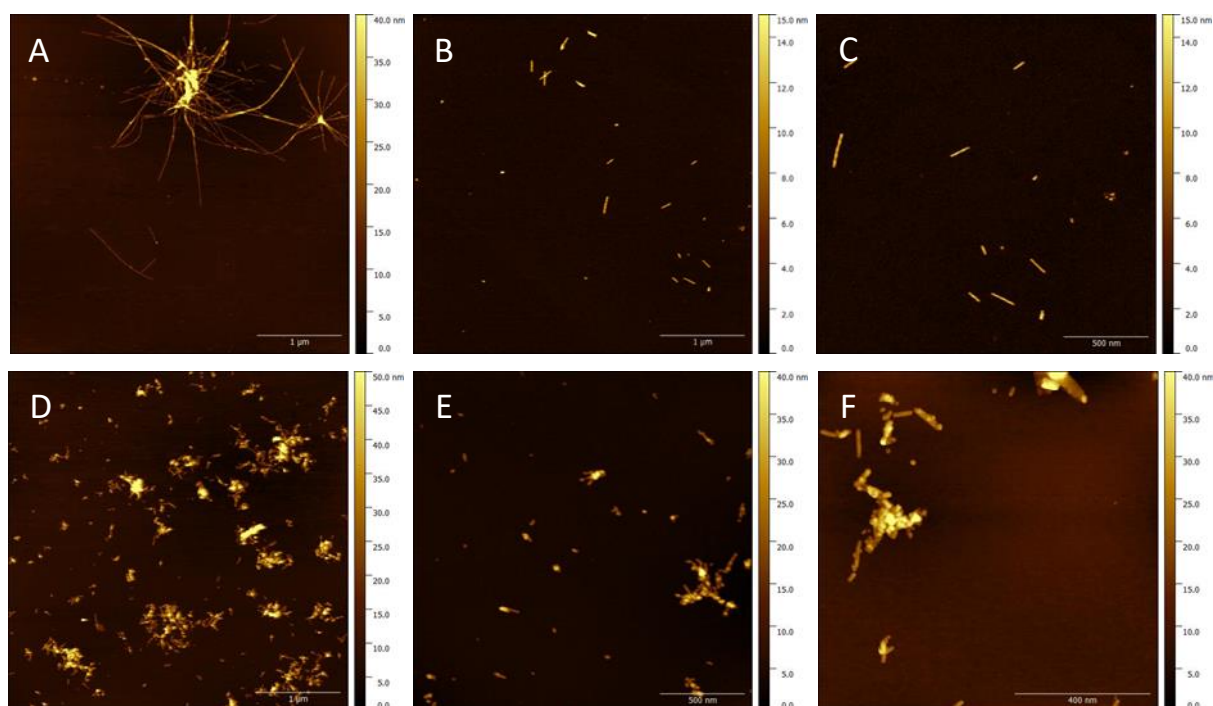
Figure 9-7: Oxm₂₋₃₇ after ThT screening in phosphate buffer pH 7.4 and PBS

10 mg mL^{-1} Oxm$_{2\text{-}37}$ in 25 mM phosphate buffer pH 7.4 (A-C) and in PBS (D-F). Images were taken after ThT assay in low binding Corning® 3881 microplates (50 µM ThT, 50 µL per well, triplicate, incubation at 37 °C with 3x5 min shaking at 600 rpm per hour for 3.5 days). AFM chips were rinsed with 100 µL water prior to imaging. All images were processed in Gwyddion to remove imaging scars and background signal. Resolution: 512x512 pixel; scanning size: 4x4 µm (A, B, D), 2x2 µm (C, E) and 1x1 µm (F).

9.2   ThT fluorescence is not well-suited to screen Oxyntomodulin self-assembly conditions

The following images show false-positive and false-negative ThT fluorescence increase in salt-, pH- and concentration-screenings of Oxyntomodulin. For description and interpretation see chapter 3.2.6.
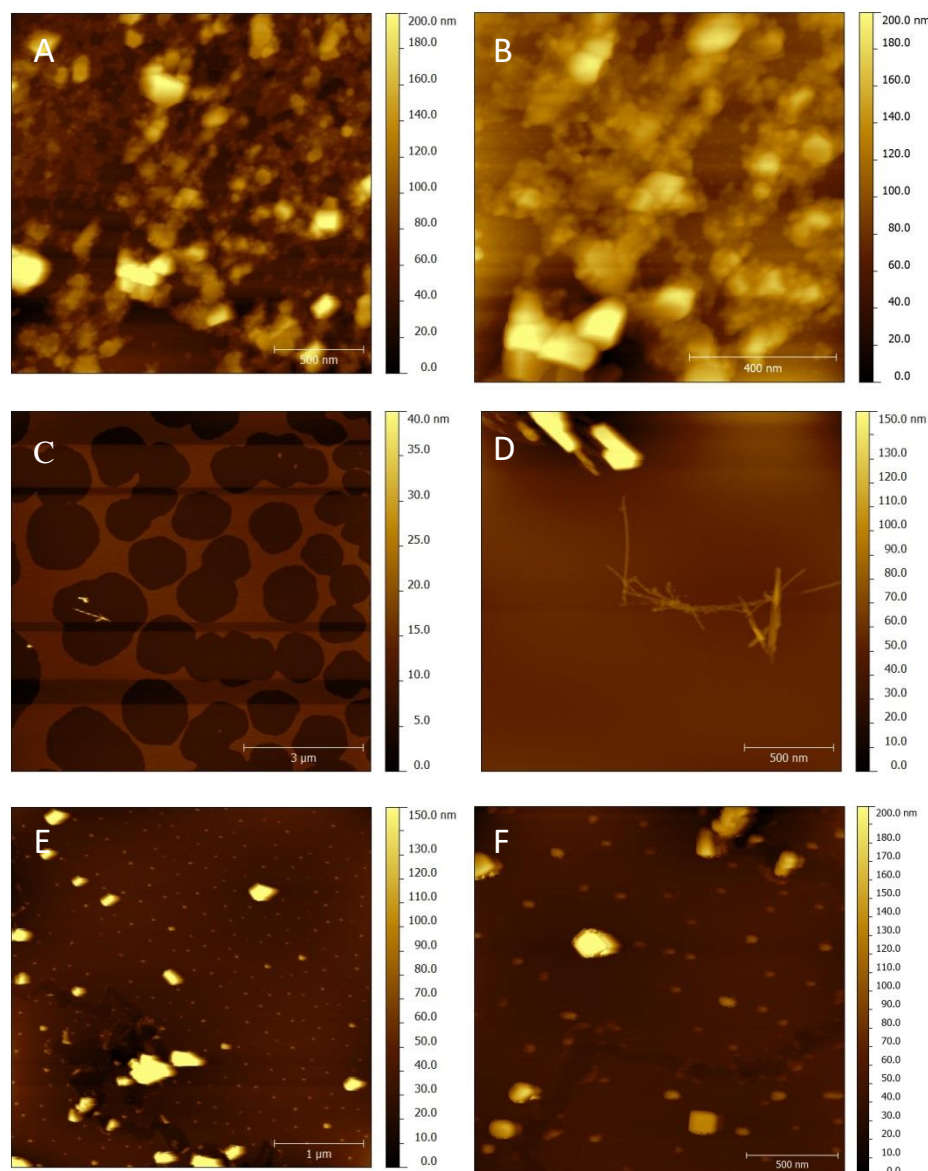
Figure 9-8: Representative AFM images of Oxyntomodulin ThT screening for different salt solutions

Images taken after 48 h of incubation in ThT conditions. 1 mg mL^{-1} Oxyntomodulin in 25 mM salts with increasing chaotropicity, with 50 mM ThT. 50 µL per well, triplicate. Cycles of 5 min shaking at 600 rpm and 15 min quiescent incubation at 37 °C for 5 days. A and B, Na$_2$SO$_4$; C and D, NaCl; E and F, NH$_4$Cl. Fibrils are only seen in NaCl even though all conditions showed amyloid-typical ThT fluorescence increase, as shown in **Figure *9-9***. All images were processed in Gwyddion to remove imaging scars and background signal. Resolution: 512x512 pixel at 9*9 µm scanning size (C) and 4*4 µm scanning size (E); 1024*1024 pixel at scanning size 2*2 µm (A, D, E) and 1x1 µm (B).
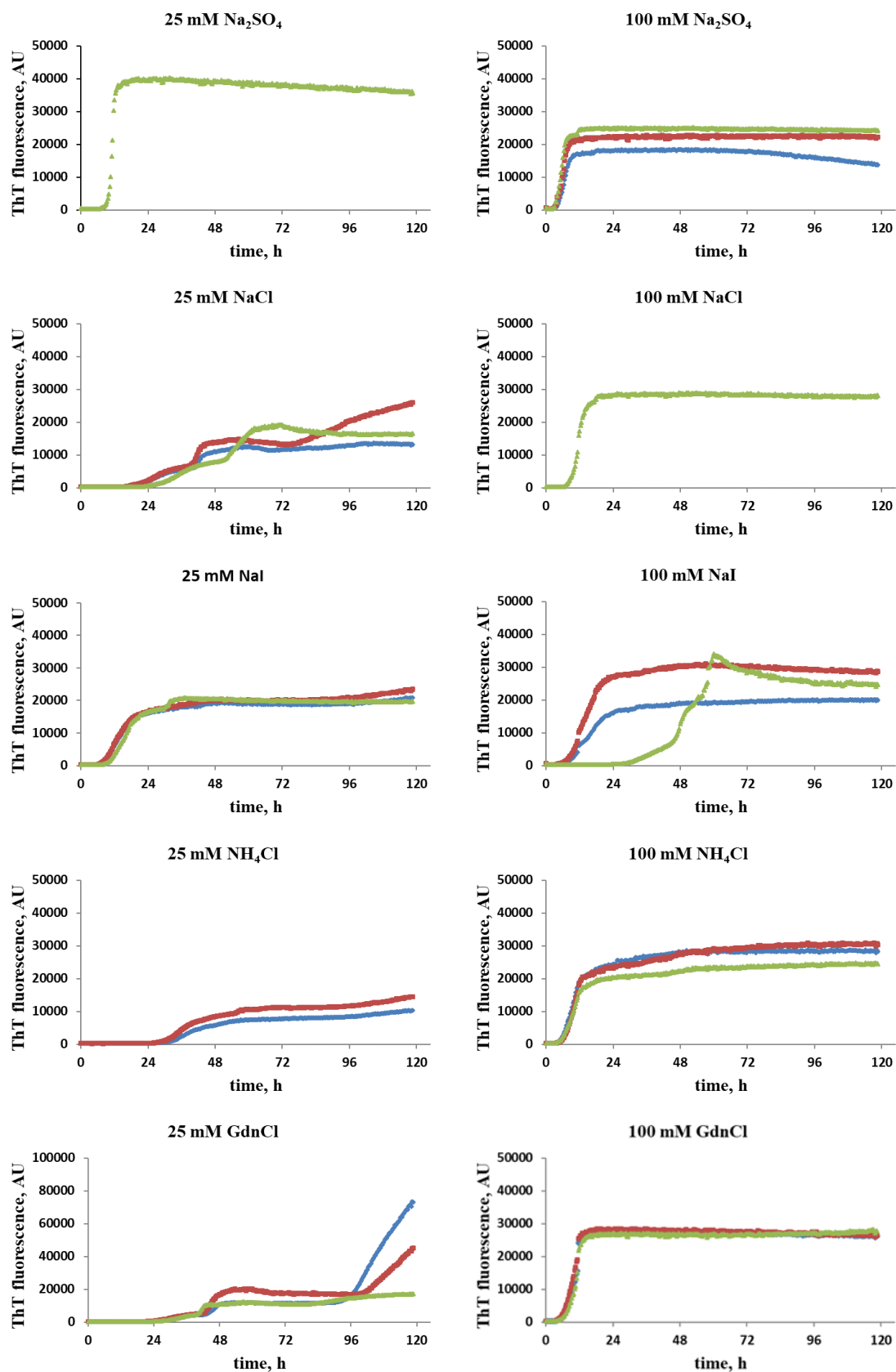
Figure 9-9: ThT fluorescence screening of Oxyntomodulinm self-assembly in different salt solutions

(continued from figure 10-9) 1 mg mL^{-1} Oxyntomodulin in 25 mM salts with increasing chaotropicity, with 50 mM ThT. 50 μL per well, triplicate. Some wells dried during incubation (not shown). Cycles of 5 min shaking at 600 rpm and 15 min quiescent incubation at 37 °C for 5 days.
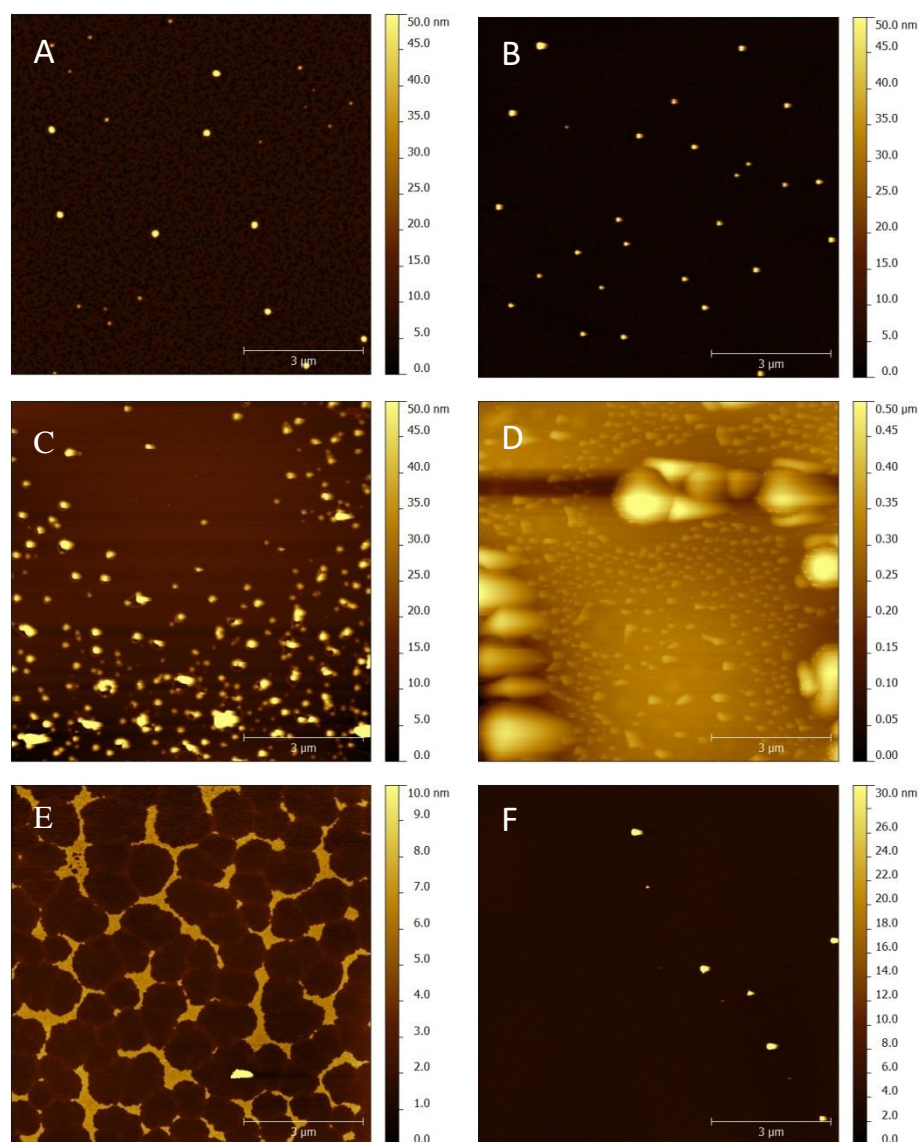
Figure 9-10: Representative AFM images of ThT fluorescence screening at pH 6 to 8

ThT conditions analogous to description in *Figure 9-11*, in 25 mM phosphate buffers at increasing pH. A, pH 6; B, pH 6.5; C, pH 7; D, pH 7.4; E, pH 8; F, pH 6 with additional 25 mM NaCl. No fibril formation although all conditions showed amyloid-typical ThT increase in all conditions, as shown in **Figure *9-11***. All images were processed in Gwyddion to remove imaging scars and background signal. Resolution: 512x512 pixel at scanning size 9*9 μm.
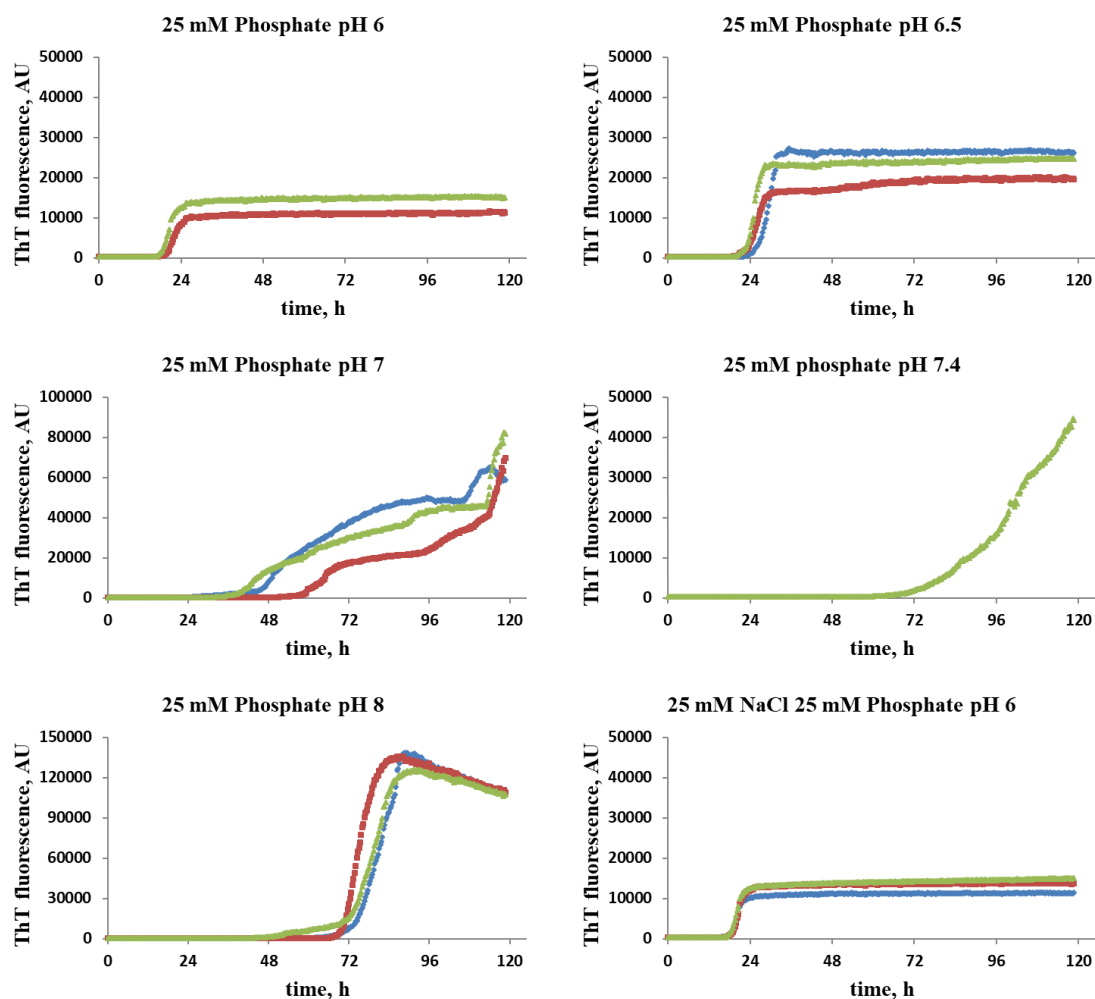
Figure 9-11: ThT fluorescence of Oxyntomodulin self-assembly at different pH

1 mg mL^{-1} Oxyntomodulin in 25 mM phosphate buffer pH 6-8, with 50 mM ThT. 50 μL per well, triplicate. Some wells dried during incubation (no shown). Cycles of 5 min shaking at 600 rpm and 15 min quiescent incubation at 37 °C for 5 days.
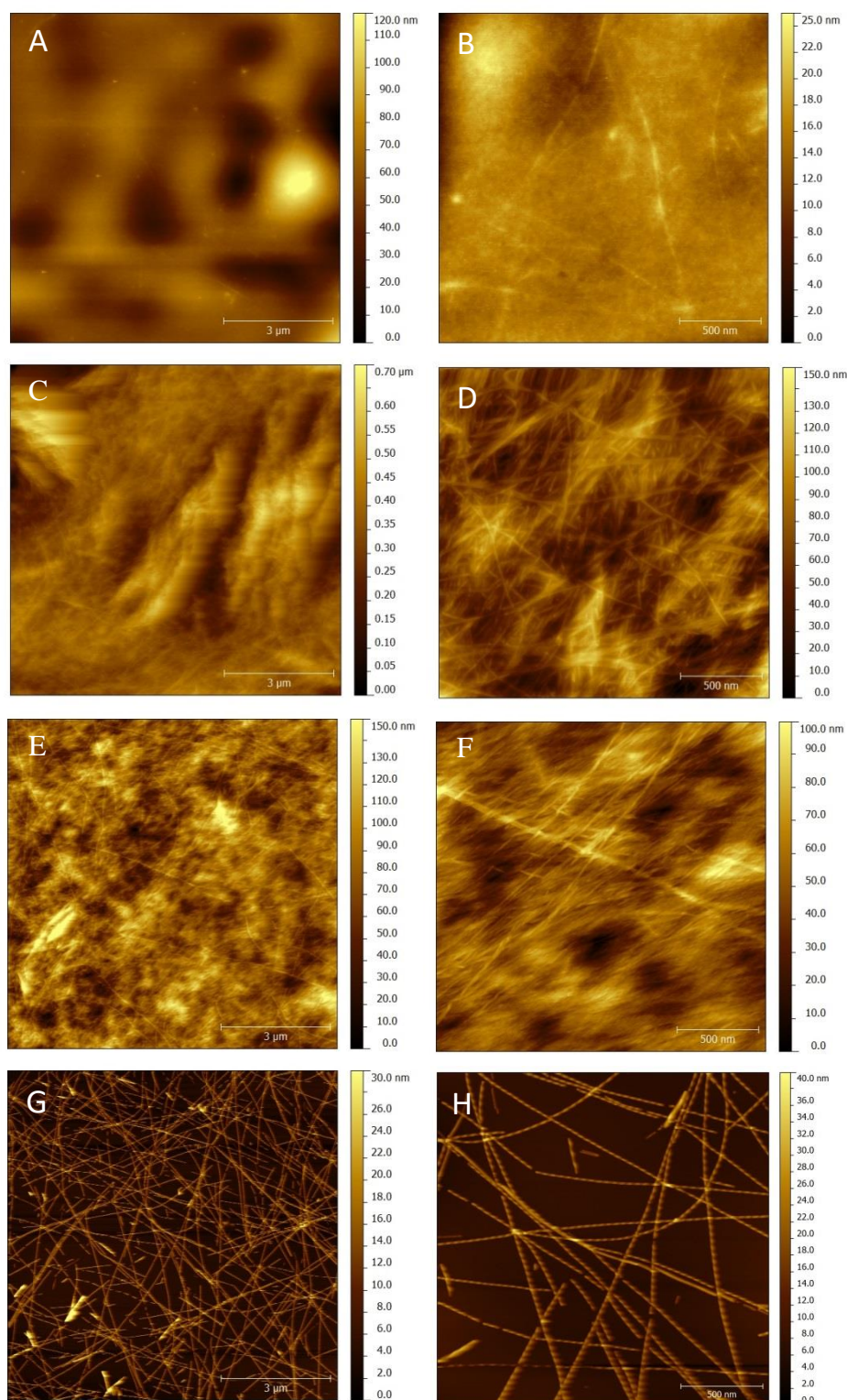
Figure 9-12: Representative AFM images of ThT fluorescence screening at increasing peptide concentrations

Imaging analogous to *Figure 9-8*. A, B: 1 mg mL^{-1}; C, D: 5 mg mL^{-1}; E, F: 10 mg mL^{-1}; G; H: 10 mg mL^{-1} 100x dilute in water before deposition on mica. Fibril formation despite very limited ThT fluorescence increase shown in **Figure *9-13***. All images were processed in Gwyddion to remove imaging scars and background signal. Resolution: 512x512 pixel at scanning size 9*9 µm (A, C, E, G), 1024*1024 pixel at scanning size 2x2 µm (B, D, F, H).
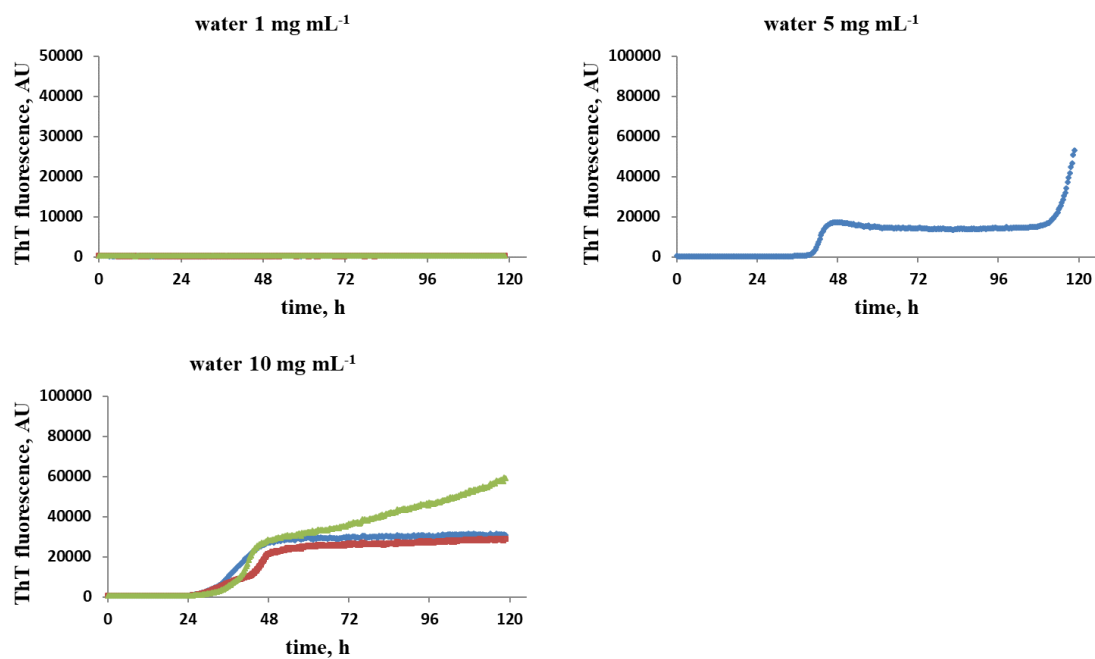
Figure 9-13: ThT fluorescence screening of Oxyntomodulin self-assembly in water

Oxyntomodulin with 50 mM ThT at increasing concentration. 50 μL per well, triplicate. Some wells dried during incubation (no shown). Cycles of 5 min shaking at 600 rpm and 15 min quiescent incubation at 37 °C for 5 days.

10 List of figures

11 List of tables

12 References

[1]   L. Guariguata, D. R. R. Whiting, I. Hambleton, J. Beagley, U. Linnenkamp, and J. E. E. Shaw, "Global estimates of diabetes prevalence for 2013 and projections for 2035," *Diabetes Res. Clin. Pract.*, vol. 103, no. 2, pp. 137–149, Feb. 2014.

[2]   K. Wynne and S. R. Bloom, "The role of oxyntomodulin and peptide tyrosine–tyrosine (PYY) in appetite control," *Nat. Clin. Pract. Endocrinol. & Metab.*, vol. 2, no. 11, pp. 612–620, 2006.

[3]   L. Zhu, C. Tamvakopoulos, D. Xie, J. Dragovic, X. Shen, J. E. Fenyk-Melody, K. Schmidt, a. Bagchi, P. R. Griffin, N. a. Thornberry, and R. Sinha Roy, "The Role of Dipeptidyl Peptidase IV in the Cleavage of Glucagon Family Peptides: IN VIVO METABOLISM OF PITUITARY ADENYLATE CYCLASE-ACTIVATING POLYPEPTIDE-(1-38)," *J. Biol. Chem.*, vol. 278, no. 25, pp. 22418–22423, 2003.

[4]   F. Chiti and C. M. Dobson, "Protein misfolding, functional amyloid, and human disease.," *Annu. Rev. Biochem.*, vol. 75, pp. 333–366, 2006.

[5]   S. K. Maji, D. Schubert, C. Rivier, S. Lee, J. E. Rivier, and R. Riek, "Amyloid as a depot for the formulation of long-acting drugs," *PLoS Biol.*, vol. 6, no. 2, pp. 0240–0252, 2008.

[6]   M. M. Ouberai, A. L. G. Dos Santos, S. Kinna, S. Madalli, D. C. Hornigold, D. Baker, J. Naylor, L. Sheldrake, D. J. Corkill, J. Hood, P. Vicini, S. Uddin, S. Bishop, P. G. Varley, and M. E. Welland, "Controlling the bioactivity of a peptide hormone in vivo by reversible self-assembly," *Nat. Commun.*, vol. 8, no. 1, 2017.

[7]   International Diabetes Federation, "IDF Diabetes Atlas," 2018.

[8]   L. Chen, D. J. Magliano, and P. Z. Zimmet, "The worldwide epidemiology of type 2 diabetes mellitus—present and future perspectives," *Nat. Rev. Endocrinol.*, vol. 8, no. 4, pp. 228–236, 2011.

[9]   B. C. T. Field, O. B. Chaudhri, and S. R. Bloom, "Bowels control brain: gut hormones and obesity.," *Nat. Rev. Endocrinol.*, vol. 6, no. 8, pp. 444–453, 2010.

[10]   S. E. Kahn, M. E. Cooper, and S. Del Prato, "Pathophysiology and treatment of type 2 diabetes: perspectives on the past, present, and future," *Lancet (London, England)*, vol. 383, no. 9922, pp. 1068–1083, Mar. 2014.

[11]   S. M. Grundy, "Pre-diabetes, metabolic syndrome, and cardiovascular risk.," *J. Am. Coll. Cardiol.*, vol. 59, no. 7, pp. 635–43, Feb. 2012.

[12]   T. A. Wadden, D. S. West, L. Delahanty, J. Jakicic, J. Rejeski, D. Williamson, R. I. Berkowitz, D. E. Kelley, C. Tomchee, J. O. Hill, and S. Kumanyika, "The Look AHEAD Study: A Description of the Lifestyle Intervention and the Evidence Supporting It*," *Obesity*, vol. 14, no. 5, pp. 737–752, May 2006.

[13]   T. Tan and S. Bloom, "Gut hormones as therapeutic agents in treatment of diabetes and obesity," *Curr. Opin. Pharmacol.*, vol. 13, no. 6, pp. 996–1001, 2013.

[14]   M. Yu, M. M. Benjamin, S. Srinivasan, E. E. Morin, and E. I. Shishatskaya, "Battle of GLP-1 delivery technologies," *Adv. Drug Deliv. Rev.*, vol. 130, pp. 113–130, May 2018.

[15]   "Effect of intensive blood-glucose control with metformin on complications in overweight patients with type 2 diabetes (UKPDS 34)," *Lancet*, vol. 352, no. 9131, pp.

854–865, Sep. 1998.

[16] H. C. Gerstein, M. E. Miller, R. P. Byington, D. C. Goff, J. T. Bigger, J. B. Buse, W. C. Cushman, S. Genuth, F. Ismail-Beigi, R. H. Grimm, J. L. Probstfield, D. G. Simons-Morton, and W. T. Friedewald, "Effects of intensive glucose lowering in type 2 diabetes.," *N. Engl. J. Med.*, vol. 358, no. 24, pp. 2545–59, Jun. 2008.

[17] S. a Sadry and D. J. Drucker, "Emerging combinatorial hormone therapies for the treatment of obesity and T2DM.," *Nat. Rev. Endocrinol.*, vol. 9, no. 7, pp. 425–33, 2013.

[18] J. J. Holst, "The Physiology of Glucagon-like Peptide 1," *Physiol. Rev.*, vol. 87, no. 4, pp. 1409–1439, Oct. 2007.

[19] A. Pocai, "Action and therapeutic potential of oxyntomodulin," *Mol. Metab.*, vol. 3, no. 3, pp. 241–251, 2014.

[20] X. Du, J. R. Kosinski, J. Lao, X. Shen, A. Petrov, G. G. Chicchi, G. J. Eiermann, and A. Pocai, "Differential effects of oxyntomodulin and GLP-1 on glucose metabolism," *Am. J. Physiol. Metab.*, vol. 303, no. 2, pp. E265–E271, Jul. 2012.

[21] a. Pocai, "Unraveling oxyntomodulin, GLP1's enigmatic brother," *J. Endocrinol.*, vol. 215, no. 3, pp. 335–346, 2012.

[22] A. D. Green, S. Vasu, R. C. Moffett, and P. R. Flatt, "Co-culture of clonal beta cells with GLP-1 and glucagon-secreting cell line impacts on beta cell insulin secretion, proliferation and susceptibility to cytotoxins," *Biochimie*, vol. 125, pp. 119–125, Jun. 2016.

[23] E. L. Lim, K. G. Hollingsworth, B. S. Aribisala, M. J. Chen, J. C. Mathers, and R. Taylor, "Reversal of type 2 diabetes: normalisation of beta cell function in association with decreased pancreas and liver triacylglycerol," *Diabetologia*, vol. 54, no. 10, pp. 2506–2514, Oct. 2011.

[24] M. A. Nauck, G. Kemmeries, J. J. Holst, and J. J. Meier, "Rapid tachyphylaxis of the glucagon-like peptide 1-induced deceleration of gastric emptying in humans.," *Diabetes*, vol. 60, no. 5, pp. 1561–5, May 2011.

[25] L. van Bloemendaal, D. J. Veltman, J. S. ten Kulve, P. F. C. Groot, H. G. Ruhé, F. Barkhof, J. H. Sloan, M. Diamant, and R. G. Ijzerman, "Brain reward-system activation in response to anticipation and consumption of palatable food is altered by glucagon-like peptide-1 receptor activation in humans," *Diabetes, Obes. Metab.*, vol. 17, no. 9, pp. 878–886, Sep. 2015.

[26] A. Secher, J. Jelsing, A. F. Baquero, J. Hecksher-Sørensen, M. A. Cowley, L. S. Dalbøge, G. Hansen, K. L. Grove, C. Pyke, K. Raun, L. Schäffer, M. Tang-Christensen, S. Verma, B. M. Witgen, N. Vrang, and L. Bjerre Knudsen, "The arcuate nucleus mediates GLP-1 receptor agonist liraglutide-dependent weight loss," *J. Clin. Invest.*, vol. 124, no. 10, pp. 4473–4488, Oct. 2014.

[27] D. J. Drucker, "Cell Metabolism The Cardiovascular Biology of Glucagon-like Peptide-1," *Cell Metab.*, 2016.

[28] R. Jorgensen, V. Kubale, M. Vrecl, T. W. Schwartz, and C. E. Elling, "Oxyntomodulin Differentially Affects Glucagon-Like Peptide-1 Receptor beta-Arrestin Recruitment and Signaling through G ," *J. Pharmacol. Exp. Ther.*, vol. 322, no. 1, pp. 148–154, Mar. 2007.

[29] N. Irwin, V. Pathak, N. M. Pathak, V. A. Gault, and P. R. Flatt, "Sustained treatment with a stable long-acting oxyntomodulin analogue improves metabolic control and islet morphology in an experimental model of type 1 diabetes," *Diabetes, Obes. Metab.*, vol. 17, no. 9, pp. 887–895, Sep. 2015.

[30] G. L. Sowden, D. J. Drucker, D. Weinshenker, and S. J. Swoap, "Oxyntomodulin increases intrinsic heart rate in mice independent of the glucagon-like peptide-1 receptor.," *Am. J. Physiol. Regul. Integr. Comp. Physiol.*, vol. 292, no. 2, pp. R962-70, Mar. 2007.

[31] C. L. Dakin, C. J. Small, R. L. Batterham, N. M. Neary, M. A. Cohen, M. Patterson, M. A. Ghatei, and S. R. Bloom, "Peripheral oxyntomodulin reduces food intake and body weight gain in rats.," *Endocrinology*, vol. 145, no. 6, pp. 2687–95, Jun. 2004.

[32] B. Schjoldager, P. E. Mortensen, J. Myhre, J. Christiansen, and J. J. Holst, "Oxyntomodulin from distal gut," *Dig. Dis. Sci.*, vol. 34, no. 9, pp. 1411–1419, Sep. 1989.

[33] A. Astrup, S. Rössner, L. Van Gaal, A. Rissanen, L. Niskanen, M. Al Hakim, J. Madsen, M. F. Rasmussen, and M. E. J. Lean, "Effects of liraglutide in the treatment of obesity: a randomised, double-blind, placebo-controlled study.," *Lancet (London, England)*, vol. 374, no. 9701, pp. 1606–16, Nov. 2009.

[34] M. Zander, S. Madsbad, J. L. Madsen, and J. J. Holst, "Effect of 6-week course of glucagon-like peptide 1 on glycaemic control, insulin sensitivity, and β-cell function in type 2 diabetes: a parallel-group study," *Lancet*, vol. 359, no. 9309, pp. 824–830, Mar. 2002.

[35] A. Maida, J. A. Lovshin, L. L. Baggio, and D. J. Drucker, "The Glucagon-Like Peptide-1 Receptor Agonist Oxyntomodulin Enhances β-Cell Function but Does Not Inhibit Gastric Emptying in Mice," *Endocrinology*, vol. 149, no. 11, pp. 5670–5678, Nov. 2008.

[36] E. T. Parlevliet, A. C. Heijboer, J. P. Schröder-van der Elst, L. M. Havekes, J. A. Romijn, H. Pijl, and E. P. M. Corssmit, "Oxyntomodulin ameliorates glucose intolerance in mice fed a high-fat diet," *Am. J. Physiol. Metab.*, vol. 294, no. 1, pp. E142–E147, Jan. 2008.

[37] J. R. Kosinski, J. Hubert, P. E. Carrington, G. G. Chicchi, J. Mu, C. Miller, J. Cao, E. Bianchi, A. Pessi, R. SinhaRoy, D. J. Marsh, and A. Pocai, "The Glucagon Receptor Is Involved in Mediating the Body Weight-Lowering Effects of Oxyntomodulin," *Obesity*, vol. 20, no. 8, pp. 1566–1571, Aug. 2012.

[38] J. Escorihuela, A. Miguel, J. Luis, R. Puchades, A. Maquieira, and D. Gimenez-romero, "Dual-Polarization Interferometry : A Novel Technique To Light up the Nanomolecular World," *Chem. Rev.*, vol. 144(1), pp.265-294, Jan. 2014.

[39] S. S. Shankar, R. R. Shankar, L. A. Mixson, D. L. Miller, B. Pramanik, A. K. O'dowd, D. M. Williams, C. B. Frederick, C. R. Beals, S. A. Stoch, H. O. Steinberg, and D. E. Kelley, "Native Oxyntomodulin Has Significant Glucoregulatory Effects Independent of Weight Loss in Obese Humans With and Without Type 2 Diabetes," Diabetes, vol. 67(6), pp. 1105-1112, Jan. 2018.

[40] N. M. Pathak, V. Pathak, A. M. Lynch, N. Irwin, V. A. Gault, and P. R. Flatt, "Stable oxyntomodulin analogues exert positive effects on hippocampal neurogenesis and gene expression as well as improving glucose homeostasis in high fat fed mice.," *Mol. Cell.*

Endocrinol., vol. 412, pp. 95–103, Sep. 2015.

[41]   C. Dakin, C. Small, A. Park, … A. S.-A. J. of, and   undefined 2002, "Repeated ICV administration of oxyntomodulin causes a greater reduction in body weight gain than in pair-fed rats," *Am. J. Physiol. Endocrinol. Metab.*, vol. 283(6), pp. 1173-1177, Dec. 2002.

[42]   M. a. Cohen, S. M. Ellis, C. W. Le Roux, R. L. Batterham, A. Park, M. Patterson, G. S. Frost, M. a. Ghatei, and S. R. Bloom, "Oxyntomodulin Suppresses Appetite and Reduces Food Intake in Humans," *J. Clin. Endocrinol. Metab.*, vol. 88, no. 10, pp. 4696–4701, Oct. 2003.

[43]   K. Wynne, a. J. Park, C. J. Small, M. Patterson, S. M. Ellis, K. G. Murphy, a. M. Wren, G. S. Frost, K. Meeran, M. a. Ghatei, and S. R. Bloom, "Subcutaneous Oxyntomodulin Reduces Body Weight in Overweight and Obese Subjects: A Double-Blind, Randomized, Controlled Trial," *Diabetes*, vol. 54, no. 8, pp. 2390–2395, Aug. 2005.

[44]   R. Scott, J. Minnion, T. Tan, and S. R. Bloom, "Oxyntomodulin analogue increases energy expenditure via the glucagon receptor," *Peptides*, vol. 104, pp. 70–77, Jun. 2018.

[45]   S. Al-Sabah and D. Donnelly, "The Primary Ligand-Binding Interaction At The Glp-1 Receptor Is Via The Putative Helix Of The Peptide Agonists," *Protein Pept. Lett.*, vol. 11, no. 1, pp. 9–14, Feb. 2004.

[46]   K. Adelhorst, B. B. Hedegaard, L. B. Knudsen, and O. Kirk, "Structure-activity studies of glucagon-like peptide-1.," *J. Biol. Chem.*, vol. 269, no. 9, pp. 6275–8, Mar. 1994.

[47]   M. R. Druce, J. S. Minnion, B. C. T. Field, S. R. Patel, J. C. Shillito, M. Tilby, K. E. L. Beale, K. G. Murphy, M. A. Ghatei, and S. R. Bloom, "Investigation of Structure-Activity Relationships of Oxyntomodulin (Oxm) Using Oxm Analogs," *Endocrinology*, vol. 150, no. 4, pp. 1712–1722, Apr. 2009.

[48]   A. Muppidi, H. Zou, P. Y. Yang, E. Chao, L. Sherwood, V. Nunez, A. K. Woods, P. G. Schultz, Q. Lin, and W. Shen, "Design of Potent and Proteolytically Stable Oxyntomodulin Analogs," *ACS Chem. Biol.*, vol. 11, no. 2, pp. 324–328, Feb. 2016.

[49]   A. Santoprete, E. Capitò, P. E. Carrington, A. Pocai, M. Finotto, A. Langella, P. Ingallinella, K. Zytko, S. Bufali, S. Cianetti, M. Veneziano, F. Bonelli, L. Zhu, E. Monteagudo, D. J. Marsh, R. SinhaRoy, E. Bianchi, and A. Pessi, "DPP-IV-resistant, long-acting oxyntomodulin derivatives," *J. Pept. Sci.*, vol. 17, no. 4, pp. 270–280, Apr. 2011.

[50]   C. Jarrousse, M.-P. Audousset-Puech, M. Dubrasquet, H. Niel, J. Martinez, and D. Bataille, "Oxyntomodulin (glucagon-37) and its C-terminal octapeptide inhibit gastric acid secretion," *FEBS Lett.*, vol. 188, no. 1, pp. 81–84, Aug. 1985.

[51]   E. Bianchi, P. E. Carrington, P. Ingallinella, M. Finotto, A. Santoprete, A. Petrov, G. Eiermann, J. Kosinski, D. J. Marsh, A. Pocai, R. SinhaRoy, and A. Pessi, "A PEGylated analog of the gut hormone oxyntomodulin with long-lasting antihyperglycemic, insulinotropic and anorexigenic activity," *Bioorg. Med. Chem.*, vol. 21, no. 22, pp. 7064–7073, 2013.

[52]   Y.-L. Liu, H. E. Ford, M. R. Druce, J. S. Minnion, B. C. T. Field, J. C. Shillito, J. Baxter, K. G. Murphy, M. A. Ghatei, and S. R. Bloom, "Subcutaneous oxyntomodulin analogue administration reduces body weight in lean and obese rodents," *Int. J. Obes.*,

vol. 34, no. 12, pp. 1715–1725, Dec. 2010.

[53] A. M. Lynch, N. Pathak, Y. E. Flatt, V. A. Gault, F. P. M. O'Harte, N. Irwin, and P. R. Flatt, "Comparison of stability, cellular, glucose-lowering and appetite supressing effects of oxyntomodulin analogues modified at the N-terminus.," *Eur. J. Pharmacol.*, vol. 743, pp. 69–78, Nov. 2014.

[54] S. L. Price, J. S. Minnion, and S. R. Bloom, "Increased food intake with oxyntomodulin analogues," *Peptides*, vol. 73, pp. 95–100, Nov. 2015.

[55] D. Balchin, M. Hayer-Hartl, and F. U. Hartl, "In vivo aspects of protein folding and quality control.," *Science*, vol. 353, no. 6294, p. aac4354, Jul. 2016.

[56] S. A. Broadley and F. U. Hartl, "The role of molecular chaperones in human misfolding diseases," *FEBS Lett.*, vol. 583, no. 16, pp. 2647–2653, Aug. 2009.

[57] T. Eichner and S. E. Radford, "A Diversity of Assembly Mechanisms of a Generic Amyloid Fold," *Mol. Cell*, vol. 43, no. 1, pp. 8–18, Jul. 2011.

[58] C. J. Francis, K. Lindorff-Larsen, R. B. Best, and M. Vendruscolo, "Characterization of the residual structure in the unfolded state of the Δ131Δ fragment of staphylococcal nuclease," *Proteins Struct. Funct. Bioinforma.*, vol. 65, no. 1, pp. 145–152, Jul. 2006.

[59] D. M. Walther, P. Kasturi, M. Zheng, S. Pinkert, G. Vecchi, P. Ciryam, R. I. Morimoto, C. M. Dobson, M. Vendruscolo, M. Mann, and F. U. Hartl, "Widespread Proteome Remodeling and Aggregation in Aging C. elegans," *Cell*, vol. 161, no. 4, pp. 919–932, May 2015.

[60] T. P. J. Knowles, M. Vendruscolo, and C. M. Dobson, "The physical basis of protein misfolding disorders," *Phys. Today*, vol. 68, no. 3, pp. 36–41, Mar. 2015.

[61] Y. Loo, S. Zhang, and C. a E. Hauser, "From short peptides to nanofibers to macromolecular assemblies in biomedicine," *Biotechnol. Adv.*, vol. 30, no. 3, pp. 593–603, May 2012.

[62] K. Matsuurua, "Rational design of self-assembled proteins and peptides for nano- and micro-sized architectures," *RSC Adv.*, vol. 4, no. 6, pp. 2942–2953, Nov. 2014.

[63] S. Vauthey, S. Santoso, H. Gong, N. Watson, and S. Zhang, "Molecular self-assembly of surfactant-like peptides to form nanotubes and nanovesicles," *Proc. Natl. Acad. Sci.*, vol. 99, no. 8, pp. 5355–5360, Apr. 2002.

[64] F. Chiti and C. M. Dobson, "Protein Misfolding, Amyloid Formation, and Human Disease: A Summary of Progress Over the Last Decade," *Annu. Rev. Biochem.*, vol. 86, no. 1, pp. 27–68, Jun. 2017.

[65] T. P. J. Knowles, M. Vendruscolo, and C. M. Dobson, "The amyloid state and its association with protein misfolding diseases.," *Nat. Rev. Mol. Cell Biol.*, vol. 15, no. 6, pp. 384–96, Jul. 2014.

[66] D. M. Fowler, A. V. Koulov, W. E. Balch, and J. W. Kelly, "Functional amyloid – from bacteria to humans," *Trends Biochem. Sci.*, vol. 32, no. 5, pp. 217–224, May 2007.

[67] S. J. Saupe, "A Short History of Small s," *Prion*, vol. 1, no. 2, pp. 110–115, Apr. 2007.

[68] K. Si, S. Lindquist, and E. R. Kandel, "A Neuronal Isoform of the Aplysia CPEB Has Prion-Like Properties," *Cell*, vol. 115, no. 7, pp. 879–891, Dec. 2003.

[69] D. M. Fowler, A. V Koulov, C. Alory-Jost, M. S. Marks, W. E. Balch, and J. W. Kelly, "Functional amyloid formation within mammalian tissue.," *PLoS Biol.*, vol. 4, no. 1, p. e6, Jan. 2006.

[70] R. Riek, "The three-dimensional structures of amyloids," *Cold Spring Harb. Perspect. Biol.*, vol. 9, no. 2, Feb. 2017.

[71] S. K. Maji, M. H. Perrin, M. R. Sawaya, S. Jessberger, K. Vadodaria, R. a Rissman, P. S. Singru, K. P. R. Nilsson, R. Simon, D. Schubert, D. Eisenberg, J. Rivier, P. Sawchenko, W. Vale, and R. Riek, "Functional amyloids as natural storage of peptide hormones in pituitary secretory granules.," *Science*, vol. 325, no. 5938, pp. 328–332, Jul. 2009.

[72] F. Zhao, M. L. Ma, and B. Xu, "Molecular hydrogels of therapeutic agents.," *Chem. Soc. Rev.*, vol. 38, no. 4, pp. 883–891, Apr. 2009.

[73] R. Hilgenfeld, G. Seipke, H. Berchtold, and D. R. Owens, "The Evolution of Insulin Glargine and its Continuing Contribution to Diabetes Care," *Drugs*, vol. 74, no. 8, pp. 911–927, Jun. 2014.

[74] A. Dasgupta, J. H. Mondal, and D. Das, "Peptide hydrogels," *RSC Adv.*, vol. 3, no. 24, p. 9117, Feb. 2013.

[75] P. K. Vemula, N. Wiradharma, J. A. Ankrum, O. R. Miranda, G. John, and J. M. Karp, "Prodrugs as self-assembled hydrogels: a new paradigm for biomaterials.," *Curr. Opin. Biotechnol.*, vol. 24, no. 6, pp. 1174–82, Dec. 2013.

[76] U. Shimanovich, G. J. L. Bernardes, T. P. J. Knowles, and A. Cavaco-Paulo, "Protein micro- and nano-capsules for biomedical applications," *Chem. Soc. Rev.*, vol. 43, no. 5, p. 1361, Dec. 2014.

[77] A. S. Hoffman, "Hydrogels for biomedical applications," *Adv. Drug Deliv. Rev.*, vol. 64, pp. 18–23, Dec. 2012.

[78] R. Kisilevsky, S. Raimondi, and V. Bellotti, "Historical and Current Concepts of Fibrillogenesis and In vivo Amyloidogenesis: Implications of Amyloid Tissue Targeting," *Front. Mol. Biosci.*, vol. 3, p. 17, May 2016.

[79] W. T. Astbury, S. Dickinson, and K. Bailey, "The X-ray interpretation of denaturation and the structure of the seed globulins.," *Biochem. J.*, vol. 29, no. 10, p. 2351–2360.1, Oct. 1935.

[80] C. M. Dobson and C. M. Dobson, "Protein misfolding, evolution and disease.," *Trends Biochem. Sci.*, vol. 24, no. 9, pp. 329–32, Sep. 1999.

[81] K. Rajagopal and J. P. Schneider, "Self-assembling peptides and proteins for nanotechnological applications.," *Curr. Opin. Struct. Biol.*, vol. 14, no. 4, pp. 480–6, Aug. 2004.

[82] J. Greenwald and R. Riek, "Biology of Amyloid: Structure, Function, and Regulation," *Structure*, vol. 18, no. 10, pp. 1244–1260, Oct. 2010.

[83] J. Adamcik, J.-M. Jung, J. Flakowski, P. De Los Rios, G. Dietler, and R. Mezzenga, "Understanding amyloid aggregation by statistical analysis of atomic force microscopy images," *Nat. Nanotechnol.*, vol. 5, no. 6, pp. 423–428, Jun. 2010.

[84] R. Nelson, M. R. Sawaya, M. Balbirnie, A. Ø. Madsen, C. Riekel, R. Grothe, and D. Eisenberg, "Structure of the cross-beta spine of amyloid-like fibrils.," *Nature*, vol. 435,

no. 7043, pp. 773–8, Jun. 2005.

[85] A. W. P. Fitzpatrick, G. T. Debelouchina, M. J. Bayro, D. K. Clare, M. A. Caporini, V. S. Bajaj, C. P. Jaroniec, L. Wang, V. Ladizhansky, S. A. Müller, C. E. MacPhee, C. A. Waudby, H. R. Mott, A. De Simone, T. P. J. Knowles, H. R. Saibil, M. Vendruscolo, E. V Orlova, R. G. Griffin, and C. M. Dobson, "Atomic structure and hierarchical assembly of a cross-β amyloid fibril.," *Proc. Natl. Acad. Sci. U. S. A.*, vol. 110, no. 14, pp. 5468–73, Apr. 2013.

[86] T. Stromer and L. C. Serpell, "Structure and morphology of the Alzheimer's amyloid fibril," *Microsc. Res. Tech.*, vol. 67, no. 3–4, pp. 210–217, Jul. 2005.

[87] W. Fitzpatrick, G. T. Debelouchina, M. J. Bayro, D. K. Clare, M. Caporini, V. S. Bajaj, C. P. Jaroniec, L. Wang, V. Ladizhansky, S. Muller, C. E. MacPhee, C. Waudby, H. R. Mott, De Simone, T. P. Knowles, H. R. Saibil, M. Vendruscolo, E. V. Orlova, R. G. Griffin, and C. M. Dobson, "Atomic structure and hierarchical assembly of a cross-beta amyloid fibril.," *Proc.Natl.Acad.Sci.USA*, vol. 110, pp. 5468–5473, Apr. 2013.

[88] K. L. De Jong, B. Incledon, C. M. Yip, and M. R. DeFelippis, "Amyloid fibrils of glucagon characterized by high-resolution atomic force microscopy.," *Biophys. J.*, vol. 91, no. 5, pp. 1905–1914, Sep. 2006.

[89] A. Aggeli, M. Bell, L. M. Carrick, C. W. G. Fishwick, R. Harding, P. J. Mawer, S. E. Radford, A. E. Strong, and N. Boden, "pH as a trigger of peptide β-sheet self-assembly and reversible switching between nematic and isotropic phases," *J. Am. Chem. Soc.*, vol. 125, no. 32, pp. 9619–9628, Jul. 2003.

[90] E. Frare, M. F. Mossuto, P. Polverino de Laureto, M. Dumoulin, C. M. Dobson, and A. Fontana, "Identification of the Core Structure of Lysozyme Amyloid Fibrils by Proteolysis," *J. Mol. Biol.*, vol. 361, no. 3, pp. 551–561, Jul. 2006.

[91] T. P. J. Knowles and M. J. Buehler, "Nanomechanics of functional and pathological amyloid materials," *Nat. Nanotechnol.*, vol. 6, no. 8, pp. 469–479, Jul. 2011.

[92] R. Tycko, "Physical and structural basis for polymorphism in amyloid fibrils," *Protein Sci.*, vol. 23, no. 11, Nov. 2014.

[93] R. Tycko and R. B. Wickner, "Molecular structures of amyloid and prion fibrils: consensus versus controversy.," *Acc. Chem. Res.*, vol. 46, no. 7, pp. 1487–96, Jul. 2013.

[94] C. B. Andersen, D. Otzen, G. Christiansen, and C. Rischel, "Glucagon amyloid-like fibril morphology is selected via morphology-dependent growth inhibition," *Biochemistry*, vol. 46, no. 24, pp. 7314–7324, Jun. 2007.

[95] C. Wasmer, A. Lange, H. Van Melckebeke, A. B. Siemer, R. Riek, and B. H. Meier, "Amyloid Fibrils of the HET-s(218-289) Prion Form a Solenoid with a Triangular Hydrophobic Core," *Science (80-.).*, vol. 319, no. 5869, pp. 1523–1526, Mar. 2008.

[96] M. Mompeán, R. Hervás, Y. Xu, T. H. Tran, C. Guarnaccia, E. Buratti, F. Baralle, L. Tong, M. Carrión-Vázquez, A. E. McDermott, and D. V. Laurents, "Structural Evidence of Amyloid Fibril Formation in the Putative Aggregation Domain of TDP-43," *J. Phys. Chem. Lett.*, vol. 6, no. 13, pp. 2608–2615, Jul. 2015.

[97] A. B. Soriaga, S. Sangwan, R. Macdonald, M. R. Sawaya, and D. Eisenberg, "Crystal Structures of IAPP Amyloidogenic Segments Reveal a Novel Packing Motif of Out-of-Register Beta Sheets," *J. Phys. Chem. B*, vol. 120, no. 26, pp. 5810–5816, Jul. 2016.

[98] M. R. Sawaya, S. Sambashivan, R. Nelson, M. I. Ivanova, S. A. Sievers, M. I. Apostol, M. J. Thompson, M. Balbirnie, J. J. W. Wiltzius, H. T. McFarlane, A. Ø. Madsen, C. Riekel, and D. Eisenberg, "Atomic structures of amyloid cross-β spines reveal varied steric zippers," *Nature*, vol. 447, no. 7143, pp. 453–457, May 2007.

[99] L. C. Serpell and J. M. Smith, "Direct visualisation of the β-sheet structure of synthetic Alzheimer's amyloid," *J. Mol. Biol.*, vol. 299, no. 1, pp. 225–231, May 2000.

[100] A. K. Paravastu, R. D. Leapman, W.-M. Yau, and R. Tycko, "Molecular structural basis for polymorphism in Alzheimer's beta-amyloid fibrils.," *Proc. Natl. Acad. Sci. U. S. A.*, vol. 105, no. 47, pp. 18349–54, Nov. 2008.

[101] A. T. Petkova, R. D. Leapman, Z. Guo, W.-M. Yau, M. P. Mattson, and R. Tycko, "Self-Propagating, Molecular-Level Polymorphism in Alzheimer's β-Amyloid Fibrils," *Science*, vol. 307, no. 5707, pp. 262–265, Jan. 2005.

[102] A. T. Petkova, Y. Ishii, J. J. Balbach, O. N. Antzutkin, R. D. Leapman, F. Delaglio, and R. Tycko, "A structural model for Alzheimer's -amyloid fibrils based on experimental constraints from solid state NMR," *Proc. Natl. Acad. Sci.*, vol. 99, no. 26, pp. 16742–16747, Dec. 2002.

[103] S. Ghodke, S. B. Nielsen, G. Christiansen, H. a. Hjuler, J. Flink, and D. Otzen, "Mapping out the multistage fibrillation of glucagon," *FEBS J.*, vol. 279, no. 5, pp. 752–765, Jan. 2012.

[104] I. Usov, J. Adamcik, and R. Mezzenga, "Polymorphism complexity and handedness inversion in serum albumin amyloid fibrils," *ACS Nano*, vol. 7, no. 12, pp. 10465–10474, Oct. 2013.

[105] D. J. Pochan, J. P. Schneider, J. Kretsinger, B. Ozbas, K. Rajagopal, and L. Haines, "Thermally reversible hydrogels via intramolecular folding and consequent self-assembly of a de novo designed peptide," *J. Am. Chem. Soc.*, vol. 125, no. 39, pp. 11802–11803, Sep. 2003.

[106] M. Owczarz, S. Bolisetty, R. Mezzenga, and P. Arosio, "Sol–gel transition of charged fibrils composed of a model amphiphilic peptide," *J. Colloid Interface Sci.*, vol. 437, pp. 244–251, Jan. 2015.

[107] L. R. Volpatti, M. Vendruscolo, C. M. Dobson, and T. P. J. Knowles, "A Clear View of Polymorphism, Twist and Chirality in Amyloid Fibril Formation," *ACS Nano*, vol. 7(12), pp. 10443–10448, Dec. 2013.

[108] F. Macchi, S. V Hoffmann, M. Carlsen, B. Vad, A. Imparato, C. Rischel, and D. E. Otzen, "Mechanical stress affects glucagon fibrillation kinetics and fibril structure.," *Langmuir*, vol. 27, no. 20, pp. 12539–49, Oct. 2011.

[109] T. Sneideris, D. Darguzis, A. Botyriute, M. Grigaliunas, R. Winter, and V. Smirnovas, "pH-Driven Polymorphism of Insulin Amyloid-Like Fibrils," *PLoS One*, vol. 10, no. 8, p. e0136602, Aug. 2015.

[110] J. S. Pedersen, "The Nature of Amyloid-like Glucagon Fibrils," *J. Diabetes Sci. Technol.*, vol. 4, no. 6, pp. 1357–1367, Nov. 2010.

[111] C. B. Andersen, M. R. Hicks, V. Vetri, B. Vandahl, H. Rahbek-Nielsen, H. Thøgersen, I. B. Thøgersen, J. J. Enghild, L. C. Serpell, C. Rischel, and D. E. Otzen, "Glucagon fibril polymorphism reflects differences in protofilament backbone structure," *J. Mol. Biol.*, vol. 397, no. 4, pp. 932–946, Apr. 2010.

[112] J. S. Pedersen, J. M. Flink, D. Dikov, and D. E. Otzen, "Sulfates Dramatically Stabilize a Salt-Dependent Type of Glucagon Fibrils," *Biophys. J.*, vol. 90, no. 11, pp. 4181–4194, Jun. 2006.

[113] J. S. Pedersen, D. Dikov, J. L. Flink, H. A. Hjuler, G. Christiansen, and D. E. Otzen, "The Changing Face of Glucagon Fibrillation: Structural Polymorphism and Conformational Imprinting," *J. Mol. Biol.*, vol. 355, no. 3, pp. 501–523, Jan. 2006.

[114] M. Sunde, L. C. Serpell, M. Bartlam, P. E. Fraser, M. B. Pepys, and C. C. . Blake, "Common core structure of amyloid fibrils by synchrotron X-ray diffraction," *J. Mol. Biol.*, vol. 273, no. 3, pp. 729–739, Oct. 1997.

[115] M. Sunde and C. Blake, "The Structure of Amyloid Fibrils by Electron Microscopy and X-Ray Diffraction," *Adv. Protein Chem.*, vol. 50, pp. 123–159, Jan. 1997.

[116] K. L. Morris and L. C. Serpell, "X-Ray Fibre Diffraction Studies of Amyloid Fibrils," *Methods Mol. Biol.*, vol. 849, pp. 121–135, Jan. 2012.

[117] J. L. Jiménez, E. J. Nettleton, M. Bouchard, C. V Robinson, C. M. Dobson, and H. R. Saibil, "The protofilament structure of insulin amyloid fibrils.," *Proc. Natl. Acad. Sci. U. S. A.*, vol. 99, no. 14, pp. 9196–9201, Jul. 2002.

[118] A. W. P. Fitzpatrick, B. Falcon, S. He, A. G. Murzin, G. Murshudov, H. J. Garringer, R. A. Crowther, B. Ghetti, M. Goedert, and S. H. W. Scheres, "Cryo-EM structures of tau filaments from Alzheimer's disease," *Nature*, vol. 547, no. 7662, pp. 185–190, Jul. 2017.

[119] R. Zhang, X. Hu, H. Khant, S. J. Ludtke, W. Chiu, M. F. Schmid, C. Frieden, and J.-M. Lee, "Interprotofilament interactions between Alzheimer's Abeta1-42 peptides in amyloid fibrils revealed by cryoEM.," *Proc. Natl. Acad. Sci. U. S. A.*, vol. 106, no. 12, pp. 4653–8, Mar. 2009.

[120] N. D. Younan and J. H. Viles, "A Comparison of Three Fluorophores for the Detection of Amyloid Fibers and Prefibrillar Oligomeric Assemblies. ThT (Thioflavin T); ANS (1-Anilinonaphthalene-8-sulfonic Acid); and bisANS (4,4-Dianilino-1,1-binaphthyl-5,5-disulfonic Acid)," *Biochemistry*, vol. 54, no. 28, Jul. 2015.

[121] P. Arosio, T. Cedervall, T. P. J. Knowles, and S. Linse, "Analysis of the length distribution of amyloid fibrils by centrifugal sedimentation," *Anal. Biochem.*, vol. 504, pp. 7–13, Jul. 2016.

[122] K. M. Batzli and B. J. Love, "Agitation of amyloid proteins to speed aggregation measured by ThT fluorescence: A call for standardization," *Mater. Sci. Eng. C*, vol. 48, pp. 359–364, Mar. 2015.

[123] K. Gade Malmos, L. M. Blancas-Mejia, B. Weber, J. Buchner, M. Ramirez-Alvarado, H. Naiki, and D. Otzen, "ThT 101: a primer on the use of thioflavin T to investigate amyloid formation," *Amyloid*, vol. 24(1), pp. 1-16, Apr. 2017.

[124] M. Biancalana and S. Koide, "Molecular mechanism of Thioflavin-T binding to amyloid fibrils.," *Biochim. Biophys. Acta*, vol. 1804, no. 7, pp. 1405–12, Jul. 2010.

[125] B. D. van Rooijen, K. A. van Leijenhorst-Groener, M. M. A. E. Claessens, and V. Subramaniam, "Tryptophan Fluorescence Reveals Structural Features of α-Synuclein Oligomers," *J. Mol. Biol.*, vol. 394, no. 5, pp. 826–833, Dec. 2009.

[126] Y. Zou, Y. Li, W. Hao, X. Hu, and G. Ma, "Parallel β-Sheet Fibril and Antiparallel β-Sheet Oligomer: New Insights into Amyloid Formation of Hen Egg White Lysozyme

under Heat and Acidic Condition from FTIR Spectroscopy," *J. Phys. Chem. B*, vol. 117, no. 15, pp. 4003–4013, Apr. 2013.

[127] S. D. Moran and M. T. Zanni, "How to get insight into amyloid structure and formation from infrared spectroscopy," *J. Phys. Chem. Lett.*, vol. 5(11), pp. 1984–1993, May 2014.

[128] K. Škerget, A. Vilfan, M. Pompe-Novak, V. Turk, J. P. Waltho, D. Turk, and E. Žerovnik, "The mechanism of amyloid-fibril formation by stefin B: Temperature and protein concentration dependence of the rates," *Proteins Struct. Funct. Bioinforma.*, vol. 74, no. 2, pp. 425–436, Feb. 2009.

[129] A. K. Buell, A. Dhulesia, D. a. White, T. P. J. Knowles, C. M. Dobson, and M. E. Welland, "Detailed analysis of the energy barriers for amyloid fibril growth," *Angew. Chemie*, vol. 51, no. 21, pp. 5247–5251, May 2012.

[130] T. Miti, M. Mulaj, J. D. Schmit, and M. Muschol, "Stable, metastable, and kinetically trapped amyloid aggregate phases," *Biomacromolecules*, vol. 16(1), Dec. 2015.

[131] D. R. Booth, M. Sunde, V. Bellotti, C. V. Robinson, W. L. Hutchinson, P. E. Fraser, P. N. Hawkins, C. M. Dobson, S. E. Radford, C. C. F. Blake, and M. B. Pepys, "Instability, unfolding and aggregation of human lysozyme variants underlying amyloid fibrillogenesis," *Nature*, vol. 385, no. 6619, pp. 787–793, Feb. 1997.

[132] S.-Y. Ow and D. E. Dunstan, "The effect of concentration, temperature and stirring on hen egg white lysozyme amyloid formation," *Soft Matter*, vol. 9, no. 40, p. 9692, Sep. 2013.

[133] Wojciech Dzwolak, Revanur Ravindra, and Julia Lendermann, and Roland Winter, "Aggregation of Bovine Insulin Probed by DSC/PPC Calorimetry and FTIR Spectroscopy," *Biochemistry*, vol. 42(38), pp. 11347-11355, Sep. 2003.

[134] A. Irbäck and S. Mohanty, "Folding Thermodynamics of Peptides," *Biophys. J.*, vol. 88, no. 3, pp. 1560–1569, Mar. 2005.

[135] V. Muñoz, P. A. Thompson, J. Hofrichter, and W. A. Eaton, "Folding dynamics and mechanism of β-hairpin formation," *Nature*, vol. 390, no. 6656, pp. 196–199, Nov. 1997.

[136] Y. Kusumoto, A. Lomakin, D. B. Teplow, and G. B. Benedek, "Temperature dependence of amyloid beta-protein fibrillization," *Biophys. Contrib. by Georg. B. Benedek*, vol. 95, pp. 12277–12282, Oct. 1998.

[137] W. Qiang, K. Kelley, and R. Tycko, "Polymorph-Specific Kinetics and Thermodynamics of β-Amyloid Fibril Growth," *J. Am. Chem. Soc.*, vol. 135, no. 18, pp. 6860–6871, May 2013.

[138] P. Arosio, T. P. J. Knowles, and S. Linse, "On the lag phase in amyloid fibril formation," *Phys. Chem. Chem. Phys.*, vol. 17, no. 12, pp. 7606–7618, Mar. 2015.

[139] T. C. T. Michaels and T. P. J. Knowles, "Mean-field master equation formalism for biofilament growth," *Am. J. Phys.*, vol. 82, no. 5, pp. 476–483, Apr. 2014.

[140] D. A. White, A. K. Buell, C. M. Dobson, M. E. Welland, and T. P. J. Knowles, "Biosensor-based label-free assays of amyloid growth," *FEBS Lett.*, vol. 583, no. 16, pp. 2587–2592, Aug. 2009.

[141] A. K. Buell, C. Galvagnion, R. Gaspar, E. Sparr, M. Vendruscolo, T. P. J. Knowles, S.

Linse, and C. M. Dobson, "Solution conditions determine the relative importance of nucleation and growth processes in α-synuclein aggregation.," *Proc. Natl. Acad. Sci. U. S. A.*, vol. 111, no. 21, pp. 7671–7676, May 2014.

[142] T. C. T. Michaels, L. X. Liu, G. Meisl, and T. P. J. Knowles, "Physical principles of filamentous protein self-assembly kinetics.," *J. Phys. Condens. Matter*, vol. 29, no. 15, p. 153002, Apr. 2017.

[143] T. P. J. Knowles, C. a Waudby, G. L. Devlin, S. I. a Cohen, A. Aguzzi, M. Vendruscolo, E. M. Terentjev, M. E. Welland, and C. M. Dobson, "An analytical solution to the kinetics of breakable filament assembly.," *Science*, vol. 326, no. 5959, pp. 1533–1537, Dec. 2009.

[144] D. Kashchiev, "Protein fibrillation due to elongation and fragmentation of initially appeared fibrils: A simple kinetic model," *J. Chem. Phys.*, vol. 139, no. 10, Sep. 2013.

[145] J. D. Schmit and J. D., "Kinetic theory of amyloid fibril templating.," *J. Chem. Phys.*, vol. 138, no. 18, p. 185102, May 2013.

[146] T. C. T. Michaels, G. a. Garcia, and T. P. J. Knowles, "Asymptotic solutions of the Oosawa model for the length distribution of biofilaments," *J. Chem. Phys.*, vol. 140, no. 19, May 2014.

[147] J. Kardos, K. Yamamoto, K. Hasegawa, H. Naiki, and Y. Goto, "Direct Measurement of the Thermodynamic Parameters of Amyloid Formation by Isothermal Titration Calorimetry," *J. Biol. Chem.*, vol. 279, no. 53, pp. 55308–55314, Dec. 2004.

[148] B. O'Nuallain, S. Shivaprasad, I. Kheterpal, and R. Wetzel, "Thermodynamics of Aβ(1−40) Amyloid Fibril Elongation †," *Biochemistry*, vol. 44, no. 38, pp. 12709–12718, Sep. 2005.

[149] M. So, D. Hall, and Y. Goto, "Revisiting supersaturation as a factor determining amyloid fibrillation," *Curr. Opin. Struct. Biol.*, vol. 36, pp. 32–39, Feb. 2016.

[150] R. P. McGlinchey, J. M. Gruschus, A. Nagy, and J. C. Lee, "Probing Fibril Dissolution of the Repeat Domain of a Functional Amyloid, Pmel17, on the Microscopic and Residue Level," *Biochemistry*, vol. 50, no. 49, pp. 10567–10569, Dec. 2011.

[151] R. K. Brummitt, J. M. Andrews, J. L. Jordan, E. J. Fernandez, and C. J. Roberts, "Thermodynamics of amyloid dissociation provide insights into aggregate stability regimes," *Biophys. Chem.*, vol. 168–169, pp. 10–18, Jul. 2012.

[152] G. I. Makhatadze and P. L. Privalov, "Energetics of Protein Structure," *Adv. Protein Chem.*, vol. 47, pp. 307–425, Jan. 1995.

[153] K. Sasahara, H. Naiki, and Y. Goto, "Kinetically Controlled Thermal Response of β 2 - Microglobulin Amyloid Fibrils." *Journal of Mol. Biol.*, vol. 352(3), pp. 700-711, Sep. 2005.

[154] M. D. Jeppesen, P. Westh, and D. E. Otzen, "The role of protonation in protein fibrillation," *FEBS Lett.*, vol. 584, no. 4, pp. 780–784, Feb. 2010.

[155] M. D. Jeppesen, K. Hein, P. Nissen, P. Westh, and D. E. Otzen, "A thermodynamic analysis of fibrillar polymorphism," *Biophys. Chem.*, vol. 149, no. 1–2, pp. 40–46, Jun. 2010.

[156] A. Arora, C. Ha, and C. B. Park, "Insulin amyloid fibrillation at above 100°C: New insights into protein folding under extreme temperatures," *Protein Sci.*, vol. 13, no. 9,

pp. 2429–2436, Sep. 2004.

[157] B. Morel, L. Varela, and F. Conejero-Lara, "The Thermodynamic Stability of Amyloid Fibrils Studied by Differential Scanning Calorimetry," *J. Phys. Chem. B*, vol. 114, no. 11, pp. 4010–4019, Mar. 2010.

[158] E. Shakhnovich, "Protein Folding Thermodynamics and Dynamics: Where Physics, Chemistry, and Biology Meet," *ACS Chem. Rev.*, vol. 106(5), pp. 1559-1588, Apr. 2006.

[159] A. K. Buell, J. R. Blundell, C. M. Dobson, M. E. Welland, E. M. Terentjev, and T. P. J. Knowles, "Frequency factors in a landscape model of filamentous protein aggregation," *Phys. Rev. Lett.*, vol. 104, no. 22, pp. 1–4, Jun. 2010.

[160] D. R. Picout and S. B. Ross-Murphy, "Rheology of Biopolymer Solutions and Gels," *Sci. World J.*, vol. 3, pp. 105–121, 2003.

[161] N. Sreerama and R. W. Woody, "Estimation of Protein Secondary Structure from Circular Dichroism Spectra: Comparison of CONTIN, SELCON, and CDSSTR Methods with an Expanded Reference Set," *Anal. Biochem.*, vol. 287, no. 2, pp. 252–260, Dec. 2000.

[162] L. Whitmore and B. A. Wallace, "Protein secondary structure analyses from circular dichroism spectroscopy: Methods and reference databases," *Biopolymers*, vol. 89, no. 5, pp. 392–400, May 2008.

[163] S. M. Kelly, T. J. Jess, and N. C. Price, "How to study proteins by circular dichroism," *Biochim. Biophys. Acta - Proteins Proteomics*, vol. 1751, no. 2, pp. 119–139, Aug. 2005.

[164] R. Sarroukh, E. Goormaghtigh, J.-M. Ruysschaert, and V. Raussens, "ATR-FTIR: A 'rejuvenated' tool to investigate amyloid proteins," *Biochim. Biophys. Acta - Biomembr.*, vol. 1828, no. 10, pp. 2328–2338, Oct. 2013.

[165] R. J. Tidy, V. Lam, N. Fimognari, J. C. Mamo, and M. J. Hackett, "FTIR studies of the similarities between pathology induced protein aggregation in vivo and chemically induced protein aggregation ex vivo," *Vib. Spectrosc.*, vol. 91, pp. 68–76, Jul. 2017.

[166] A. Barth, "Infrared spectroscopy of proteins," *Biochim. Biophys. Acta - Bioenerg.*, vol. 1767, no. 9, pp. 1073–1101, Sep. 2007.

[167] H. Yagi, Y. Abe, N. Takayanagi, and Y. Goto, "Elongation of amyloid fibrils through lateral binding of monomers revealed by total internal reflection fluorescence microscopy," *Biochim. Biophys. Acta - Proteins Proteomics*, vol. 1844(10), pp. 1881-1888, Oct. 2014.

[168] S. E. Glassford, B. Byrne, and S. G. Kazarian, "Recent applications of ATR FTIR spectroscopy and imaging to proteins," *Biochim. Biophys. Acta - Proteins Proteomics*, vol. 1834, no. 12, pp. 2849–2858, Dec. 2013.

[169] J. Kong and S. Yu, "Fourier transform infrared spectroscopic analysis of protein secondary structures.," *Acta Biochim. Biophys. Sin. (Shanghai).*, vol. 39, no. 8, pp. 549–59, Aug. 2007.

[170] M. Calero and M. Gasset, "Fourier Transform Infrared and Circular Dichroism Spectroscopies for Amyloid Studies," *Amyloid Proteins*, n: Sigurdsson E.M. (eds) Amyloid Proteins. Methods in Molecular Biology™ vol. 299, pp. 129–152, 2005.

[171] E. Frare, M. F. Mossuto, P. Polverino de Laureto, M. Dumoulin, C. M. Dobson, and A. Fontana, "Identification of the Core Structure of Lysozyme Amyloid Fibrils by Proteolysis," *J. Mol. Biol.*, vol. 361, no. 3, pp. 551–561, Aug. 2006.

[172] I. Kheterpal, A. Williams, C. Murphy, B. Bledsoe, and R. Wetzel, "Structural features of the Abeta amyloid fibril elucidated by limited proteolysis.," *Biochemistry*, vol. 40, no. 39, pp. 11757–67, Oct. 2001.

[173] I. Kheterpal, M. Chen, K. D. Cook, and R. Wetzel, "Structural Differences in Aβ Amyloid Protofibrils and Fibrils Mapped by Hydrogen Exchange – Mass Spectrometry with On-line Proteolytic Fragmentation," *J. Mol. Biol.*, vol. 361, no. 4, pp. 785–795, Aug. 2006.

[174] P. Polverino de Laureto, N. Taddei, E. Frare, C. Capanni, S. Costantini, J. Zurdo, F. Chiti, C. M. Dobson, and A. Fontana, "Protein Aggregation and Amyloid Fibril Formation by an SH3 Domain Probed by Limited Proteolysis," *J. Mol. Biol.*, vol. 334, no. 1, pp. 129–141, Nov. 2003.

[175] E. Nogales, "The development of cryo-EM into a mainstream structural biology technique," *Nat. Methods*, vol. 13, no. 1, pp. 24–27, Jan. 2016.

[176] J. L. Jiménez, J. I. Guijarro, E. Orlova, J. Zurdo, C. M. Dobson, M. Sunde, and H. R. Saibil, "Cryo-electron microscopy structure of an SH3 amyloid fibril and model of the molecular packing.," *EMBO J.*, vol. 18, no. 4, pp. 815–21, Feb. 1999.

[177] A. K. Buell, C. M. Dobson, and M. E. Welland, "Measuring the Kinetics of Amyloid Fibril Elongation Using Quartz Crystal Microbalances," in *Methods in molecular biology (Clifton, N.J.)*, vol. 849, pp. 101–119, 2012.

[178] T. P. J. Knowles, W. Shu, G. L. Devlin, S. Meehan, S. Auer, C. M. Dobson, and M. E. Welland, "Kinetics and thermodynamics of amyloid formation from direct measurements of fluctuations in fibril mass.," *Proc. Natl. Acad. Sci. U. S. A.*, vol. 104, no. 24, pp. 10016–10021, Jun. 2007.

[179] G. Sauerbrey, "Verwendung von Schwingquarzen zur Wägung dünner Schichten und zur Mikrowägung," *Zeitschrift für Phys.*, vol. 155, no. 2, pp. 206–222, Apr. 1959.

[180] F. Höök and B. Kasemo, "The QCM-D Technique for Probing Biomacromolecular Recognition Reactions," In: Janshoff A., Steinem C. (eds) Piezoelectric Sensors. Springer Series on Chemical Sensors and Biosensors (Methods and Applications), vol 5., pp. 425–447, 2006.

[181] D. Johannsmann, I. Reviakine, and R. P. Richter, "Dissipation in Films of Adsorbed Nanospheres Studied by Quartz Crystal Microbalance (QCM)," *Anal. Chem.*, vol. 81, no. 19, pp. 8167–8176, Oct. 2009.

[182] A. K. Buell, D. a. White, C. Meier, M. E. Welland, T. P. J. Knowles, and C. M. Dobson, "Surface attachment of protein fibrils via covalent modification strategies," *J. Phys. Chem. B*, vol. 114, no. 34, pp. 10925–10938, Aug. 2010.

[183] T. Takeda and D. K. Klimov, "Temperature-Induced Dissociation of Aβ Monomers from Amyloid Fibril," *Biophys. J.*, vol. 95, no. 4, pp. 1758–1772, Aug. 2008.

[184] O. G. Jones and R. Mezzenga, "Inhibiting, promoting, and preserving stability of functional protein fibrils." *Soft Matter*, vol. 4, pp. 876-895, Oct. 2011.

[185] J. Kardos, A. Micsonai, H. Pál-Gábor, E. Petrik, L. Gráf, J. Kovács, Y.-H. Lee, H. Naiki, and Y. Goto, "Reversible Heat-Induced Dissociation of β $_2$ -Microglobulin

Amyloid Fibrils," *Biochemistry*, vol. 50, no. 15, pp. 3211–3220, Apr. 2011.

[186] Kenji Sasahara, and Hironobu Naiki, and Yuji Goto, "Exothermic Effects Observed upon Heating of β2-Microglobulin Monomers in the Presence of Amyloid Seeds," *Biochemistry*, vol. 45(29), pp.8760-8769, Jun 2006.

[187] O. Gursky and S. Aleshkov, "Temperature-dependent β-sheet formation in β-amyloid Aβ1–40 peptide in water: uncoupling β-structure folding from aggregation," *Biochim. Biophys. Acta - Protein Struct. Mol. Enzymol.*, vol. 1476, no. 1, pp. 93–102, Jan. 2000.

[188] M. Kjaergaard, A.-B. Nørholm, R. Hendus-Altenburger, S. F. Pedersen, F. M. Poulsen, and B. B. Kragelund, "Temperature-dependent structural changes in intrinsically disordered proteins: Formation of α-helices or loss of polyproline II?," *Protein Sci.*, vol. 19, no. 8, pp. 1555–1564, Jul. 2010.

[189] L. J. Young, G. S. Kaminski Schierle, and C. F. Kaminski, "Imaging Aβ(1–42) fibril elongation reveals strongly polarised growth and growth incompetent states," *Phys. Chem. Chem. Phys.*, vol. 19, no. 41, pp. 27987–27996, Oct. 2017.